UNDERSTANDING HYDROLOGICAL EXTREMES AND THEIR IMPACT IN A CHANGING CLIMATE: OBSERVATIONS, MODELING AND ATTRIBUTION

EDITED BY: Xingcai Liu, Pedram Attarod and Zhe Li
PUBLISHED IN: Frontiers in Earth Science

frontiers Research Topics

ISSN 1664-8714
ISBN 978-2-88966-594-5
DOI 10.3389/978-2-88966-594-5

About Frontiers

Frontiers is more than just an open-access publisher of scholarly articles: it is a pioneering approach to the world of academia, radically improving the way scholarly research is managed. The grand vision of Frontiers is a world where all people have an equal opportunity to seek, share and generate knowledge. Frontiers provides immediate and permanent online open access to all its publications, but this alone is not enough to realize our grand goals.

Frontiers Journal Series

The Frontiers Journal Series is a multi-tier and interdisciplinary set of open-access, online journals, promising a paradigm shift from the current review, selection and dissemination processes in academic publishing. All Frontiers journals are driven by researchers for researchers; therefore, they constitute a service to the scholarly community. At the same time, the Frontiers Journal Series operates on a revolutionary invention, the tiered publishing system, initially addressing specific communities of scholars, and gradually climbing up to broader public understanding, thus serving the interests of the lay society, too.

Dedication to Quality

Each Frontiers article is a landmark of the highest quality, thanks to genuinely collaborative interactions between authors and review editors, who include some of the world's best academicians. Research must be certified by peers before entering a stream of knowledge that may eventually reach the public - and shape society; therefore, Frontiers only applies the most rigorous and unbiased reviews.
Frontiers revolutionizes research publishing by freely delivering the most outstanding research, evaluated with no bias from both the academic and social point of view. By applying the most advanced information technologies, Frontiers is catapulting scholarly publishing into a new generation.

What are Frontiers Research Topics?

Frontiers Research Topics are very popular trademarks of the Frontiers Journals Series: they are collections of at least ten articles, all centered on a particular subject. With their unique mix of varied contributions from Original Research to Review Articles, Frontiers Research Topics unify the most influential researchers, the latest key findings and historical advances in a hot research area! Find out more on how to host your own Frontiers Research Topic or contribute to one as an author by contacting the Frontiers Editorial Office: frontiersin.org/about/contact

UNDERSTANDING HYDROLOGICAL EXTREMES AND THEIR IMPACT IN A CHANGING CLIMATE: OBSERVATIONS, MODELING AND ATTRIBUTION

Topic Editors:
Xingcai Liu, Chinese Academy of Sciences, China
Pedram Attarod, University of Tehran, Iran
Zhe Li, University of Wisconsin-Madison, United States

Citation: Liu, X., Attarod, P., Li, Z., eds. (2021). Understanding Hydrological Extremes and their Impact in a Changing Climate: Observations, Modeling and Attribution. Lausanne: Frontiers Media SA. doi: 10.3389/978-2-88966-594-5

Table of Contents

frontiers in Earth Science

EDITORIAL
published: 18 February 2021
doi: 10.3389/feart.2020.632186

Editorial: Understanding Hydrological Extremes and Their Impact in a Changing Climate: Observations, Modeling and Attribution

Xingcai Liu[1]*, *Zhe Li*[2] *and Pedram Attarod*[3]

[1]Institute of Geographic Sciences and Natural Resources Research, Chinese Academy of Sciences, Beijing, China, [2]Department of Civil and Environmental Engineering, University of Wisconsin-Madison, Madison, WI, United States, [3]Department of Forestry and Forest Economics, Faculty of Natural Resources, College of Agriculture and Natural Resources,University of Tehran, Karaj, Iran

Keywords: hydrological extremes, climate change, detection and attribution, models, drought index, human activities

Editorial on the Research Article

Understanding Hydrological Extremes and their Impact in a Changing Climate: Observations, Modeling and Attribution

The hydrological regimes have been significantly altered by climate change and human activities, which have resulted in increased hydrological extreme events such as floods and drought over the world (Samaniego et al., 2018) and it seems likely this trend will continue in the future (Liu et al., 2019a). Better understanding and forecast of hydroclimatic extremes are required for mitigating the impacts of the extreme events in the context of global warming. This calls for in-depth investigations on evolution and mechanism of hydroclimatic extremes. So far, the assessment and attribution of the hydrological extremes and their impacts on the regional/global scales remain a great challenge (Schewe et al., 2019). Hydrological models are powerful and physically-based tools for the assessment of hydrological extremes, while the statistical indices are efficient and data-driven approaches based on hydroclimatic observations for identifying and assessing flood and drought events. This special issue focuses on the development and application of various model- and index-based techniques for the detection and attribution of the changes in hydroclimatic extremes induced by climate change and human activities.

To understand the uncertainty in the widely used Standardized Precipitation Index (SPI), Zhang and Li (2020) investigated the effects of probability distributions and parameter errors on the estimates of SPI in the Heihe River basin, northwest China. Ten probability distributions were tested and the SPI using log-logistic-type distribution produced similar results as the benchmark SPI using the gamma distribution. As one of the most sensitive regions to climate change, the assessment and attribution of the changes in water resources in the Yarlung Zangbo river have attracted much attention of hydrologists during the 21st century (Yao et al., 2010; Tang et al., 2019). Niu et al. (2020) evaluated the drought characteristics in the Yarlung Zangbo River basin from a different perspective by using SPI, Soil Water Deficit Index (SWDI), and self-calibrating Palmer Drought Severity Index (PDSI) based on the output from Global Land Data Assimilation System and the Climate Research Unit dataset. The three indices indicated that drought conditions have aggregated to different degrees over the basin. The increased drought may be partly due to climate change in this basin (Lutz et al., 2014), however, the attribution of the changes in hydroclimatic extremes remains subject to large

Edited and reviewed by:
Nick Van De Giesen,
Delft University of Technology,
Netherlands

***Correspondence:**
Xingcai Liu
xingcailiu@igsnrr.ac.cn

Specialty section:
This article was submitted to Hydrosphere a section of the journal Frontiers in Earth Science

Received: *22 November 2020*
Accepted: *27 November 2020*
Published: *18 February 2021*

Citation:
Liu X, Li Z and Attarod P (2021) Editorial: Understanding Hydrological Extremes and Their Impact in a Changing Climate: Observations, Modeling and Attribution. Front. Earth Sci. 8:632186. doi: 10.3389/feart.2020.632186

uncertainty because of human interventions and the lack of high-quality observations in such mountainous river basins.

The regional extremes are often not merely caused by the hydroclimatic variations on the local scale. Hamal et al. (2020) pointed out that dry and wet conditions over the Tibetan Plateau and surrounding areas might be significantly associated with large-scale circulations, e.g., the cyclonic and anticyclonic circulation in northern India. They showed that surface air temperature over these regions was colder in wet years than dry years. Further investigation on the relations linking dry/wet conditions, large-scale circulations, and heat extremes would definitely benefit the forecasts of regional extreme weather (Liu et al., 2019b).

Human activities would often aggregate hydroclimatic extremes under climate change, which can be better represented via hydrological models. By developing a water resources allocation model, Zeng et al. (2020) showed that water deficit would be largely mitigated along the east route of the South-to-North Water Transfer Project in Jiangsu Province, China. Based on remote sensing data, Song et al. (2020) pointed out that the coastal wetland has shrunk substantially during the past four decades mainly due to seaward shifting caused by human interventions such as intensive land reclamation. Intertidal wetland conservation should be a high priority over this region because the sea level was projected to rise more than 0.5 m around China seas in the future due to global warming (Qu et al., 2019). In the research report of Xiao and Li (2020), a simulation of the downward groundwater leakage rate based on the MODFLOW model was conducted to examine the risk of sinkhole hazards induced by human activities. Hydroclimatic extremes can have further impacts on water resources. Dang et al. (2020) reported that the intensification of extreme precipitation would significantly increase sediment yield in many branches of the Yellow River based on a scenario analysis, which may cause deterioration of the water environment in the Yellow River basin.

AUTHOR CONTRIBUTIONS

XL wrote the draft of the manuscript, ZL and PA editted and commented on the draft. All authors approved the manuscript for publication.

ACKNOWLEDGMENTS

We thank all the reviewers for reviewing the papers in the special issue. This research was funded by the National Natural Science Foundation of China (No. 41877164).

REFERENCES

Liu, X., Tang, Q., Liu, W., Veldkamp, T. I. E., Boulange, J., Liu, J., et al. (2019a). A spatially explicit assessment of growing water stress in China from the past to the future. *Earths Future* 7, 1027–1043. doi:10.1029/2019ef001181

Liu, X., Tang, Q., Liu, W., Yang, H., Groisman, P. Y., Leng, G., et al. (2019b). The asymmetric impact of abundant preceding rainfall on heat stress in low latitudes. *Environ. Res. Lett.* 14, 044010. doi:10.1088/1748-9326/ab018a

Lutz, A. F., Immerzeel, W. W., Shrestha, A. B., and Bierkens, M. F. P. (2014). Consistent increase in High Asia's runoff due to increasing glacier melt and precipitation. *Nature Clim. Change* 4, 587–592. doi:10.1038/nclimate2237

Qu, Y., Jevrejeva, S., Jackson, L. P., and Moore, J. C. (2019). Coastal Sea level rise around the China Seas. *Global Planet. Change* 172, 454–463. doi:10.1016/j.gloplacha.2018.11.005

Samaniego, L., Thober, S., Kumar, R., Wanders, N., Rakovec, O., Pan, M., et al. (2018). Anthropogenic warming exacerbates European soil moisture droughts. *Nat. Clim. Change* 8, 421–426. doi:10.1038/s41558-018-0138-5

Schewe, J., Gosling, S. N., Reyer, C., Zhao, F., Ciais, P., Elliott, J., et al. (2019). State-of-the-art global models underestimate impacts from climate extremes. *Nat. Commun.* 10, 1005. doi:10.1038/s41467-019-08745-6

Tang, Q., Lan, C., Su, F., Liu, X., Sun, H., Ding, J., et al. (2019). Streamflow change on the Qinghai-Tibet Plateau and its impacts. *Chin. Sci. Bull.,* 64, 2807–2821. doi:10.1360/TB-2019-0141

Yao, T., Li, Z., Yang, W., Guo, X., Zhu, L., Kang, S., et al. (2010). Glacial distribution and mass balance in the Yarlung Zangbo River and its influence on lakes. *Chin. Sci. Bull.* 55 (20), 2072–2078. doi:10.1007/s11434-010-3213-5

Conflict of Interest: The authors declare that the research was conducted in the absence of any commercial or financial relationships that could be construed as a potential conflict of interest.

frontiers in Earth Science

ORIGINAL RESEARCH
published: 14 February 2020
doi: 10.3389/feart.2020.00016

Mapping the Rapid Decline of the Intertidal Wetlands of China Over the Past Half Century Based on Remote Sensing

Song Song[1], *Zhifeng Wu*[1]*, *Yuefeng Wang*[2]*, *Zheng Cao*[1], *Zhenyu He*[1,3] and *Yongsong Su*[1,3]

[1] School of Geographical Sciences, Guangzhou University, Guangzhou, China, [2] School of Geography and Tourism, Chongqing Normal University, Chongqing, China, [3] Southern Marine Science and Engineering Guangdong Laboratory, Guangzhou, China

Intertidal wetland, located at the interface of the continent and ocean, provides significant support to human society. With China being the largest developing country and the second-biggest economy in the world, the intertidal wetland along its coast has been exposed to climate change and over-exploitation for decades. Despite its ecological and economic significance, the distribution and variation of the intertidal wetland remains unknown. In this study, based on a multi-temporal remote sensing archive accumulated since the 1970s, we detected the dynamics of the intertidal wetland along China's coast, at a spatial resolution of 30 m and a time interval of 20 years, over the course of four decades (1970s–2015). The main objectives of this study lie in (1) examining the distribution of and variation in intertidal wetland extent in temporal and spatial aspects; (2) identifying the main driving force of the intertidal wetland dynamics; and (3) making suggestions for future research and management. The results suggest that the extent of intertidal wetland declined substantially during the last four decades, from 7848 km^2 in the 1970s, to 6017 km^2 in 1995, and finally to 4895 km^2 in 2015. On average, the intertidal wetland was 0.22 km in width along the coast, and about 40% of the extent of intertidal wetland was located along the Jiangsu and Shandong coast in 2015. Width shrinkage was detected to be primarily due to seaward migration of the intertidal wetland as a result of intensive land reclamation for tourism, communication, and transportation, as well as the fishery industry. This study improved our understanding of the vulnerable but valuable transition zone covered by intertidal wetland. A high priority should be given to intertidal wetland conservation and habitat reconstruction with a view to a sustainable future.

Keywords: intertidal wetland loss, land reclamation, seaward migration, China, anthropogenic activity

Edited by:
Xingcai Liu,
Institute of Geographic Sciences and Natural Resources Research (CAS), China

Reviewed by:
Guy Jean-Pierre Schumann,
University of Bristol, United Kingdom
Jike Chen,
Nanjing University of Information Science and Technology, China
Deirdre McKay,
Keele University, United Kingdom

***Correspondence:**
Zhifeng Wu
zfwu@gzhu.edu.cn
Yuefeng Wang
yuefeng_wang@cqnu.edu.cn

Specialty section:
This article was submitted to Hydrosphere, a section of the journal Frontiers in Earth Science

Received: *12 November 2019*
Accepted: *20 January 2020*
Published: *14 February 2020*

Citation:
Song S, Wu Z, Wang Y, Cao Z, He Z and Su Y (2020) Mapping the Rapid Decline of the Intertidal Wetlands of China Over the Past Half Century Based on Remote Sensing. Front. Earth Sci. 8:16. doi: 10.3389/feart.2020.00016

INTRODUCTION

Intertidal wetlands are environmentally significant coastal zones linking the freshwater river system and the salty oceanic system and serve as a buffer zone between the oceanic and terrestrial ecosystems that is characterized by diverse physicochemical, morphological, and hydrological conditions (Deegan et al., 2012; Murray et al., 2019). The combination of highly varying environmental parameters brings both valuable services (Airoldi and Beck, 2007; Barbier, 2015; Gabler et al., 2017) and ecological vulnerability (Vafeidis et al., 2008; Jankowski et al., 2017; Vázquez-González et al., 2019) to the intertidal wetlands. The services provided by intertidal wetlands include storm protection (Barbier, 2015), shoreline stabilization (Fujii, 2012; Kirwan and Megonigal, 2013), habitat support (Davidson, 2018), pollution purification (Nwipie et al., 2019), carbon sequestration (Ribaudo et al., 2016), and goods and energy generation (Murray et al., 2019; Paterson et al., 2019). Despite the invaluable environmental role and exceptional economic value of intertidal wetland (Costanza et al., 2014; Vázquez-González et al., 2019), intertidal wetland is being lost at an unprecedented rate due to the overwhelming stress caused by climate change, and human interference (Deegan et al., 2012; Murray et al., 2014; Davidson, 2018). Monitoring and management of intertidal flats toward a more sustainable pattern are consequently becoming crucial to prevent coastal erosion, degradation, and destruction of the inhabitants (Syvitski et al., 2009; Mason et al., 2010). Recent research shows the applicability of remote sensing data from earth observation satellites in coastline and coastal wetland tracking, especially at large spatial scale (Murray et al., 2014, 2019; Sagar et al., 2017). Extensive research on coastal flats at local and national scales has been implemented with various data sources, for example, IGBP-DISCover data (Loveland et al., 2000), 500-m MODIS information, the 30-m Landsat TM and ETM + images (Gong et al., 2010), LIDAR model output (Crowell et al., 2011), and the combination of aerial photographs and satellite imagery (Ford, 2013). The majority of studies have focused on coastal parameters, like the coastline, ecosystem, or coastal land use pattern, while the intertidal wetland has not received sufficient investigation. National-wide research on the intertidal zone in China highlighted the social-economic role of the coastal system and mainly focused on description and estimation of the ecological service, biodiversity, management strategy, and countermeasures for the degradation of the coastal wetland, based on statistical information and published reports (Ma et al., 2014; Cui et al., 2016; Gu et al., 2018). Estimation of Chinese intertidal flats and wetland based on remote sensing data has attracted a large amount of attention in recent years, especially at local scale (Wei et al., 2015; Chen et al., 2016; Wu X. et al., 2017). A recent national-wide study provided a glimpse of the intertidal flats from 1986 to 2016 based on the google earth engine (GEE) (Wang et al., 2018), but it missed the crucial time range since the Opening Up policy was put in place in 1976. In addition, the GEE results are advantageous for data acquisition efficiency but are relatively higher and might need further calibration to be compatible with the observed data (Murray et al., 2014).

The accelerating rate of intertidal wetland loss and deterioration, and its significance in coastal defense and ecological service supporting result in severe human-wetland conflicts. Dynamic intertidal wetland monitoring would fully investigate this valuable resource to a uniform standard and provide a database foundation for further evaluation, restoration, and protection analysis, especially in rapidly developing countries like China. Besides, only statistical data and paper maps were available as information sources in related research on coastal wetland. The difficulty of effective data acquisition impeded the survey, estimation, and assessment of the intertidal wetland at a large spatial scale. The accumulation of a long-term remote sensing archive with sufficient spatial resolution had enabled synoptic, integrated, and spatio-temporal perspectives in the comprehensive research of land-use change and natural resource management. Despite the widespread application of remote sensing data and its related techniques in intertidal flats and coastal resources all over the world, no systematic investigation of intertidal wetland along the entire Chinese coast has been carried out to our knowledge. In this study, we mapped the multi-temporal intertidal wetland patterns at national and provincial scales based on the high-resolution remoting sensing images in the 1970s, 1995, and 2015. Through the comparison of slices at two-decade intervals, the exceptional dynamics of the intertidal wetland are illustrated, the spatial and temporal variation of the intertidal wetland is analyzed, and the driving mechanisms of the variation are discussed.

MATERIALS AND METHODS

Study Area

The continental coastline of China starts in Dandong, Liaoning Province, and ends in Zhushan, Guangxi Province, stretching over 18000 km; the remaining 14000 km is composed of island coastline (**Figure 1A**). The continental part stretches over nearly 20 latitudes and covers three climatic regions, namely warm temperate, subtropical, and tropical regions from north to south (Hou et al., 2016).

A variety of coast types have been recognized, including bedrock, sandy, silty mud, artificial, and estuary. In total, 14 administrative areas with various economic strengths sit beside the coastline (**Figure 1A** and **Table 1**). To the east of the coastline are the Bohai Sea, Yellow Sea, East China Sea, and South China Sea from north to south, whose tidal fluctuations generate a strip of intertidal wetland along the coast. In 2015 documents, 4873 km^2 of intertidal wetland was identified, spanning unevenly over the coast, and within the administrative regions (**Figure 1B**). The combination of the varied physical and economic environments results in multiple exploitation levels of the intertidal region.

Data Acquisition and Processing

The term intertidal wetland refers to the region between the highest and lowest tide level, which is regularly submerged at high tide but exposed above sea level at low tide (**Figure 2**). Landsat-MSS/TM/8 multi-temporal satellite image data from the 1970s, 1995, and 2015 covering the study area were collected and interpreted with human-PC interactive technology (**Table 2**). The intertidal wetland can be clearly recognized from the false-color composited images of the remote-sensed data according to characteristic symbols. Unified interpretation

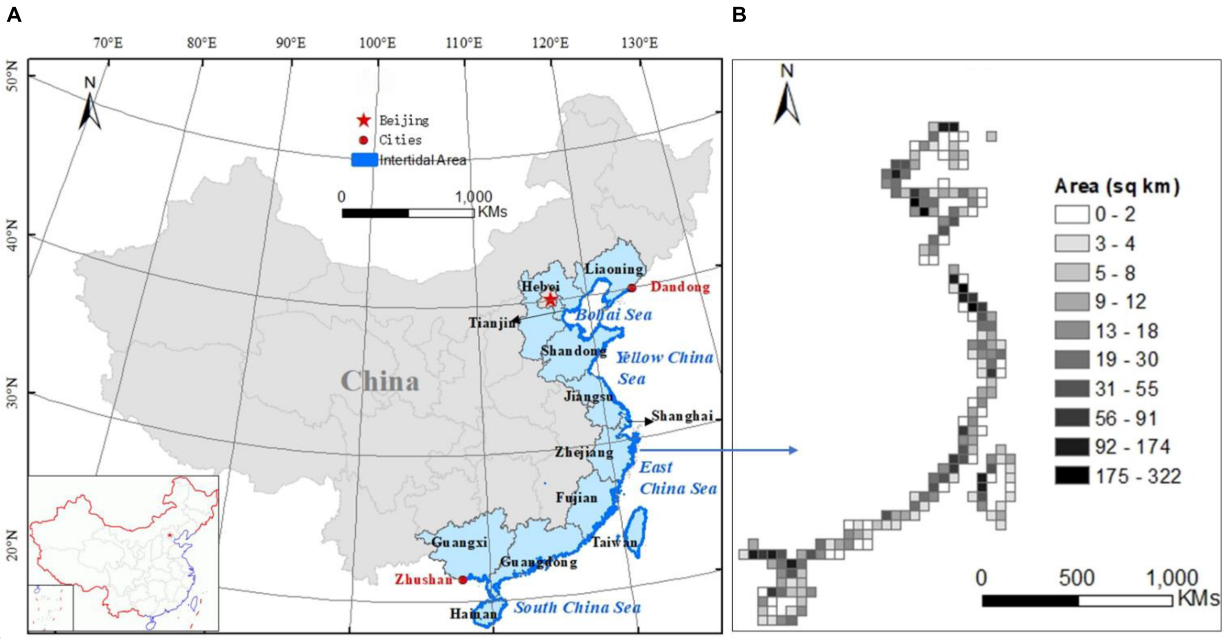

FIGURE 1 | The location of the Chinese intertidal zone **(A)** and its area distribution at 50-km resolution **(B)**. The location and distribution map are based on 2015 data.

TABLE 1 | Intertidal wetland distribution and coast type among provinces.

Administrative region	Coastline length (km)	Area) (km^2)	IW[1] area (km^2)	GDP (100 million rmb)[2]	Coast type
Liaoning	2110	146106	281.41	28669	Bedrock, sandy, silty mud, artificial, and estuaries
Hebei	485	186504	184.04	29806	Bedrock, sandy, silty mud, artificial, and estuaries
Tianjin	153	11462	123.31	16538	Artificial
Shandong	3345	156516	884.74	63002	Bedrock, sandy, silty mud, artificial, and estuaries
Jiangsu	744	103370	**972.55**	70116	Sandy, silty mud, artificial, and estuaries
Shanghai	211	8006	90.30	25123	Artificial
Zhejiang	2218	101453	261.78	42886	Bedrock, sandy, artificial, and estuaries
Fujian	3752	121586	533.46	25980	Bedrock, sandy, silty mud, artificial, estuaries, and biological
Guangdong[3]	**4114**	178073	514.75	72812	Bedrock, sandy, silty mud, artificial, and estuaries
Guangxi	1629	236839	368.04	16803	Bedrock, sandy, silty mud, artificial, estuaries, and biological
Hainan	1823	34244	191.62	3702	Bedrock, sandy, silty mud, artificial, and biological
Taiwan	1576	36244	467.17	–	–
Total	22160	1320403	4895.56	395440	–

[1] IW represents intertidal wetland. [2] The GDP is from the yearbook of the Chinese coastal region. [3] Macao and Hongkong are included in the Guangdong Province during analysis. All data are from the 2015 database. Bold underlines highlight the highest value of each row.

symbols are essential for the participating experts. After discussion and literature study, the unified symbols were defined as a stripped or patched area along the visible shoreline, yellow-white, gray-white, or white in color with red-yellow stripes. Generally, the intertidal wetland exhibited a relatively even image structure compared with the part of the coastal region further inland.

The procedure of the image human-PC interpretation is shown in **Figure 3**. In order to improve the accuracy of the mapping, the national land use land cover thematic maps with a scale of 1:10 were integrated into the intertidal wetland classification. By carefully selecting images with a low amount of cloud and high visibility, the intertidal wetland extents in the 1970s, 1995, and 2015 were extracted. The national costal map of the corresponding time period was adopted to correct and improve the mapping quality.

Precision Validation

The error of patch location or interpretation was mainly caused by the image quality and human error. We adopted a random sampling inspection of field survey points to check the accuracy of the final inter-tidal wetland maps. The accuracy level was

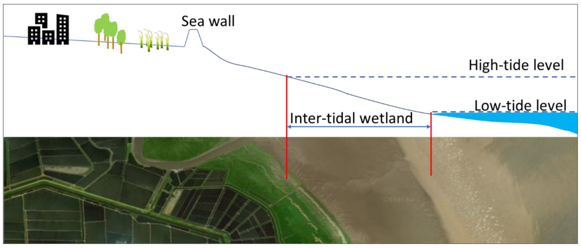

FIGURE 2 | Selection and processing of a satellite image.

TABLE 2 | Data sources for the intertidal wetland mapping.

Study period	1970s	1995	2015
Time	1975–1979	1995–1996	2015
Satellite source	Landsat MSS	Landsat TM	Landsat 8 OLI, GF-2

classified on a scale of 0 to 10, where 0 meant totally incorrect and 10 represented 100% correct. The overall precision was calculated as follows,

$$\textit{Overall precision} = \textit{number of}\ 100\%\textit{correct patches}/\ \textit{all samples}^{*}100\%$$

We sampled 653 patches of different coastal line types along the Bohai Sea, Yellow China Sea, East China Sea, and South China Sea and compared the field survey results and interpreted map of 2015 (**Figure 4**). The accuracy is related to the coast type (**Table 3**). Intertidal wetland located on an artificial coastal line showed the highest accuracy, while silty mud coastal wetland demonstrated relatively low accordance between the field surveyed and interpreted data. The overall precision of the intertidal wetland-identification reached 88.51% (**Table 3**).

RESULTS

Current Distribution of the Intertidal Wetlands

Decline in the Intertidal Area

The areal extent of intertidal flats along China's coast showed an extensive decline, from 7848.21 km^2 in the 1970s, decaying to 6017 km^2 in 1995, and, finally, to only 4895 km^2 two decades later (**Table 4**). Almost 37.62% of the intertidal wetland has disappeared in the last 40 years, with a relatively higher decrease rate from the 1970s to 1995. In addition to the areal decrease, the patch number of the intertidal wetland has grown during the study period, implying increased fragmentation of the intertidal wetland. The average area of each wetland patch increased slightly from 1.27 to 1.49 km^2 in the former period and reduced substantially to 0.51 km^2 in the latter period.

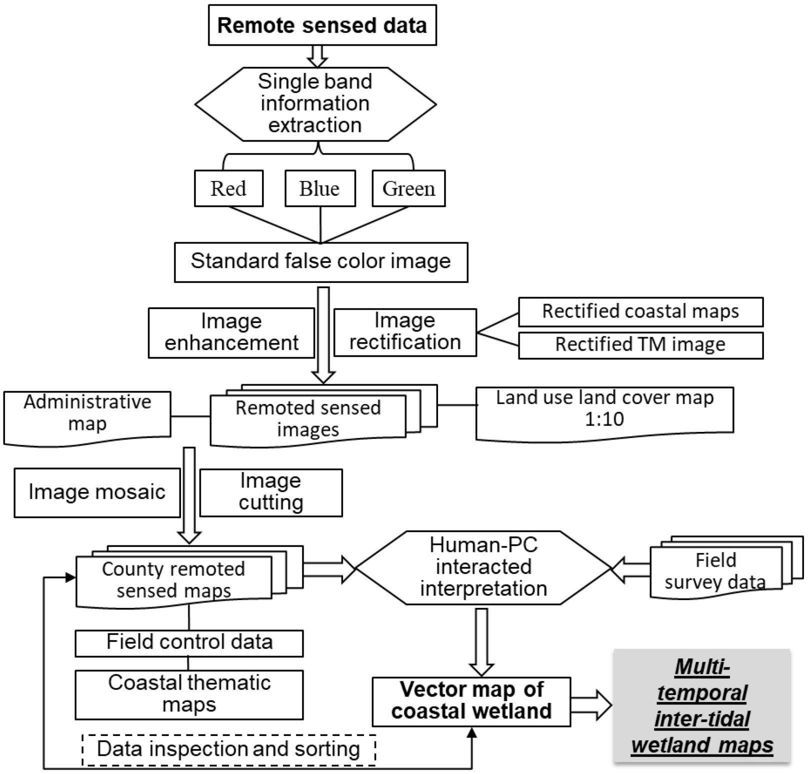

FIGURE 3 | Image interpretation procedure.

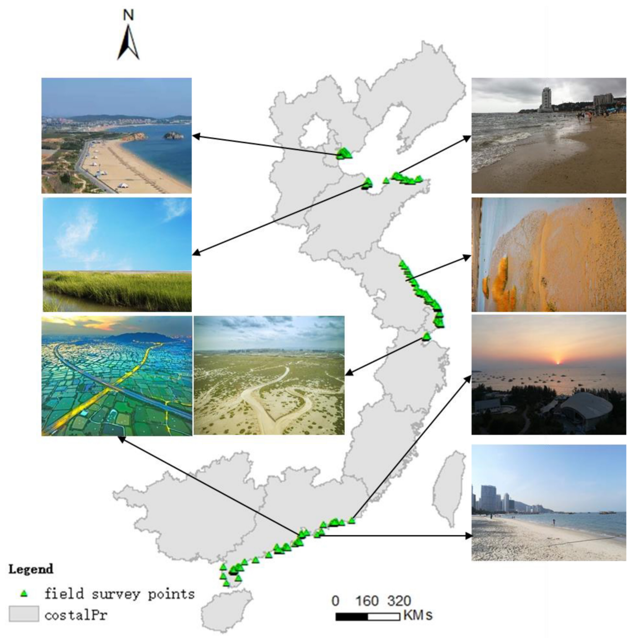

FIGURE 4 | Distribution of the field survey points.

TABLE 3 | Precision of the 2015 interpreted intertidal wetland validated by field survey.

Sample		Accuracy level											Overall precision (%)
		0	1	2	3	4	5	6	7	8	9	10	
Bedrock	256	6		2		2			3	3		230	89.84
Silty mud	261	4	3	3		3	7	8	6	3	2	222	85.05
Artificial	136			1		2	1		1	2	3	126	92.65
Total	653	10	3	6		7	8	8	10	8	5	578	88.51

Provincial Distribution and Change

As shown in **Table 1**, the intertidal wetland was unevenly distributed along the administrative coast. Guangdong has the highest coastline length, while the most significant contributor of intertidal wetland area was Shandong during the 1970s to 1995, shifting to Jiangsu in 2015 (**Figure 5A**). Shandong and Jiangsu constituted nearly 40% of the total extent of intertidal wetland in 2015. Tianjin and Shanghai have relatively little intertidal wetland, due to their short coastlines and small administrative areas.

All administrative regions, except Taiwan, showed a decreasing trend in the intertidal wetland area from the 1970s to 1995. There was a slight increase in intertidal wetland area in Tianjin, Shanghai, and Guangxi from 1995 to 2015, while that in all the other administrative units illustrated a continuous decline in the same period (**Figure 5A**).

Similarly to the total area, the intertidal wetland area per unit coastline (A/L) in China has been on the decline in general, from 0.35 km^2/km in the 1970s to 0.27 km^2/km in 1995 and then to 0.22 km^2/km in 2015. Jiangsu exhibited the highest absolute amount and decline range in intertidal wetland area per unit coastline, shrinking from 2.34 km^2/km to 1.30 km^2/km during the last 40 years, equating to an average reduction of 1.04 km in width along the coast (**Figure 5B**). The intertidal wetland area per unit coastline in nearly all other areas except Tianjin was lower than 0.5 km^2/km in 2015.

The area ratio of intertidal wetland to administrative region (IWR) revealed distinct spatial and temporal variation (**Figure 5C**). On average, the IWR reduced from 0.59% to 0.45% in the earlier period and then declined to 0.37% in the latter period. In the 1970s, four regions had an IWR of over 1%: Shandong, Jiangsu, Shanghai, and Taiwan. With the loss of intertidal wetland, the IWR of Shandong decreased severely by 0.3% in 1990s, while those of the other three regions were still over 1%. Continuous degradation of intertidal wetland in Jiangsu and an abrupt area increase in new intertidal wetland in Tianjin occurred in the following period. Finally, the IWR values of Tianjin, Shanghai, and Taiwan were higher than 1% in 2015.

Change Rate of the Intertidal Wetland

The change rates of the intertidal wetland in the two periods studied are given in **Table 5**. The decline rate from the 1970s to 1995 was slightly higher than that between 1995 and 2015, with an annual average of 1.17% and 0.94%, respectively. Spatially, the highest rate of wetland loss in both periods was in Jiangsu, and Shandong ranked second in wetland loss rate in the previous period. In Tianjin and Guangxi, a fast growth rate of wetland area was revealed, and minor gains of wetland occurred in Shanghai from 1995 to 2015.

Temporal-Spatial Dynamics of the Intertidal Wetlands

Dynamic Spatial Variation

Intertidal wetland loss along China's coast was spatially pervasive (**Figure 6**). From the 1970s to 1995, 60% of the grid squares suggested loss of intertidal wetland, with an average decline of 34.90 km^2 in each, while the remaining 40% remained the same or indicated minor growth by 3.53 km^2 each. By contrast, intertidal wetland degradation occurred in 67% of the grid squares, with a loss of 20.46 km^2 per grid square from 1995 to 2015, and the remaining 33% showed a similar growth range to the previous period. This suggested even more widespread and fragmented intertidal wetland loss, with a smaller decline magnitude in the latter period.

Reduction in Wetland Widths

The intertidal wetland edge on the continental side has been pushed rapidly seaward due to wetland occupation during the study period, according to the satellite archive. This correspondingly resulted in a reduction in the width of the intertidal wetland. We mapped the extent of the intertidal wetland across the northern Shandong and Jiangsu coastal region at three time periods, the 1970s, 1995, and 2015 (**Figures 7A–H**). In the northern Shandong coastal region, a vast extent of intertidal wetland disappeared on the continental side, especially from the 1970s to 1995 (**Figure 7A**). The average width of the intertidal wetland dropped from 4.52 km to 2.03 km and then

TABLE 4 | Total intertidal wetland conditions in the 1970s, 1995, and 2015.

Year	Area (km^2)	*N*[1]	Fragmentation	Averaged area (km^2)	Decrease rate (km^2/yr)	Relative decrease (%)
1970s	7848.21	6156	0.78	1.27	–	–
1995	6017.42	4037	0.67	1.49	−91.54	23.33
2015	4895.56	9598	1.96	0.51	−56.09	18.65

[1] *N represents the total number of patches of intertidal wetland.*

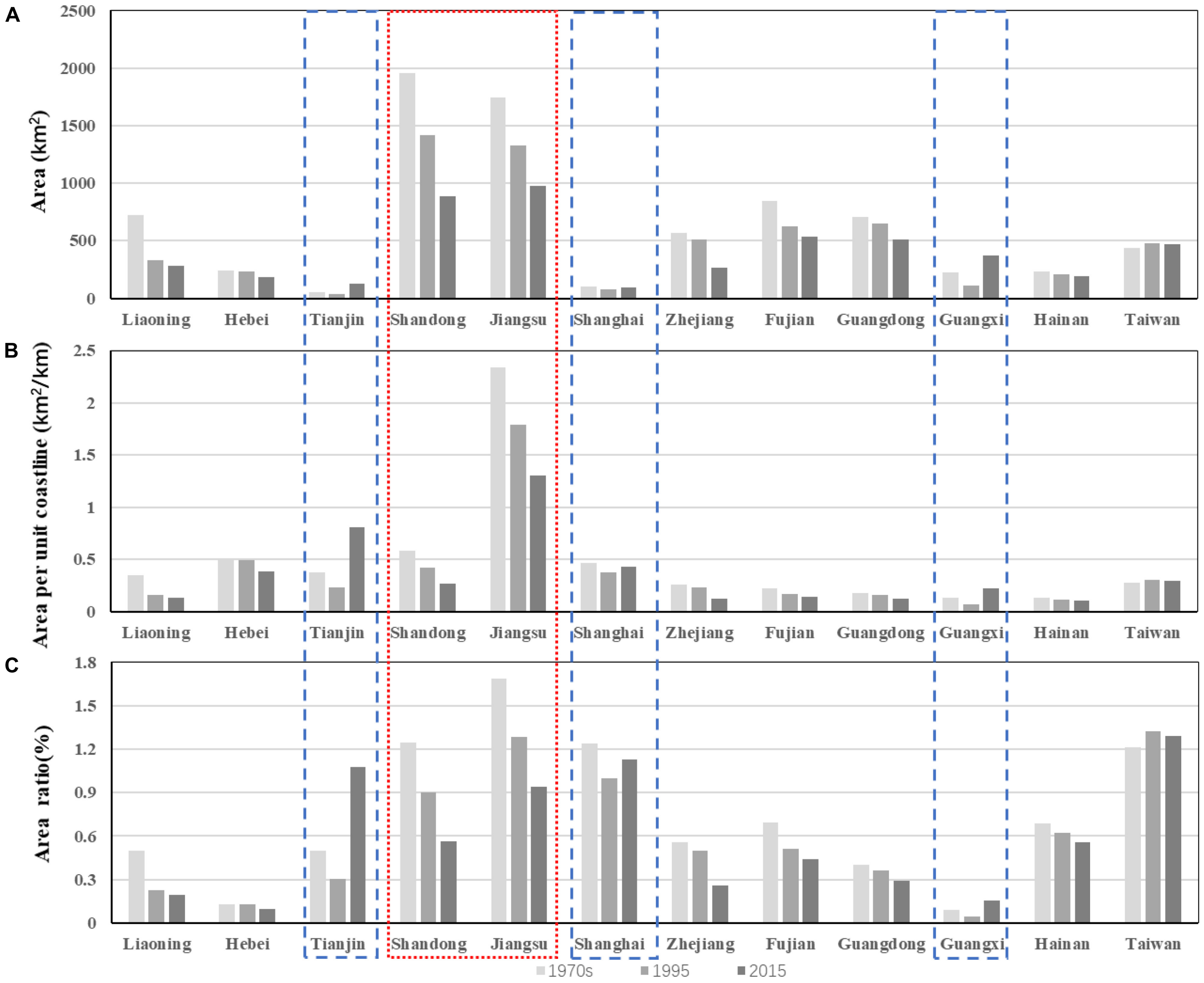

FIGURE 5 | Decrease in the intertidal area of each administrative region, **(A)** total area, **(B)** area per coastal line, **(C)** intertidal area to provincial area ratio. The regions in the red dotted rectangule are the major contributor to the degradation of the intertidal wetland area, while those in blue dashed rectangles represent the areas that increased in the later period.

to 0.91 km in the 20-year time intervals during the study period (**Figures 7A–D**). Due to the influence of the mouth of the Yellow River, slight gains in intertidal wetland happened around the mouth. Jiangsu possesses a straight coastline and a wide tidal flat with sufficient sediment supply, generating the widest stretches of intertidal wetland in China (**Figures 7E–H**). The irregular patches of intertidal wetland on the continental side were wiped out in the earlier period, causing a loss of 30% of the intertidal wetland (**Figure 7E**). The inner side of the intertidal wetland continued migrating seaward from 1995 to 2015, leading to another 35% decay of the intertidal wetland extent, equating to a shrinkage of 0.57 km in width. Approximately, the width of the intertidal wetland in Jiangsu has declined by 1.3 km in the last four decades.

Hotspots of Wetland Gain

Compared with the losses, the gains in intertidal wetland were much more minor, both in number of spatial locations and extent.

TABLE 5 | Change rate of the area and A/L of intertidal wetland.

Change rate (%)	Area 1970s–1995	Area 1995–2015	A/L 1970s–1995	A/L 1995–2015
Liaoning	−54.56	−14.68	−18.76	−2.29
Hebei	−2.59	−22.34	−1.30	−10.92
Tianjin	−38.80	254.17	−14.43	57.84
Shandong	−27.57	−37.46	−**16.10**	−**15.84**
Jiangsu	−23.61	−26.87	−**55.26**	−**48.03**
Shanghai	−19.24	12.96	−9.02	4.91
Zhejiang	−10.40	−48.35	−2.65	−11.05
Fujian	−26.18	−14.38	−5.89	−2.39
Guangdong	−8.71	−20.66	−1.50	−3.26
Guangxi	−51.11	240.38	−6.94	15.96
Hainan	−10.16	−9.65	−1.32	−1.12
Taiwan	9.38	−2.58	2.61	−0.78
Total	−23.36	−18.84	−23.36	−18.84

A gray background indicates an increase in intertidal wetland area in 1995–2015, and bold, underlined numbers are used where there was a strong decline in both periods.

Intertidal wetland area increased in a few isolated locations, such as the Bohai Rim, Yangtze River mouth, and Guangxi coastal region, which were regarded as the hotspots of wetland gain (**Figures 8A–L**). Across the municipalities directly under the Central Government, Tianjin and Shanghai, newly constructed intertidal wetland contributed to the area gains. Along the Tianjin coastline, simultaneously with the loss of intertidal wetland on the continental side, the newly emerged wetlands with regular geometric shapes appeared, mainly located in the marine region (**Figures 8A–D**). The seaward growth of the intertidal wetland units suggested a strong impact from anthropogenic interference. Distinct loss of the intertidal wetland along the southern coast of Shanghai was witnessed (**Figures 8E–H**). In contrast, in the northern part, a few patches of intertidal wetland around the Yangtze River mouth enlarged from 1995 to 2015. Newly constructed island intertidal wetland was another source of the extent gains for Shanghai (**Figures 8E–H**). In comparison with Tianjin and Shanghai, the coast of Guangxi is more meandering and tortuous in shape, with two narrow and winding estuaries. A massive amount of intertidal wetland was created along the coast and estuaries (**Figures 8I–L**), equivalent to an amplification of 0.15 km in the width of the intertidal wetland.

DISCUSSION

Intertidal Wetland Loss Locally and Globally

China shares the second-highest portion of the tidal-flat extent, closely following Indonesia (Murray et al., 2019). Our results were broadly in accordance with other monitoring of intertidal flat

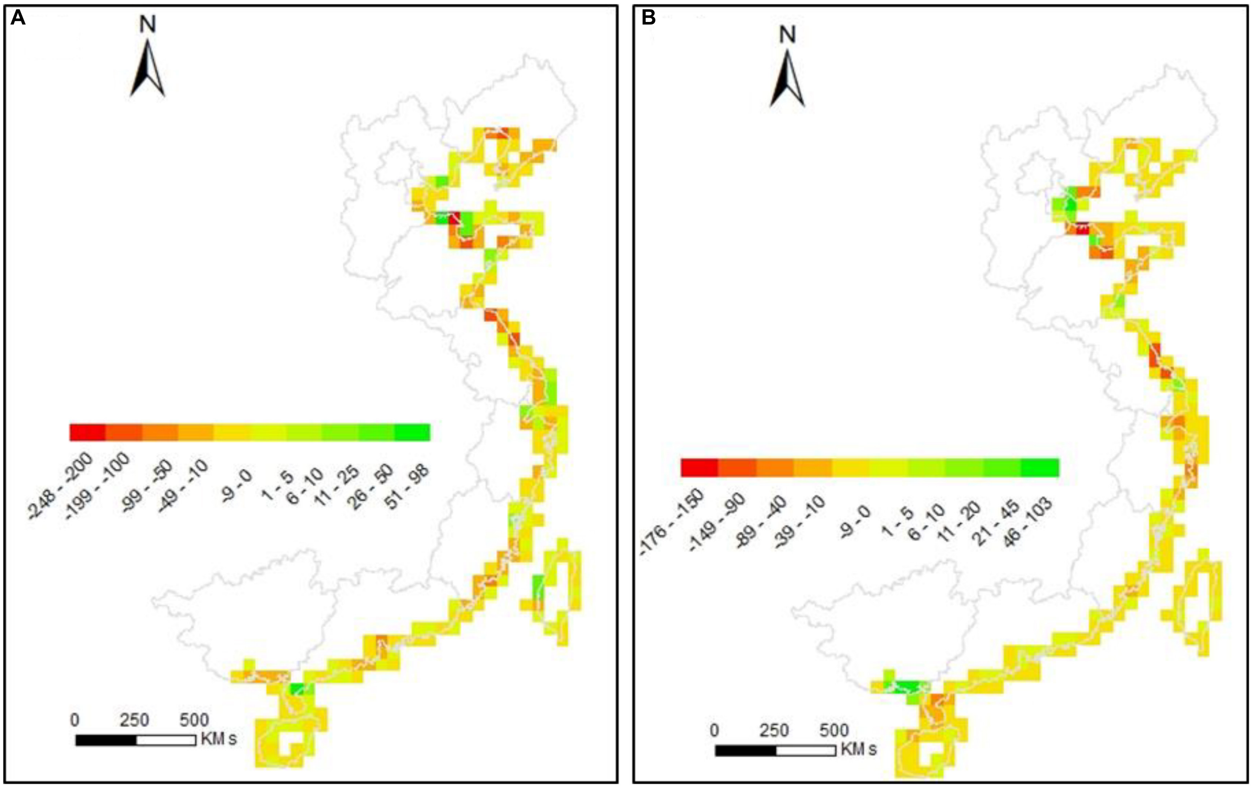

FIGURE 6 | Area change of intertidal wetland from the 1970s to 1995 **(A)**, and from 1995 to 2015 **(B)** at a spatial resolution of 50 km.

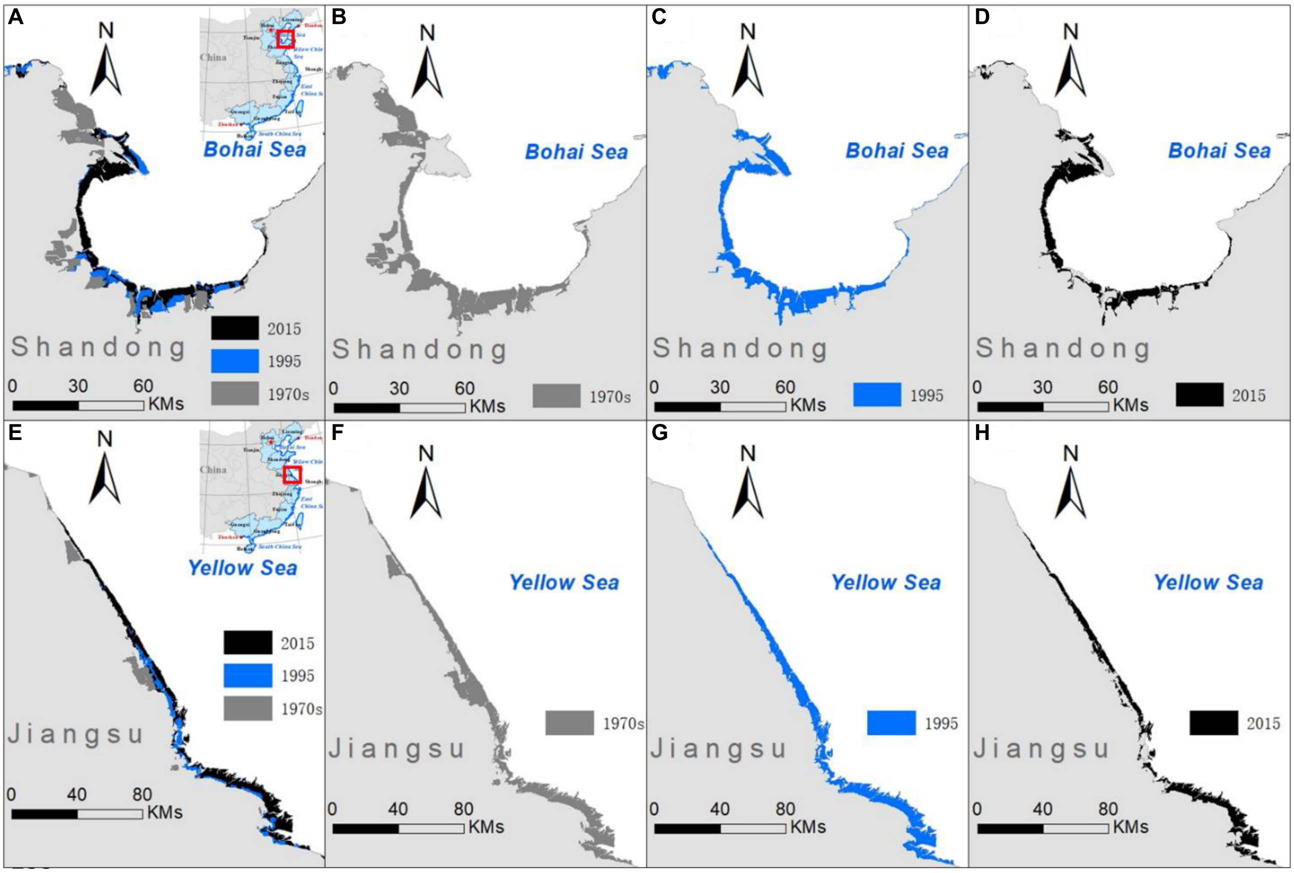

FIGURE 7 | Reduction in the inter-tidal width of the Bohai Rim **(A–D)** and Yellow sea coast **(E–H)**.

or wetland dynamics (**Table 6**). Intertidal wetland loss tracking around the Yellow Sea reflected an extent of 2678 km^2 and 1611 km^2 in the 1980s and 2000s, with an annual loss rate of 1.8% (Murray et al., 2014), which were quite similar to our results both in extent and loss rate. Compared with the global reported estimation, the intertidal wetland in China has been lost at a much faster rate. Annually, 0.94–1.17% of intertidal wetland loss occurred in China, which was roughly twice the global average rate, 0.55% every year since 1984 (Murray et al., 2019). Although rates of loss are currently low or slowing down in some parts of the world (e.g., Europe and North America), high losses are continuing elsewhere, especially in Asia (Davidson, 2018). The intertidal wetland loss rate in China is expected to accelerate without adaption or regulation measures in the following decade.

Driving Forces of the Intertidal Wetland Dynamics

Substantial losses of intertidal wetland were mainly driven by the multiple stressors functioning at both local and national scales. The vast region along the Chinese coastline has been under intense pressure from anthropogenic interference. The explosive growth of the economy and population in the coastal region created intensified land use conflict, which then resulted in huge open-coast wetland reclamation for aquaculture, agriculture, tourism construction, and hydrologic engineering. China alone contributed over 60% of the global aquaculture volume and more than one-third of global aquaculture production (FAO, 2014; Zhao and Shen, 2016). The area devoted to fish farming doubled from 1990s to 2012, resulting in intensified exploitation of coastal ponds (Cao et al., 2015; Zhao and Shen, 2016).

Owing to the extensive land reclamation, seawall construction has been expanding at an unprecedented rate and is referred as the new Great Wall of China (Ma et al., 2014). The seawall serves as the boundary between coastal land use and the intertidal wetland, protecting the land resource inside from the invasion of tides and waves, and at the same time enclosing more wetlands for agricultural and industrial purposes (Lotze et al., 2006; Airoldi and Beck, 2007). The total length of such seawalls has escalated from 3240 km to 10980 km in the two decades since 1990s, covering 61% of the coastline length in 2010 (Guan, 2013). Accelerating seawall construction and land reclamation started in 1990s and had encroached over 950 km^2 of the intertidal wetland extent by 2010 (Ma et al., 2014). With the current exploitation rate and development plans, another 580 km^2 of intertidal wetland was expected to be occupied by 2020

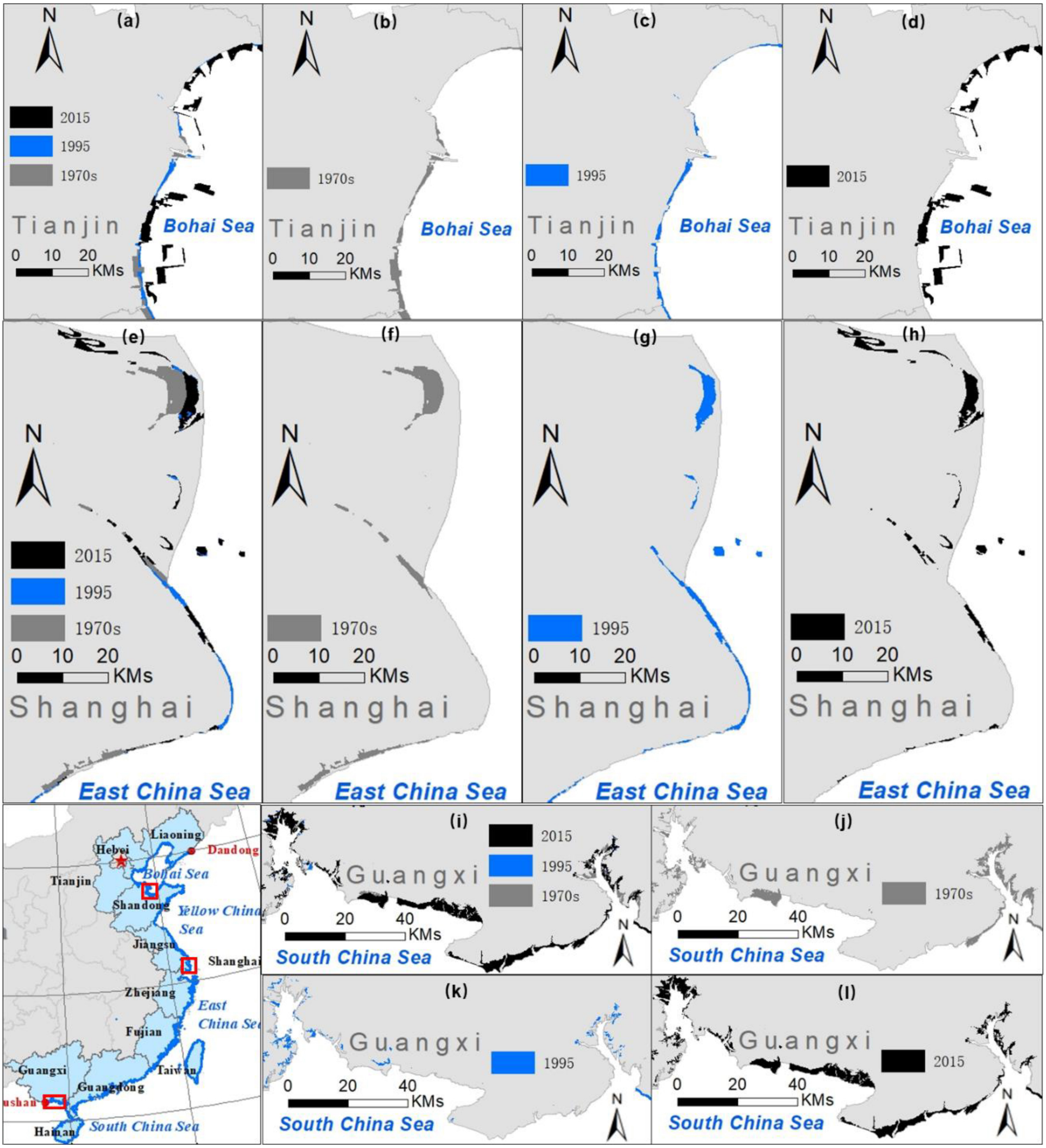

FIGURE 8 | Increase in human-constructed intertidal wetland at the Bohai Rim **(A–D)**, coastal Shanghai region **(E–H)**, and coastal Guangxi region **(I–L)**.

(Chinese Oceanography Bureau, 2012). The combined pressure of land reclamation and seawall construction squeezed the extent of intertidal wetland to the coastline and finally resulted in the reduction in the intertidal wetland width (**Figure 7**).

According to the China Marine Statistical Yearbook of 2016, the growth in the marine economy in 2015 was mainly contributed by coastal tourism, followed by the marine communication and transportation industry and marine fishery industry (**Figure 9**; State Oceanic Administration People's Republic of China, 2016). The top three contributors made up more than 77% of the marine economic growth. Coastal tourism, the communication and transportation industry, and the fishery industry are considered to be land consuming and occupied the coastal space, causing severe intertidal wetland loss.

TABLE 6 | Extent of intertidal wetlands around the Yellow sea from different studies.

Around Yellow Sea (km^2)	1950s	1970s	1980s	1995	2000s	2015/2016
Murray's	5398	–	2678	–	1611	–
Current study	–	4720	–	2016	–	1473
Wang's	–	–	–	–	–	3811

Landward and Seaward Migration of Intertidal Wetland

Previous research pointed out that unprecedented sea-level rise and continued coastal development have altered coastal landscapes substantially across the globe (Kirwan and Megonigal, 2013; Spencer et al., 2016; Parker and Boyer, 2017). Accelerated sea-level rise connected to climate change is estimated to have the largest impact on coastal wetlands because of the amplification of the inundation extent and salinity regime (Schuerch et al., 2018; Woodruff, 2018), which triggers coastal ecosystems to shift landward into newly sea-inundated areas. On the other hand, the intense economic development and population growth concentrated in the near-coast region have strongly constrained the wetland migration landward (Parker and Boyer, 2017), and oceanward land reclamation is still in high demand due to the sustained prosperity of the coastal regions. These two stressors intertwined at the land-sea margin and jointly determined how and where the wetland would migrate (Wu W. et al., 2017). For example, in one of the wetland rich regions of the world, the northern Gulf of Mexico, landward migration of the intertidal wetland along the coast was detected (Enwright et al., 2016), suggesting the sea-level rise sensitivity of this region. In a developing country like China, notably, coastal wetlands have been increasingly lost to numerous anthropologic activities, especially reclamation (Murray et al., 2014; Cui et al., 2016). In our analysis, we found that the intertidal wetlands were primarily squeezed seaward by anthropogenic interference (**Figures 5A–H**). The exception occurred along the Guangxi coast (**Figures 6I–L**), where the intertidal wetland invaded further into the continent, revealing the dominant influence of local sea-level rise and the relatively weak pressure from humans. In addition to the wetland migration landward, sea-level rise drove tides and waves further upstream and generated striped intertidal wetland along the tidal river estuary (**Figures 6E–L**). In general, seaward migrations of the intertidal wetland have been documented globally. The historical loss of coastal wetlands worldwide has been dominated by the direct conversion of wetlands to space for agriculture and aquaculture instead of climate change (Kirwan and Megonigal, 2013). However, given the prediction of increasing sea-level rise and the limited spatial extent for inundation in the near future, robust protection of the coastal infrastructure from higher flood and storm surge risk is required in the long run.

Impact of Intertidal Wetland Loss

Apart from hydrological disasters such as floods, seawater backwash, storm surge, etc., which have been discussed extensively in previous research, intertidal wetland loss will also result in tremendous environmental, ecological, and biological impacts due to the destruction of the habitat (Musseau et al., 2017; Spivak et al., 2019). A recent forecast estimates a net loss of intertidal wetland coverage ranging from 28% to 57% by the year 2100 (McLachlan, 2018). Artificial restoration of intertidal wetland might reduce the intertidal wetland loss ratio and rebuild the buffer zone for hydrological disaster but can only make a limited contribution to the natural biotic assemblages due to the difficulty of restoring the hydrological connectivity with the ocean and the complicated habitat (Wu et al., 2019). A study related to the shorebirds of Austria pointed out that population declines are occurring despite high levels of intertidal habitat protection (Dhanjal-Adams et al., 2016). These findings highlight the immediate and concerted effort needed both nationally and internationally to effectively habitat conservation.

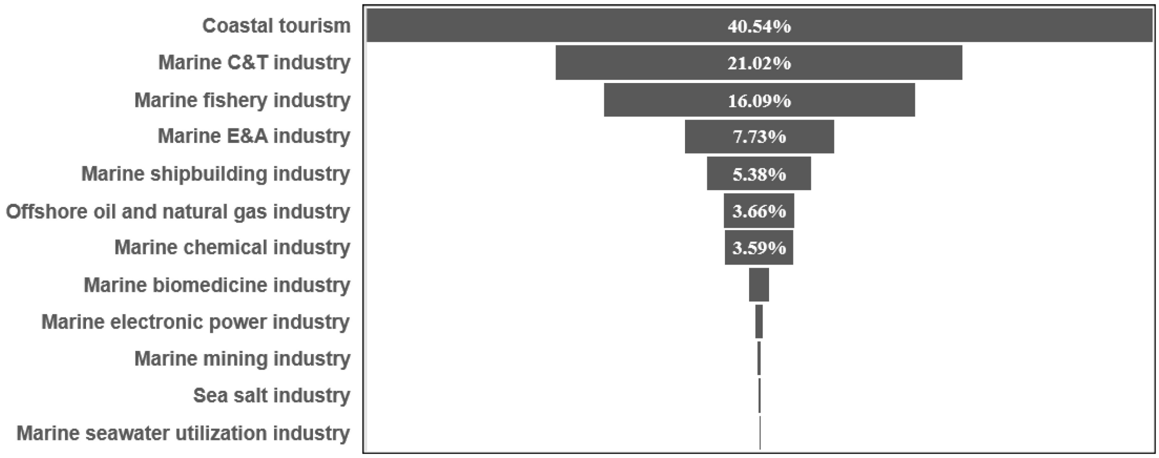

FIGURE 9 | Composition of marine economy growth in 2015. C and T refers to communication and transportation, while E and A means engineering and architecture.

CONCLUSION AND OUTLOOK

The mapping and dynamic detection of intertidal wetland, especially at a large spatial scale and with a long time course, remains a difficult task, mainly due to the scarcity of accurate data. This is particularly the case in rapidly developing China, where the coastal regions were undergoing co-evolution with intense human development and have strong dynamics in temporal and spatial pattern. Multi-temporal remote sensed images and related techniques provide access to a long-term monitor of these living systems. In the face of over-reclamation of coastal land, a huge loss of intertidal wetland has been documented by the high-resolution satellite images, as follows.

(1) An overall decline trend of the intertidal wetland was witnessed along China's coast, especially in Shandong and Jiangsu, which contributed the highest portion to the total extent. Slight gains of intertidal wetland occurred in isolated regions, mainly in Shanghai, Tianjin, and Guangxi.
(2) The extent of intertidal wetland declined by from 7848 km^2 to 6017 km^2 from the 1970s to 1995 and then to 4895 km^2 in 2015, equaling losses of 23.33% and 18.65% in the former and latter period, respectively.
(3) Squeezed by the over-reclamation of coastal land, the intertidal wetland exhibited seaward migration and severe width shrinkage, stretching 0.35 km, 0.27 km, and 0.22 km in the direction perpendicular to the coast in the three periods, respectively.

The fundamental importance of coastal ecosystems is becoming recognized by government and the public. In the short term, human activities through direct exploitation will continuously dominate the landscape pattern of the coastal region. In the long run, however, accelerated sea-level rise will play a major role in the narrowing and landward migration of the intertidal wetland. Strict legislation for intertidal wetlands, outreach education of ecosystem services, and more active participation by local communities will effectively promote the protection of wetland from over-exploitation. Intrinsic linkages among government and scientists are strongly encouraged to formulate a better strategy for the conservation of the intertidal wetland from the long-term sea-level rise scenario.

DATA AVAILABILITY STATEMENT

The datasets generated in this article are not publicly available. Requests to access the datasets should be directed to geossong@gzhu.edu.cn.

AUTHOR CONTRIBUTIONS

SS wrote the draft of this manuscript. ZW designed the research and guided the analysis process. YW contributed to the image processing, data collection, and analysis. ZC made contribution in language revision and data validation. ZH and YS helped in data collection and background information collection.

FUNDING

This research was supported by the National Natural Science Foundation of China (Grant No. 41601018), the Guangdong Province Universities and Colleges Pearl River Scholar Funded Scheme (2019), the Key Special Project for Introduced Talents Team of Southern Marine Science and Engineering Guangdong Laboratory (Guangzhou) (GML2019ZD0301), and the NSFC-Guangdong Joint Fund Key Project (U1901219).

REFERENCES

Airoldi, L., and Beck, M. W. (2007). Loss, status and trends for coastal marine habitats of Europe. *Oceanogr. Mar. Biol. Annu. Rev.* 45, 345–405. doi: 10.1201/9781420050943.ch7

Barbier, E. B. (2015). Valuing the storm protection service of estuarine and coastal ecosystems. *Ecosyst. Serv.* 11, 32–38. doi: 10.1016/j.ecoser.2014.06.010

Cao, L., Naylor, R., Henriksson, P., Leadbitter, D., Metian, M., Troell, M., et al. (2015). China's aquaculture and the world's wild fisheries. *Science* 347, 133–135. doi: 10.1126/science.1260149

Chen, Y., Dong, J., Xiao, X., Zhang, M., Tian, B., Zhou, Y., et al. (2016). Land claim and loss of tidal flats in the Yangtze Estuary. *Sci. Rep.* 6:24018. doi: 10.1038/srep24018

Chinese Oceanography Bureau (2012). *Marine Function Zoning Plans (2011–2020) of Coastal Provinces [in Chinese]*. Beijing: Chinese Oceanography Bureau.

Costanza, R., de Groot, R., Sutton, P., van der Ploeg, S., Anderson, S. J., Kubiszewski, I., et al. (2014). Changes in the global value of ecosystem services. *Glob. Environ. Change* 26, 152–158. doi: 10.1016/j.gloenvcha.2014.04.002

Crowell, N., Webster, T., and O'Driscoll, N. J. (2011). GIS modelling of intertidal wetland exposure characteristics. *J Coast. Res.* 27, 44–51. doi: 10.2112/JCOASTRES-D-10-00187.1

Cui, B., He, Q., Gu, B., Bai, J., and Liu, X. (2016). China's coastal wetlands: understanding environmental changes and human impacts for management and conservation. *Wetlands* 36, 1–9. doi: 10.1007/s13157-016-0737-8

Davidson, N. C. (2018). "Wetland losses and the status of wetland-dependent species," in *The Wetland Book: II: Distribution, Description, and Conservation*, eds M. C. Finlayson, G. R. Milton, R. C. Prentice, and N. C. Davidson, (Dordrecht: Springer).

Deegan, L. A., Johnson, D. S., Warren, R. S., Peterson, B. J., Fleeger, J. W., Fagherazzi, S., et al. (2012). Coastal eutrophication as a driver of salt marsh loss. *Nature* 490, 388–392. doi: 10.1038/nature11533

Dhanjal-Adams, K. L., Hanson, J. O., Murray, N. J., Phinn, S. R., Wingate, V. R., Mustin, K., et al. (2016). The distribution and protection of intertidal habitats in Australia. *EMU Austral Ornithol.* 116, 208–214. doi: 10.1071/MU15046

Enwright, N. M., Griffith, K. T., and Osland, M. J. (2016). Barriers to and opportunities for landward migration of coastal wetlands with sea-level rise. *Front. Ecol. Environ.* 14, 307–316. doi: 10.1002/fee.1282

FAO, (2014). *The State of World Fisheries and Aquaculture.*Rome: Food and Agriculture Organization of the United Nations.

Ford, M. (2013). Shoreline changes interpreted from multi-temporal aerial photographs and high resolution satellite images: Wotje Atoll, Marshall Islands. *Remote Sens. Environ.* 135, 130–140. doi: 10.1016/j.rse.2013.03.027

Fujii, T. (2012). Climate change, sea-level rise and implications for coastal and estuarine shoreline management with particular reference to the ecology of intertidal benthic macrofauna in NW Europe. *Biology* 1, 597–616. doi: 10.3390/biology1030597

Gabler, C. A., Osland, M. J., Grace, J. B., Stagg, C. L., Day, R. H., Hartley, S. B., et al. (2017). Macroclimatic change expected to transform coastal wetland ecosystems this century. *Nat. Clim. Change* 7, 142–147. doi: 10.1038/nclimate3203

Gong, P., Niu, Z., Cheng, X., Zhao, K., Zhou, D., and Guo, J., et al. (2010). China's wetland change (1990–2000) determined by remote sensing. *Sci. China Earth Sci.* 53, 1036–1042. doi: 10.1007/s11430-010-4002-3

Gu, J., Luo, M., Zhang, X., Christakos, G., Agusti, S., Duarte, C. M., et al. (2018). Losses of salt marsh in China: trends, threats and management. *Estuar. Coast. Shelf Sci.* 214, 98–109. doi: 10.1016/j.ecss.2018.09.015

Guan, D. M. (2013). *Study on the National Marine Function Zonation*. Beijing: Ocean Press.

Hou, X., Wu, T., Hou, W., Chen, Q., Wang, Y., and Yu, L. (2016). Characteristics of coastline changes in mainland China since the early 1940s. *Sci. China Earth Sci.* 59, 1791–1802. doi: 10.1007/s11430-016-5317-5

Jankowski, K. L., Törnqvist, T. E., and Fernandes, A. M. (2017). Vulnerability of Louisiana's coastal wetlands to present-day rates of relative sea-level rise. *Nat. Commun.* 8:14792. doi: 10.1038/ncomms14792

Kirwan, M. L., and Megonigal, J. P. (2013). Tidal wetland stability in the face of human impacts and sea-level rise. *Nature* 504, 53–60. doi: 10.1038/nature12856

Lotze, H. K., Lenihan, H. S., Bourque, B. J., Bradbury, R. H., Cooke, R. G., Kay, M. C., et al. (2006). Depletion, degradation, and recovery potential of estuaries and coastal seas. *Science* 312, 1806–1809. doi: 10.1126/science.1128035

Loveland, T. R., Reed, B. C., Brown, J. F., Ohlen, D. O., Zhu, Z., Yang, L., et al. (2000). Development of a global land cover characteristics database and IGBP DISCover from 1 km AVHRR data. *Int. J. Remote Sens.* 21, 1303–1330. doi: 10.1080/014311600210191

Ma, Z., Melville, D. S., Liu, J., Chen, Y., Yang, H., Ren, W., et al. (2014). Rethinking China's new great wall. *Science* 346, 912–914. doi: 10.1126/science.1257258

Mason, D. C., Scott, T. R., and Dance, S. L. (2010). Remote sensing of intertidal morphological change in Morecambe Bay, U.K., between 1991 and 2007. *Estuar. Coast. Shelf Sci.* 87, 487–496. doi: 10.1016/j.ecss.2010.01.015

McLachlan, J. R. (2018). Highnet loss of intertidal Wetland coverage in a maine Estuary by year 2100. *J. Conserv. Sustain.* 2. doi: 10.13140/RG.2.2.36748.56962

Murray, N. J., Clemens, R. S., Phinn, S. R., Possingham, H. P., and Fuller, R. A. (2014). Tracking the rapid loss of tidal wetlands in the Yellow Sea. *Front. Ecol. Environ.* 12, 267–272. doi: 10.1890/130260

Murray, N. J., Phinn, S. R., DeWitt, M., Ferrari, R., Johnston, R., Lyons, M. B., et al. (2019). The global distribution and trajectory of tidal flats. *Nature* 565:222. doi: 10.1038/s41586-018-0805-8

Musseau, R., Beslic, S., and Kerbiriou, C. (2017). Importance of intertidal wetlands for the French coastal endemic Bluethroat Cyanecula svecica namnetum and conservation implications in the context of global changes. *Ardeola* 64, 325–345. doi: 10.13157/arla.64.2.2017.ra3

Nwipie, G. N., Hart, A. I., Zabbey, N., Sam, K., Prpich, G., and Kika, P. E. (2019). Recovery of infauna macrobenthic invertebrates in oil-polluted tropical soft-bottom tidal flats: 7 years post spill. *Environ. Sci. Pollut. Res.* 26, 22407–22420. doi: 10.1007/s11356-019-05352-2

Parker, V. T., and Boyer, K. E. (2017). Sea-level rise and climate change impacts on an urbanized Pacific Coast estuary. *Wetlands* 1–14. doi: 10.1007/s13157-017-0980-7

Paterson, D. M., Fortune, I., Aspden, R. J., and Black, K. S. (2019). "Chapter 11 – Intertidal flats: form and function," in *Coastal Wetlands*, eds G. M. E Perillo, E. Wolanski, D. R. Cahoon, and C. S Hopkinson, (Amsterdam: Elsevier), 383–406. doi: 10.1016/B978-0-444-63893-9.00011-3

Ribaudo, C., Plus, M., Ganthy, F., and Auby, I. (2016). Carbon sequestration loss following Zostera noltei decline in the Arcachon Bay (France). *Estuar. Coast. Shelf Sci.* 179, 4–11. doi: 10.1016/j.ecss.2016.01.024

Sagar, S., Roberts, D., Bala, B., and Lymburner, L. (2017). Extracting the intertidal extent and topography of the Australian coastline from a 28year time series of landsat observations. *Remote Sens. Environ.* 195, 153–169. doi: 10.1016/j.rse.2017.04.009

Schuerch, M., Spencer, T., Temmerman, S., Kirwan, M. L., Wolff, C., Lincke, D., et al. (2018). Future response of global coastal wetlands to sea-level rise. *Nature* 561, 231–234. doi: 10.1038/s41586-018-0476-5

Spencer, T., Schuerch, M., Nicholls, R. J., Hinkel, J., Lincke, D., Vafeidis, A. T., et al. (2016). Global coastal wetland change under sea-level rise and related stresses: the DIVA wetland change model. *Glob. Planet. Change* 139, 15–30. doi: 10.1016/j.gloplacha.2015.12.018

Spivak, A. C., Sanderman, J., Bowen, J. L., Canuel, E. A., and Hopkinson, C. S. (2019). Global-change controls on soil-carbon accumulation and loss in coastal vegetated ecosystems. *Nat. Geosci.* 12, 685–692. doi: 10.1038/s41561-019-0435-2

State Oceanic Administration People's Republic of China (2016). *China Marine Statistical Yearbook 2016*. Beijing: Ocean Press.

Syvitski, J. P. M., Kettner, A. J., Overeem, I., Hutton, E. W. H., Hannon, M. T., Brakenridge, G. R., et al. (2009). Sinking deltas due to human activities. *Nat. Geosci.* 2, 681–686. doi: 10.1038/ngeo629

Vafeidis, A. T., Nicholls, R. J., McFadden, L., Tol, R. S. J., Hinkel, J., Spencer, T., et al. (2008). A new global coastal database for impact and vulnerability analysis to sea-level rise. *J. Coast. Res.* 24, 917–924. doi: 10.2112/06-0725.1

Vázquez-González, C., Moreno-Casasola, P., Peralta Peláez, L. A., Monroy, R., and Espejel, I. (2019). The value of coastal wetland flood prevention lost to urbanization on the coastal plain of the Gulf of Mexico: an analysis of flood damage by hurricane impacts. *Int. J. Disaster Risk Reduct.* 37:101180. doi: 10.1016/j.ijdrr.2019.101180

Wang, X., Xiao, X., Zou, Z., Chen, B., Ma, J., Dong, J., et al. (2018). Tracking annual changes of coastal tidal flats in China during 1986–2016 through analyses of landsat images with google earth engine. *Remote Sens. Environ.* 238:110987. doi: 10.1016/j.rse.2018.11.030

Wei, W., Tang, Z., Dai, Z., Lin, Y., Ge, Z., and Gao, J. (2015). Variations in tidal flats of the Changjiang (Yangtze) estuary during 1950s–2010s: future crisis and policy implication. *Ocean Coast. Manag.* 108, 89–96. doi: 10.1016/j.ocecoaman.2014.05.018

Woodruff, J. D. (2018). Future of tidal wetlands depends on coastal management. *Nature* 561, 183–185. doi: 10.1038/d41586-018-06190-x

Wu, H., Guan, Q., Lu, K., Han, G., Li, B., and Yang, M. (2019). Effects of hydrological connectivity on snail assemblages in the intertidal zone of coastal wetlands. *Wetlands* 1–8. doi: 10.1007/s13157-019-01241-z

Wu, W., Zhou, Y., and Tian, B. (2017). Coastal wetlands facing climate change and anthropogenic activities: a remote sensing analysis and modelling application. *Ocean Coast Manag.* 138, 1–10. doi: 10.1016/j.ocecoaman.2017.01.005

Wu, X., Bi, N., Xu, J., Nittrouer, J. A., Yang, Z., Saito, Y., et al. (2017). Stepwise morphological evolution of the active Yellow River (Huanghe) delta lobe (1976–2013): dominant roles of riverine discharge and sediment grain size. *Geomorphology* 292, 115–127. doi: 10.1016/j.geomorph.2017.04.042

Zhao, W., and Shen, H. (2016). A statistical analysis of China's fisheries in the 12th five-year period. *Aquac. Fish.* 1, 41–49. doi: 10.1016/j.aaf.2016.11.001

Conflict of Interest: The authors declare that the research was conducted in the absence of any commercial or financial relationships that could be construed as a potential conflict of interest.

frontiers in Earth Science

ORIGINAL RESEARCH
published: 02 April 2020
doi: 10.3389/feart.2020.00076

Uncertainty Analysis of Standardized Precipitation Index Due to the Effects of Probability Distributions and Parameter Errors

*Ying Zhang and Zhanling Li**

MOE Key Laboratory of Groundwater Circulation and Environmental Evolution, School of Water Resources and Environment, China University of Geosciences (Beijing), Beijing, China

The standardized precipitation index (SPI) is widely used in drought assessments due to its simple data requirement and multiscale characteristics. However, there are some uncertainties in the process of its calculation. This study, taking the Heihe River basin in northwest of China as the study area, mainly focuses on the uncertainty issues both in SPI calculation and in drought characteristics associated with the probability distributions and parameter estimation errors. Ten probability distributions (two- and three-parameter log-logistic and log-normal, generalized extreme value, Pearson type III, burr, gamma, inverse Gaussian, and Weibull) are employed to estimate the SPI. Maximum likelihood estimation is used to estimate distribution parameters. Randomly generating parameters based on the normality assumption is applied to quantify the uncertainty of parameter estimations. Results show that log-logistic–type distribution presents quite close performance with the benchmark gamma distribution and thus is recommended as an alternative in fitting the precipitation data over the study area. Effects of both uncertainty sources (probability distribution functions and parameter estimation errors) are more reflected on extreme droughts (extremely dry or wet). The more extreme the SPI value, the greater uncertainties caused by both sources. Furthermore, the drought characteristics vary a lot from different distributions and parameter errors. These findings highlight the importance of uncertainty analysis of drought assessments, given that most studies in climatology focus on extreme values for drought analysis.

Keywords: standardized precipitation index, uncertainty, probability distribution, drought assessment, Heihe River basin, China

OPEN ACCESS

Edited by:
Xingcai Liu,
Institute of Geographic Sciences and Natural Resources Research (CAS), China

Reviewed by:
Ahmed Kenawy,
Mansoura University, Egypt
Zengliang Luo,
Peking University, China

****Correspondence:***
Zhanling Li
zhanling.li@cugb.edu.cn

Specialty section:
This article was submitted to Hydrosphere, a section of the journal Frontiers in Earth Science

Received: *21 November 2019*
Accepted: *02 March 2020*
Published: *02 April 2020*

Citation:
Zhang Y and Li Z (2020) Uncertainty Analysis of Standardized Precipitation Index Due to the Effects of Probability Distributions and Parameter Errors. Front. Earth Sci. 8:76. doi: 10.3389/feart.2020.00076

INTRODUCTION

Drought is one of the most common natural disasters usually with a high degree of damage and a wide range of influences (Xu et al., 2005; Mishra and Singh, 2010; Wang et al., 2012), which has become a hot topic in the fields of ecology, meteorology, and hydrology (Lynch et al., 2018; Zhou and Liu, 2018). Drought index is a useful tool in drought researches and drought assessments. Among the drought indices, standardized precipitation index (SPI) is widely used (Moreira, 2015; Zhang et al., 2017; Merabti et al., 2018; Oliveira-Júnior et al., 2018; Tirivarombo et al., 2018) because it can determine drought at different time scales and only requires precipitation data (Ma et al., 2013). However, some uncertainties exist in its calculation due to the probability distribution functions in fitting the precipitation data, parameter estimation methods and errors, time scales and data length, and so on (e.g., Wu et al., 2005; Stagge et al., 2015; Vergni et al., 2017; Beyaztas et al., 2018). McKee et al. (1993), the proposers of SPI, suggested using gamma distribution to fit the cumulative precipitation in calculating this index, whereas many scholars such as like Cindrić et al. (2012), Hong et al. (2013), Gabriel and Monica (2015), Wu et al. (2016), and Vergni et al. (2017) indicated that the applicability of theoretical distributions in describing the cumulative precipitation was inconsistent across different regions. Specifically, Guttman (1999) verified that the Pearson type III distribution is a better universal model in America; Sienz et al. (2012) concluded that the Weibull-type distributions give distinctly improved fits compared to gamma in Europe; Angelidis et al. (2012) found that the log-normal distribution gives almost the same results as gamma in the calculation of SPI at 12- and 24-month scales in Guadiana (Portugal); Gabriel and Monica (2015) demonstrated that the generalized normal distribution presents the best performance in fitting precipitation series in Brazil.

In estimating the distribution parameters, some literatures preferred to investigate the validity of different parameter estimation methods (e.g., Thai et al., 2013; Beguería et al., 2014). Thai et al. (2013) compared maximum likelihood estimation (MLE) and restricted MLE (RMLE) in estimating the parameters in linear mixed-effects model and found that RMLE is advantageous when data are limited. Beguería et al. (2014) contrasted MLE and unbiased probability weighted moments method in estimating parameters in three-parameter log-logistic distribution and concluded that these two methods yield similar results, whereas the calculation of MLE is ∼2-fold more time consuming. Carbone et al. (2018) discussed the relationship between the stability of parameter estimation and data record length and found that the stability in parameter estimation increases non-linearly as record length increases.

As to the input data, a large number of studies have concerned about the uncertainties associated with input data sources, data length, and sampling uncertainty in the calculation of drought index (e.g., Hao et al., 2014, 2016; Liu et al., 2014; Hu et al., 2015; Katiraie-Boroujerdy et al., 2016; Vergni et al., 2017; Zambrano et al., 2017; Beyaztas et al., 2018; Carbone et al., 2018). Vu et al. (2018) compared the performance of rain-gauge data and gridded precipitation data in the calculation of SPI over Vietnam. Carbone et al. (2018) demonstrated that the SPI estimates derived from 30-year record have considerably more uncertainty than those from the 60-year record. Liu et al. (2014), Hu et al. (2015), Vergni et al. (2017), and Beyaztas et al. (2018) quantified the sampling uncertainties and their effects on the estimation of drought index.

All the above studies have made great contributions in enriching the uncertainty analysis in drought assessments, whereas most of them were concerned about the influences of uncertainty sources on the drought index itself and lack of the consideration of their effects on drought events and drought characteristics. Therefore, this study aims to investigate the effects of uncertainty sources on both SPI values and drought characteristics, specifically drought intensity, peak, number, duration, and frequency. Two uncertainty sources are mainly considered; one is the different probability distribution functions, and the other is parameter estimation errors, which would also cause the uncertainty in drought assessments, while it was seldom concerned in literatures.

To be specific, as many as 10 probability distribution functions are employed here, including five three-parameter distributions and five two-parameter distributions. Maximum likelihood estimation approach is used to estimate the distribution parameters, and a large set of randomly generated parameters, which are based on the normality assumption, is used to quantify the uncertainties of parameter estimations. These methods will be described in the next section, preceded by a brief description of the case study area and data sets. The results and discussion will then be presented, and the conclusions from this study will be given in the last section.

MATERIALS AND METHODS

Study Area and Data Description

The Heihe River basin (97° 37′-102° 06′ E, 37° 44′-42°40’N) is the second largest inland river basin in northwest of China, with a drainage area of nearly 1.429×10^5 km^2. The Heihe River flows through Qinghai, Gansu, and Inner Mongolia provinces from south to north, spanning three different geographical regions: semiarid to semi-humid, semiarid, and extreme arid desert (Feng et al., 2001). The annual mean precipitation amounts to 400 to 500 mm in the southern mountainous area of the upper reach, 100 to 150 mm in the middle reach, and $<$50 mm in the lower reach, whereas the evaporation rate is much higher, ranging from 1,000 to 2,200 mm from the upper reach to the lower reach (Li, 2010). In recent years, temperatures show upward trends for the whole basin (Liu et al., 2017). Droughts have great effects on the local economic and social development and also on the fragile ecological environment over the basin.

There are nine national meteorological stations in the basin, Tuole (TL), Yeniugou (YNG), and Qilian (QL) stations in the upper reach; Sandan (SD), Zhangye (ZY), Jiuquan (JQ), Gaotai (GT), and Dingxin (DX) in the middle reach; and Ejinaqi (EJNQ) station in the lower reach (**Figure 1**). The name in the parentheses is the abbreviated name of each station. Precipitation data covering the period of 1960–2015 at these nine stations are used for the drought analysis, without missing or outliers and with good quality. All data used in the study is available from China Meteorological Data Network (http://data.cma.cn/).

The Standardized Precipitation Index

The SPI requires only precipitation data and can be used for drought assessments on different time scales (e.g., 3, 6, 12-months). It is calculated by fitting the cumulative precipitation with an appropriate probability density function to characterize the deficit of precipitation. As recommended by McKee et al. (1993), the two-parameter gamma distribution is used as a probability function to fit the cumulative precipitation for each month. The calculation process is as follows (McKee et al., 1993; Angelidis et al., 2012):

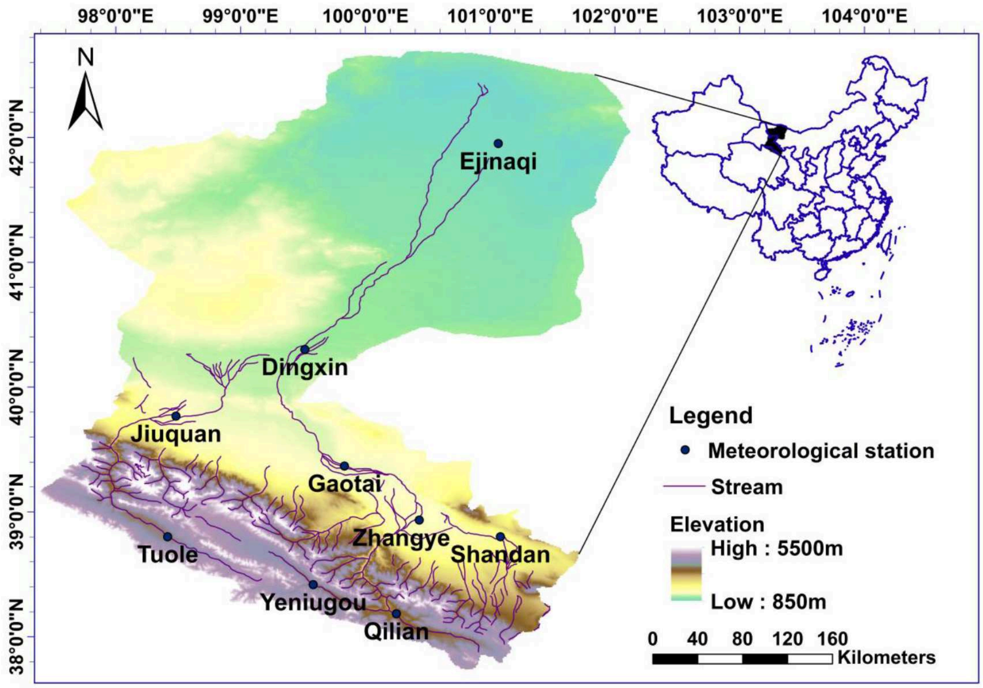

FIGURE 1 | Meteorological stations in Heihe River basin.

Establishing cumulative precipitation sequences at different time scales:

$$X_{i,j}^{k} = \sum_{t=0}^{k-1} \left(x_{i,j-t}\right) \tag{1}$$

where $x_{i,j}$ is the precipitation, i is the specified year, j is the month, and $X_{i,j}^{k}$ is the cumulative precipitation when the time scale is k. The time scales vary from 1 to 48-months (generally include1, 3, 6, 12, 24, or 48-months). Shorter time scales (3 or 6-months) can best represent soil moisture and are more conducive to the discovery of agricultural drought (Komuscu, 1999; Sims et al., 2002). Longer time scales are considered to better monitor the surface water resources (12-month) or the aquifer water state with slow response to drought (24 or 48-months) (Hayes et al., 1999). The time scale of 12-months is selected in this study.

The probability density function of gamma distribution is formulated as

$$g\left(x\right) = \frac{1}{\beta^{\alpha}\Gamma(\alpha)} x^{\alpha-1} e^{\frac{-x}{\beta}} \tag{2}$$

where α and β are the shape and scale parameters, respectively, x is the cumulative precipitation, and $\Gamma(\alpha)$ is a gamma function.

The cumulative probability for a given length of time can be calculated as

$$G\left(x\right) = \int_{0}^{x} g(x)dx \tag{3}$$

It is possible to have several zero values in a precipitation data, so the cumulative probability function of gamma distribution with the $x = 0$ case is modified to

$$H\left(x\right) = q + \left(1 - q\right) G(x) \tag{4}$$

where q is the probability of zero precipitation.

Finally, the cumulative probability distribution is normalized to produce an SPI:

$$\mathrm{SPI} = \begin{cases} -\left(t - \frac{c_0+c_1t+c_2t^2}{1+d_1t+d_2t^2+d_3t^3}\right),\ t = \sqrt{\ln\left(\frac{1}{(H(x))^2}\right)} \\ \quad \textit{for}\ 0 < H\left(x\right) < 0.5 \\ t - \frac{c_0+c_1t+c_2t^2}{1+d_1t+d_2t^2+d_3t^3},\ t = \sqrt{\ln\left(\frac{1}{(1.0-H(x))^2}\right)} \\ \quad \textit{for}\ 0.5 < H\left(x\right) < 1.0 \end{cases} \tag{5}$$

where $c_0 = 2.515517$, $c_1 = 0.802853$, $c_2 = 0.010328$, $d_1 = 1.432788$, $d_2 = 0.189269$, and $d_3 = 0.001308$.

The SPI values are classified into seven grades following the classification criteria in the SPI User Guide (http://www.wamis.org/agm/pubs/SPI/WMO_1090_EN.pdf) and are given in **Table 1**.

Probability Distributions in Fitting SPI

As illustrated above, SPI requires a theoretical probability distribution to fit the cumulative precipitation process. McKee et al. (1993) suggested using a two-parameter gamma distribution when they first proposed this index. However, this distribution is not always the optimal choice when considering practical reasons

TABLE 1 | Drought classification according to SPI values.

SPI value	Classification
≥2.0	Extremely wet
1.5 to 1.99	Very wet
1.0 to 1.49	Moderately wet
−0.99 to 0.99	Near normal
−1.0 to −1.49	Moderately dry
−1.5 to −1.99	Severely dry
≤-2.0	Extremely dry

such as different research areas or research needs (Guttman, 1999; Angelidis et al., 2012; Sienz et al., 2012; Gabriel and Monica, 2015).

In this study, as many as 10 distributions are selected for comparative analysis, including three-parameter log-logistic (LL3), three-parameter log-normal (LN3), generalized extreme value (GEV), Pearson type III (PE3), Burr, gamma, two-parameter log-logistic (LL2), two-parameter log-normal (LN2), inverse Gaussian (IG), and Weibull. The name in the parentheses is the abbreviated name of each distribution. The former five-are three-parameter distributions and the latter five are two-parameter distributions. The probability density function of each distribution is shown in **Table 2**.

Method for Quantifying the Effects of Parameter Estimation Errors

Maximum likelihood estimation is one of the most commonly used approaches to estimate parameters in probability distribution functions and has been verified to be preferable when the sample size is more than 50 (Madsen et al., 1997). Thus, it is employed to estimate the parameters of gamma distribution in this research. The theory of MLE states that for large sample sizes n and a k-dimensional parameter vector, MLE estimators are approximately distributed as a multivariate normal. Thus, the uncertainties of distribution parameters are then quantified by randomly generating parameters based on the multivariate asymptotic normality assumption (Nixon et al., 2010; Degeling et al., 2017). The detailed process is as follows:

- fitting the original cumulative precipitation data set $X = (x_1, x_2, ..., x_n)$ (n is the length of the data set) with gamma distribution and obtaining the optimal parameter sets (α^*, β^*) and the variance–covariance matrix;
- randomly generating N sets of parameters [(α_1, β_1), (α_2, β_2),..., (α_N, β_N)] based on the optimal parameter sets and the variance–covariance matrix under the assumption of asymptotic normality (N can be set, in this study $N = 1000$);
- calculating N sets of SPI values according to Equations (2) to (5) with N sets of parameters; and
- identifying the (a/2)th and (1- a/2)th percentiles based on N sets of SPI values, which are assumed to be the lower and upper bounds of SPI confidence intervals (CIs). a is set to be 0.05 herein.

TABLE 2 | Probability density function of each distribution.

Distribution		Probability density function
3-Parameter	LL3	$f(x) = \frac{\alpha}{\beta}(\frac{x-\gamma}{\beta})^{\alpha-1}(1+(\frac{x-\gamma}{\beta})^{\alpha})^{-2}$
	LN3	$f(x) = \frac{1}{(x-\gamma)\beta\sqrt{2\pi}}e^{(-\frac{1}{2}(\frac{ln(x-\gamma)-\alpha}{\beta})^2)}$
	GEV	$f(x) = \begin{cases} \frac{1}{\beta}e^{(-(1+\alpha\frac{x-\gamma}{\beta})^{-\frac{1}{\alpha}}}\left(1+\alpha\frac{x-\gamma}{\beta}\right)^{-1-\frac{1}{\alpha}} & \alpha \neq 0 \\ \frac{1}{\beta}e^{(-\frac{x-\gamma}{\beta}-e^{-\frac{x-\gamma}{\beta}})} & \alpha = 0 \end{cases}$
	PE3	$f(x) = \frac{1}{\beta^{\alpha}\Gamma(\alpha)}(x-\gamma)^{\alpha-1}e^{-\frac{(x-\gamma)}{\beta}}$
	Burr	$f(x) = \frac{\mu\alpha(\frac{x}{\beta})^{\mu-1}}{\beta(1+(\frac{x}{\beta})^{\mu})^{\alpha+1}}$
2-Parameter	Gamma	$f(x) = \frac{1}{\beta^{\alpha}\Gamma(\alpha)}x^{\alpha-1}e^{\frac{-x}{\beta}}$
	LL2	$f(x) = \frac{\alpha}{\beta}(\frac{x}{\beta})^{\alpha-1}(1+(\frac{x}{\beta})^{\alpha})^{-2}$
	LN2	$f(x) = \frac{1}{x\beta\sqrt{2\pi}}e^{(-\frac{1}{2}(\frac{lnx-\alpha}{\beta})^2)}$
	IG	$f(x) = \sqrt{\frac{\beta}{2\pi x^3}}e^{-\frac{\beta(x-\gamma)^2}{2\gamma^2 x}}$
	Weibull	$f(x) = \frac{\alpha}{\beta}(\frac{x}{\beta})^{\alpha-1}e^{-(\frac{x}{\beta})^{\alpha}}$

α, β, γ, and μ are shape, scale, location, and inequality parameters, respectively.

Drought Characteristics

Drought event can be characterized by multiple variables, for example, drought event number, intensity, peak, duration, and frequency. All these characteristics are often suggested to be used for drought assessments (e.g., Loukas and Vasiliades, 2004; Sheffield and Wood, 2008; He et al., 2018) and thus selected in this analysis. According to the Run theory (Yevjevich, 1967), when SPI is below the threshold value, for example, −1, a drought event is considered to have occurred. The intensity of a drought event is defined as the mean value of a drought index below the threshold level. The peak is the minimum value of a drought index below the threshold value. Duration is the amount of time that a drought index is continuously below the threshold level. Drought frequency is defined as the ratio of drought event number to the total length of the time series. It is calculated with the formula of $P = \frac{n}{N} \times 100\%$, in which N means the total number of SPI values, and n means the total number of SPI values belonging to each grade.

RESULTS

Effects of Probability Distributions

Performance of Different Probability Distributions

Figure 2, taking the 12-month cumulative precipitation in January at Tuole station as an example, shows the comparison of the empirical cumulative probability distribution and the 10 theoretical ones. Note that the abbreviated names of stations and distributions are used in all figures for convenience. No clear differences are observed from **Figure 2**, and all the alternative distributions seem to give satisfactory fits to the series. For evaluating the performance of different probability distributions in more details, goodness-of-fit tests including the Kolmogorov–Smirnov (K-S) and Anderson–Darling (A-D) tests are carried out (Svensson et al., 2017; Vergni et al., 2017). Also taking the cumulative precipitation data in January as an example, the calculated statistic values for both tests are given in **Table 3**. The

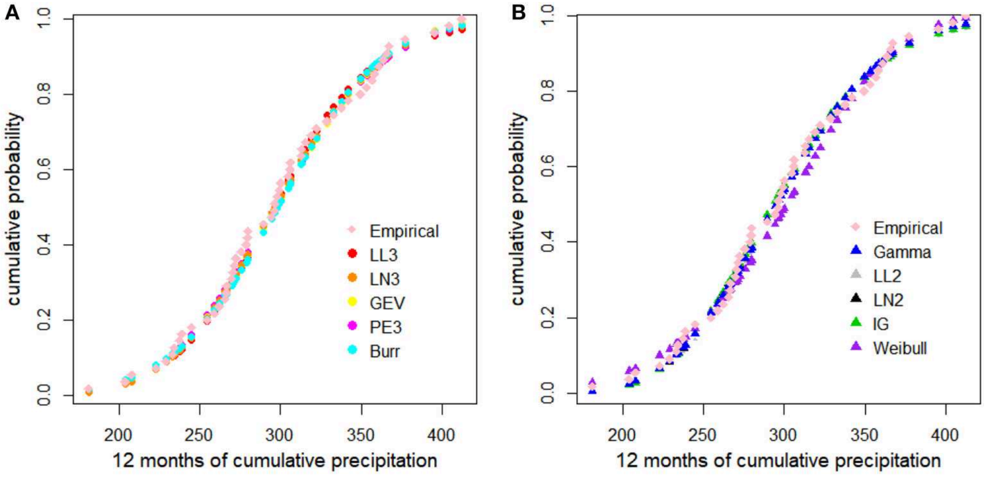

FIGURE 2 | Cumulative probability for 12-month cumulative precipitation in January at Tuole station (LL3, LL2, LN3, LN2, GEV, PE3, and IG represent the three- and two-parameter log-logistic and log-normal, generalized extreme value, Pearson-III, and inverse Gaussian distributions, respectively). **(A)** The cumulative probability of empirical and three-parameter theoretical distributions. **(B)** The cumulative probability of empirical and two-parameter theoretical distributions.

TABLE 3 | The statistic values of Kolmogorov–Smirnov and Anderson–Darling tests for January cumulative precipitation series at *a* of 0.05.

Distribution		Tuole	Yeniugou	Qilian	Sandan	Zhangye	Jiuquan	Gaotai	Dingxin	Ejinaqi
		Kolmogorov–Smirnov								
3-Parameter	LL3	0.067	0.076	0.064	**0.079**	**0.071**	0.073	**0.055**	0.070	**0.054**
	LN3	**0.062**	**0.059**	**0.054**	0.095	0.093	0.074	0.063	0.066	0.064
	GEV	0.064	0.060	0.056	0.097	0.095	0.079	0.061	0.062	0.060
	PE3	**0.062**	0.060	0.056	0.096	0.096	**0.068**	0.069	0.069	0.076
	Burr	0.075	0.072	0.063	**0.079**	0.076	0.080	0.052	**0.059**	0.059
2-Parameter	Gamma	0.055	**0.058**	0.097	0.088	0.094	0.084	0.074	**0.052**	0.086
	LL2	0.059	0.076	**0.069**	**0.075**	**0.083**	0.084	**0.052**	0.069	**0.052**
	LN2	**0.054**	0.063	0.090	0.081	0.111	0.080	0.065	0.068	0.074
	IG	0.056	0.063	0.091	0.083	0.113	**0.078**	0.068	0.069	0.090
	Weibull	0.085	0.099	0.138	0.133	0.107	0.116	0.115	0.074	0.115
		Anderson–Darling								
3-Parameter	LL3	0.228	**0.175**	**0.150**	**0.302**	**0.398**	0.264	0.230	0.332	**0.187**
	LN3	0.180	0.195	0.167	0.460	0.525	0.213	0.291	0.248	0.226
	GEV	0.182	0.210	**0.150**	0.495	0.555	0.253	0.275	0.251	0.207
	PE3	**0.179**	0.199	0.222	0.473	0.550	**0.197**	0.338	**0.244**	0.289
	Burr	0.245	0.18	0.172	0.307	0.404	0.311	**0.205**	0.268	0.208
2-Parameter	Gamma	**0.173**	0.197	0.706	0.444	**0.535**	0.483	0.368	**0.219**	0.326
	LL2	0.229	**0.171**	**0.393**	**0.279**	0.575	0.343	**0.205**	0.324	**0.193**
	LN2	0.207	0.196	0.558	0.440	0.695	0.297	0.273	0.257	0.274
	IG	0.210	0.200	0.564	0.458	0.715	**0.281**	0.284	0.254	0.375
	Weibull	0.424	0.761	2.121	1.077	0.788	0.987	1.181	0.422	0.682

The bold numbers correspond to the smallest statistical values of Kolmogorov–Smirnov and Anderson–Darling tests for each station.

critical values equal 0.18 and 2.50 at 0.05 significance level for K-S and A-D tests, respectively. If the statistic value is lower than the critical value, it indicates that the data set passes the corresponding test at 0.05 significance level; otherwise, it fails.

According to **Table 3**, all the statistic values are lower than the critical values, indicating that all the alternative distributions can provide satisfactory performance in fitting the cumulative precipitations. Comparatively, the three-parameter distributions show better than those two-parameter ones. Among the three-parameter distributions, three-parameter log-logistic performs the best, with 9 of 18 critical values being the smallest (in bold in **Table 3**). Among the two-parameter distributions, two-parameter log-logistic performs the best, with 10 of 18 critical values being the smallest, and Weibull performs the worst, with the highest statistic values.

The same work is done for the precipitation data of other months. The results still demonstrate that three- and two-parameter log-logistics perform best among the three-parameter and two-parameter distributions, respectively, with 67 and 95 smallest critical values of the total, accounting for 31 and 44%. By contrast, three-parameter log-logistic performs better than the two-parameter one owing to the smaller critical values of K-S and A-D tests. That is, log-logistic–type distribution can be used as alternatives in fitting the cumulative precipitation across the study area. In contrast, gamma performs moderately, with 25% of the critical values being the smallest in this case. Note that among all the precipitation data and all the distributions only Burr fails to fit the data in August at Jiuquan station.

Effects of Probability Distributions to SPI

Figure 3 shows the SPI values derived from the 10 different probability distributions. The blue line is from the benchmark gamma distribution, and other colored lines are from the other nine alternative distributions. Most of the lines coincide with each other as a whole, and the differences are generally observed at the lower and upper limits of SPI values (extremely dry and extremely wet conditions). For example, more wet conditions (higher SPI values) are detected from Weibull distribution at Qilian station in 1999, and more dry conditions (smaller SPI values) are detected from Pearson type III at Qilian station in 1971.

In order to further analyze the inconsistency of SPI values obtained from the various probability distributions, the differences calculated from $\mathrm{SPI}_{\mathrm{alternative}}$ minus $\mathrm{SPI}_{\mathrm{gamma}}$ are presented in **Figure 4** ($\mathrm{SPI}_{\mathrm{alternative}}$ and $\mathrm{SPI}_{\mathrm{gamma}}$ mean the SPI values derived from the nine alternative distributions and from the benchmark gamma distribution, respectively). Clearly, the differences are minimal for normal and moderate classifications (corresponding to $-1.5 < \mathrm{SPI} < 1.5$), conditions nearly within the range of ± 0.1. As the SPI values vary to the extremes, the differences become lager. The more extreme (dry or wet) the events, the greater the differences, and the more dispersed the scatter points (**Figure 4**). These indicate that although little effects are on the normal and moderate classifications, greater effects are on the extreme classifications (extremely dry or wet) from the different probability distributions in SPI calculation. Note that the differences derived from Burr distribution vary greatly for Jiuquan station (in cyan in **Figure 4**) due to the fact that Burr fails to pass the tests in fitting the August cumulative precipitation at this station.

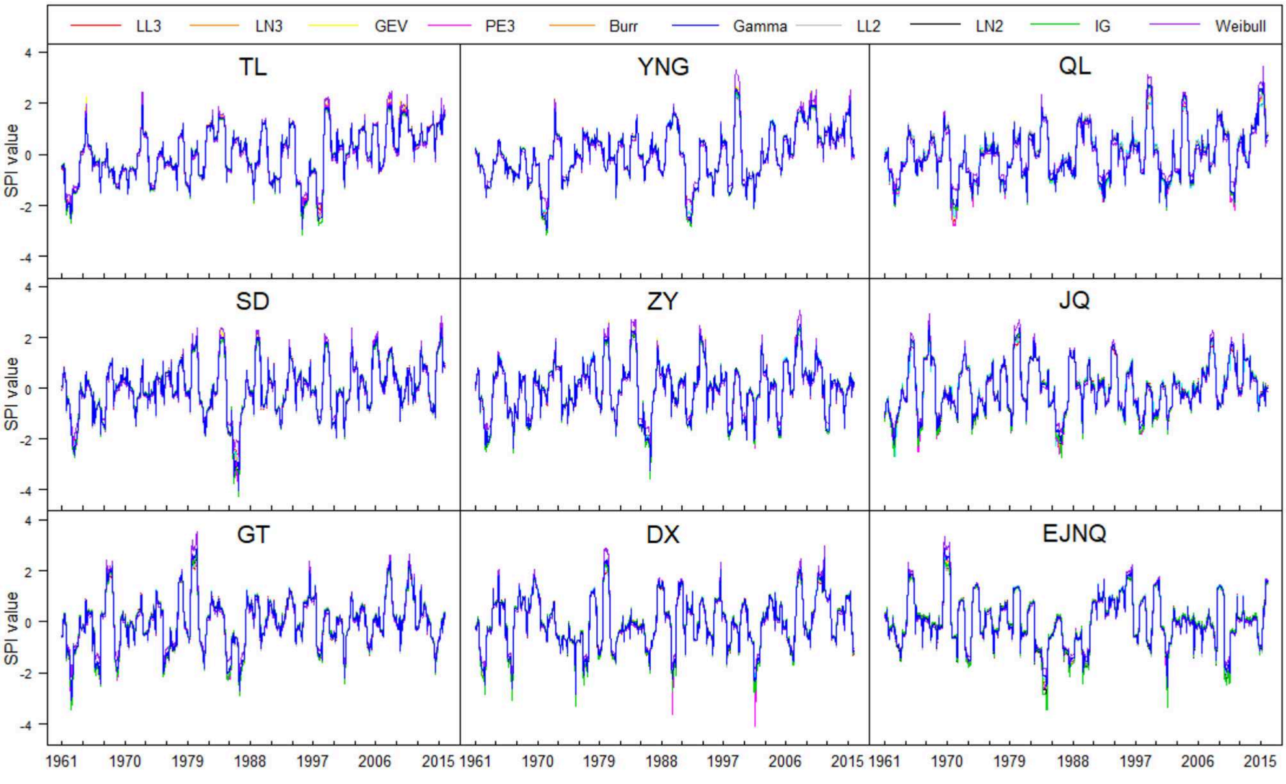

FIGURE 3 | SPI values modeled by different probability distributions (LL3, LL2, LN3, LN2, GEV, PE3, and IG represent the three- and two-parameter log-logistic and log-normal, generalized extreme value, Pearson-III, and inverse Gaussian distributions, respectively; TL, YNG, QL, SD, ZY, JQ, GT, DX, and EJNQ are Tuole, Yeniugou, Qilian, Sandan, Zhangye, Jiuquan, Gaotai, Dingxin, and Ejinaqi stations, respectively).

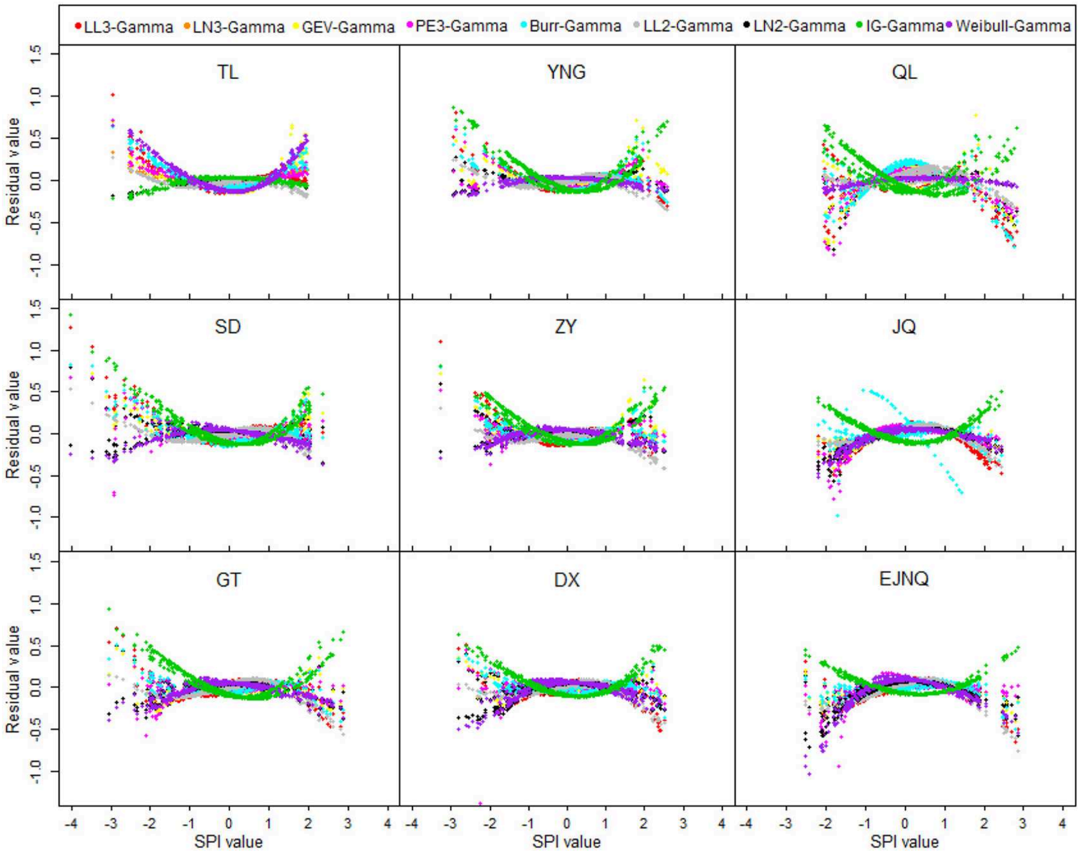

FIGURE 4 | The differences of SPI modeled by gamma and alternative distributions (the abbreviations are the same as in **Figure 3**).

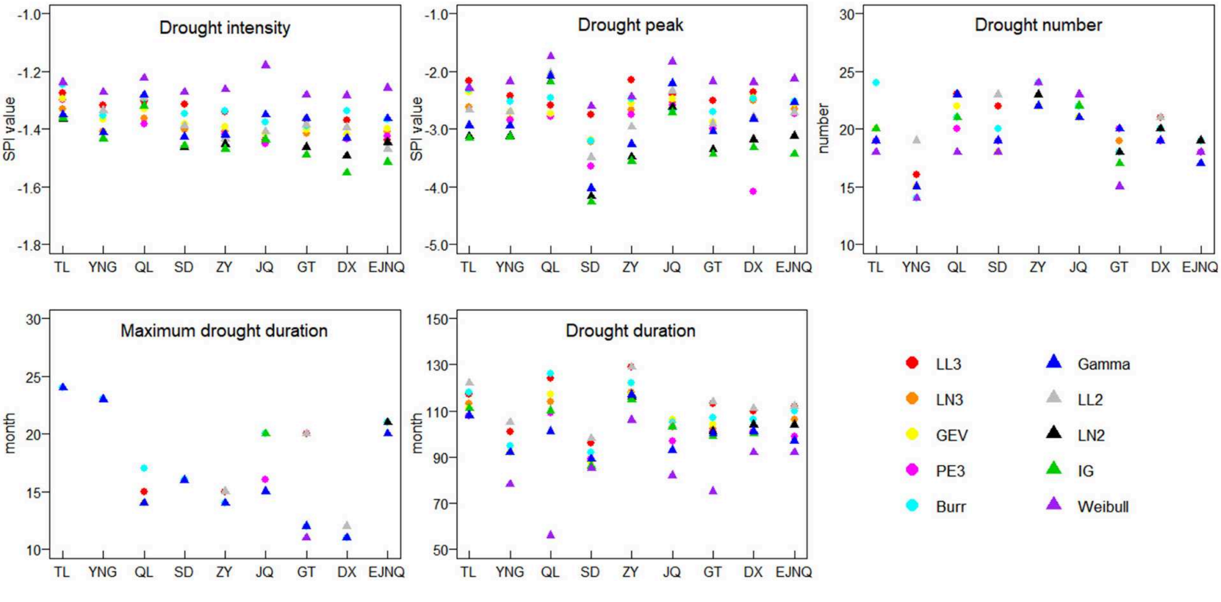

FIGURE 5 | Drought characteristics derived from different probability distributions (the abbreviations are the same as in **Figure 3**).

Effects of Probability Distribution to Drought Characteristics

The drought assessment based on drought characteristics is more informative than the numerical value itself for most practical applications (Guttman, 1999). Five characteristics of drought events are considered here: intensity, peak, event number, the maximum and total duration, and frequency. As observed in **Figure 5**, the drought characteristics derived from the different probability distributions differ greatly. Inverse Gaussian distribution tends to derive the droughts with higher drought intensity and peak, two-parameter log-logistic derives more droughts with longer drought duration, whereas Weibull derives more droughts with lower intensity, lower peak, and shorter duration. As to the maximum drought duration, most distributions detect longer duration than gamma. As to the drought event number, the performance of different distributions at different stations is inconsistent.

Figure 6 presents the drought frequency of each drought grade. As observed, differences can be found in drought frequency derived from different probability distributions, especially at the extremely wet and extremely dry levels. When SPI ≥2.0 (extremely wet), for example, the occurrence frequency is 2.3% from gamma for Jiuquan station, whereas 0% from three-parameter log-logistic and 4.4% from Weibull. When SPI ≤-2.0 (extremely dry), the occurrence frequency is 0.6% from gamma for Jiuquan station and 3.0% from Pearson type III.

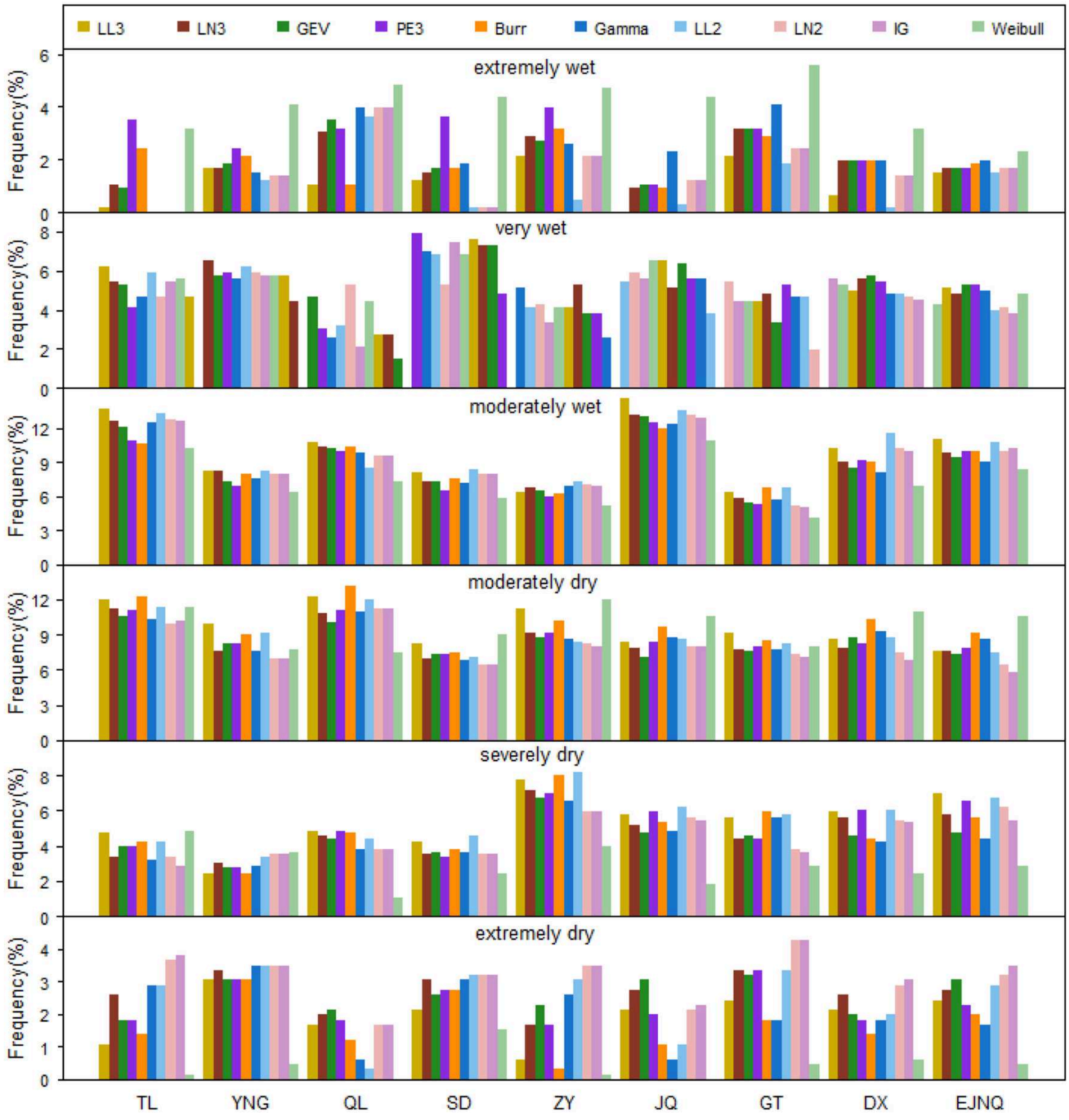

FIGURE 6 | Drought frequency of SPI modeled by different probability distributions (the abbreviations are the same as in **Figure 3**).

Comparatively, Weibull distribution detected more extreme wet and almost no extreme dry in this study. The findings of great effects on extreme droughts from different probability distributions highlight the importance of the selection of suitable probability distribution in the calculation of SPI, because extremes (rather than the moderate) are usually the main focuses of many meteorological and disaster researches.

Effects of Parameter Estimation Errors

Parameter Estimation and Its Uncertainty

The shape and scale parameters in gamma distribution are estimated by the MLE method, with the results shown in **Figure 7**. The optimal shape parameters vary greatly at different stations, whereas the scale parameters are relatively close. Method of L moment is used as well for comparison. Clearly, these two methods give quite close parameter estimations as a whole.

Figure 7 also shows the 95% CIs of each parameter derived from the standard errors, with the normality assumption according to MLE. The width of 95% CIs of a given variable is usually used as a measure of its uncertainty (Liu et al., 2014; Hu et al., 2015; Vergni et al., 2017). From the figure, the uncertainties range from 16.93 to 47.40, 21.70 to 61.90, 33.71 to 92.64, 12.12 to 30.42, 8.51 to 22.43, 3.92 to 11.79, 6.04 to 18.10, 4.36 to 18.10, and 2.18 to 5.09 for shape parameters at Tuole, Yeniugou, Qilian, Sandan, Zhangye, Jiuquan, Gaotai, Dingxin, and Ejinaqi stations and range from 6.36 to 18.23, 6.81 to 19.24, 4.35 to 12.50, 6.63 to 17.15, 5.56 to 16.67, 7.14 to 25.00, 5.91 to 18.51, 4.98 to 13.25, and 6.67 to 16.67 for scale parameters at each station.

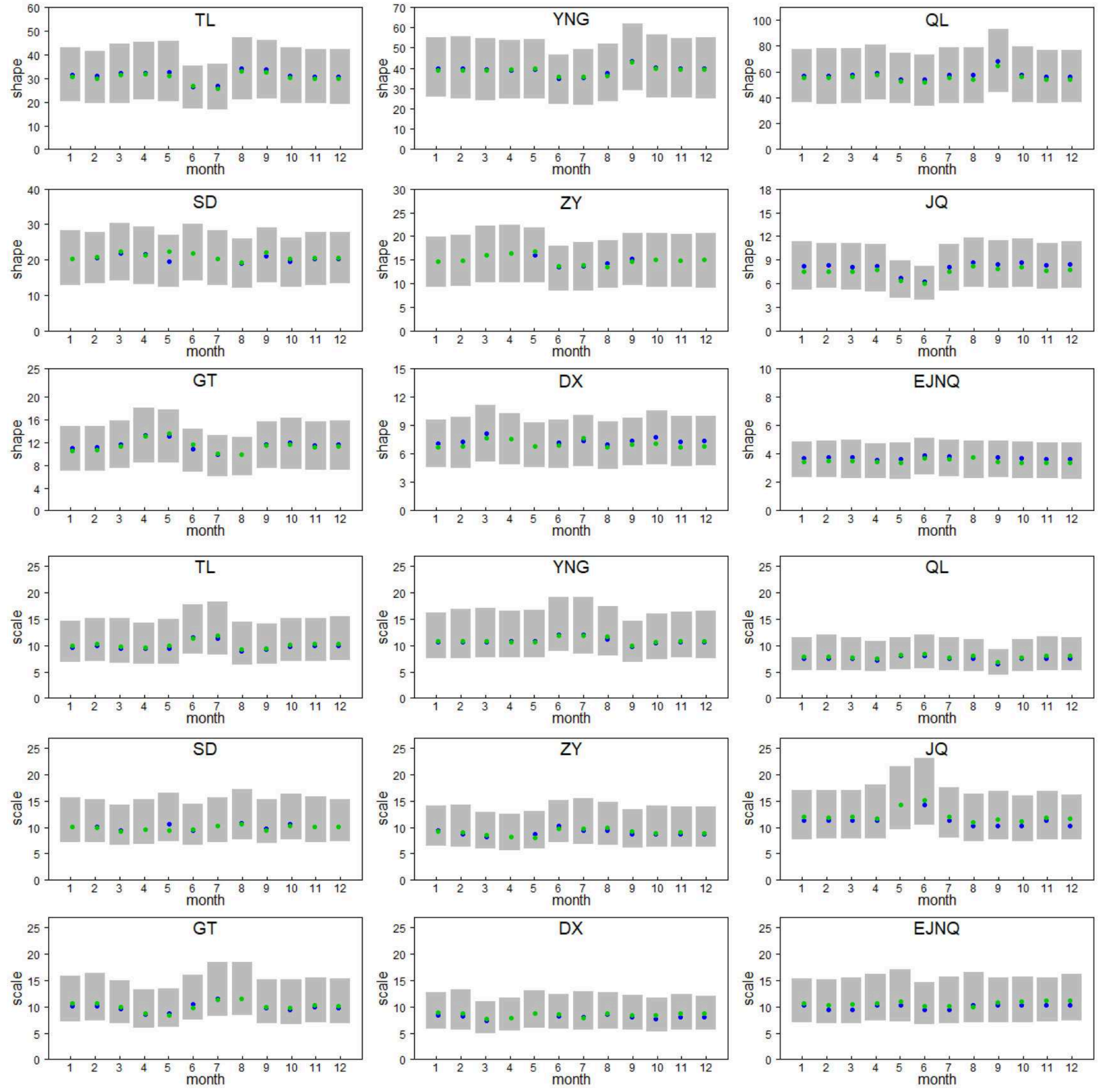

FIGURE 7 | The optimal values and 95% CIs for shape and scale parameters in gamma distribution (the gray shade represents the 95% CIs; the blue and green points represent the optimal parameters from MLE and L moment methods, respectively; the abbreviated names of stations are the same as in **Figure 3**).

Effects of Parameter Estimation Errors to SPI

Figure 8 gives the SPI estimations, and their 95% CIs resulted from the parameter estimation errors. It is observed that the 95% CIs are wider for extreme events than for other cases, no matter extremely wet or extremely dry. In order to investigate the uncertainty of SPI values originating from parameter estimation errors in more details, the widths of 95% CIs of SPI are presented in **Figure 9**, together with the mean absolute error (MAE) values, which are derived from the equation of MAE $= \frac{1}{n}\sum_{i=1}^{n}|X_i - Y_i|$, where n is the total sample size, X_i is the ith original SPI value, and Y_i is the ith SPI value considering the parameter estimation errors. For making **Figure 9** more clearly, we fix the widths of 95% CIs and *MAE* facing down when the SPI values are negative, and vice versa.

It can be seen that the fluctuations of the curves for 95% CIs width (in pink) are close to those of SPI values, showing increasing (getting larger) with SPI values changing to the extremes. For example, the average widths of 95% CIs vary from 0.58 to 0.87 for Qilian station when $-1.99 \leq$ SPI ≤ 1.99 and increase to 1.10 when SPI $\geq$2.0 and 0.95 when SPI $\leq$-2.0. The more extreme the SPI value, the larger the average width. The widest 95%CIs (1.24, 1.24, 1.24, 1.59, 1.13, 1.11, 1.31, 1.21, and 1.29 for Tuole, Yeniugou, Qilian, Sandan, Zhangye, Jiuquan, Gaotai, Dingxin, and Ejinaqi stations) are nearly twice of the average widths of 95% CIs (0.65, 0.65, 0.65, 0.64, 0.65, 0.54, 0.65, 0.66, and 0.64, respectively) at each station. The fluctuations of the curves for *MAE* (in green) also show similar tendency with the 95% CIs curves, getting larger with the SPI increasing or decreasing to the extremes.

Effects of Parameter Estimation Errors to Drought Characteristics

The intervals of each drought characteristic caused by parameter estimation uncertainty are shown in **Table 4**. Consistent with the results caused by different probability distributions, drought peak, event number, and drought duration are greatly affected. The deviation amounts to 0.10 to 0.29 for drought intensity, 0.93 to 1.60 for drought peak, 8 to 18 times for drought event number, 4 to 15-months for the maximum drought duration, and 68 to 123-months for the total duration. Specifically, Jiuquan station experienced the largest difference in drought event number (18 times), Sandan station experienced the largest difference in both drought peak (1.60) and the maximum drought duration (15-months), and Qilian station experienced the largest difference in the total drought duration (123-months). In addition, the intervals of drought event number and the maximum drought duration caused by parameter estimation errors are larger than those caused by different probability distributions.

Figure 10 displays the frequency of seven drought grades associated with the uncertainty of parameter estimations. As expected, the classification results for the upper and lower limits of 95%CIs are different. For instance, when SPI $\geq$2.0, the extremely wet frequency is 6.5% from the upper limit for Jiuquan station, and it is 0 from the lower limit. When SPI $\leq$-2.0, the extremely dry frequency is 0.2% from the upper limit for Zhangye station and increases to 6.1% from the lower limit. This difference occurs not only in extremes, but also in other cases. For example, the frequency of moderate drought (corresponding to $-1.5 <$ SPI ≤ -1.0) is 5.3% from the

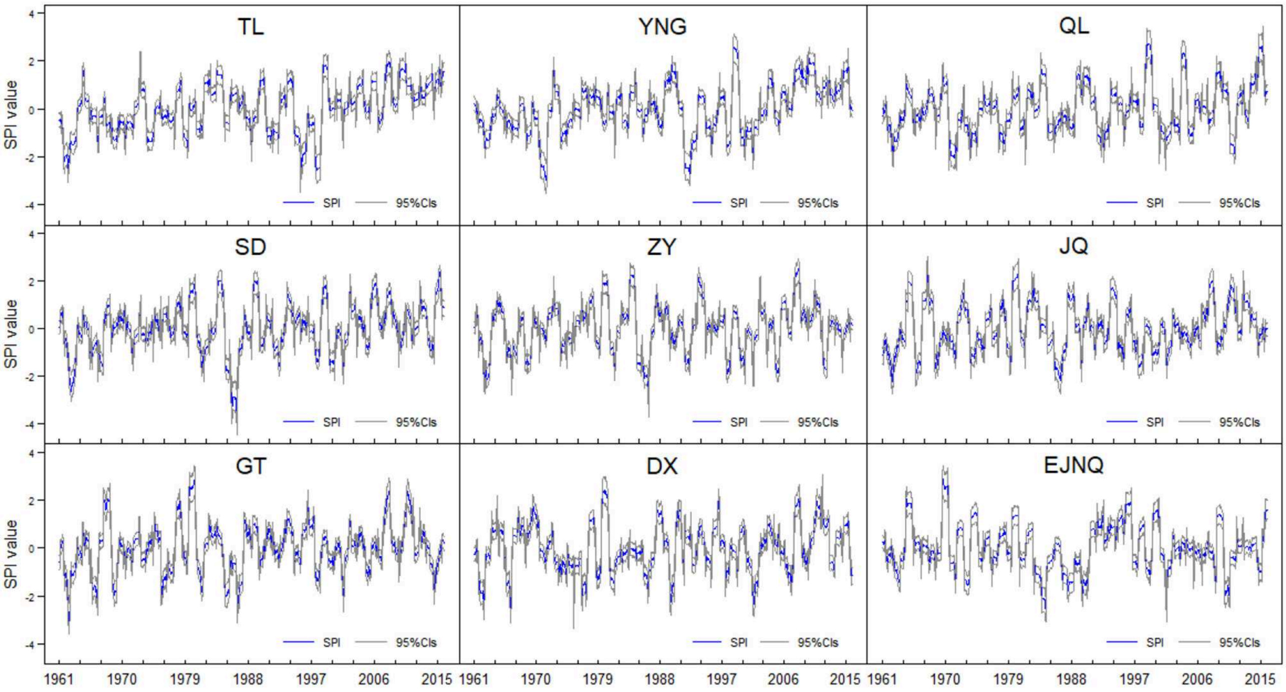

FIGURE 8 | SPI values and their 95% CIs estimations considering the parameter estimation errors (the abbreviated names of stations are the same as in **Figure 3**).

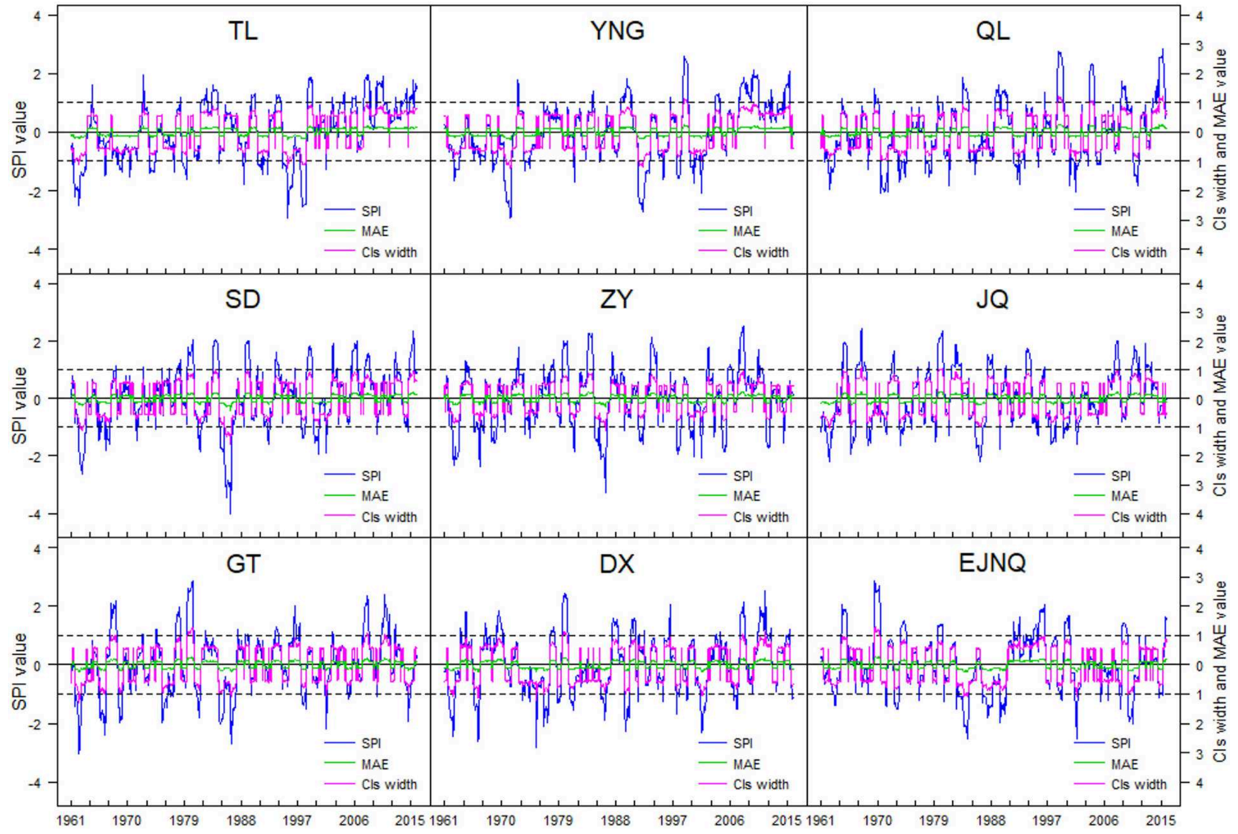

FIGURE 9 | SPI 95% CIs width of and the MAE value considering the parameter estimation errors (the black dotted lines correspond to SPI value of ± 0.99; the abbreviated names of stations are the same as in **Figure 3**).

TABLE 4 | The intervals of drought characteristics considering parameter estimation errors.

Station	Drought intensity	Drought peak	Drought number	Maximum drought duration	Drought duration
Tuole	[−1.49, −1.22]	[−3.46, −2.22]	[12, 22]	[13, 24]	[49, 147]
Yeniugou	[−1.41, −1.28]	[−3.51, −2.27]	[9, 22]	[15, 23]	[47, 148]
Qilian	[−1.36, −1.26]	[−2.56, −1.63]	[15, 32]	[12, 19]	[41, 164]
Sandan	[−1.40, −1.26]	[−4.46, −2.86]	[16, 27]	[14, 29]	[51, 143]
Zhangye	[−1.54, −1.27]	[−3.70, −2.57]	[19, 25]	[12, 16]	[85, 153]
Jiuquan	[−1.38, −1.20]	[−2.76, −1.74]	[12, 30]	[14, 21]	[52, 158]
Gaotai	[−1.47, −1.28]	[−3.58, −2.27]	[13, 24]	[11, 20]	[57, 144]
Dingxin	[−1.41, −1.30]	[−3.35, −2.13]	[13, 30]	[11, 17]	[54, 160]
Ejinaqi	[−1.52, −1.23]	[−3.07, −1.99]	[12, 20]	[11, 24]	[56, 132]

upper limit and reaching 15.5% from the lower limit at Qilian station. This reminds us that we should not ignore the effects of parameter estimation errors on drought index calculation, because they probably affect the classifications of drought grades, which associates closely to the decision-making of the local drought management.

DISCUSSION

Drought index is an important indicator for drought researches. However, uncertainties exist in its calculation. This study discusses the effects of probability distributions and parameter estimation errors on both SPI values and drought characteristics.

It is found that the three-parameter distributions show better performance in fitting the precipitation data than those two-parameter distributions. This result keeps consistent with the finding of Vergni et al. (2017), who concluded that the two-parameter gamma distribution provides less reliable estimates of the precipitation probability than the three-parameter Pearson type III and the generalized normal distribution in their study case. Cindrić et al. (2012) suggested that as to the choice of the most appropriate

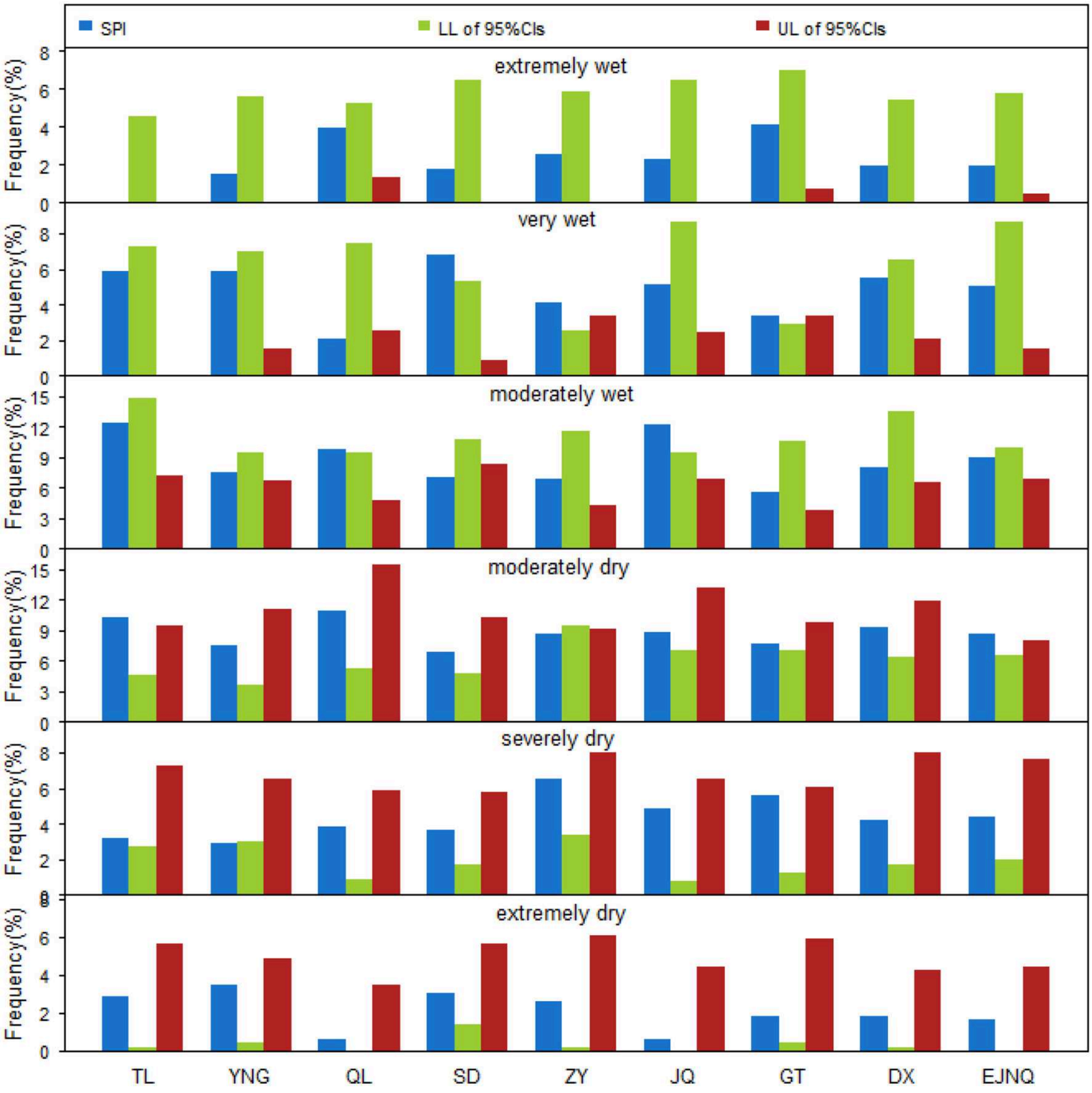

FIGURE 10 | Drought classification frequency based on SPI values considering parameter estimation errors (LL and UL are the lower and upper limits of 95% CIs, respectively; the abbreviated names of stations are the same as in **Figure 3**).

distribution for a particular region the ratio of skewness and the coefficient of variation for the precipitation data can be used as an indicator. Angelidis et al. (2012) and Stagge et al. (2015) deemed that the suitable probability distribution is related with the time scale of precipitation data to be fitted. Angelidis et al. (2012) found that the log-normal distribution can produce almost the same results with gamma for 12- or 24-months SPI. Stagge et al. (2015) compared the seven probability distributions and concluded that the gamma distribution produces the most consistently good fit for the long-accumulation precipitation (>6-months), whereas Weibull is consistently the best for the short accumulation (1–3-months). In our case, log-logistic–type distribution can be used as alternatives in fitting the cumulative precipitation across the study area. Even though for avoiding the interpretability issues and potential extrapolation issues with complex distributions that may be overfit, to use a single and simple distribution may be a good choice (Stagge et al., 2015).

Considering the effects of different probability distributions on SPI and drought characteristics, less influence is found for normal and moderate classifications, while as the SPI values vary to the extremes, the influence becomes lager. This conclusion keeps in line with those from Angelidis et al. (2012) and Vergni et al. (2017), who concluded that the consistency of the SPI calculated with different distributions is good for normal periods, while becoming poor for very dry or very wet periods. It is also found in our case that different probability distributions lead to great differences in drought peak, event number, duration, and frequency.

With regard to the effects of parameter estimation errors on SPI values and drought characteristics, the resulted 95% CIs are becoming larger with the SPI value increasing or decreasing to the extremes. Furthermore, the intervals of drought event number and the maximum drought duration caused by parameter estimation errors are even larger than those caused by different probability distributions. As stated by Wu et al. (2005), the parameter estimates with little confidence would result in the SPI values with little confidence. To ensure the parameter estimates with high confidence, a long record of precipitation data is usually required for the analysis, because MLE presents unstable behavior for small samples (Martins and Stedinger, 2000), and preferable performance when the sample size becomes larger (more than 50) (Beguería et al., 2014). McKee et al. (1993) regarded that a continuous period of at least 30-years seems ideal in the SPI calculation, while Guttman (1994) found that ∼40 to 60-years of record is needed for parameter estimation stability in the central part of the distribution and ∼70 to 80-years of record for stability in the tails. Carbone et al. (2018) suggested that record lengths of 60-years are basically enough in general, which typically results in stable parameters and representative SPI values. In addition, the minimum length of record also depends on whether the precipitation pattern changes (Wu et al., 2005). Carbone et al. (2018) found that extreme events also have a significant influence on SPI estimates, even over 60-years of records.

CONCLUSIONS

The estimation of SPI involves uncertainties originated from many aspects. This article mainly focuses on the effects of two uncertainty sources (probability distribution functions and parameter estimation errors) on both the calculation of SPI of 12-months and drought characteristics.

Five three-parameter and five two-parameter distributions were employed. Results indicate that the log-logistic–type distribution (2-parameter and 3-parameter) presents the best performance in fitting the cumulative precipitation series over the Heihe River basin, better than the suggested gamma distribution, whereas Burr and Weibull present the worst. Results also show that the influences of different probability distributions on SPI values and on droughts are mainly manifested in the extreme classifications (extremely dry and extremely wet conditions with SPI $\leq$-2.0 and SPI $\geq$2.0), rather than in the normal and moderate classifications (corresponding to $-1.5 <$ SPI < 1.5). This finding highlights the importance of selecting the suitable probability distribution in the calculation of SPI, because extremes are usually the primary focuses of many meteorological and disaster researches.

The effects of parameter estimation errors illustrate that the more extreme the SPI value (more drought or the more wet), the wider the 95% CIs, and the greater the uncertainty caused by parameter estimation errors. The parameter estimation errors also result in different drought characteristics. It indicates that the effects of parameter estimation errors should not be ignored because it probably affects the decision-making on drought analysis. A long record of precipitation data is essential to ensure that the parameter error is small. As to how long the records are sufficient over the study area will be discussed in the future analysis. Noted that, because all the findings here are in the context of the SPI at 12-month scale and limited stations, more works should be extended over further scales and regions, to define the most appropriate statistical distribution to fit precipitation data and properly characterize drought.

To sum up, both the probability distribution functions and parameter errors lead to the uncertainties in the estimation of SPI values and drought assessments, especially in the extreme values, which is just the focus of many extreme studies. Consequently, we should be vigilant about the uncertainty issues in drought assessment and strengthen the researches on quantifying and reducing such uncertainties, which will help decision-making becoming more confident.

DATA AVAILABILITY STATEMENT

All data used in the study is available from China Meteorological Data Network (http://data.cma.cn/).

AUTHOR CONTRIBUTIONS

YZ calculated the drought index, performed the uncertainty analysis using R programming language, and wrote the first draft of the manuscript. ZL provided the original data, helped to analyze and interpret the results, reviewed, and revised the manuscript.

FUNDING

This study was supported by the Fundamental Research Funds for the Central Universities (No. 35832015028) and NSFC (No. 41101038).

ACKNOWLEDGMENTS

The authors thank the financial support of the China Scholarship Council and China University of Geosciences (Beijing). We also acknowledge the editor and reviewers for carefully reading the manuscript and providing comments, which have improved the quality of the paper.

REFERENCES

Angelidis, P., Maris, F., Kotsovinos, N., and Hrissanthou, V. (2012). Computation of drought index SPI with alternative distribution functions. *Water Resour. Manage.* 26, 2453–2473. doi: 10.1007/s11269-012-0026-0

Beguería, S., Vicente-Serrano, S. M., Reig, F., and Latorre, B. (2014). Standardized precipitation evapotranspiration index (SPEI) revisited: parameter fitting, evapotranspiration models, tools, datasets and drought monitoring. *Int. J. Climatol.* 34, 3001–3023. doi: 10.1002/joc.3887

Beyaztas, U., Arikan, B. B., Beyaztas, B. H., and Kahya, E. (2018). Construction of prediction intervals for palmer drought severity index using bootstrap. *J. Hydrol.* 559, 461–470. doi: 10.1016/j.jhydrol.2018.02.021

Carbone, G. J., Lu, J., and Brunetti, M. (2018). Estimating uncertainty associated with the standardized precipitation index. *Int. J. Climatol.* 38, 607–616. doi: 10.1002/joc.5393

Cindrić, K., Juras, J., and Pasarić, Z. (2012). "Statistical distributions for the SPI computation," in *EMS Annual Meeting AbstractsBerlin: EMS* (Berlin). GF48: EMS2012-316.

Degeling, K., Ijzerman, M. J., Koopman, M., and Koffijberg, H. (2017). Accounting for parameter uncertainty in the definition of parametric distributions used to describe individual patient variation in health economic models. *BMC Med. Res. Methodol.* 17:170. doi: 10.1186/s12874-017-0437-y

Feng, Q., Cheng, G. D., and Endo, K. N. (2001). Towards sustainable development of the environmentally degraded River Heihe basin, China. *Hydrobiol. Sci. J.* 46, 647–658. doi: 10.1080/02626660109492862

Gabriel, C. B., and Monica, C. M. (2015). Inadequacy of the gamma distribution to calculate the standardized precipitation index. *Rev. Bras. Eng. Agríc. Ambient.* 19, 1129–1135. doi: 10.1590/1807-1929/agriambi.v19n12p1129-1135

Guttman, N. B. (1994). On the sensitivity of sample L moments to sample size. *J. Climatol.* 7, 1026–1029. doi: 10.1175/1520-0442(1994)007<1026:OTSOSL>2.0.CO;2

Guttman, N. B. (1999). Accepting the standardized precipitation index:a calculation algorithm. *J. Am. Water Res. Assoc.* 35, 311–322. doi: 10.1111/j.1752-1688.1999.tb03592.x

Hao, G., Anming, B., Tie, L., Sheng, C., and Felix, N. (2016). Evaluation of PERSIANN-CDR for meteorological drought monitoring over China. *Remote Sens*. 8:379. doi: 10.3390/rs8050379

Hao, Z., Aghakouchak, A., Nakhjiri, N., and Farahmand, A. (2014). Global integrated drought monitoring and prediction system. *Sci. Data* 1:140001. doi: 10.1038/sdata.2014.1

Hayes, M. J., Svoboda, M. D., Wilhite, D. A., and Vanyarkho, O. V. (1999). Monitoring the 1996 drought using the standardized precipitation index. *Bull. Am. Meteorol. Soc.* 80, 429–438. doi: 10.1175/1520-0477(1999)080<0429:MTDUTS>2.0.CO;2

He, Z. H., Liang, H., Yang, C. H., Huang, F. S., and Zeng, X. B. (2018). Temporal-spatial evolution of the hydrologic drought characteristics of the karst drainage basins in South China. *Int. J. Appl. Earth Obs. Geoinf.* 64, 22–30. doi: 10.1016/j.jag.2017.08.010

Hong, X. J., Guo, S. H. L., and Zhou, Y. L. (2013). Applicability of standardized precipitation index with alternative distribution functions. *J. Water Res. Res.* 2, 33–41. doi: 10.12677/JWRR.2013.21006

Hu, Y. M., Liang, Z. M., Liu, Y. W., Wang, J., Yao, L., and Ning, Y. W. (2015). Uncertainty analysis of SPI calculation and drought assessment based on the application of bootstrap. *Int. J. Climatol.* 35, 1847–1857. doi: 10.1002/joc.4091

Katiraie-Boroujerdy, P. S., Nasrollahi, N., Hsu, K. L., and Sorooshian, S. (2016). Quantifying the reliability of four global datasets for drought monitoring over a semiarid region. *Theor. Appl. Climatol.* 123, 387–398. doi: 10.1007/s00704-014-1360-3

Komuscu, A. U. (1999). Using the SPI to analyze spatial and temporal patterns of drought in Turkey. *Drought Network News*, 49.

Li, W. P. (2010). *Regulation and Optimization of Water Resources in Typical Inner Basin in Northwest China – A Case Study of Heihe Basin*. Beijing: Geological Press.

Liu, L., Liu, L. L., and Suo, Y. (2017). Spatiotemporal evolution of hydro-meteorological variables in the Heihe River Basin in recent 53 years. *Arid Zone Res.* 34, 465–478. doi: 10.13866/j.azr.2017.03.01

Liu, Y. W., Wang, W., Hu, Y. M., and Liang, Z. M. (2014). Drought assessment and uncertainty analysis for dapoling basin. *Nat. Hazards* 74, 1613–1627. doi: 10.1007/s11069-014-1259-4

Loukas, A., and Vasiliades, L. (2004). Probabilistic analysis of drought spatiotemporal characteristics in Thessaly region, Greece. *Nat. Hazards Earth Syst. Sci*. 4, 719–731. doi: 10.5194/nhess-4-719-2004

Lynch, D. T., Leasure, D. R., and Magoulick, D. D. (2018). The influence of drought on flow-ecology relationships in Ozark highland streams. *Freshw. Biol.* 63, 946–968. doi: 10.1111/fwb.13089

Ma, H. J., Yan, D. H., Weng, B. S., Fang, H. Y., and Shi, X. L. (2013). Applicability of typical drought indexes in the Luanhe River Basin. *Arid Zone Res.* 30, 728–734. doi: 10.13866/j.azr.2013.04.016

Madsen, H., Rasmussen, P. F., and Rosbjerg, D. (1997). Comparison of annual maximum series and partial duration series methods for modeling extreme hydrologic events: 1. At-site modeling. *Water Resour. Res.* 33, 747–757. doi: 10.1029/96WR03848

Martins, E. S., and Stedinger, J. R. (2000). Generalized maximum-likelihood generalized extreme-value quantile estimators for hydrologic data. *Water Resour. Res.* 36, 737–744. doi: 10.1029/1999WR900330

McKee, T. B., Doesken, N. J., and Kleist, J. (1993). "The relationship of drought frequency and duration to time scales," in: *Proceedings of the 8th Conference on Applied Climatology*, ed P. J. Lamb (Anaheim, CA: American Meteorological Society), 179–184.

Merabti, A., Martins, D. S., Meddi, M., and Pereira, L. S. (2018). Spatial and time variability of drought based on SPI and RDI with various time scales. *Water Resour. Manage.* 32, 1087–1100. doi: 10.1007/s11269-017-1856-6

Mishra, A. K., and Singh, V. P. (2010). A review of drought concepts. *J. Hydrol.* 391, 202–216. doi: 10.1016/j.jhydrol.2010.07.012

Moreira, E. E. (2015). SPI drought class prediction using log-linear models applied to wet and dry seasons. *Phys. Chem. Earth A/B/C* 94, 136–145. doi: 10.1016/j.pce.2015.10.019

Nixon, R. M., Wonderling, D., and Grieve, R. D. (2010). Non-parametric methods for costeffectiveness analysis: the central limit theorem and the bootstrap compared. *Health Econ.* 19, 316–333. doi: 10.1002/hec.1477

Oliveira-Júnior, J. F. D., Gois, G. D., Terassi, P. M. D. B., Junior, C. A. D. S., Blanco, C. J. C., Sobral, B. S., et al. (2018). Drought severity based on the SPI index and its relation to the ENSO and PDO climatic variability modes in the regions North and Northwest of the State of Rio de Janeiro - Brazil. *Atmos. Res.* 212, 91–105. doi: 10.1016/j.atmosres.2018.04.022

Sheffield, J., and Wood, E. F. (2008). Global trends and variability in soil moisture and drought characteristics, 1950–2000, from observation-driven simulations of the terrestrial hydrologic cycle. *J. Clim.* 21, 432–458. doi: 10.1175/2007JCLI1822.1

Sienz, F., Bothe, O., and Fraedrich, K. (2012). Monitoring and quantifying future climate projections of dryness and wetness extremes: SPI bias. *Hydrol. Earth Syst. Sci.* 16, 2143–2157. doi: 10.5194/hess-16-2143-2012

Sims, A. P., Niyogi, D. D. S., and Raman, S. (2002). Adopting drought indices for estimating soil moisture: a North Carolina case study. *Geophys. Res. Lett.* 29, 24-1–24-4. doi: 10.1029/2001GL013343

Stagge, J. H., Tallaksen, L. M., Gudmundsson, L., Van Loon, A. F., and Stahl, K. (2015). Candidate distributions for climatological drought indices (SPI and SPEI). *Int. J. Climatol.* 35, 4027–4040. doi: 10.1002/joc.4267

Svensson, C., Hannaford, J., and Prosdocimi, I. (2017). Statistical distributions for monthly aggregations of precipitation and streamflow in drought indicator applications. *Water Resour. Res.* 53, 999–1018. doi: 10.1002/2016WR019276

Thai, H. T., France, M., Holford, N. H. G., Veyrat-Follet, C., and Comets, E. (2013). A comparison of bootstrap approaches for estimating uncertainty of parameters in linear mixed-effects models. *Pharm. Stat.* 12, 129–140. doi: 10.1002/pst.1561

Tirivarombo, S., Osupile, D., and Eliasson, P. (2018). Drought monitoring and analysis: standardised precipitation evapotranspiration index (SPEI) and standardised precipitation index (SPI). *Phys. Chem. Earth A/B/C* 106, 1–10. doi: 10.1016/j.pce.2018.07.001

Vergni, L., Di, L. B., Todisco, F., and Mannocchi, F. (2017). Uncertainty in drought monitoring by the standardized precipitation index: the case study of the Abruzzo region (Central Italy). *Theor. Appl. Climatol.* 128, 13–26. doi: 10.1007/s00704-015-1685-6

Vu, T. M., Raghavan, S. V., Liong, S. Y., and Mishra, A. K. (2018). Uncertainties of gridded precipitation observations in characterizing spatio-temporal drought and wetness over Vietnam. *Int. J. Climatol*. 38, 2067–2081. doi: 10.1002/joc.5317

Wang, J. S., Li, Y. H., Wang, R. Y., Feng, J. Y., and Zhao, Y. X. (2012). Preliminary analysis on the demand and review of progress in the field of meteorological drought research. *J. Arid Meteorol*. 30, 497–508.

Wu, H., Hayes, M. J., Wilhite, D. A., and Svoboda, M. D. (2005). The effect of the length of record on the standardized precipitation index calculation. *Int. J. Climatol.* 25, 505–520. doi: 10.1002/joc.1142

Wu, S. F., Zhang, X., Wang, J. X., Liu, J. F., and Pan, G. Y. (2016). Calculation of the SPI based on the best fitted distribution functions to the precipitation series. *Arid Land Geogr.* 39, 555–564.

Xu, Q. Y., Zhang, Q., Zhang, C. J., Yin, X. Z., Guo, H., Zhang, D. Q., et al. (2005). Research on drought early warning system of China. *J. Desert Res.* 25, 785–789. doi: 10.3321/j.issn:1000-694X.2005.05.028

Yevjevich, V. (1967). *An Objective Approach to Definitions and Investigations of Continental Hydrologic Droughts,* Vol. 6. Fort Collins, CO: Colorado State University, 23–30.

Zambrano, F., Wardlow, B., Tadesse, T., Lillo-Saavedra, M., and Lagos, O. (2017). Evaluating satellite- derived long-term historical precipitation datasets for drought monitoring in Chile. *Atmos. Res*. 186, 26–42. doi: 10.1016/j.atmosres.2016.11.006

Zhang, Y. H., Li, W. W., Chen, Q. H., Pu, X., and Xiang, L. (2017). Multi-models for SPI drought forecasting in the north of Haihe River Basin, China. *Stoch. Environ. Res. Risk Assess*. 31, 2471–2481. doi: 10.1007/s00477-017-1437-5

Zhou, H., and Liu, Y. (2018). Spatio-temporal pattern of meteorological droughts and its possible linkage with climate variability. *Int. J. Climatol.* 38, 2082–2096. doi: 10.1002/joc.5319

Conflict of Interest: The authors declare that the research was conducted in the absence of any commercial or financial relationships that could be construed as a potential conflict of interest.

frontiers in Earth Science

ORIGINAL RESEARCH
published: 22 May 2020
doi: 10.3389/feart.2020.00161

Inter-Annual Variability of Winter Precipitation Over Nepal Coupled With Ocean-Atmospheric Patterns During 1987–2015

Kalpana Hamal[1,2], Shankar Sharma[2,3]*, Binod Baniya[2,4,5], Nitesh Khadka[2,6] and Xu Zhou[3]

[1] International Center for Climate and Environment Sciences, Institute of Atmospheric Physics, Chinese Academy of Sciences, Beijing, China, [2] University of Chinese Academy of Sciences, Beijing, China, [3] National Tibetan Plateau Data Center, Institute of Tibetan Plateau Research, Chinese Academy of Sciences, Beijing, China, [4] Land Surface Processes and Global Change Research Group, Institute of Geographic Sciences and Natural Resources Research, Chinese Academy of Sciences, Beijing, China, [5] Department of Environmental Science, Patan Multiple Campus, Tribhuvan University, Patan, Nepal, [6] Institute of Mountain Hazards and Environment, Chinese Academy of Sciences, Chengdu, China

OPEN ACCESS

Edited by:
Xingcai Liu,
Chinese Academy of Sciences, China

Reviewed by:
Jing Yang,
Beijing Normal University, China
Navaraj Pokharel,
Tribhuvan University, Nepal

***Correspondence:**
Shankar Sharma
Sharma.sh969@gmail.com

Specialty section:
This article was submitted to Interdisciplinary Climate Studies, a section of the journal Frontiers in Earth Science

Received: 15 November 2019
Accepted: 29 April 2020
Published: 22 May 2020

Citation:
Hamal K, Sharma S, Baniya B, Khadka N and Zhou X (2020) Inter-Annual Variability of Winter Precipitation Over Nepal Coupled With Ocean-Atmospheric Patterns During 1987–2015. Front. Earth Sci. 8:161. doi: 10.3389/feart.2020.00161

Nepal is a mountainous country located on the southern slope of the central Himalayas, where the winter season contributes ∼3% of the total annual rainfall. This study sought to investigate the inter-annual variability and associated ocean-atmospheric pattern with winter precipitation during 1987–2015. A high-resolution APHRODITE and ERA5 reanalysis datasets are used to study the Empirical Orthogonal Function (EOF), Wavelet, Composites, and Correlation analysis, respectively. The results show that the leading EOF mode captures 53.2% of the total variance, exhibiting a single mode of variability. Wavelet analysis determined 2 to 2.6 years of the significant power spectrum. The time-series of winter precipitation anomalies revealed the years 1996, 1998, 2000, 2005, 2007, and 2008 as precipitation deficit years which is supported by negative precipitation anomalies with positive outgoing longwave radiation (OLR) and vertical velocity. These phenomena are converse for wet events during the years 1988, 1995, 1997, 2002, 2012, and 2014. Furthermore, the wet (dry) years exhibit moisture convergence (divergence) with strong southwesterly (northwesterly) wind anomalies. In the wave train of westerly flow, the cyclonic and anticyclonic circulation in northern India affects the moisture transport in wet and dry years, respectively. In excess precipitation years, Surface Air Temperature (SAT) over entire northern India and adjoining Nepal and Tibetan Plateau (TP) regions have a colder temperature than in deficit precipitation years. The correlation suggests the instance of Indian Ocean Basin Mode (IOBM) and NINO3.4 impacts on the inter-annual variability of the winter precipitation. Moreover, the warming and cooling over the Indo-Pacific regions affect the Walker and Hadley circulation bringing above and below-normal precipitation, respectively, over Nepal. The observed changes in the dry and wet years during winter are useful for disaster preparedness and the planning and monitoring of water resources and agriculture.

Keywords: winter precipitation variability, dry events, wet events, westerlies, Nepal

INTRODUCTION

Nepal is considered to be one of the most vulnerable countries to extreme weather events (Eckstein et al., 2018). In recent years, the country has been suffering from many meteorological disasters, such as floods and droughts due to the above and below-average rainfall (Krishnamurthy et al., 2013; Adhikari, 2018). High intensity related to extreme precipitation events is the principal cause of landslides, debris flows, and flood disasters in the country (Talchabhadel et al., 2018). Flooding has been reported to contribute to about 49% of the total disaster events in Nepal from 2000 to 2017 (CRED, 2018). Moreover, a flood is a complex hazard resulting in a cascade of secondary hazards, such as landslides and debris flow. Flood and drought events are leading to tremendous losses of life, property, and affecting socio-economic development (Eckstein et al., 2018). According to World Food Agricultural Organization, severe winter drought reduced the yield and quality of major food crops (barley and wheat) by 15% between 2008 and 2009 (World Food Programme, 2009). The seasonal variability of extreme events is expected to increase with ongoing climate change (Field et al., 2012).

The winter precipitation occurs in December, January, and February, and has a small contribution (∼3%) to the total annual rainfall in Nepal (Sigdel and Ikeda, 2012). However, it is an essential source of water to glaciers, rivers, and ecosystems in the dry season. In contrast to summer precipitation (June-September), winter precipitation is relatively less explored due to its limited contribution to annual rainfall (Sigdel and Ikeda, 2012; Sigdel and Devkota, 2013). The country has frequently been experiencing several extreme events in the winter season (Wang et al., 2013). The winter season is influenced by an eastward-moving synoptic weather system called Western Disturbances (WD; Yadav et al., 2012; Dimri, 2013a). The WDs are originated over the Mediterranean Sea or Mid-Atlantic Ocean and travel eastward over Iran, Afghanistan, Pakistan, and northwest India (Dimri, 2007) and finally enter into Nepal through the western region bringing winter precipitation. Comparably, the western region of Nepal gets more winter precipitation than the central and eastern regions (Kansakar et al., 2004; Ichiyanagi et al., 2007). Moreover, Western Himalayas is the area of significant importance as it receives the above-normal rainfall amount because of the cyclogenesis (Dimri, 2006).

The global forcing that controls the climate of the Northern Hemisphere is El Niño/Southern Oscillation (ENSO), Arctic Oscillation (AO), and Northern Atlantic Oscillation (NAO). Cannon et al. (2014) has investigated the role of the AO and ENSO on the on multi-annual variations in winter westerly disturbance activity affecting the Himalaya. In the context of recent global warming, precipitation variability is linked with Sea Surface Temperature (SST; Dimri, 2013a). The interannual variability of the winter precipitation, mainly drought in Central and Southwest Asia is linked with the SST changes in the Indian and Pacific Oceans (POs; Barlow et al., 2002). ENSO is the most widely studied ocean-atmospheric phenomenon on the variability of the precipitation (Yadav et al., 2012). The strong relationship between ENSO and winter precipitation over the Indian region has been reported in recent decades (Yadav et al., 2013; Kar and Rana, 2014). Further, the role between ENSO and the winter precipitation in northwest India has enhanced, whereas, the role of NAO/AO is diminishing in recent years (Yadav et al., 2009). The intensified WDs are observed over northwest India and Western Himalayas during the warm phase of the ENSO (Yadav et al., 2013; Dimri, 2013a). Moreover, the positive (negative) response of the India ocean Dipole (IOD) has favored (unfavored) the precipitation variability in south peninsular India (Kripalani and Kumar, 2004). The previous study shows that IOD develops in boreal summer and reaches a peak in the boreal fall (Saji et al., 1999). The dipole is characterized by the positive SST anomalies over the equatorial western Indian Ocean and negative SST anomalies over the equatorial eastern Indian Ocean. However, the pronounced warming of the Indian Ocean in recent decades acted as a capacitor to delay and prolong the influence of the ENSO (Yang et al., 2007; Lu et al., 2019). Thus, it is necessary to study the whole Indian Ocean Basin Mode (IOBM) impacts on the interannual variability of the winter precipitation over south Asia.

Many studies have been conducted in Nepal for studying spatio-temporal variation of summer precipitation and its related extreme events (Kansakar et al., 2004; Karki et al., 2017; Talchabhadel et al., 2018). The relation of summer monsoon variability has been linked with ENSO (Shrestha et al., 2000; Sigdel and Ikeda, 2012). Recently, Pokharel et al. (2019) studied the east-west division of precipitation over Nepal during 1951–2007 and found that mean annual precipitation has decreased in western Nepal due to the interannual variability of the IO SST. However, studies related to winter precipitation variability of Nepal are limited. For instance, (Wang et al., 2013) examined the drought over the western region of Nepal and discussed the mechanism on how AO can influence this variability. Their finding shows the decadal variability of winter precipitation between the 2001–2010 and 1991–2000 periods. Sigdel and Devkota (2013) found a weak relation of NAO and the strong relation of the Dipole Moment Index (DMI) with winter precipitation variability in Nepal. However, the above-mentioned studies have not quantified the physical mechanism relating to IO and PO on the precipitation change over the region. By studying different seasonal SST, it is possible to acquire predictive information on the interannual variability of precipitation. In particular, lead/lag response of the IO and PO with winter precipitation over the region is yet to be investigated because IOD, IOBM, and ENSO has developing and decaying phase (Saji et al., 1999; Lu et al., 2019; Zhou et al., 2019). For instance, there is a weak response between ENSO and North Xinjiang summer precipitation, however, a robust relation occurs in post-spring and summer (Lu et al., 2019). Further, the mechanical and thermal processes over the Tibetan Plateau (TP) are affecting global atmospheric circulation and global precipitation (Duan et al., 2012; Maussion et al., 2014). In the present study, we aim to link the temperature changes in TP, IO, and PO; cyclonic/anticyclonic circulation; and divergent/convergent wind patterns affecting winter precipitation of Nepal with recently released high-resolution reanalysis data (ERA5). For this, we analyze the year-to-year variability of excess or deficit winter precipitation over Nepal between 1987 and 2015 and present the physical mechanism of inter-annual variability. Understanding the variability of the winter precipitation is of great importance in the economy of Nepal because December to February is the winter copping season (Rohwerder, 2016). Further, it will help us to understand the occurrences of the past extreme events as being the basis for forecasting and monitoring drought and floods over Nepal.

STUDY AREA

The study area, Nepal is a South Asian country located between 26.36°–30.45°N and 80.06°–88.2°E encompassing an area of 147,181 km^2 bordering with Tibet, China in the north and India in the east, west and south (**Figure 1**). According to the Department of Hydrology and Meteorology (DHM), the mean annual precipitation and temperature of Nepal are 1,857.6 mm and 20°C, respectively, from 1971 to 2012 (Department of Hydrology and Meteorology [DHM], 2017). The four climatological seasons that exists in Nepal are the pre-monsoon (MAM), summer monsoon (JJAS), post-monsoon (ON), and winter (DJF). The Asian monsoon system governs the climate of Nepal, bringing more than 80% of precipitation during summer (Nayava, 1980; Shrestha et al., 2000). In the winter season, the country receives about 3% of its annual rainfall from the westerlies (Karki et al., 2017; Sharma et al., 2020). The interaction of two extensive weather systems; monsoon and westerly disturbances are two main phenomena causing inter-annual precipitation variability over Nepal. For climate study, the study area is divided into three categories, i.e., western (Western boundary to 83°E) central (from 83° to 85°E) and eastern (from 85°E to eastern boundary) regions (Kansakar et al., 2004; **Figure 1**). All three regions features same physiographic regions (Terai, hills and mountain) but with difference in distribution and duration of precipitation (Sharma et al., 2020). In this study, the South Asian region (5°S–39°N, 60°W–95°E) was selected for the study of the atmospheric circulation pattern.

DATA AND METHODS

Data

Asian Precipitation-Highly-Resolved Observational Data Integration toward Evaluation of Water Resources (APHRODITE) is a gridded precipitation dataset covering more than 57 years was created by collecting and analyzing rain gage observation data across Asia. This data set is based on observed precipitation data around the globe (from 5,000–12,000 stations) in conjunction with other pre-compiled datasets (Yatagai et al., 2009; Yatagai et al., 2012). For generating the gridded data sets, it has used maximum possible gages available across Nepal (Yatagai et al., 2009). The APHRODITE project contributes to studies, such as the determination of Asian monsoon precipitation change, evaluation of water resources,

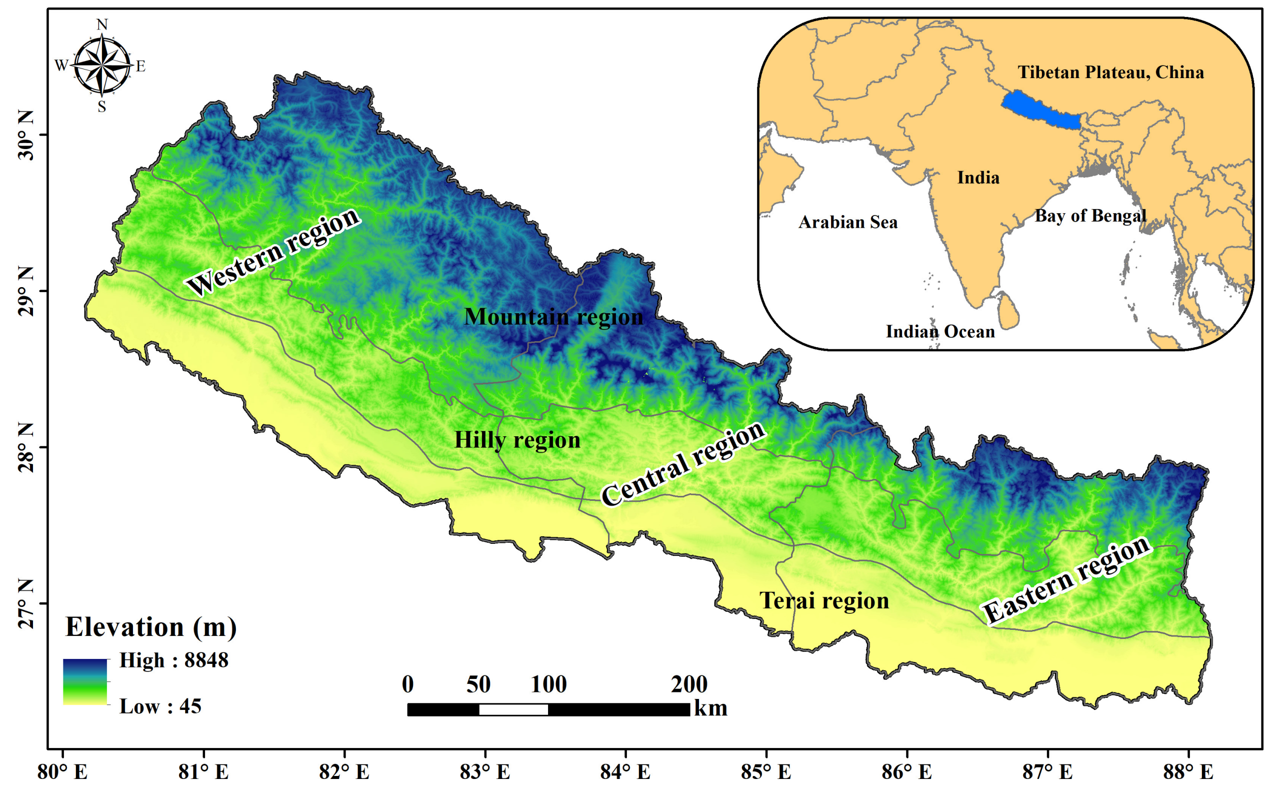

FIGURE 1 | The study area, Nepal with different regions. The inset shows the location of Nepal in relation to the ocean and landmasses.

verification of high–resolution model simulations and satellite precipitation estimates, and improvement of precipitation forecasts. Here, 0.25° × 0.25° resolution monthly average data APHRODITE (APHRODITE-1 and APHRODITE-2) over monsoon Asia between 1987 and 2015 was used. APHRODITE data has followed the quality control procedures for refining and avoid inconsistency in data (Sunilkumar et al., 2019). Meanwhile, the validation of the APHRODITE gridded data set (1987–2015) with the data from 80 meteorological station data across Nepal showed a strong correlation of 0.80 in the same period (**Figure 2**). The observed data for validation were collected from the meteorological stations managed by the Department of Hydrology and Meteorology, Government of Nepal (DHM).

The large scale atmospheric circulation parameters used are wind (*u* and *v* components), relative humidity, moisture flux, OLR, vertical velocity, 2 m Surface Air Temperature (SAT), and SST provided by ERA5 reanalysis dataset with the spatial resolution of 0.25° × 0.25°. ERA5 has recently released the fifth generation ECMWF reanalysis for the global climate and weather spanning between 1979 and 2019 (Copernicus Climate Change Service Climate [C3S], 2017). The SST indices: NINO3.4, DMI, and IOBM used in this study were calculated from the same ERA5 SST. NINO3.4 index is a widely used indicator of ENSO, which is the average SST anomaly in the region of 5°N to 5°S and 170°W to 120°W. Similarly, the IOD is the temperature difference between the western (50°E–70°E and 10°S–10°N) and the eastern (90°E–110°E and 10°S–10°N) equatorial Indian Ocean (Saji et al., 1999). DMI is an indicator of the intensity calculation of IOD. IOBM is defined as the averaged SST within 40°E–110E°; 20°S–20°N (Lu et al., 2019).

Methods

Empirical Orthogonal Function (EOF) analysis is a computation of the Eigenmodes for a covariance matrix based on precipitation giving the spatial pattern, time series, and percentage of variance (Sein et al., 2015). Here, EOF analysis was conducted to determine the dominant mode of winter rainfall over Nepal. The eigenvalues express the importance of the EOFs/Principal Components (PCs), whereas the first EOF (EOF1) is crucial, followed by the second EOF (EOF2), and so on (Wang X. et al., 2015). The theories and algorithms were adopted from Lorenz (1956), Zhang and Moore (2015) to analyze EOF. The wavelet analysis was carried out to visualize the potential signal in the standardized winter precipitation time series by following the methods described in the previous studies (Torrence and Compo, 1998; Mchugh, 2006; Dieppois et al., 2016). The composite analysis gives information about the common features and patterns of the variable in the atmosphere (Kar and Rana, 2014; Ngarukiyimana et al., 2018). Composite analysis of precipitation, OLR, wind, moisture flux, vertical velocity, velocity potential, relative humidity, and 2 m SAT was performed. The statistical significance test of composite analysis in this study is assessed using the student *t*-test at a 95% confidence interval. Several studies have revealed the application of this analysis over the South Asian countries (Shrestha, 2000; Krishnamurthy and Kirtman, 2009; Dimri, 2013a). In this study, the Pearson correlation analysis aims at displaying the relationship between the variables at a 95% confidence level. The time series of all the climatic parameters were detrended before passing through EOF, composite, and correlation analysis.

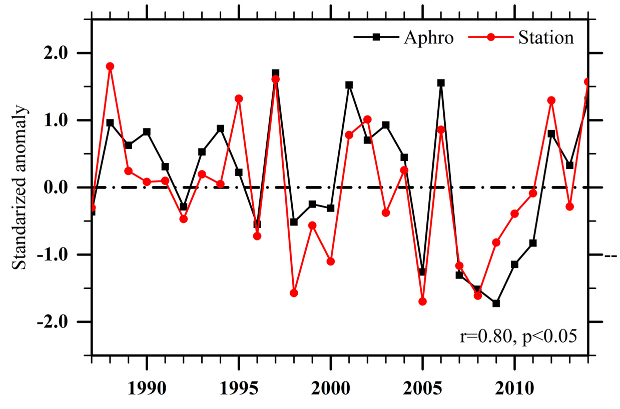

FIGURE 2 | Validation of APHRODITE (Aphro) data with 80 meteorological station data using correlation analysis between 1987 and 2015.

RESULTS AND DISCUSSION

Characteristic of Winter (DJF) Precipitation

The seasonal precipitation cycle over Nepal was analyzed using the APHRODITE data set during 1987–2015 (**Figure 3A**). The analysis revealed that the rainfall is highest in the summer monsoon (JJAS) season and the lowest in the winter season (DJF). The climatology of winter precipitation over Nepal is presented in **Figure 3B**. The average winter precipitation of Nepal is 20.13 mm/month during the study period. The winter precipitation is higher (above 30 mm/month) in the far-western region than eastern and central regions (about 10–20 mm/month) of Nepal. The westerlies bringing winter precipitation are pronounced in the western region and weakens from west to east (Kansakar et al., 2004; Ichiyanagi et al., 2007). The previous study also showed a spatial variation of winter precipitation is more substantial in the western region than in the central and eastern regions (Ichiyanagi et al., 2007).

The Dominant Mode of Winter Rainfall

The precipitation time series was de-trended, and EOF analysis was obtained for the winter precipitation. The dominant modes of variability of the mean winter precipitation over Nepal are presented in **Figure 4**. EOF1 and EOF2 cannot explain whether Nepal is receiving high or low precipitation based on EOF maps; however, it gives precipitation field variation with eigenvalues. The leading EOF1 mode captures 53.2% of the variance, and the EOF2 contributes 17% of the total variance. Further, EOF1 exhibits a single mode of variability, with strong loadings in the central and western regions (**Figure 4A**). Meanwhile, EOF2 shows an intricate pattern (negative-positive-negative,

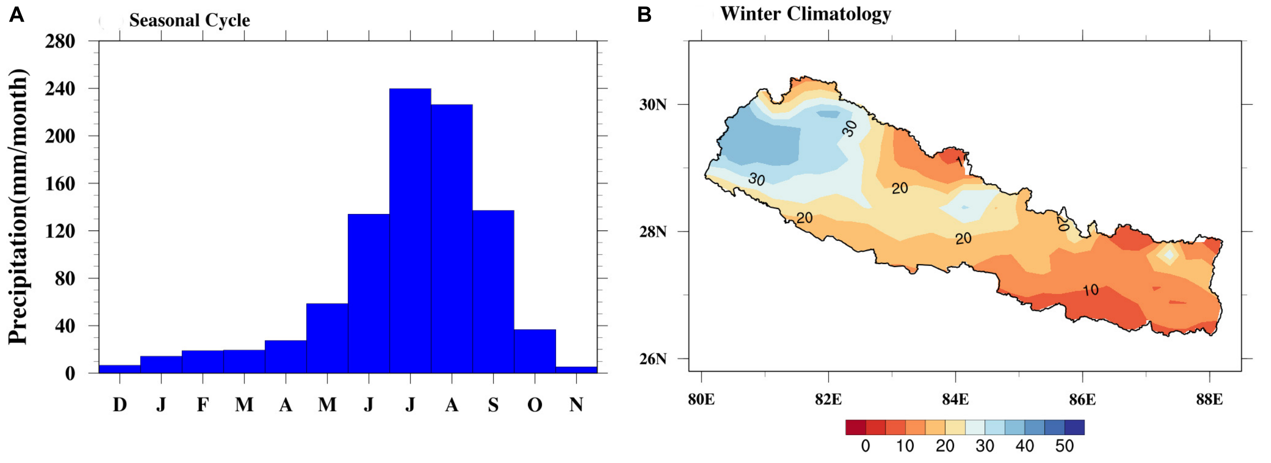

FIGURE 3 | (A) Seasonal cycle and **(B)** Climatology of winter precipitation (mm/month) over Nepal using APHRODITE data from 1987 to 2015.

from west to east **Figure 4B**). This pattern displays conflicting signals of variability in the far western and eastern regions. The distribution of precipitation in Nepal varies spatially due to local scale parameters, such as orography, wind exposure, and direction of the mountain range (Kansakar et al., 2004; Talchabhadel et al., 2018).

The respective principal components (PC1 and PC2) of EOF1 and EOF2 are shown in **Figures 5A,B**, respectively. The PC1 and PC2 give information about the interannual and decadal variation of precipitation over Nepal from 1987 to 2015. The higher value of PC1, i.e., standardized anomalies exceeding + 1, shows the above-average precipitation and vice-versa (**Figure 5A**). Thus, 1988, 1995, 1997, 2002, 2012, and 2014 are above-normal precipitating years, whereas 1996, 1998, 2000, 2005, 2007, and 2008 are below-normal precipitating years. PC2 time series show decadal variability of precipitation, since, a negative decadal anomaly of precipitation (1987–2001) has changed to a positive anomaly during the next decade (2001–2015) over Nepal (**Figure 5B**). This implies that in these decades, the spatial distribution of precipitation was inverse mainly in the far western and eastern regions (**Figure 4B**). Similar findings also reported by Wang et al. (2013), where the second mode of EOF revealed the decadal variability of winter precipitation in the western region during 1991–2010, which is linked with AO.

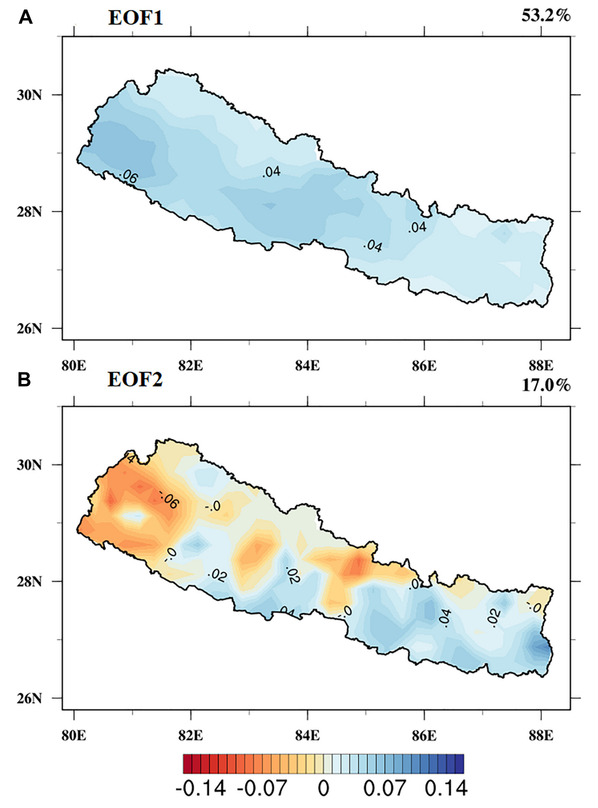

FIGURE 4 | (A) The first dominant mode of variability (EOF1) explains 53.2% of the total variance of the mean winter precipitation and **(B)** the second dominant mode of variability (EOF2) explains 17% of the total variance of the mean winter precipitation over Nepal, based on APHRODITE data during 1987–2015.

Inter-Variability of DJF Precipitation

The inter-annual variability of winter precipitation and PC1 over Nepal between 1987 and 2015 is presented in **Figure 6**. A strong correlation coefficient (0.97) was observed between EOF1 and detrended averaged winter precipitation over Nepal during the analysis period (**Table 1**). The EOF1 and PC1 mode contributes to the highest variance and capable of characterizing the winter precipitation variability in Nepal over the study period. The temporal analysis revealed that the country experienced a below-average rainfall amount in between 1995 and 2010. The anomalous strong or weak years were selected using standardized anomalies exceeding ± 1 (**Figure 6**). The result shows six of each positive (strong: 1988, 1995, 1997, 2002, 2012, and 2014) and negative (weak: 1996, 1998, 2000, 2005, 2007, and 2008) anomaly years.

Morlet wavelet power spectrum analysis was performed on winter standardized precipitation anomalies to investigate the presence of significant signals that might be embedded in the

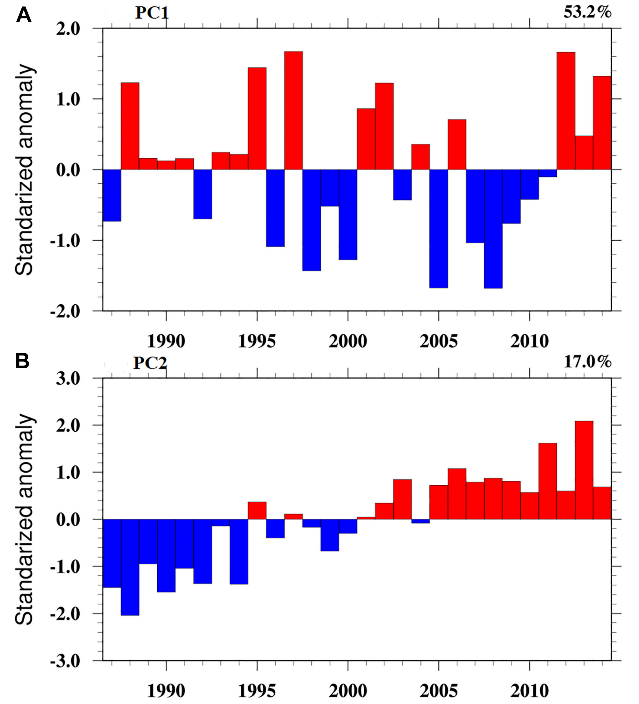

FIGURE 5 | **(A)** The first Principal Component associated with EOF1 (PC1) and **(B)** The second Principle Component associated with EOF2 (PC2) of winter precipitation over Nepal, based on APHRODITE data from 1987 to 2015.

TABLE 1 | Correlation between two modes of EOF and winter precipitation.

EOF	Correlation
EOF1	0.97 ($p < 0.05$)
EOF2	−0.13 ($p = 0.50$)

study period. The detrended precipitation time series was passed through wavelet analysis. It was observed 2–2.6 years of the power spectrum between 1995 and 2005, which is statistically significant at a 95% confidence interval (**Figure 7**). The power spectrum of 8 years has been observed in 2000, which is not significant. The results indicate the inter-annual variability pattern of winter precipitation over Nepal, which can be associated with ENSO. The 1–2 years of the periodicity of power spectrum was observed in the years 1982/1983 and 1991/1992 that is linked with ENSO in winter westerly disturbance in the western Himalayas (Cannon et al., 2014). The decadal variability of a signal has been observed in 2000, which can be linked with AO. The previous study shows a 2–7 years variability pattern is associated with the influence of ENSO, while the longer duration of 7–12 years to AO/NAO (Torrence and Compo, 1998; Mpeta and Jury, 2001; Dieppois et al., 2016).

Circulation Anomaly Associated With Dry and Wet Years

The composites of precipitation anomalies during dry and wet years are shown in **Figure 8**. The dry year composite (**Figure 8A**) has significant negative anomalies all over the country with strong negative loading in the western and central regions, which coincides with the dominant mode of EOF1, as in **Figure 4A**. The converse pattern was observed in the wet years (**Figure 8B**). To understand the reason for negative and positive anomalies of precipitation over Nepal, **Figures 9A,B** was produced to show a composite of OLR of dry and wet years. Precipitation has a close inverse relation with OLR in tropical and subtropical areas (Shen et al., 2017). In a dry (wet) year, positive (negative) anomalies are observed over Pakistan, northern India, Nepal, and TP. Similarly, positive and negative OLR appeared over the Bay of Bengal

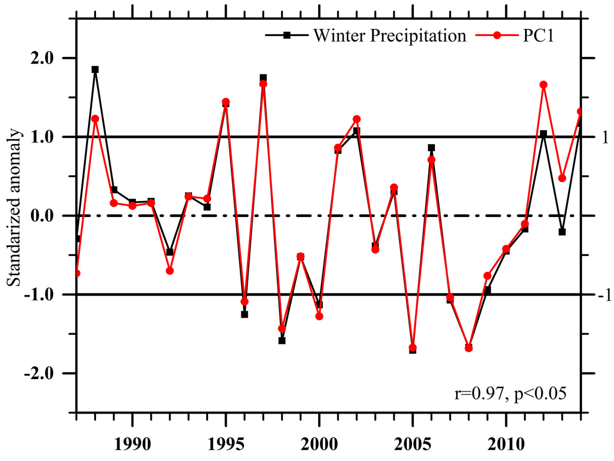

FIGURE 6 | Inter–annual variability of PC1 and winter precipitation anomaly over Nepal. The black dotted line represents the reference line and blackline separates the wet and dry years during 1987–2015.

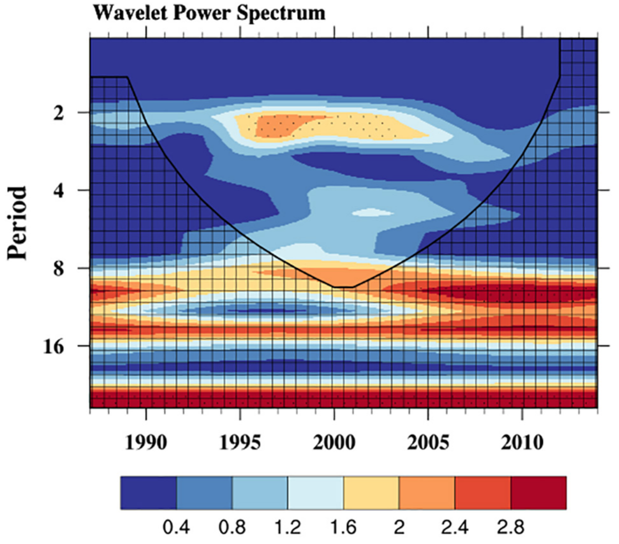

FIGURE 7 | The wavelet power spectrum for the winter season from 1987 to 2015 using the Morlet wavelet method. The shaded color denotes wavelet power. The hatched area delimits the "cone of influence," which influenced by edge effect. The dotted points represent the significant at a 95% confidence interval.

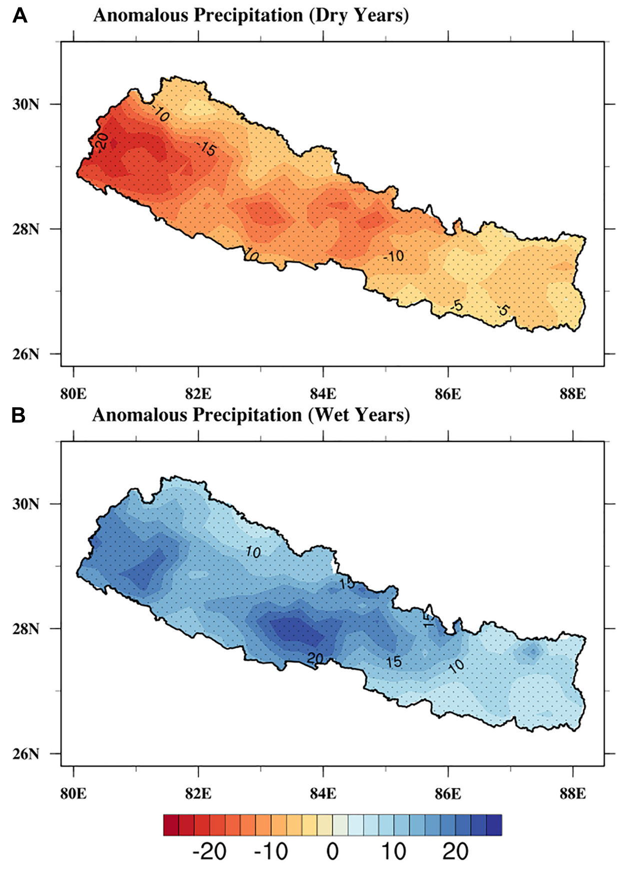

FIGURE 8 | Composite precipitation anomalies (mm/month) for **(A)** dry years and **(B)** wet years based on APHRODITE data between 1987 and 2015. The dotted points represent the significance at a 95% confidence level.

region in wet and dry years, respectively. The high (low) values of OLR indicate lower (higher) cloud tops and consequent less (more) precipitation in the dry (wet) years (Ngarukiyimana et al., 2018). Moreover, vertical velocity explains the sinking and rising characteristics of clouds (Wang L. et al., 2015). The composite of vertical velocity anomalies at 500 hpa for the dry and wet years is presented in **Figures 9C,D**. Negative anomalies have been observed in Afghanistan, Pakistan, and northern India in wet years whereas positive anomalies during dry years. This pattern is not clear over the TP region. There are significant positive anomalies of vertical velocity at 500 hpa across the east-west of the country (79–90°E) favoring a strong subsidence motion, pointing toward a deficit precipitation amount (**Figure 9C**). The converse pattern was observed in wet years, i.e., negative vertical velocity anomalies over the study region; suitable for convection which results in enhanced precipitation (**Figure 9D**). The negative values of vertical velocity enhance the convective activity over the Indo-Pakistan region and produce a significant area of precipitation (Ahmed et al., 2019).

The WDs enters Nepal following the route of Iran, Afghanistan, Pakistan, and northwest India. They are fast-moving air-currents that get intensified and captured by topography and orography of South Asia (Lang and Barros, 2004). The wind plays a significant role in carrying and supplying moisture to the migratory WDs (Yadav et al., 2013). **Figures 10A,B** displays the wind vector calculated from zonal and meridional components of Wind at 850 hPa during the dry and wet years, respectively. Analysis reveals that the stronger northwesterly wind anomalies are associated with a rainfall deficit in Pakistan, northern India, and Nepal (**Figure 10A**). **Figure 10B** shows opposite characteristics, indicating a strengthening of the southwesterly wind vectors during the wet years. By comparing, the wind flow patterns at 850 hpa, it is evident that cyclonic circulation persists at 15–30°N during wet years, whereas, the anticyclonic circulation is observed during dry years. The southwesterly winds anomalies are entered from the Arabian Sea (10–20°N). It is similar to the previous finding that, the westerly winds that originate from the Arabian Sea carry moisture to Nepal in the winter season (Sigdel and Ikeda, 2012). However, **Figures 10C,D** represents the vertically integrated moisture transport and wind vectors during wet and dry years calculated from surface pressure level (1000 hpa) to the top of the atmosphere (200 hpa) in this study during 1987–2015. The moisture transport during wet and dry cases show a clear difference in magnitude, the direction of the wind, and a way of moisture transport to the study area. In the dry years, the positive anomalous moisture (divergence) dominates over the study region (**Figure 10C**). In contrast, the negative anomalous moisture (convergence) is dominant over the western Himalayas and Nepal (**Figure 10D**). The central part of India (around 15–20°N) also shows intense convergent/divergent fluxes. An anomalous cyclonic (anticyclonic) circulation persists over the northern India and Pakistan during wet (dry) years (**Figures 10C,D**). The previous study reported that such circulations enhance (reduce) the supplements of moisture from nearby seas in the study region (Dimri, 2013b).

Air temperature is a useful parameter for determining extreme conditions. The strong positive anomalies of air temperature are observed over Nepal, India, Pakistan, and TP region during dry years (**Figure 11A**). In contrast, the strong negative anomalies are observed over TP, northern India, and Nepal during the wet years (**Figure 11B**). It is reported there is a significant negative and positive correlation of winter precipitation of Nepal with TP and IO, respectively (**Supplementary Figure S1**). Similarly, Dimri (2014) also presented the opposite relationship between air temperature and winter precipitation in the Himalayas. Himalayas and TP play an important role in the modification of the westerly system and moisture transport (Ahmed et al., 2019). The cooling over the TP region and warming over the IO corresponds to south-north transport of moisture, resulting in positive precipitation anomalies over the study region (**Figure 8B**) during winter. The results of this study are in good agreement with a previous study (Dimri, 2013a). Moreover, the heating and cooling of TP can affect the atmospheric circulation and large–scale teleconnections in the different seasons. For instance, TP loses its latent heat strength during the springtime; a reason for reduced precipitation along the southern and eastern slopes of the TP and increased area over northeastern India and Bay of Bengal (Duan et al., 2012). The decrease in summer precipitation trends is observed in Nepal because of the accelerated warming in the Hindu-Kush Himalayan and TP (Krishnan et al., 2019; Pokharel et al., 2019). Furthermore, the negative anomalies of relative

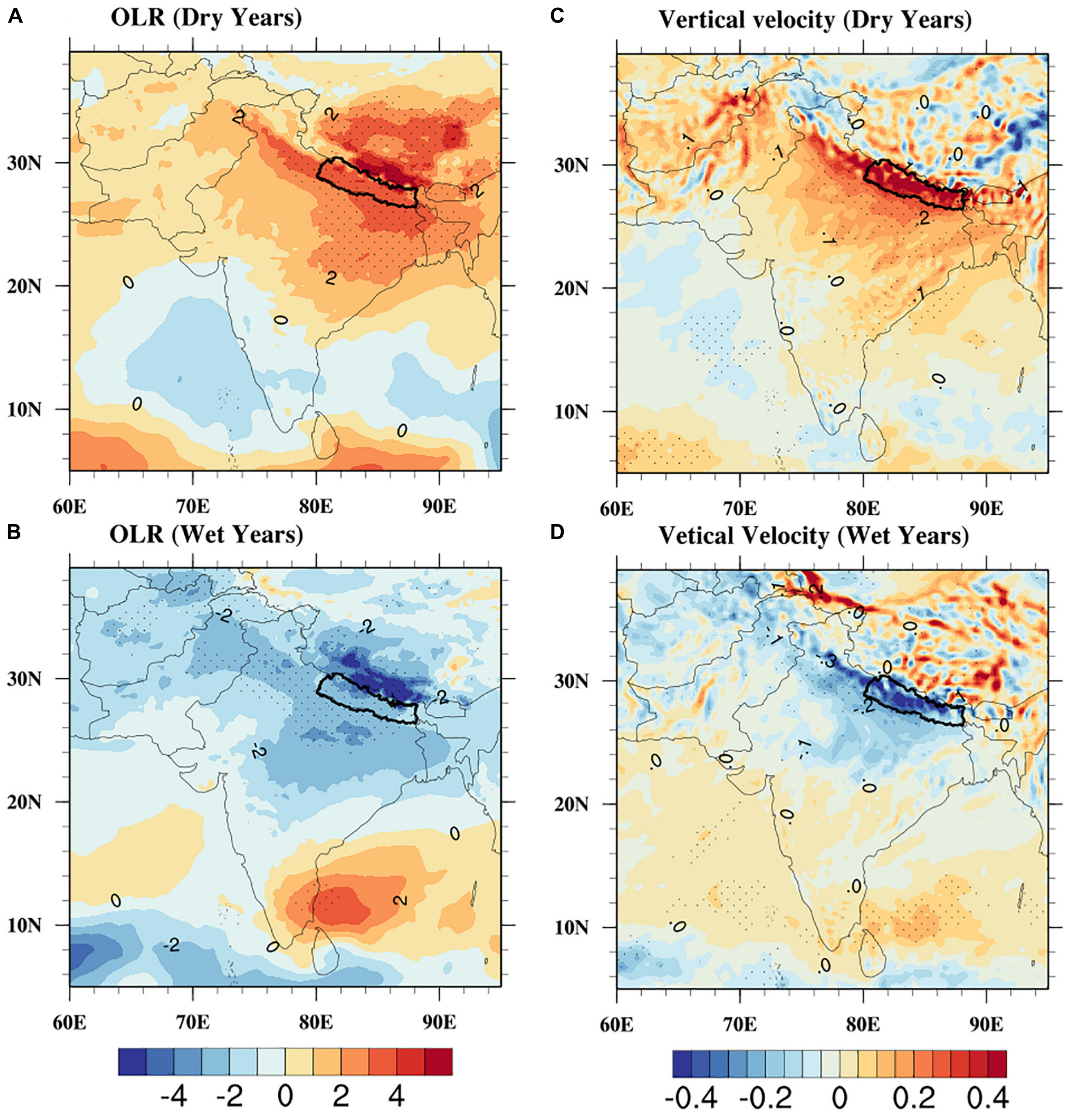

FIGURE 9 | Composite OLR anomalies (10^{-5}, W/m^2) for **(A)** dry years, **(B)** wet years, and Vertical velocity (10, Pas^{-1}) for **(C)** dry years, and **(D)** wet years based on ERA5 reanalysis data during 1987–2015. The dotted points represent the significance at a 95% confidence level.

humidity dominate at 850 hPa widely in the study area during the dry years (**Figure 11C**). In wet years, positive humidity anomalies are created over Nepal (**Figure 11D**). The humidity patterns inversely correspond with air temperature patterns in the study region. The higher temperatures are often associated with water-deficient conditions, whereas lower temperatures are associated with wet conditions (He et al., 2015). The temperature variability over the TP has a strong relation with winter precipitation over Nepal.

Relation With Ocean

Previous studies focus on a large part of the climate and weather predictability linked to the ocean, while a small portion is linked with inter-atmospheric variability (Saha et al., 2011; Syed and Kucharski, 2016). The lagged correlation between detrended winter precipitation and SST for 29 years (1987–2015) is presented in **Figure 12**, to observe the dependency of winter precipitation on large scale global force. From previous spring (**Figure 12B**), relations with eastern equatorial warming start to build up and the area of significant correlation increases in summer and fall (**Figures 12C,D**). By season approaches (winter), warming covers a large portion of the eastern equatorial Pacific (**Figure 12E**). The small patches of negative SST anomalies are found over the western equatorial Pacific. It gives the characteristics of ENSO. Furthermore, from the previous summer onwards, a positive correlation (warming) with the IO starts to build up (**Figure 12C**). However, the more substantial portion of significant correlation is evident only when it reached the fall (**Figure 12D**). The negative anomalies of the western Pacific extend into the eastern Tropical Indian Ocean (TIO) and

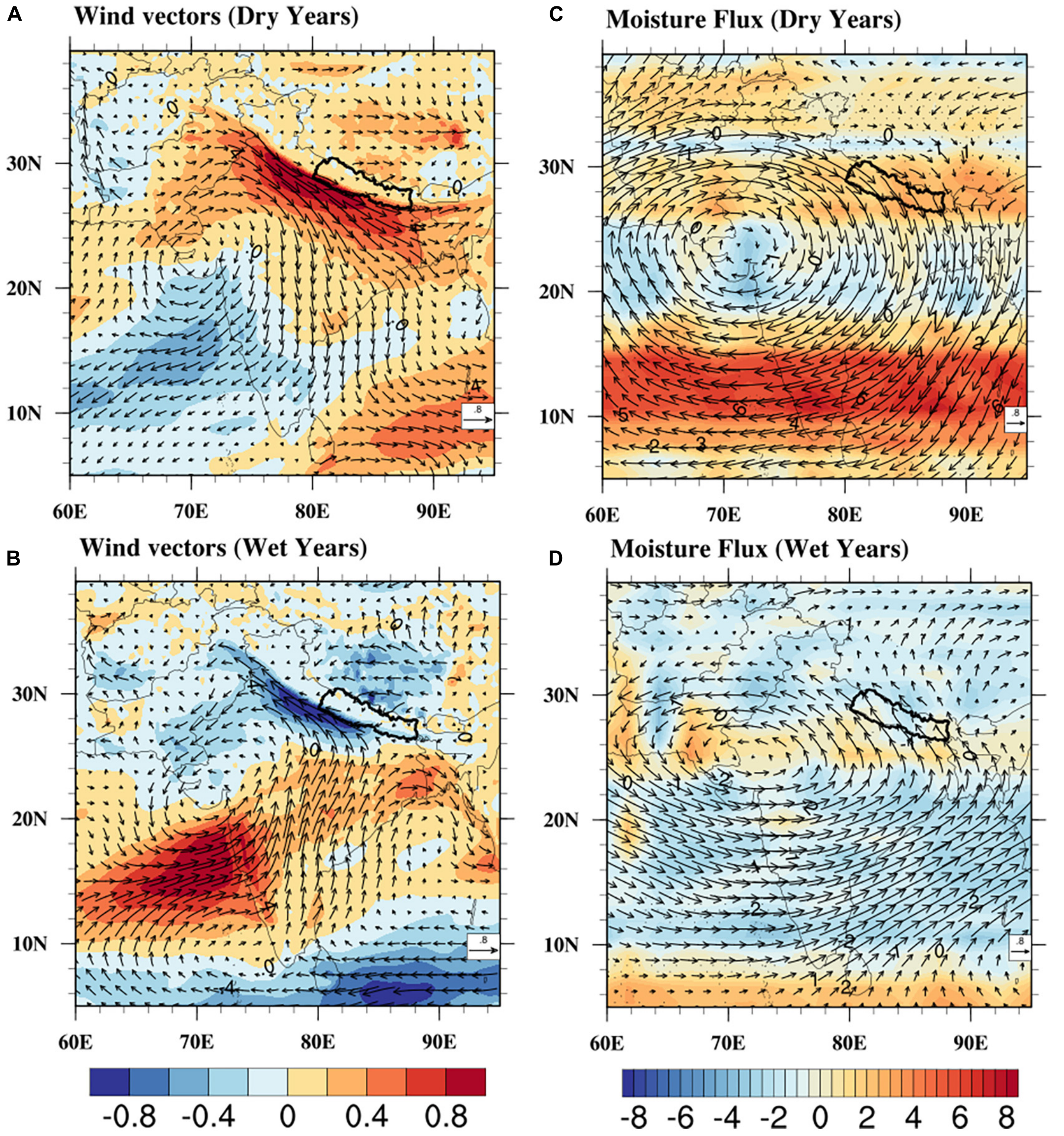

FIGURE 10 | Wind anomaly vectors (ms^{-1}) at 850 hPa (shading indicates the zonal component of wind anomalies) for **(A)** dry years, **(B)** wet years. Vertically Integrated Water Vapour Flux (10^{-5}, kg m^{-2} s^{-1}, the shading indicates negative anomalies convergence and positive anomalies divergence) for **(C)** dry years, and **(D)** wet years based on ERA5 reanalysis data from 1987 to 2015. The dotted points represent the significance at a 95% confidence level.

northern Australia. The strong warm SST in the western TIO and a small portion of cold SST in the eastern TIO give the characteristics of the IOD pattern (**Figure 12D**). By the time, when the warming in the eastern equatorial Pacific reaches its peak phase, eastern TIO is replaced by western TIO with warm SST. Moreover, warming becomes vivid and strong over the whole basin in the study season. The finding is quite interesting as IOBM may have an impact on the winter precipitation of Nepal (**Figure 12E**). The oceanic wave dynamics involves in the evolution of IOBM from IOD as Rossy waves propagating westward reflects Kelvin waves in the eastern TIO, it would help to damp negative SST to positive SST (Yu et al., 2005; Wu et al., 2012).

NINO3.4, IOBM, and DMI are the indicators of SST over the PO and the IO. The influence of the ENSO signals on precipitation can persist from year to year (Li and Zhao, 2019). So, the lagged relationship between winter precipitation, NINO3.4, IOBM, and DMI between 1987 and 2015 was calculated (**Table 2**). The robust relation of winter precipitation is observed with the summer, fall, and winter's NINO3.4. However, the concurrent response of NINO3.4 to winter precipitation for the study period is 0.40 ($p < 0.05$). The results also demonstrate that the increased precipitation over Nepal is associated with above-normal SST in the equatorial eastern PO (**Figure 12E**). It suggests that during the warm phase of ENSO, more rainfall is expected due to enhanced southwesterly winds (Tippett et al.,

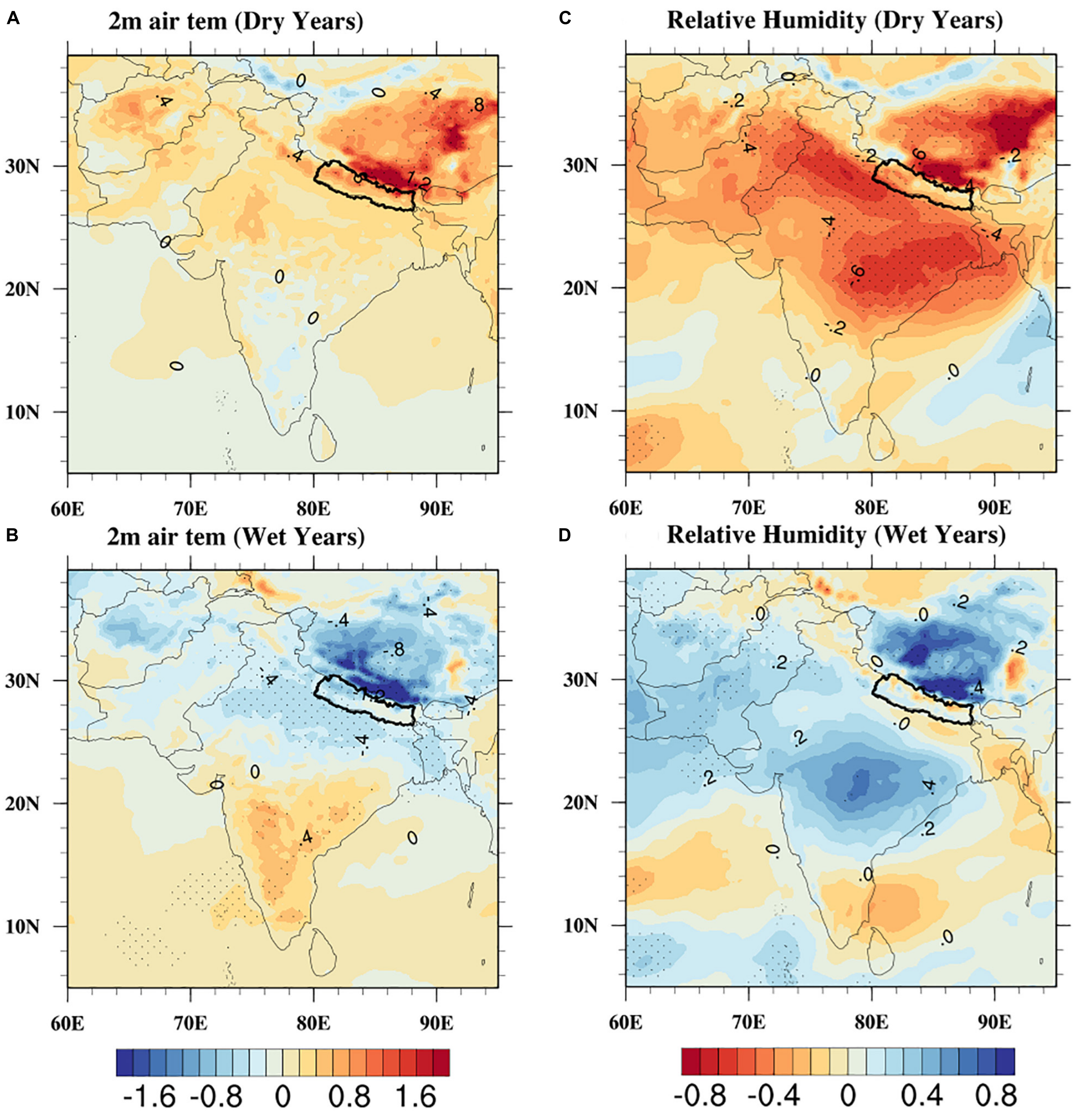

FIGURE 11 | Composite 2 m surface air temperature (°C) for **(A)** dry years, **(B)** wet years, and relative humidity (10^{-1}, %) during **(C)** dry years, and **(D)** wet years based on ERA5 reanalysis data from 1987 to 2015. The dotted points represent the significance at a 95% confidence level.

2003). The wind circulation pattern (**Figures 10A,B**) is affected during La Nina (El Nino) events; that involves northwesterly (southwesterly) moisture transport (**Figures 10C,D**) which brings below (above) normal precipitation (**Figures 8A,B**) over the study region (Mariotti, 2007; Dimri, 2013b). Also, ENSO affects the vertical baroclinic response over the Himalayan region and TP (as suspected in **Figures 9C,D**), which induces the WDs (Yadav et al., 2010; Yadav et al., 2013; Dimri, 2013a).

The concurrent response of DMI to winter precipitation for the period of 1987 to 2015 is positive; however, it has an insignificant correlation of 0.18. The fall DMI (r = 0.41, $p < 0.05$) is a clear indicator for the forecast of the following year's winter precipitation over Nepal. An earlier study mentioned that the positive (negative) mode of IOD is favorable (unfavorable) for precipitation over South peninsular India and Pakistan (Kripalani and Kumar, 2004; Hussain et al., 2016).

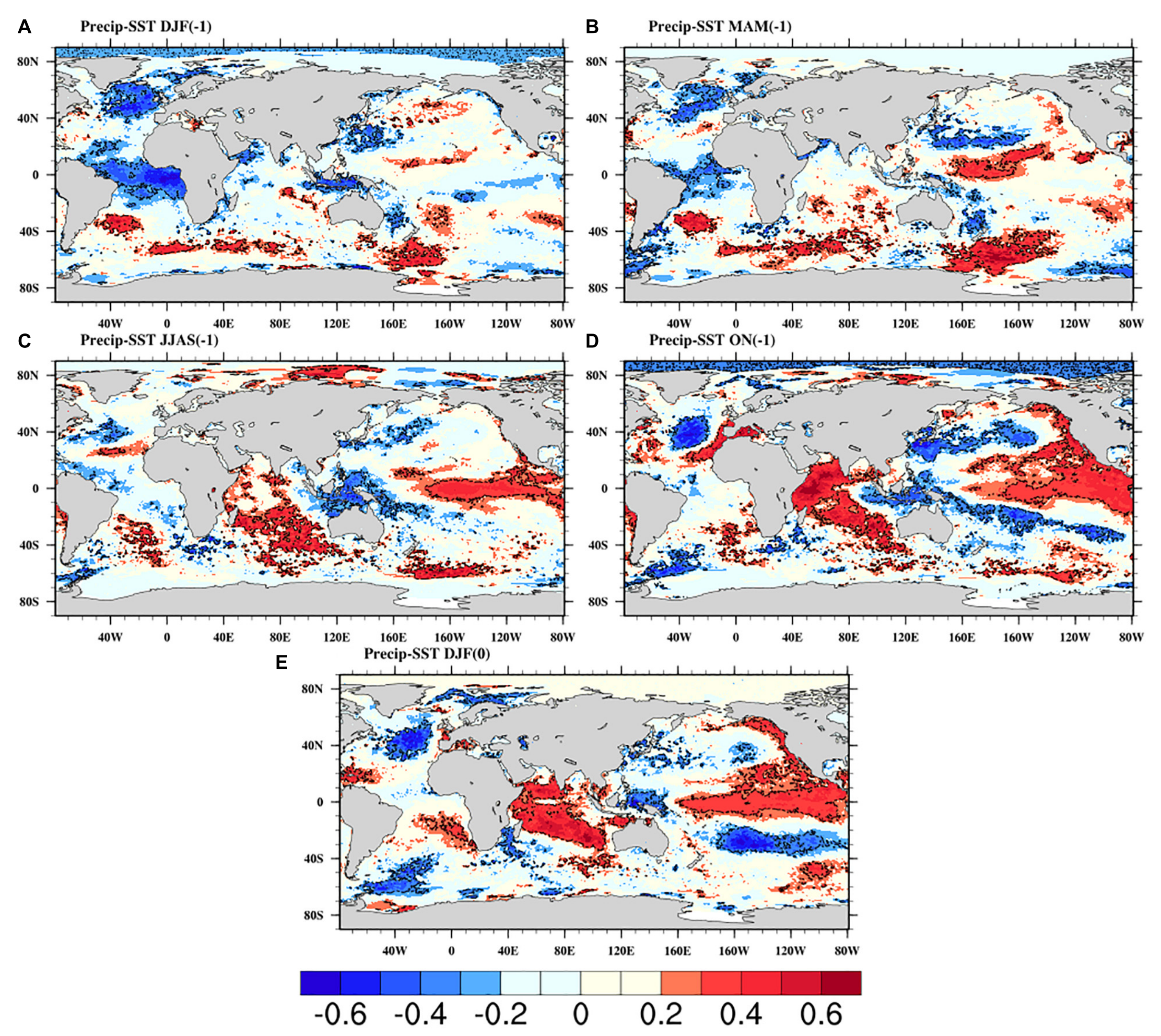

FIGURE 12 | Correlation between averaged winter precipitation and SST during 1987–2015 **(A)** DJF(−1), **(B)** MAM(−1), **(C)** JJAS(−1), **(D)** ON(−1), **(E)** DJF(0), respectively. −1 and 0 represents lag and corresponding season, respectively. The black dotted contours represent the significance at a 95% confidence level.

The significant correlation between fall and winter IOBM with winter precipitation during the study period was 0.44 and 0.50, respectively. The result suggests that warming of the IO can prolong or delay the influence of ENSO on winter precipitation (Yang et al., 2007). These results are in good agreement with a study conducted over the region of North China, Xinjiang (Lu et al., 2019). Furthermore, the increased rainfall over the study area is associated with above-normal SST in the equatorial central PO and IO, which heightened the response of the Walker and Hadley Circulation (Wang et al., 2013; Dimri, 2013a). The warm SST over the IO intensifies the convention that helps in shifting the Subtropical Westerly Jet (SWJ) to northern India (Yadav et al., 2013). The SWJ intensifies the WDs resulting in the excess precipitation over Nepal and northern India (Kar and Rana, 2014). The presence of the cyclonic circulation over 15–30°N (**Figure 10B**) helps in bringing moisture from the Arabian Sea and supplying to the migratory WDs. Furthermore, the cooling over TP and heating over IO (**Figures 11B**, **12E**, and **Supplementary Figure S1**) correspond to the south-north transport of moistures to the study region. These phenomena for wet years which are reversible for the dry years.

The key finding is that warming and cooling in the PO and the IO is related to the interannual variability of winter precipitation in Nepal. The drought events are increasing in Nepal, mainly after 2000 (Wang et al., 2013; Adhikari, 2018). Therefore, the Walker circulation over the PO and IO for dry years (La Nina years) is present in **Figure 13**. The pattern observed in the given figure indicates that the equatorial Indo-pacific walker circulation is affected by ENSO. The dry years are related to negative SST over the eastern PO and the IO, whereas, positive SST over the western Pacific and maritime continent. The two cell Walker circulations were observed over the tropical IO and the tropical PO, with one ascending arm over the maritime continent and two descending arms over the IO and the eastern PO, respectively. Further, it shows the upper-level divergence of wind anomalies over the maritime continent and convergent

TABLE 2 | Lag correlation between winter precipitation, NINO3.4, DMI, and IOBM.

Index	DJF(−1)	MAM(−1)	JJAS(−1)	ON(−1)	DJF(0)
NINO3.4	−0.16 ($p = 0.40$)	0.13 ($p = 0.48$)	0.32 ($p < 0.05$)	0.34 ($p < 0.05$)	0.40 ($p < 0.05$)
DMI	−0.14 ($p = 0.45$)	0.23 ($p = 0.22$)	0.14 ($p = 0.47$)	0.41 ($p < 0.05$)	0.18 ($p = 0.33$)
IOBM	−0.25 ($p = 0.18$)	−0.17 ($p = 0.37$)	−0.12 ($p = 0.38$)	0.44 ($p < 0.05$)	0.50 ($p < 0.05$)

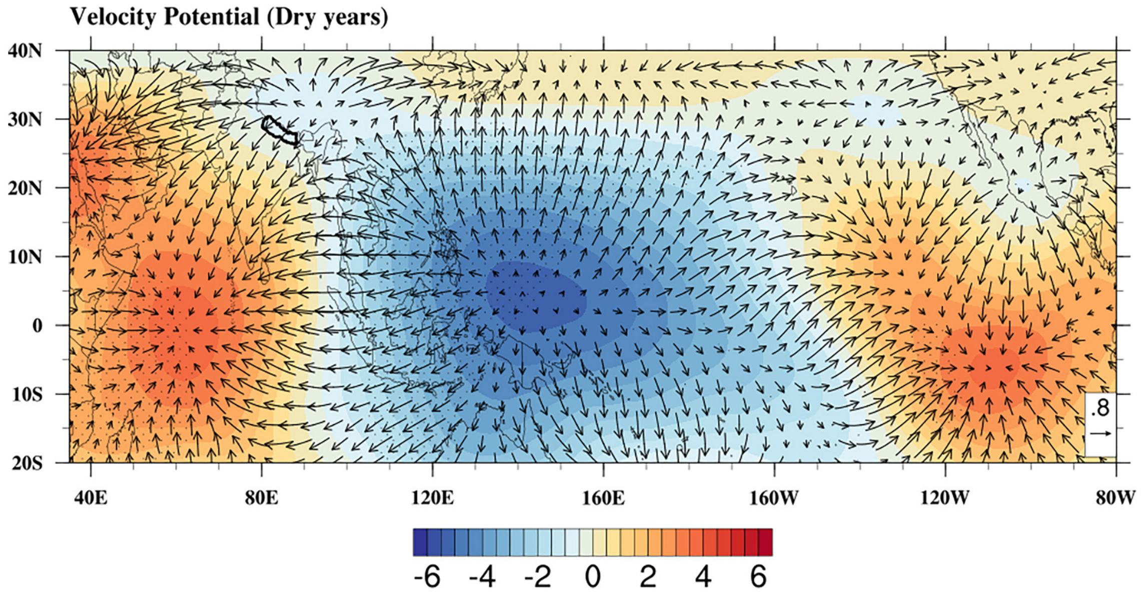

FIGURE 13 | 200 hPa divergent/convergent winds (vectors; m^2 s^{-1}) and velocity potential (contours; 10^{-6}, m^2 s^{-1}) for dry years based on ERA5 reanalysis data from 1987 to 2015. The dotted points represent the significance at a 95% confidence level.

over the IO and the eastern PO. The warming occurs in the TP region during dry years (**Figure 11A**), shows the upper-level divergence of wind anomalies (around 30°N 90°E, **Figure 13**). The pattern counteracts a suppressed response of Walker circulation over the Indian and Pacific regions. This phenomenon triggers the enhanced convective activity over the maritime continent. Further, suppressed convention and descending air masses over IO and anomalous anticyclonic circulation over the north of India (**Figure 10C**) reduces the moisture transport to the Himalayan region and Nepal. Moreover, it reduces the moisture supply to the migratory mid-latitude disturbance passing through it (Yadav et al., 2010; Yadav et al., 2013). The sinking (descending) atmospheric motion over the IO and rising (ascending) motion over the TP weaken the Hadley circulation (**Figure 13**) resulting in the dry years. These phenomena are reversible during El Nino years (wet years) as intensified Walker and Hadley circulation shows the enhanced upper-tropospheric meridional transport from the Southern Hemisphere to the Northern Hemisphere (Dimri, 2013a).

CONCLUSION

This study investigated the inter-annual variability of winter precipitation (DJF) over Nepal during the historical period from 1987 to 2015, coupled with the ocean-atmosphere patterns. A high-resolution APHRODITE and ERA5 reanalysis datasets are used to study the EOF, Wavelet, Composites, and Correlation analysis, respectively. Nepal receives very less amount (about 3%) of precipitation in the winter season. EOF analysis displayed two dominant modes, whereas the leading mode captures 53.2% of the total variance exhibiting a single mode of variability. Wavelet analysis determined 2 to 2.6 years of the significant power spectrum on winter precipitation. The standardized anomalies of winter precipitation showed deficit precipitation in 1996, 1998, 2000, 2005, 2007, and 2008, whereas, excess precipitation in 1988, 1995, 1997, 2002, 2012, and 2014. The results displayed positive (negative) anomalies of OLR and vertical velocity over Nepal during dry (wet) years. Moisture divergence (positive anomalies) with strong northwesterly wind anomalies is dominated during the dry years, whereas convergence (negative anomalies) with strong southwesterly in the wet years. The increase in SAT over the TP creates an upper-level divergence of wind anomalies that impact on the reduction of winter precipitation. Furthermore, the negative SST over the tropical IO suppressed the convective activity, which reduced the moisture transport to the Himalayan region, resulting in dry years. The correlation suggests the instance of IOBM and NINO3.4 impacts on the inter-annual variability of the winter precipitation. Moreover, the warming and cooling over the Indo-Pacific regions affect the Walker and Hadley circulation bringing above and below normal precipitation, respectively, over Nepal. The response of indices

(NINO3.4, IOBM, and IOD) on winter precipitation, needs further investigation. The comprehensive evaluation of winter precipitation helps to understand the occurrences of the past extreme events as being the basis for forecasting and monitoring drought and floods over Nepal.

DATA AVAILABILITY STATEMENT

The datasets generated for this study are available on request to the corresponding author.

AUTHOR CONTRIBUTIONS

Concept and data KH, SS. KH wrote the manuscript. NK, BB, and XZ corrected and improved the manuscript. KH and SS compiled all the experiments and analyses with the help of NK.

ACKNOWLEDGMENTS

The authors express their sincere thanks to the scientists of the APHRODITE and ECMFW for providing ERA5 datasets. The Department of Hydrology and Meteorology, Government of Nepal is also acknowledged for providing the observed precipitation datasets. Additionally, we would like to thank three reviewers for their constructive and insightful reviews and comments which has significantly helped to improve the manuscript.

SUPPLEMENTARY MATERIAL

The Supplementary Material for this article can be found online at: https://www.frontiersin.org/articles/10.3389/feart.2020.00161/full#supplementary-material

FIGURE S1 | Correlation between averaged winter precipitation and 2 m surface air temperature during 1987–2015, based on ERA5 data. The dotted points represent the significance at a 95% confidence level.

REFERENCES

Adhikari, S. (2018). Drought impact and adaptation strategies in the mid-hill farming system of western nepal. *Environments* 5:101.

Ahmed, F., Adnan, S., and Latif, M. (2019). Impact of jet stream and associated mechanisms on winter precipitation in Pakistan. *Meteorol. Atmos. Phys.* 132, 225–238. doi: 10.1007/s00703-019-00683-8

Barlow, M., Cullen, H., and Lyon, B. (2002). Drought in central and southwest Asia: La Niña, the warm pool, and Indian Ocean precipitation. *J. Clim.* 15, 697–700.

Cannon, F., Carvalho, L. M. V., Jones, C., and Bookhagen, B. (2014). Multi-annual variations in winter westerly disturbance activity affecting the Himalaya. *Clim. Dynam.* 44, 441–455. doi: 10.1007/s00382-014-2248-8

Copernicus Climate Change Service Climate [C3S] (2017). *ERA5: Fifth Generation of ECMWF Atmospheric Reanalyses of the Global Climate. Copernicus Climate Change Service Climate Data Store (CDS).* Available Online at: https://cds.climate.copernicus.eu/cdsapp#!/home (accessed 12 Jan 2020).

CRED (2018). *Decoding the Monsoon Floods.*(New Delhi: SEEDS and CRECD), Available Online at: https://reliefweb.int/sites/reliefweb.int/files/resources/Decoding-the-monsoon-floods-report.pdf (accessed November 2019).

Department of Hydrology and Meteorology [DHM] (2017). *Observed Climate Trend Analysis in the Districts and Physiographic Regions of Nepal (1971-2014).* (Kathmandu: Department of Hydrology and Meteorology). Available Online at: https://www.dhm.gov.np/uploads/climatic/467608975Observed%20Climate%20Trend%20Analysis%20Report_2017_Final.pdf (accessed November 2019).

Dieppois, B., Pohl, B., Rouault, M., New, M., Lawler, D., and Keenlyside, N. (2016). Interannual to interdecadal variability of winter and summer southern African rainfall, and their teleconnections. *J. Geophys. Res. Atmos.* 121, 6215–6239.

Dimri, A. (2006). Surface and upper air fields during extreme winter precipitation over the western Himalayas. *Pure Appl. Geophy.* 163, 1679–1698.

Dimri, A. (2007). The transport of momentum, sensible heat, potential energy and moisture over the western Himalayas during the winter season. *Theor. Appl. Climatol.* 90, 49–63.

Dimri, A. (2013a). Interannual variability of Indian winter monsoon over the Western Himalayas. *Global Planet. Change* 106, 39–50.

Dimri, A. (2013b). Relationship between ENSO phases with Northwest India winter precipitation. *Int. J. Climatol.* 33, 1917–1923.

Dimri, A. (2014). Sub-seasonal interannual variability associated with the excess and deficit Indian winter monsoon over the Western Himalayas. *Clim. Dynam.* 42, 1793–1805.

Duan, A., Wu, G., Liu, Y., Ma, Y., and Zhao, P. (2012). Weather and climate effects of the Tibetan Plateau. *Adv. Atmos. Sci.* 29, 978–992.

Eckstein, D., Hutfils, M.-L., and Winges, M. (2018). *Global Climate Risk Index 2019: Who Suffers Most From Extreme Weather Events? Weather-related Loss Events in 2017 and 1998 to 2017.* Berlin: Germanwatch Nord-Süd Initiative eV.

Field, C. B., Barros, V., Stocker, T., Qin, D., Dokken, D., Ebi, K., et al. (2012). *Managing the Risks of Extreme Events and Disasters to Advance Climate Change Adaptation: A Special Report of the Intergovernmental Panel on Climate Change.* Cambridge: Cambridge University Press.

He, B., Wang, H., Wang, Q., and Di, Z. (2015). A quantitative assessment of the relationship between precipitation deficits and air temperature variations. *J. Geophys. Res. Atmos.* 120, 5951–5961.

Hussain, M. S., Kim, S., and Lee, S. (2016). On the relationship between Indian Ocean Dipole events and the precipitation of Pakistan. *Theor. Appl. Climatol.* 130, 673–685. doi: 10.1007/s00704-016-1902-y

Ichiyanagi, K., Yamanaka, M. D., Muraji, Y., and Vaidya, B. K. (2007). Precipitation in Nepal between 1987 and 1996. *Int. J. Climatol. A J. R. Meteorol. Soc.* 27, 1753–1762.

Kansakar, S. R., Hannah, D. M., Gerrard, J., and Rees, G. (2004). Spatial pattern in the precipitation regime of Nepal. *Int. J. Climatol. A J. R. Meteorol. Soc.* 24, 1645–1659.

Kar, S. C., and Rana, S. (2014). Interannual variability of winter precipitation over northwest India and adjoining region: impact of global forcings. *Theor. Appl. Climatol.* 116, 609–623.

Karki, R., Schickhoff, U., Scholten, T., and Böhner, J. (2017). Rising precipitation extremes across Nepal. *Climate* 5:4.

Kripalani, R., and Kumar, P. (2004). Northeast monsoon rainfall variability over south peninsular India vis-à-vis the Indian Ocean dipole mode. *Int. J. Climatol. A J. R. Meteorol. Soc.* 24, 1267–1282.

Krishnamurthy, P., Hobbs, C., Matthiasen, A., Hollema, S., Choularton, R., Pahari, K., et al. (2013). *Climate Risk and Food Security in Nepal—analysis of Climate Impacts on Food Security and Livelihoods.* Denmark: CGIAR Research Program on Climate Change, Agriculture and Food Security (CCAFS).

Krishnamurthy, V., and Kirtman, B. P. (2009). Relation between Indian monsoon variability and SST. *J. Clim.* 22, 4437–4458.

Krishnan, R., Shrestha, A. B., Ren, G., Rajbhandari, R., Saeed, S., Sanjay, J., et al. (2019). "Unravelling climate change in the Hindu Kush Himalaya: rapid warming in the mountains and increasing extremes," in *The Hindu Kush Himalaya Assessment*, eds P. Wester, A. Mishra, A. Mukherji, and A. Bhakta Shrestha (Berlin: Springer), 57–97.

Lang, T. J., and Barros, A. P. (2004). Winter storms in the central Himalayas. *J. Meteorol. Soc. Jpn. Ser. II* 82, 829–844.

Li, C., and Zhao, T. (2019). Seasonal responses of precipitation in china to el niño and positive indian ocean dipole modes. *Atmosphere* 10:372.

Lorenz, E. N. (1956). *Empirical Orthogonal Functions and Statistical Weather Prediction*. Cambridge, MA: Massachusetts Institute of Technology.

Lu, B., Li, H., Wu, J., Zhang, T., Liu, J., Liu, B., et al. (2019). Impact of El Niño and Southern Oscillation on the summer precipitation over Northwest China. *Atmos. Sci. Lett.* 20:e928.

Mariotti, A. (2007). How ENSO impacts precipitation in southwest central Asia. *Geophys. Res. Lett.* 34. doi: 10.1029/2007GL030078

Maussion, F., Scherer, D., Mölg, T., Collier, E., Curio, J., and Finkelnburg, R. (2014). Precipitation seasonality and variability over the Tibetan Plateau as resolved by the High Asia Reanalysis. *J. Clim.* 27, 1910–1927.

Mchugh, M. J. (2006). Impact of South Pacific circulation variability on east African rainfall. *Int. J. Climatol. A J. R. Meteorol. Soc.* 26, 505–521.

Mpeta, E. J., and Jury, M. R. (2001). Intra-seasonal convective structure and evolution over tropical East Africa. *Clim. Res.* 17, 83–92.

Nayava, J. L. (1980). Rainfall in Nepal. *Himalayan Rev.* 12, 1–18.

Ngarukiyimana, J. P., Fu, Y., Yang, Y., Ogwang, B. A., Ongoma, V., and Ntwali, D. (2018). Dominant atmospheric circulation patterns associated with abnormal rainfall events over Rwanda, East Africa. *Int. J. Climatol.* 38, 187–202.

Pokharel, B., Wang, S. Y. S., Meyer, J., Marahatta, S., Nepal, B., Chikamoto, Y., et al. (2019). The east–west division of changing precipitation in Nepal. *Int. J. Climatol.* 12. doi: 10.1002/joc.6401

Rohwerder, B. (2016). *Seasonal Vulnerability and Risk Calendar in Nepal (GSDRC Helpdesk Research Report 1358)*. (Birmingham, UK: GSDRC, University of Birmingham).

Saha, S. K., Halder, S., Kumar, K. K., and Goswami, B. (2011). Pre-onset land surface processes and 'internal'interannual variabilities of the Indian summer monsoon. *Clim. Dyn.* 36, 2077–2089.

Saji, N., Goswami, B., Vinayachandran, P., and Yamagata, T. (1999). A dipole mode in the tropical Indian Ocean. *Nature* 401:360. doi: 10.1038/43854

Sein, Z. M. M., Ogwang, B. A., Ongoma, V., Ogou, F. K., and Batebana, K. (2015). Inter-annual variability of summer monsoon rainfall over Myanmar in relation to IOD and ENSO. *J. Environ. Agric. Sci.* 4, 28–36.

Sharma, S., Khadka, N., Hamal, K., Baniya, B., Luintel, N., and Joshi, B. B. (2020). Spatial and temporal analysis of precipitation and its extremities in seven provinces of nepal (2001-2016). *Appl. Ecol. Environ. Sci.* 8, 64–73.

Shen, Z., Shi, J., and Lei, Y. (2017). Comparison of the long-range climate memory in outgoing longwave radiation over the Tibetan Plateau and the Indian Monsoon Region. *Adv. Meteorol.* 2017:7.

Shrestha, A. B., Wake, C. P., Dibb, J. E., and Mayewski, P. A. (2000). Precipitation fluctuations in the Nepal Himalaya and its vicinity and relationship with some large scale climatological parameters. *Int. J. Climatol.* 20, 317–327.

Shrestha, M. (2000). Interannual variation of summer monsoon rainfall over Nepal and its relation to Southern Oscillation Index. *Meteorol. Atmos. Phys.* 75, 21–28.

Sigdel, M., and Devkota, L. (2013). Connection of winter time precipitation system in and around nepal with pacific and indian ocean indices. *Pakistan J. Meteorol.* 10.

Sigdel, M., and Ikeda, M. (2012). Seasonal contrast in precipitation mechanisms over Nepal deduced from relationship with the large-scale climate patterns. *Nepal J. Sci. Technol.* 13, 115–123.

Sunilkumar, K., Yatagai, A., and Masuda, M. (2019). Preliminary evaluation of GPM-IMERG rainfall estimates over three distinct climate zones with APHRODITE. *Earth Space Sci.* 6, 1321–1335.

Syed, F. S., and Kucharski, F. (2016). Statistically related coupled modes of South Asian summer monsoon interannual variability in the tropics. *Atmos. Sci. Lett.* 17, 183–189.

Talchabhadel, R., Karki, R., Thapa, B. R., Maharjan, M., and Parajuli, B. (2018). Spatio-temporal variability of extreme precipitation in Nepal. *Int. J. Climatol.* 38, 4296–4313.

Tippett, M. K., Barlow, M., and Lyon, B. (2003). Statistical correction of central southwest Asia winter precipitation simulations. *Int. J. Climatol.* 23, 1421–1433.

Torrence, C., and Compo, G. P. (1998). A practical guide to wavelet analysis. *Bull. Am. Meteorol. Soc.* 79, 61–78.

Wang, L., Chen, W., Zhou, W., and Huang, G. (2015). Teleconnected influence of tropical Northwest Pacific sea surface temperature on interannual variability of autumn precipitation in Southwest China. *Clim. Dyn.* 45, 2527–2539.

Wang, X., Cui, G., Wu, F., and Li, C. (2015). Analysis of temporal-spatial precipitation variations during the crop growth period in the Lancang River basin, southwestern China. *Ecol. Eng.* 76, 47–56. doi: 10.1016/j.ecoleng.2014.02.003

Wang, S.-Y., Yoon, J.-H., Gillies, R. R., and Cho, C. (2013). What caused the winter drought in western Nepal during recent years? *J. Clim.* 26, 8241–8256.

Wosrld Food Programme. (2009). *2008/09 Winter drought in Nepal – Crop and Food Security Assessment*. Rome: World Food Programme.

Wu, G., Liu, Y., He, B., Bao, Q., Duan, A., and Jin, F. (2012). Thermal controls on the Asian summer monsoon. *Sci. Rep.* 2:404. doi: 10.1038/srep00404

Yadav, R., Kumar, K. R., and Rajeevan, M. (2012). Characteristic features of winter precipitation and its variability over northwest India. *J. Earth Syst. Sci.* 121, 611–623.

Yadav, R., Rupa Kumar, K., and Rajeevan, M. (2009). Increasing influence of ENSO and decreasing influence of AO/NAO in the recent decades over northwest India winter precipitation.. *J. Geophys. Res. Atmos.* 114. doi: 10.1029/2008JD011318

Yadav, R., Ramu, D., and Dimri, A. (2013). On the relationship between ENSO patterns and winter precipitation over North and Central India. *Global Planet. Change* 107, 50–58.

Yadav, R. K., Yoo, J. H., Kucharski, F., and Abid, M. A. (2010). Why is ENSO influencing northwest India winter precipitation in recent decades? *J. Clim.* 23, 1979–1993.

Yang, J., Liu, Q., Xie, S. P., Liu, Z., and Wu, L. (2007). Impact of the Indian Ocean SST basin mode on the Asian summer monsoon. *Geophys. Res. Lett.* 34.

Yatagai, A., Arakawa, O., Kamiguchi, K., Kawamoto, H., Nodzu, M. I., and Hamada, A. (2009). A 44-year daily gridded precipitation dataset for Asia based on a dense network of rain gauges. *Sola* 5, 137–140.

Yatagai, A., Kamiguchi, K., Arakawa, O., Hamada, A., Yasutomi, N., and Kitoh, A. (2012). APHRODITE: constructing a long-term daily gridded precipitation dataset for Asia based on a dense network of rain gauges. *Bull. Am. Meteorol. Soc.* 93, 1401–1415.

Yu, W., Xiang, B., Liu, L., and Liu, N. (2005). Understanding the origins of interannual thermocline variations in the tropical Indian Ocean. *Geophys. Res. Lett.* 32. doi: 10.1029/2005gl024327

Zhang, Z., and Moore, J. C. (eds). (2015). "Chapter 6-empirical orthogonal functions," in *Mathematical and Physical Fundamentals of Climate Change* (Boston: Elsevier), 161–197.

Zhou, Z.-Q., Zhang, R., and Xie, S.-P. (2019). Interannual variability of summer surface air temperature over central india: implications for monsoon onset. *J. Clim.* 32, 1693–1706. doi: 10.1175/jcli-d-18-0675.1

Conflict of Interest: The authors declare that the research was conducted in the absence of any commercial or financial relationships that could be construed as a potential conflict of interest.

frontiers
in Earth Science

ORIGINAL RESEARCH
published: 24 June 2020
doi: 10.3389/feart.2020.00213

A Multi-Index Evaluation of Drought Characteristics in the Yarlung Zangbo River Basin of Tibetan Plateau, Southwest China

***Qiankun Niu*[1], *Liu Liu*[1,2]*, *Jingxia Heng*[1], *Hao Li*[1] and *Zongxue Xu*[3,4]**

[1] College of Water Resources and Civil Engineering, China Agricultural University, Beijing, China, [2] Center for Agricultural Water Research in China, China Agricultural University, Beijing, China, [3] College of Water Sciences, Beijing Normal University, Beijing, China, [4] Beijing Key Laboratory of Urban Hydrological Cycle and Sponge City Technology, Beijing, China

The Yarlung Zangbo River (YZR) basin occupies a crucial position in the formation and development of atmospheric circulation and climate change in the Tibetan Plateau, where is the potential trigger and amplifier in global climate fluctuations. Previous studies mainly focused on meteorological drought induced by variations of precipitation and temperature. In this study, a multi-index evaluation of drought characteristics from the perspective of meteorology and agriculture was implemented. GLDAS (Global Land Data Assimilation System) precipitation, surface air temperature and soil moisture data from 1982 to 2015 were used to calculate the meteorological drought index (Standardized Precipitation Evapotranspiration Index) and agricultural drought index (Soil Water Deficit Index), respectively. Meanwhile, the scPDSI (self-calibrating Palmer Drought Severity Index) dataset provided by CRU (Climate Research Unit) was also utilized to represent the meteorological drought, with the aim of comprehensively investigating the spatiotemporal evolution characteristics of drought in the YZR basin. Results indicated that although there was a slightly wetting tendency of the whole basin from 1982 to 2015, drought condition from the perspective of meteorology and agriculture at both annual and growing seasonal scales showed a transition from alleviation to aggravation during 1982–2015, with an abrupt change from wetting to drying occurring at the year of 2000 detected by multiple statistical tests including Mann-Kendall test, Moving *t*-test and Yamamoto test. Specifically, since the twenty-first century, the meteorological drought in the YZR basin has changed from moderate wet to moderate dry, while the agricultural drought relieved to moderate dry from severe dry with a much more complicated fluctuation. From the perspective of spatial pattern, the annual and growing season variation trends of all three drought indices were identically consistent during 1982–2015. Areas with extremely significant decreasing trend (2.24∼21.09%) were mostly distributed in the west upstream and southwest downstream dominating the overall wetting trend of the YZR basin during the period of 1982–2015, while the transition from wet to dry after 2000 was attributed to the aggravating drought of the western upstream and southeastern downstream. Results of this study have important implications for drought monitoring and eco-environmental sustainability in alpine regions.

Keywords: drought, climate change, dry-wet regime, spatio-temporal, alpine, Tibetan Plateau

Edited by:
Xingcai Liu,
Chinese Academy of Sciences, China

Reviewed by:
Xiuping Li,
Institute of Tibetan Plateau Research (CAS), China
Guangtao Fu,
University of Exeter, United Kingdom

***Correspondence:**
Liu Liu
liuliu@cau.edu.cn

Specialty section:
This article was submitted to Hydrosphere, a section of the journal Frontiers in Earth Science

Received: *13 April 2020*
Accepted: *20 May 2020*
Published: *24 June 2020*

Citation:
Niu Q, Liu L, Heng J, Li H and Xu Z (2020) A Multi-Index Evaluation of Drought Characteristics in the Yarlung Zangbo River Basin of Tibetan Plateau, Southwest China. Front. Earth Sci. 8:213. doi: 10.3389/feart.2020.00213

INTRODUCTION

Drought is a natural hazard developed slowly that would initiate considerable losses (Kelly et al., 2015; Schwalm et al., 2017; Jiang et al., 2019) which is also regarded as an elusive phenomenon with the indeterminate onset and demise (Greve et al., 2014; Bachmair et al., 2016a). Various drivers exert the occurrence of drought, among which low precipitation and high evapotranspiration are usually considered as the main causes (Mishra and Singh, 2010; Sheffield et al., 2012; Vicente-Serrano et al., 2015). A lot of studies reveal that continuous global warming has exacerbated global water cycle and triggered extreme droughts events (Dai, 2011; Huang et al., 2017; Chen and Sun, 2018). The increasing trend of drought has become a global concern during recent decades. Therefore, it is urgently necessary to detect and monitor drought under the process of global warming.

Drought is generally classified into four types in accordance with the performance characteristics and affected fields, i.e., meteorological drought, agricultural drought, hydrological drought, and socioeconomic drought (Yuan and Zhou, 2004; White and Walcott, 2009; Dai, 2011). Meteorological drought is the prerequisite for other types of drought (Tong et al., 2017). Consequently, numerous meteorological drought indices have been proposed to estimate the drought severity and improve the risk management, such as the Palmer Drought Severity Index (PDSI) (Palmer, 1965), Standard Precipitation Evapotranspiration Index (SPEI) (Vicente-Serrano et al., 2010), Standardized Wetness Index (SWI) (Liu et al., 2017), Standard Precipitation Index (SPI) (McKee et al., 1993), etc. PDSI was the first index to successfully quantify the severity of drought in various climatic conditions and played a milestone role in the development of the drought index (Zhai et al., 2010; Zambrano Mera et al., 2018), which has been widely used to evaluate meteorological drought (Shao et al., 2018; Li et al., 2019a). In order to overcome the poor applicability of PDSI in arid and semi-arid regions, scPDSI (self-calibrating Palmer Drought Severity Index) was put forward by Wells et al. (2004), which has been proven to be a particularly suitable index for detecting and monitoring the effects of global warming on drought conditions (Wang et al., 2016; Herrera and Ault, 2017; Zhu et al., 2018). It improves PDSI by adopting a self-calibration procedure that automatically adjusts the PDSI standardization coefficient to suit the local climate (Bai et al., 2020). Moreover, in the water balance model of scPDSI, dynamic changes of seasonal snowpack are considered (Van der Schrier et al., 2013), which is especially suitable for alpine region, such as the Yarlung Zangbo River (YZR) basin in the Qinghai-Tibet Plateau (QTP). And the high-resolution scPDSI dataset generated by the CRU (Climatic Research Unit) has been successfully applied around the world (Lewinska et al., 2016; Zhang et al., 2019a). With the combination of the sensitivity of the PDSI to changes in evaporation demand and robustness of the multi-temporal nature of the SPI, SPEI at various timescales has been developed and employed in an increasing number of climatological and hydrological studies (Vicente-Serrano et al., 2010; Yu et al., 2014; Spinoni et al., 2018; Li et al., 2019c). Li X. et al. (2015) evaluated the multi-scale patterns and the spatiotemporal extent of drought based on SPEI in Southwest China from 1982 to 2012. Wang et al. (2016) analyzed the performance of five climate-based drought indices, including SPEI and scPDSI, to estimate winter wheat drought threat during 2000–2013 in China. Unlike scPDSI, which obtains evapotranspiration based on the water balance model, SPEI considers the effects of evapotranspiration through the simple difference between precipitation and potential evapotranspiration (PET). In order to better analyze the drought condition in the YZR basin, two meteorological drought indices including scPDSI and SPEI were selected for cross-validation in this study.

Most meteorological drought indices are predominantly applicable to assess drought conditions in global or basin scales, while agricultural drought indices provide a fine-grained assessment of a small area during the growing season (Mishra and Singh, 2011; Zargar et al., 2011). Agricultural drought is considered to start when soil moisture availability reaches a certain low level that will lead to a negative impact on crop yield (Dai, 2011; Zhu et al., 2019). That is, meteorological drought will induce soil water deficit and further agricultural drought. In addition, the water supply of crops is mainly absorbed directly from the soil by the root system (Schoppach and Sadok, 2012). When crop canopy greenness is stressed by soil moisture, it will be lower than normal growth vegetation. In short, agricultural drought events threaten local agri-food markets and food security (Lesk et al., 2016; Yang et al., 2020). The adaptability of agricultural drought can effectively reduce the loss of agricultural drought (Dong et al., 2012). If severe agricultural drought occurs frequently in a region, local people will take long-term measures (such as crop irrigation technology) to reduce the sensitivity of agriculture to drought as well as the impact of agricultural drought on their lives. Therefore, soil water condition is a key indicator in agricultural drought prediction and assessment and irrigation management. The monitoring and early warning systems based on soil moisture are essential for agricultural activities and risk assessment (Bachmair et al., 2016b). Effective quantification of agricultural drought impacts can mitigate crop losses and ameliorate adverse effects (Liu et al., 2016; Baik et al., 2019). However, SPEI ignoring effects of soil moisture could not capture the characteristics of agricultural drought (Bezdan et al., 2019; Teweldebirhan Tsige et al., 2019). Among numerous drought indices calculated based on soil water content, the Soil Water Deficit Index (SWDI) is a more mature indicator to judge crop drought on the basis of wilting point content and field water capacity, which has been widely used in agricultural drought detection (Wagner et al., 2013; Martínez-Fernández et al., 2015; Bai et al., 2018). Martínez-Fernández et al. (2016) further demonstrated that SWDI can reproduce soil water balance dynamics and track agricultural drought preferably. Bai et al. (2018) employed SWDI to evaluate the soil moisture products of Soil Moisture Active Passive (SMAP) in China.

The Yarlung Zangbo River basin is located in the southeastern part of the QTP, China, which is characterized by complex and changeable climatic conditions, rich biological diversities, and distinct vertical vegetation belts (Liu et al., 2007; Chen B. et al., 2015). Climate change on the QTP occupies a vital position of global climate change because it is the potential trigger and amplifier in global climate fluctuations (Shen et al., 2015; Li et al., 2019a). The YZR basin is the source of precipitation on the QTP, where has vast channels carrying moisture from the Indian Ocean to the interior of the Plateau. Hence, the climate of the YZR basin plays a crucial role in the formation and development of atmospheric circulation and climate change in the QTP (Liu et al., 2002; Zhou et al., 2010; Lv et al., 2013). Scholars have done a lot of researches on climate change characteristics of the YZR basin, pointing out that a much more severe drought has been observed in recent decades (Li et al., 2014, 2019a; Li B. et al., 2015; Shen et al., 2015). However, there is a substantial resistance to conduct a study in the YZR basin due to its great altitude gradient, noticeable vertical vegetation belts and sparse observation stations, leading to research focus are limited to analyses on precipitation and temperature changes or meteorological drought only. Therefore, the objectives of this study are: (1) to implement a multi-index evaluation of drought characteristics from the comprehensively perspective of meteorology and agriculture based on multiple remotely sensed data; (2) to identify the spatiotemporal evolution mechanism of dry-wet regime through multiple statistical methods; (3) to explore possible causes of the detected variation characteristics of drought in the YZR basin. Given that few studies focus on investigating different types of drought for monitoring annual and growing season drought over the YZR basin, this study can facilitate water resources management in the YZR basin and provide a solid basis for maintaining the ecosystem sustainability of the QTP.

MATERIALS AND METHODS

Study Area

The Yarlung Zangbo River ($28°00' \sim 31°16'$N, $82°00' \sim 97°07'$E) originates from Gemma Yangzong Glacier in the southwest of Tibet, and its elevation gradually decreases from northwest to southeast, with an average elevation of more than 4,000 m and an altitude drop of 7,120 m, making it one of the highest rivers in the world. It covers an area of about 240,000 km^2 and runs east-west through the southeast of the Tibetan Plateau, traversing four prefecture-level cities and 23 counties.

The climate conditions of the YZR basin are greatly influenced by the southwest warm moist air flowing over the Bay of Bengal as well as the westerlies. Thus, the temperature exhibits an obvious vertical belt with the change of elevation, which gradually increases from northwest to southeast (You et al., 2007). Li B. et al. (2015) has proven that the warming rate of annual and seasonal air temperature from 1961 to 2014 in the YZR basin were larger than that in many other regions of the world. Due to its peculiar location and topographic characteristics, the climate of the basin from upstream to downstream shows significant heterogeneities. The period from November to April of next year that has less precipitation is considered as the winter half year and the rest of the year is considered as the summer half. **Figure 1** shows the distribution of national meteorological and hydrological stations in the YZR basin. In this study, Nugesha and Nuxia hydrological stations were taken as the outlets of the upstream and midstream, respectively, which divided the YZR basin into three sub-basins. The region between the Gemma Yangzong Glacier and Nugesha hydrological station is defined as the upstream, which is an arid and semi-arid region with annual mean precipitation of <300 mm. The region between the Nugesha and Nuxia hydrological stations is defined as the midstream, which has a temperate climate. The region below the Nuxia hydrological station, with an annual mean precipitation of more than 2,000 mm, is defined as the downstream characterized by a warm and wet climate. The glaciers in the YZR basin cause the upstream to be mostly unused land, while human activities of the downstream are much more frequent than that of the upstream.

GLDAS_NOAH Data

GLDAS (Global Land Data Assimilation System) data are jointly developed by Goddard Space Flight Center of NASA (National Aeronautics and Space Administration) and NCEP (National Centers for Environmental Prediction), a high-resolution land surface data assimilation system, of NOAA (National Oceanic and Atmospheric Administration), which is available from http://ldas.gsfc.nasa.gov/gldas/GLDASvegetation.php. Utilizing satellite remote sensing and ground observation data, this dataset drives four land surface process models, namely Mosaic, NOAH, CLM, and VIC. Through data simulation and assimilation of four different models, 28 surface variables, such as precipitation (mm), air temperature (°C), and soil moisture content (kg/m^2), are generated. At present, the land data assimilation system can provide two versions of data, GLDAS-1 and GLDAS-2, whose time series are from 1970 to 2010 and 2000 to present, respectively, with a time span of 50 years. The spatial and temporal resolutions of the data are 0.25° and 1 month, respectively. In this study, GLDAS-1 and GLDAS-2 data generated by NOAH model from 1982 to 2010 and 2010 to 2015 were spliced to obtain a new time series covering the period of 1982–2015. Performance evaluation of GLDAS data in the YZR basin has already been conducted by Liu et al. (2019) and Li et al. (2019b), indicating a good representation of spatiotemporal characteristics of precipitation, temperature and soil moisture.

Drought Indices

The Self-Calibrated Palmer Drought Severity Index (scPDSI)

The scPDSI was proposed by Wells et al. (2004) to overcome the weakness of the PDSI. Similar to the PDSI, the scPDSI is calculated based on the time series of the precipitation, temperature and the soil moisture with each position related to the surface of fixed parameters, but it can substitute actual vegetation as reference crop drought index owing to considering the seasonal changes, such as snow, thus the scPDSI owns greater spatial applicability.

The CRU-TS3.24 dataset that time series length is 1901–2016 can be acquired from www.cru.uea.ac.uk/data/, which is released by the Climatic Research Unit (CRU), University of East Anglia. The temporal and spatial resolutions of the scPDSI are one 1 month and $0.5° \times 0.5°$. It classifies the dry and wet characteristics into 9 specific grades, shown in **Table 1**. The classified scPDSI

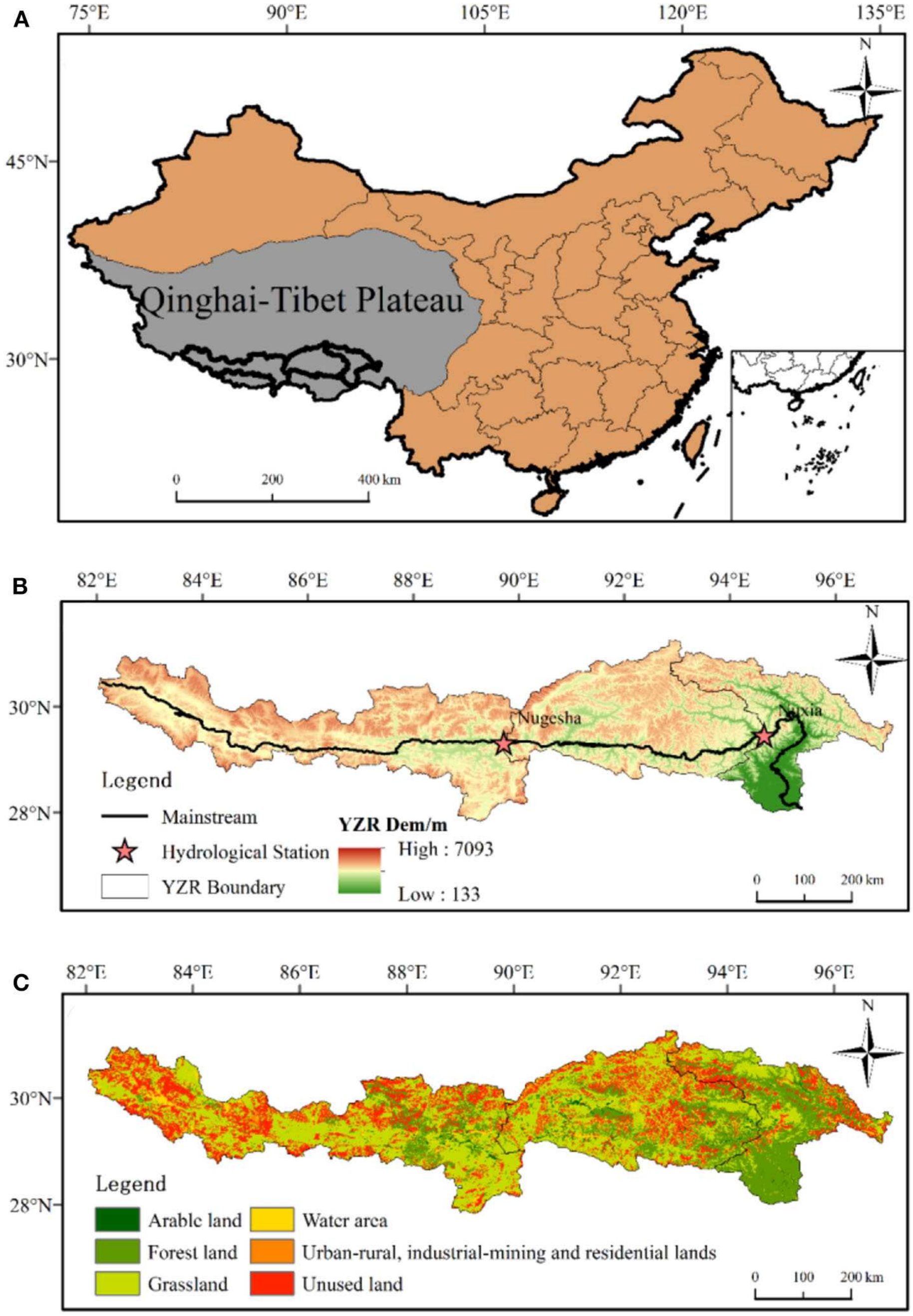

FIGURE 1 | The geographical location **(A)**, hydrometeorological stations **(B)**, and land use types of the Yarlung Zangbo River (YZR) basin **(C)**.

has been successfully applied to represent the multi-scale drought characteristics in the YZR basin according to the verification results by Li et al. (2019a).

The Standardized Precipitation Evapotranspiration Index (SPEI)

The SPEI based on the probability model is established by combining the sensitivity to sensibilities in evaporation demand of the PDSI and the robustness of the multi-temporal nature of the SPI (McKee et al., 1993), and has been widely used in many studies so far (Yu et al., 2014; Spinoni et al., 2018; Li et al., 2019c). The calculation formulas of the SPEI are as follows:

(1) PET based on the Thornthwaite method is calculated as:

$$PET = 16K\left(\frac{10T}{I}\right)^{a} \tag{1}$$

where T is the monthly mean temperature (°C); K is a correction coefficient that depends on the latitude and month; I is a heat

TABLE 1 | Drought index classification for the scPDSI (Wells et al., 2004), SPEI (Vicente-Serrano et al., 2010), and SWDI (Martínez-Fernández et al., 2016).

Drought Index Range Categories	scPDSI	SPEI	SWDI
Extremely wet	≥4	≥2	–
Severely wet	[3, 3.99]	[1.5, 1.99]	
Moderately wet	[2, 2.99]	[1.0, 1.49]	
Slightly wet	[1, 1.99]	[0.5, 0.99]	
Near normal	[−0.99, 0.99]	[−0.49, 0.49]	
No drought	–	–	>0
Slightly dry	[−1.99, −1]	[−0.99, −0.5]	[−2, 0]
Moderately dry	[−2.99, −2]	[−1.49, −1.0]	[−5, −2]
Severely dry	[−3.99, −3]	[−1.99, −1.5]	[−10, −5]
Extremely dry	≤−4	≤−2	<−10

index, which is calculated as the sum of 12 monthly index values,

$$I = \sum_{i=1}^{12} \left(\frac{T_i}{5}\right)^{1.514} \tag{2}$$

a is a coefficient depending on I, and it is computed as:

$$a = 6.75 \times 10^{-7} I^3 - 7.71 \times 10^{-5} I^2 + 1.79 \times 10^{-2} I + 0.492 \tag{3}$$

(2) Deficit or surplus of water balance between the *PET* and precipitation is defined as:

$$D_i = P_i - PET_i \tag{4}$$

where D_i is the difference between monthly precipitation P_i and potential evapotranspiration PET_i.

(3) Normalize the water balance into a log-logistic probability distribution to obtain the SPEI index series.

The log-logistic of three parameters is adopted to normalize the aggregated values of the sequence of D_i data:

$$F(x) = \left[1 + \left(\frac{\alpha}{x-\gamma}\right)^{\beta}\right]^{-1} \tag{5}$$

where *F(x)* is the probability distribution function; α, β, and γ are scale, shape, and origin parameters, respectively, which could all be estimated by the linear distance method.

The SPEI can be obtained as follows:

$$SPEI = \begin{cases} W - \frac{C_0 + C_1 W + C_2 W^2}{1 + d_1 W + d_2 W^2 + d_3 W^3}, \; p \le 0.5 \\ \frac{C_0 + C_1 W + C_2 W^2}{1 + d_1 W + d_2 W^2 + d_3 W^3} - W, p > 0.5 \end{cases} \tag{6}$$

$$W = \begin{cases} \sqrt{-2\ln(p)}, p \le 0.5 \\ \sqrt{-2\ln(1-p)}, p > 0.5 \end{cases} \tag{7}$$

$$p = 1 - F(x) \tag{8}$$

where p is the standardizing probability density function; the constants are $C_0 = 2.515517$, $C_1 = 0.802853$, $C_2 = 0.010328$, $d_1 = 1.432788$, $d_2 = 0.189269$, and $d_3 = 0.001308$. The 12-month SPEI was adopted to analyze the spatiotemporal characteristics of drought in this study due to its best performance compared with 1-, 3-, and 6-month SPEI (Liu et al., 2019).

The Soil Water Deficit Index (SWDI)

Based on the time series and basic parameters of soil moisture, SWDI can be used to capture agricultural drought conditions through biophysical principles (Vicente-Serrano et al., 2010; Martínez-Fernández et al., 2016). Soil moisture of GLDAS has been proven to have a high consistency and low bias with *in situ* measurements (Li et al., 2019b). The SWDI is formulated in this study as follows:

$$SWDI = \left(\frac{\theta - \theta_{FC}}{\theta_{AWC}}\right) \times 10 \tag{9}$$

$$\theta_{AWC} = \theta_{FC} - \theta_{WP} \tag{10}$$

where θ is the time series of 0–10 cm soil moisture data from GLDAS (kg/m^3); θ_{FC}, $\theta_{WP,}$ and θ_{AWC} represent the field capacity, wilting point, and available water capacity, respectively. The 5th percentile and 95th percentile based on GLDAS soil moisture time series are estimators of θ_{WP} and θ_{FC}.

A positive value of SWDI indicates the excess of soil water content, while negative values imply the occurrence of agricultural drought. The classification criteria of the scPDSI, SPEI and SWDI are shown in **Table 1**, respectively.

Detection of Abrupt Change

In this study, scPDSI and SPEI were used to represent the meteorological drought, while the agricultural drought was represented by SWDI. In order to accurately evaluate the spatiotemporal variation characteristics of drought in the YZR basin, non-parametric methods including Mann-Kendall test, Moving *t*-test and Yamamoto test were used to conduct abrupt change detection based on long-term time series of annual and growing season drought indices.

Mann-Kendall Test

The non-parametric Mann-Kendall test, hereinafter referred to as M-K test, was employed for detecting abrupt changes of the time series (Mann, 1945; Kendall, 1975). The advantage is that the sample to be tested does not have to obey a certain distribution, and a few outliers have little effects on the overall data sequence. Two standardized statistic series (*UB* and *UF*) are constructed for two unified data time series.

Given a time series of $X = (x_1, x_2, x_3, \ldots\ldots, x_n)$, the statistical parameter f_k is calculated as follows:

$$f_k = \sum_{i=1}^{k} \sum_{j=1}^{n} logistic\left(x_i > x_j\right), \; k = 2, 3, \cdots\cdots, n \tag{11}$$

where n is the length of the time series; when $x_i > x_j$, logistic ($x_i > x_j$) is 1, and 0 otherwise. A positive value of *UF* represents an ascending trend whereas the inverse represents a descending trend. Under the assumption that the time series is randomly independent, the standardized f_k is computed as follows:

$$UF\left(k\right) = \frac{\left[f_k - E(f_k)\right]}{\sqrt{var(f_k)}}, k = 2, 3, \cdots\cdots, n \tag{12}$$

where $E\left(f_k\right)$ and $var\left(f_k\right)$ are the mean and variance of f_k, which are defined as:

$$E\left(f_k\right) = \frac{k(k-1)}{4} \tag{13}$$

$$var\left(f_k\right) = \frac{n(n-1)(2n+5)}{72} \tag{14}$$

The equation of calculating UB that used reversed data series $X' = \left(x'_1, x'_2, x'_3, \cdots\cdots, x_n{}'\right) = (x_n, x_{n-1}, x_{n-2}, \cdots\cdots, x_1)$ is as follows:

$$UB\left(k\right) = -\frac{\left[f_k - E(f_k)\right]}{\sqrt{var(f_k)}}, k = 2, 3, \cdots\cdots, n \tag{15}$$

where f_k, $E\left(f_k\right)$, and $var\left(f_k\right)$ are calculated using the same equations of $UF(k)$. Note that if an intersection of UB and UF curves is within the confidence zone where the confidence level of 95% is treated as the boundary lines, the null hypothesis is considered to be rejected and a significant abrupt change occurred, otherwise, the detected trend is proven to be not significant.

Moving t-Test

The Moving t-test for identification of the abrupt change point is to test whether the mean values of two subsequences change significantly or not at the significance level of 0.05 (Zhao et al., 2008; Liu L. et al., 2012). Comparing mean values of the two subsequences in the climate series for significant test, analyzing variances of the two subsequences and constructing the T statistics, if the statistics pass the confidence level test, then the point where has reached the maximum absolute value of statistic is the abrupt change point most likely (Fu and Wang, 1992). Two subsequences of almost equivalent length are obtained by defining a datum point manually. The method is calculated as follows:

$$t = \frac{\bar{x}_1 - \bar{x}_2}{s.\sqrt{\frac{1}{n_1} + \frac{1}{n_2}}} \tag{16}$$

$$s = \sqrt{\frac{n_1 s_1^2 + n_2 s_2^2}{n_1 + n_2 - 2}} \tag{17}$$

where n_1 and n_2 are the lengths of two subsequences; x_1 and x_2 are the two sets of subsequences; $\bar{x}_1$, $\bar{x}_2$, s_1, and s_2 are mean values and standard deviations of x_1 and x_2, respectively. Equation (17) follows the t distribution of $n_1 + n_2 - 2$ DOF (Degree of Freedom). When $t > t_{1-\alpha/2}$ (i.e., α is the significance level of the student test and equals 0.05 in this study), it can be considered that the point of abrupt change has befallen at the significance level of 0.05.

Yamamoto Test

The principle of the Yamamoto test, which is defined mainly from the ratio of climate information and noise, is similar with Moving t-test in that an artificially defined reference point (Yamamoto et al., 1985; Fu and Wang, 1992). Two subsequences before and after the artificial reference point are defined as n_1 and n_2; the signal-to-noise ratio (SNR) is defined as follows:

$$R_{SN} = \frac{|\bar{x}_1 - \bar{x}_2|}{s_1 + s_2} \tag{18}$$

where the absolute deviations between $\bar{x}_1$ and $\bar{x}_2$ are signals of climate change; the sum of s_1 *and* s_2 is the variability of climate change; R_{SN} is the value of the SNR, namely the mutagenic index, and the mutation occurs at the certain time when $R_{SN} \geq 1$.

Trend Analysis

One-dimensional linear regression (Hao et al., 2016) was employed to conduct the long-term trend analysis on the time series of scPDSI, SPEI, and SWDI in the study area to describe the spatiotemporal variations from 1982 to 2015. The calculation formula is as follows:

$$slope = \frac{n \times \sum_{i=1}^{n}(i \times C_i) - \sum_{i=1}^{n} i \times \sum_{i=1}^{n} C_i}{n \times \sum_{i=1}^{n} i^2 - \left(\sum_{i=1}^{n} i\right)^2} \tag{19}$$

where *slope* represents the changing trends of scPDSI, SPEI, and SWDI; n is the study temporal interval, $n = 34$ in this study; and C_i represents scPDSI, SPEI, or SWDI for the year i. A significance test was performed on the variation trends of three drought indices ($P < 0.01$ indicates an extremely significant trend, $P < 0.05$ indicates a significant trend, and $P > 0.05$ implies that the variation trend is not significant).

RESULTS

A Change From Wetting to Drying Inferred by Temporal Variations

Drought is more destructive when it occurs during the growing season (Ahmed et al., 2016; Shiru et al., 2019). Scholars have revealed that vegetation conditions under global warming are significantly correlated with growing season drought (Ji and Peters, 2003; Liu X. et al., 2012; Luo et al., 2015). Thus, growing season drought was investigated along with annual drought in this study, and the growing season in the YZR basin was defined as the period from May to September within a year according to the variation characteristic of vegetation growth, precipitation, and temperature. As shown in **Figure 2**, the annual and growing season variation trends of all three drought indices were fitted by quadratic polynomial curves, showing the highest correlation with changing pattern of drought indices. It can be seen that values of scPDSI, SPEI, and SWDI at both annual and growing season scales all showed a change from increasing to declining in the later 1990s, inferring that the drought condition in the YZR basin during the period of 1982–2015 was firstly alleviated and then gradually aggravated from both the meteorological and agricultural perspectives. This phenomenon was consistent with the findings about extreme precipitation events in the YZR basin by Liu et al. (2018a), which demonstrated that almost of six extreme precipitation indices mutated in 1995 during the period of 1973–2016.

In terms of the annual scPDSI, it fluctuated between −3 and +3 corresponding to moderately dry and moderately wet in

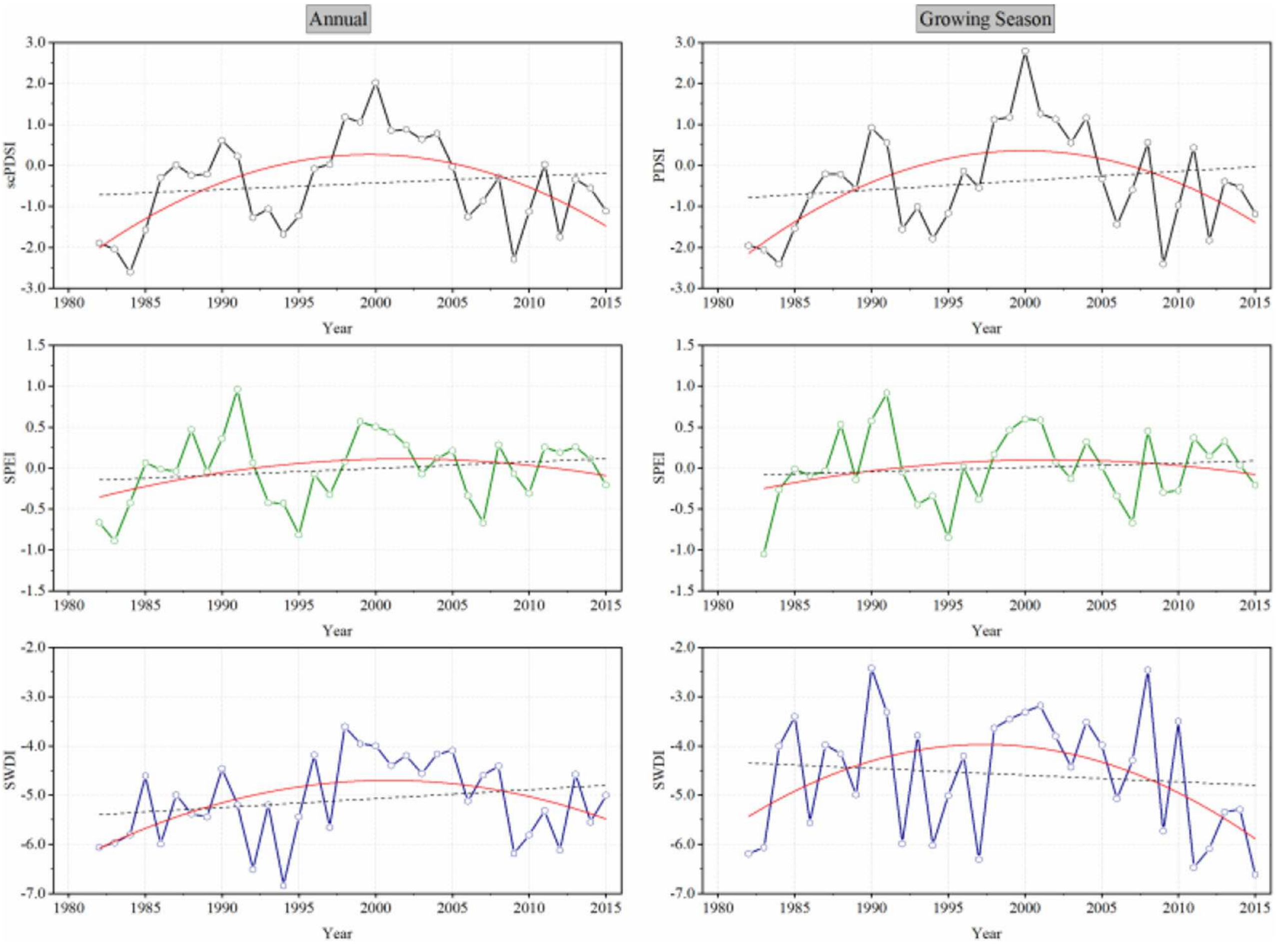

FIGURE 2 | Variation trend of three drought indices (the black, green, and blue curves are scPDSI, SPEI, and SWDI, respectively. The red solid lines are curves fitted by quadratic polynomial. The black dashed lines are linear trend lines from 1982 to 2015. And the left column is annual variations of three indices, while the left column is variations of growing season).

the past 34 years, with the maximum value (2.02) occurring in 2000. Similarly, the growing season scPDSI also experienced a fluctuating period from 1982 to 2015, with the maximum value (2.79) occurring in 2000. Similar to scPDSI, SPEI waved between −1.5 and +1.5, indicating that the dry-wet condition in the YZR basin during 1982–2015 varied between moderate humidity and moderate aridity consistent with the drought grades deduced by scPDSI. It can be seen from **Figure 2** that the highest points of the fitted curves all located around 2000, revealing that abrupt changes of meteorological drought occurred in the late 1990s and early 2000s. However, the change from wetting to drying implicated by the fitted curve of SPEI was not as significant as that of scPDSI, due to the different occurring time of the maximum value, which was located in the year of 1992. From the perspective of agricultural drought indicated by the SWDI, the YZR basin suffered a harsh drought condition where it varied between moderate drought and severe drought with a much more dramatic fluctuation. But growing season SWDI showed a downward tendency in the 34-year linear trend line, and the annual SWDI was opposite. This situation illustrates that the aggravation drought of the non-growing season made less contribution to the annual agricultural drought than that of the growing season. Contradistinguishing to the annual and growing season variation trends, although the changes of SPEI and SWDI from wet to dry implicated by fitted curves were not as significant as that of scPDSI, such as the different occurring time of maximum values and more dramatic fluctuations, the upward and downward tendencies of SPEI and SWDI were coincide with that of scPDSI on the whole. That is, they all showed a trend of wetting first and then drying around 2000. Differences between meteorological and agricultural drought indices are mainly attributed to the fact that in addition to rainfall and irrigation, other water supply ways such as meltwater of snow and glacier are also the significant water sources of the YZR basin, further illustrating that the influence of global warming on the YZR basin has progressively increased. The main reason for the differences is that the soil moisture in the YZR basin showed a persistently decreasing trend (Zhang et al., 2019b)

TABLE 2 | Results of abrupt change detection for three drought indices at annual and growing season scales.

Index	Time scale	Method		
		M-K	Moving t	Yamamoto
scPDSI	Annual	1983	1991, 1997, 2005	1997
	Growing season	1983	1991, 1997, 2005	2004
SPEI	Annual	1983	1997	1998
	Growing season	1983, 1994	1997	–
SWDI	Annual	1983	1997, 2005	1997, 2005, 2008
	Growing season	–	1997, 2008	1997

and SWDI was calculated by soil moisture parameters, implying that it would change immediately as the soil moisture changes. Other factors, such as soil properties, cropping systems, and the amount of irrigation, can also affect agricultural drought (Liu et al., 2016). However, two meteorological drought indices are more related to precipitation and evapotranspiration. If irrigation or other agricultural measures can be provided to crops in time to maintain soil moisture after meteorological drought, then there would no agricultural drought occurring.

Multi-Index Detection of the Changing Point From Wetting to Drying

In order to identify whether there was an abrupt change from wetting process to drying process in the YZR basin, the M-K test, Moving *t*-test and Yamamoto test were adopted to implement the detection at both annual and growing season time scales based on the long-term time series of scPDSI, SPEI and SWDI. As demonstrated in section A Change From Wetting to Drying Inferred by Temporal Variations, there was a tendency from wetting to drying occurred during the period of the late 1990s to the early 2000s. Li et al. (2019a) pointed out that from 1956 to 2015, scPDSI also had a transition during the mid-twentieth century through locally-weighted scatter point smoothing method, and previous studies revealed that precipitation, temperature, and PET all changed significantly around 2000 in the YZR basin (Liu, 2015; Wang, 2016). As shown in **Table 2**, the highest occurrence frequency of changing point for annual and growing season droughts indicated by three indices based on M-K test, Moving *t*-test and Yamamoto test was 1997, followed by the year of 1983 and 2005. However, the changing point of 1983 was only identified by the M-K test, while much more abrupt change points detected by Moving *t*-test and Yamamoto test were concentrated in the period from the late of 1990s to the early of 2000s, further verifying there was an abrupt change around 2000 from wetting to drying in the YZR basin.

Determination of the abrupt change point of the dry-wet condition in the YZR basin was of great importance to conduct further investigation in this study. Given that runoff has been regarded as the most direct indicator to represent the dry-wet characteristics at the river basin scale (Liu et al., 2014; Yang et al., 2017). Located in the lower reaches of the YZR basin, the Nuxia hydrological station controls nearly 80% area of the basin, and its long-term variation of runoff can effectively reflect the dry-wet condition of the whole basin. Thus, the runoff time series from 1982 to 2015 at the Nuxia hydrological station were used in this study to further identify the abrupt change point from wetting to drying. Results of the M-K test for monotonic trend showed that, taking 2000 as the changing point, the runoff from 1982 to 1999 exhibited a significant increasing trend ($P < 0.1$) and a significant decreasing trend from 2000 to 2015 ($P < 0.1$). However, if taking 1998, 1999, or any other year during the period from the late of 1990s to the early of 2000s as the changing point, runoff during the divided two periods according to the changing point could not show simultaneously significant increasing trend and significant decreasing trend (**Figure 3**). Combining with the long-term variations of drought indicated by three indices, it could be determined that there was an abrupt change from wetting to drying in the YZR basin, which occurred at the year of 2000. The transition characteristics of drought from 1982 to 2015 in the YZR basin had significant impacts on water projects and water safety in terms of water allocation, regulation, and water resource utilization (Alfieri et al., 2007; Chen X. et al., 2015). In consideration of utilizing the water resource in the downstream and relieving water shortage in some northern areas, it is an effective way to build pumped storage hydropower stations in the midstream.

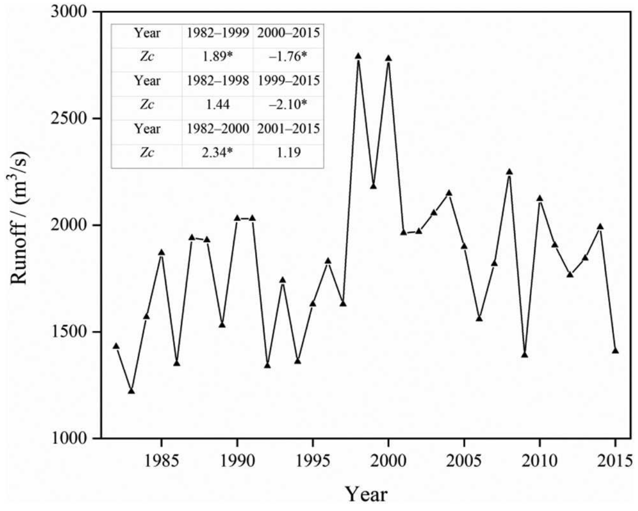

Year	1982–1999	2000–2015
Zc	1.89*	–1.76*
Year	1982–1998	1999–2015
Zc	1.44	–2.10*
Year	1982–2000	2001–2015
Zc	2.34*	1.19

FIGURE 3 | Variation trend of runoff at the Nuxia hydrological station from 1982 to 2015 (*a statistically significant variation trend at the confidence level of 90%).

Spatial Variation of Drought Associated With the Change From Wetting to Drying

In order to characterize the regional differences in meteorological and agricultural drought change trends in the watershed for 34 years, it is necessary to analyse the spatial evolution process and occurrence characteristics of drought in the YZR basin. Due to the significant spatial heterogeneities of meteorological and underlying conditions, the spatial distributions of the annual and growing season values of three drought indices in the

YZR basin before and after 2000 were obtained by using Kriging interpolation method, aiming to further investigate the drought evolution mechanism from wetting to drying. As shown in **Figure 4**, it could be obviously found that the annual spatial distribution of scPDSI, SPEI, and SWDI showed a high consistency with that of the growing season during both periods (1982–1999 and 2000–2015). Before 2000, the dry areas were mainly located in the east upstream and midstream of the study area, while the west upstream and southeast downstream were relatively wet. Similar to the temporal abrupt change phenomenon from wetting to drying at the year of 2000, the spatial pattern of scPDSI, SPEI and SWDI all displayed a reversal phenomenon from the period of 1982–1999 to the period of 2000–2015, i.e., areas where used to be wet during 1982–1999 were getting dry during 2000–2015 and formerly dry areas were getting wet, mainly attributed to the aggravation of drought in the west and southeast of the upstream and the alleviation of drought in the midstream from 1982 to 2015. These results were consistent with the finding obtained by Li et al. (2019a). However, meteorological drought represented by scPDSI and SPEI showed a different spatial variation of drought level with agricultural drought indicated by SWDI. The driest area indicated by meteorological drought in the basin moved from the midstream to the southeast downstream, while the driest area deduced by agricultural drought shifted from the east midstream and north downstream to the south downstream. Furthermore, during 1982–2015, values of SWDI decreased in the northeast midstream and northwest downstream, causing the degree of agricultural drought turned from severe drought to moderate drought. Two meteorological drought indices showed that the upstream changed from slightly wet to slightly dry, while both meteorological and agricultural drought showed a moderate drought in the downstream after 2000. According to **Figures 2**, **4**, both the annual meteorological and agricultural drought alleviated, and spatially the overall wetting tendency of the YZR basin was mainly attributed to the significant wetting trend of the midstream from 1982 to 2000, while the abrupt change from wetting to drying from 2000 to 2015 in the basin was ascribed to drought aggravation that was situated in the west upstream and south downstream.

To further probe into the mechanism of spatial variations of drought in the YZR basin, the annual and growing season variation trends with the significance test of scPDSI, SPEI, and SWDI were analyzed at the pixel scale (**Figure 5**). The area proportions occupied by extremely significant, significant and non-significant increases and decreases of the three drought indices were shown in **Figure 6**.

Although the spatial distribution of SWDI representing agricultural drought was slightly different from that of the other two meteorological drought indices (illustrated in **Figure 4**), the spatial variation trends with the significance test of all three indices at the annual scale exhibited highly consistent characteristics (shown in **Figure 5**). During 1982–2015, the northwest upstream and southeast downstream showed an increasing trend of drought, while the southeast upstream and middle reaches experienced a contrary characteristic. And areas with extremely significant decreasing trend were mostly distributed in the west upstream and southwest downstream, whereas the midstream and northwest downstream mainly showed extremely significant increasing trends, accounting for the spatial reversal phenomenon from wetting to drying after 2000. The spatial variation trends with the significance test of growing season drought were consistent with those of annual drought. Areas occupied by non-significant increasing and non-significant decreasing trends of the annual and growing season meteorological drought consistently accounted for the greatest and almost equivalent proportions, followed by area proportions occupied by the extremely significant increase, leading to the overall wetting tendency in the YZR basin from 1982 to 2015. There have some differences with the results

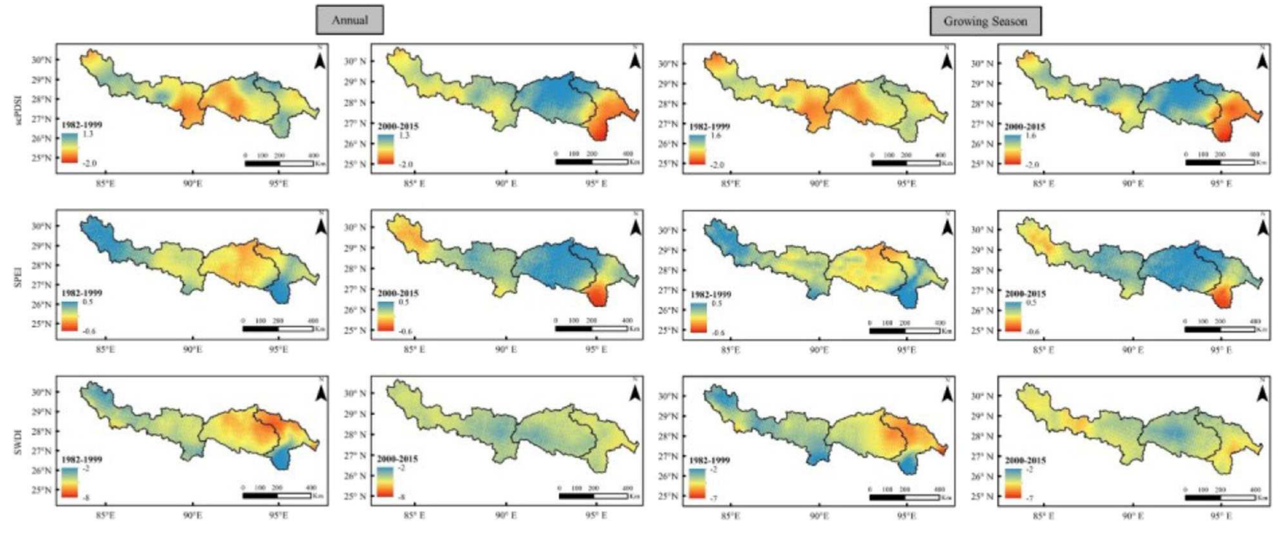

FIGURE 4 | Annual and growing season spatial distributions of three drought indices.

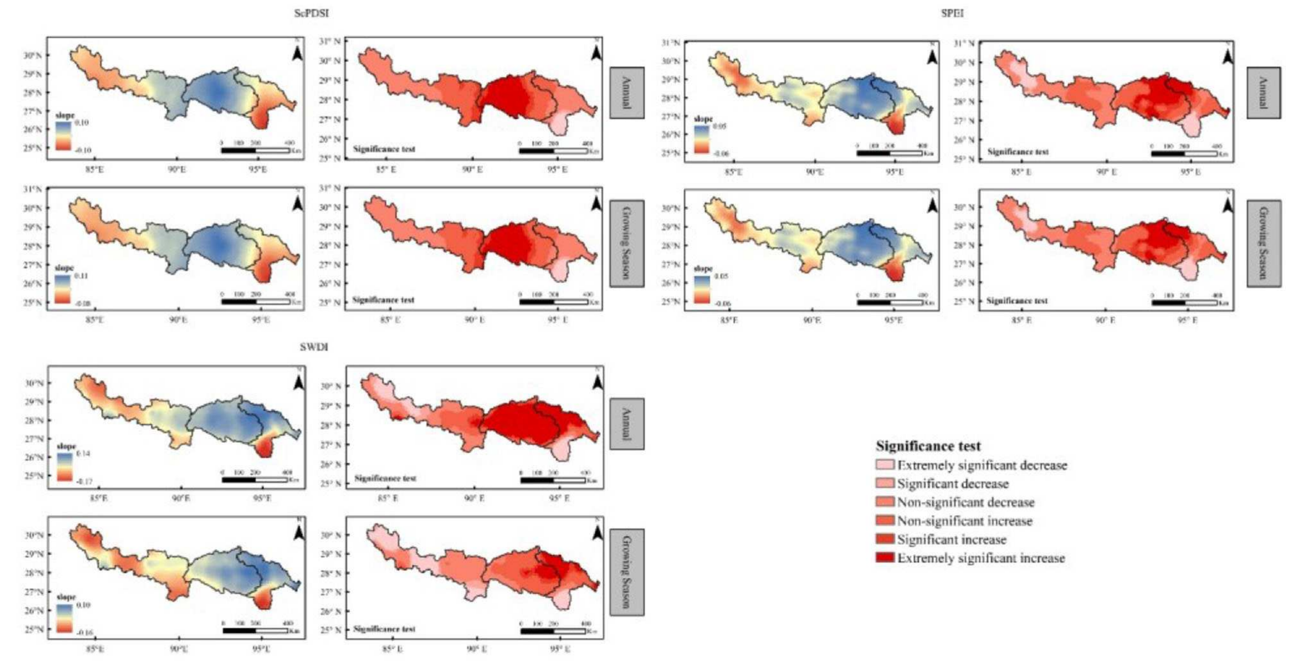

FIGURE 5 | Annual and growing season variation trends of three drought indices with the significance test.

obtained by Zhang et al. (2019c), which revealed that the trend of agricultural drought was significantly increasing at 95% confidence level during 2000–2014 in the YZR basin. This may be due to discrepancies in length of observation time series and size of the focusing study area. Nevertheless, areas with the greatest proportions for the annual and growing season SWDI were, respectively, located in extremely significant increase and non-significant decrease, and areas with an increasing trend of the annual and growing season SWDI accounted for 62.95 and 43.7% of the basin area, respectively, further giving an explanation for overall alleviated agricultural drought from severe dry to moderate dry and manifesting that the degree of alleviated agricultural drought in the YZR basin was dominated by the alleviated drought in the non-growing season period from January to April and from October to December. With the combination of the results obtained in the study and Zhang et al. (2019c), it is recommended to plant more crops with drought resistance, cold resistance and high yield, such as wheat, in some well-irrigated valleys of the middle and lower reaches for the purpose of coping with growing season drought and guaranteeing the food security in the YZR basin.

DISCUSSION

Droughts cause agricultural loss, forest mortality, and drinking water scarcity. Their current increase in recurrence and intensity poses serious threats to future food security. Still today, our knowledge of how droughts start and evolve remains limited (Zhang et al., 2017; Zhai et al., 2018; Chen et al., 2019; Huang et al., 2019). Zhang et al. (2010) pointed out that temperature rise and precipitation decrease were two important drought-causing factors in the north, northeast, and eastern part of northwest China with the most significant trend of drought since the 1980s. Feng and Fu (2013) considered the rising temperature as the main reason of global drought. Zeng et al. (2019) attributed the spring and winter drought to a decrease in relative humidity which led to an increase in reference evapotranspiration, while the duration of sunshine was the dominant factor of summer and autumn drought in southwest China from 1960 to 2000. In addition, soil drought (low soil moisture) and atmospheric aridity (high vapor pressure deficit, VPD) have been regarded as the two main factors responsible for drought, which influenced terrestrial water use and carbon uptake further (Novick et al., 2016; Zhou et al., 2019b). Ding et al. (2018) demonstrated that alpine grasslands in Tibetan Plateau would face increasingly severe meteorological drought pressure in the future due to the negative influence of VPD. What's more, there is a significant correlation between vegetation degradation and climate change in the YZR basin, emphasizing the importance of VPD as the driving factor of drought (Han et al., 2018). Meanwhile, low correlations between scPDSI and air temperature were found in the YZR basin, indicating that meteorological drought variations were largely unaffected by temperature (Li et al., 2019a). Regarded as the difference between the water vapor pressure at saturation and the actual water vapor pressure for a given temperature, VPD has been used to estimate atmospheric aridity for the implication of drought. Zhou et al. (2019a) demonstrated that VPD had a strong coupling with soil moisture and then would affect the initiation and perpetuation of drought. Increased VPD will increase the atmospheric demand of evapotranspiration water (Penman,

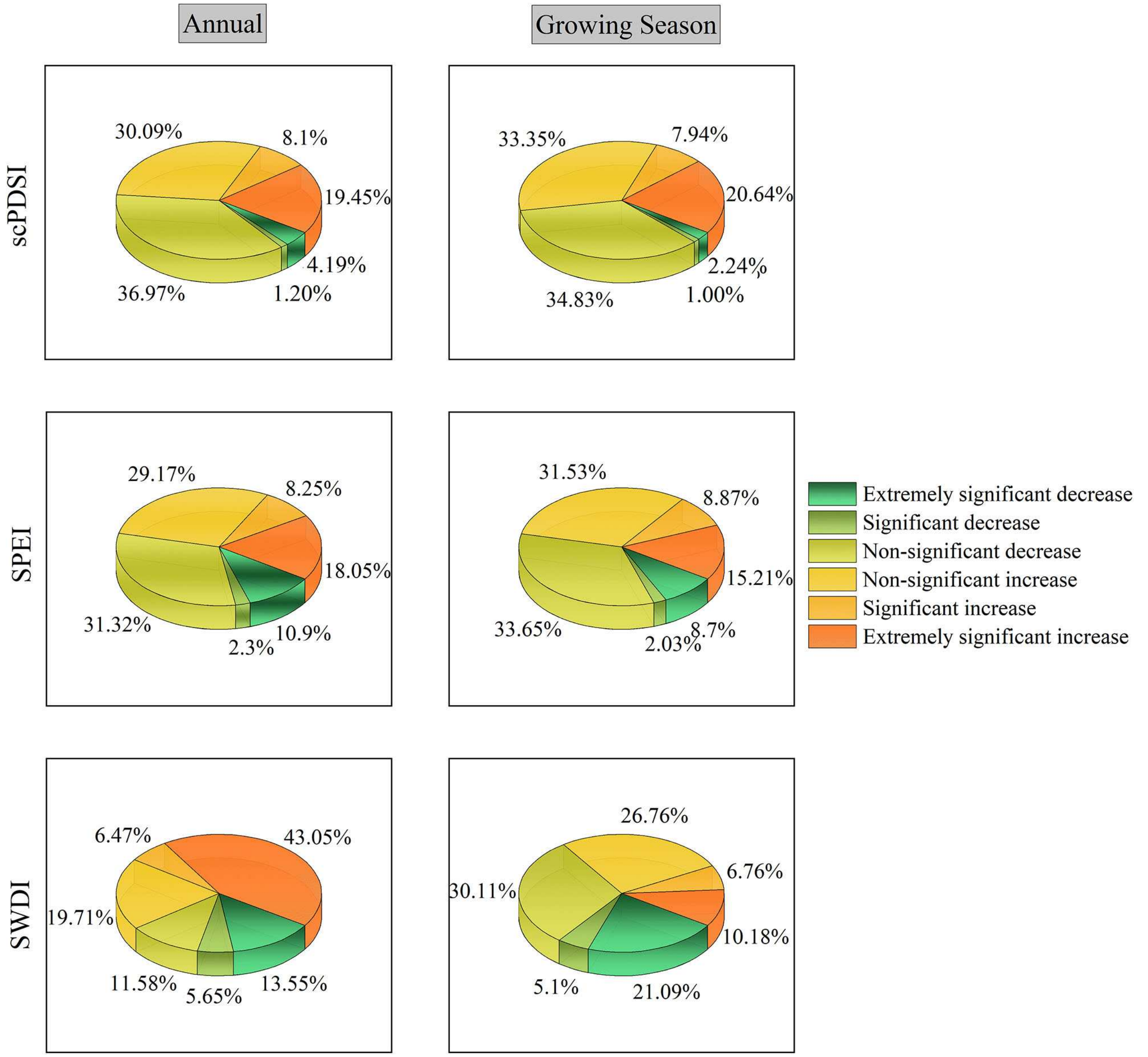

FIGURE 6 | Area proportions (%) occupied by different variation trends of the three drought indices.

1948; Monteith, 1965). It also will reduce stomatal conductance by closing stomata (Massmann et al., 2019), and changes of VPD substantially influences the terrestrial ecosystem structure and function through vegetation productivity (Konings et al., 2017), further resulting in a significant change in evapotranspiration that leads to meteorological drought (Rawson et al., 1977; Zhou et al., 2019a). Therefore, facing the significant increase of VPD under global warming, VPD calculated by the improved Magus Empirical Formula (Zeng, 1974) was taken into consideration in this study to implement a further investigation on the evolution mechanism of drought in the YZR basin.

According to the temporal variation trends of VPD (**Figure 7**), the YZR basin got drier during the period of 1982–2015. Obviously, it can be found that there was a huge jump of annual and growing season VPD in 2011 and VPD remained high in the following years. This is consistent with the historical record that severe drought had happened in 2011 (Shao et al., 2018). However, only SWDI indicated such severe drought event, while two meteorological drought indices used in this study indicated that the dry-wet condition of the YZR basin were nearly normal in 2011. The main reason for this consistent implication from VPD and SWDI could be attributed to the fact that rising temperature accelerates the deficit of soil water by increasing soil evaporation and simultaneously aggravates the difference between saturated and actual water vapor pressures by increasing VPD. Nevertheless, meteorological drought was dominated by

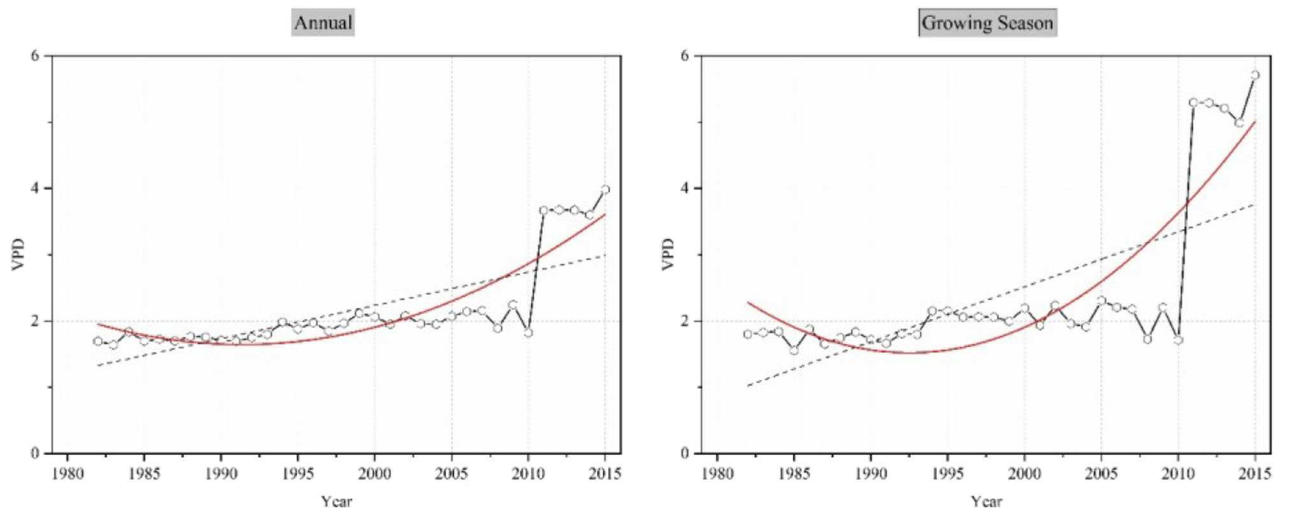

FIGURE 7 | Variation trend of annual and growing season VPD (The red solid lines are curves fitted by quadratic polynomial. The black dashed lines are linear trend lines from 1982 to 2015).

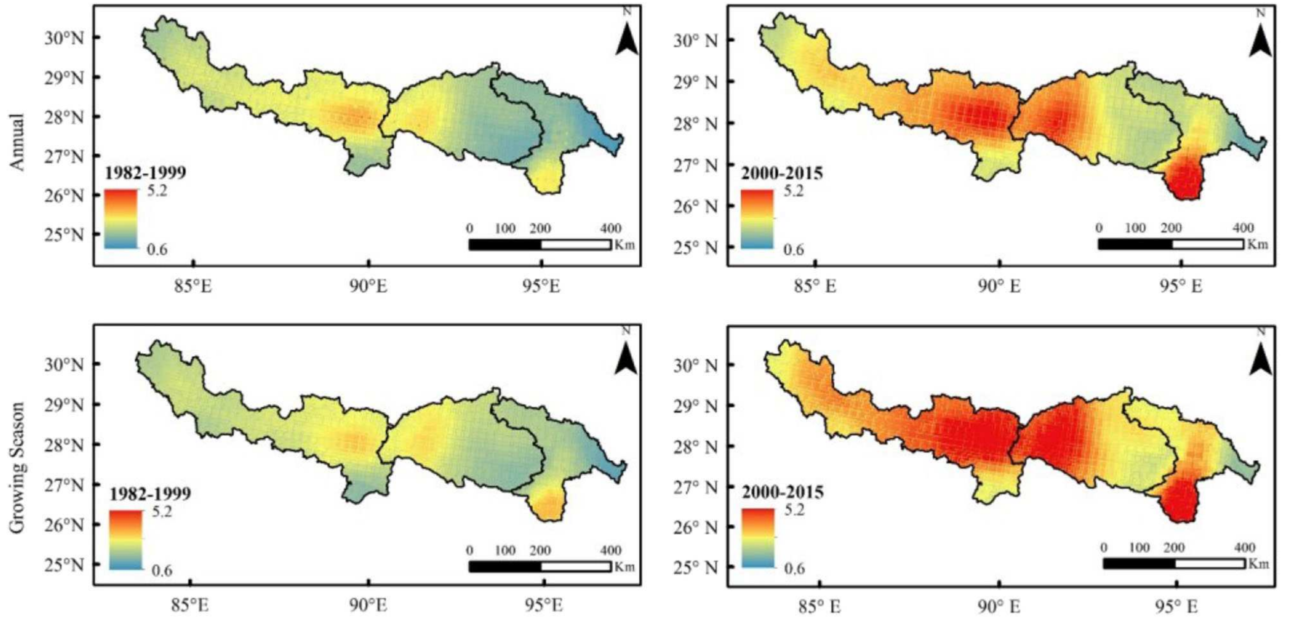

FIGURE 8 | Annual and growing season spatial distributions of VPD.

precipitation rather than temperature demonstrated by Li et al. (2019a), giving an explanation for the inconsistent implication from VPD and two meteorological drought indices, and further emphasizing that VPD could not be independently used to represent the meteorological drought in the YZR basin. As shown in **Figure 8**, values of annual and growing season VPD from 2000 to 2015 (2.6 and 3.1) were both approximately 1.5 times those from 1982 to 1999 (1.8 and 1.9). The maximum values of annual and growing season VPD (5.5 and 6.0) were all located in the southern downstream and the junction of upstream and midstream, which were consistent with the agricultural drying tendency of upstream and southeast downstream of the basin represented by SWDI. However, the agricultural drought in the northeast midstream and the northwest downstream were alleviating from 1982 to 2015, which is not in line with the spatial distribution of VPD. That may be due to a decrease trend of snow cover in these places, which in turn leads to an increase in soil water content (Liu et al., 2018b). The meteorological drought in the east upstream, nearly the entire midstream and the northwest downstream changed from slightly dry to near normal while

VPD of almost the whole basin has increased, which further confirmed that other factors besides VPD comprehensively affect the meteorological drought in the YZR basin. Similar results were also obtained by Liu et al. (2019), demonstrating a trend of humidification occurring in the eastern upstream and midstream regions. Combined **Figures 1C**, **8**, the drought characteristics inferred by VPD might be related to frequent human activities concentrated in the midstream. Although VPD has been well-known to play an important role in the evolution mechanism of drought, it is not suitable to be independently applied as an indicator of drought in alpine regions like the YZR basin. Even more noteworthy is the fact that VPD does not have a clear drought classification yet. Given that VPD has a consistency with agricultural drought and a heterogeneity with meteorological drought, it is better to comprehensively analyze rather than pick out a single factor separately when identifying the influencing factors of drought in the YZR basin, and more attention should be paid to VPD variation characteristics to improve the understanding of drought variation and its impacts on ecosystem.

CONCLUSION

Based on the scPDSI, SPEI, and SWDI derived from GLDAS and CRU datasets, a multi-index evaluation of drought characteristics during 1982–2015 in the Yarlung Zangbo River basin from the perspective of meteorology and agriculture was conducted in this study. Non-parametric statistical tests including M-K test, Moving *t*-test and Yamamoto test were adopted to implement long-term trend analysis and abrupt change detection, further exploring the possible causes of drought evolution. The conclusions are as follows:

(1) The whole basin presented a wetting trend during 1982 to 2015. Meteorological and agricultural drought of annual and growing season scales in the YZR basin showed an abrupt change from wetting to drying in the year of 2000, indicating a trend of alleviating first and then aggravating during 1982 to 2015. Meteorological drought represented by scPDSI and SPEI changed from moderate drought to moderate wet before 2000 while it was opposite after 2000, and agricultural drought alleviated from severe drought to moderate drought during 34 years.

(2) Both meteorological and agricultural drought in the basin showed a moderate drought in the downstream after 2000 and the upstream changed to slightly dry. The driest area indicated by meteorological drought in the basin moved from the midstream to the southeast downstream, while it indicated by agricultural drought shifted from the east midstream and north downstream to the south downstream.

(3) Non-significant increasing and non-significant decreasing trends of the annual and growing season meteorological drought consistently hold the greatest and almost equivalent proportions. Areas with extremely significant decreasing trend were mostly distributed in the west upstream and southwest downstream, whereas the midstream and northwest downstream mainly showed extremely significant increasing trends.

DATA AVAILABILITY STATEMENT

Publicly available datasets were analyzed in this study. This data can be found here: Land Data Assimilation System (http://ldas.gsfc.nasa.gov/gldas/GLDASvegetation.php) and Climatic Research Unit (www.cru.uea.ac.uk/data/).

AUTHOR CONTRIBUTIONS

LL: conceptualization, resources, and supervision. LL and JH: methodology. JH: software. QN, JH, and LL: validation. QN and JH: formal analysis and investigation. JH, HL, and QN: data curation and visualization. QN and LL: writing—original draft preparation and writing—review and editing. LL and ZX: project administration and funding acquisition. All authors contributed to the article and approved the submitted version.

FUNDING

This research was financially supported by the National Key R&D Program of China (No. 2018YFC1508702) and the National Natural Science Foundation of China (91647202, 41890822, and 51509247).

ACKNOWLEDGMENTS

The authors would like to thank the Climatic Research Unit at the University of East Anglia and the Global Land Data Assimilation System team for making the data freely available.

REFERENCES

Ahmed, K., Shahid, S., Harun, S. B., and Wang, X. (2016). Characterization of seasonal droughts in balochistan province, Pakistan. *Stoch. Environ. Res. Risk Assess.* 30, 747–762. doi: 10.1007/s00477-015-1117-2

Alfieri, J. G., Blanken, P. D., Yates, D. N., and Steffen, K. (2007). Variability in the environmental factors driving evapotranspiration from a grazed rangeland during severe drought conditions. *J. Hydrometeorol.* 8, 207–220. doi: 10.1175/JHM569.1

Bachmair, S., Stahl, K., Collins, K., Hannaford, J., Acreman, M., Svoboda, M., et al. (2016a). Drought indicators revisited: the need for a wider consideration of environment and society. *Wiley Interdiscip. Rev. Water* 3, 516–536. doi: 10.1002/wat2.1154

Bachmair, S., Svensson, C., Hannaford, J., Barker, L. J., and Stahl, K. (2016b). A quantitative analysis to objectively appraise drought indicators and model drought impacts. *Hydrol. Earth Syst. Sci.* 20, 2589–2609. doi: 10.5194/hess-20-2589-2016

Bai, J., Cui, Q., Chen, D., Yu, H., Mao, X., Meng, L., et al. (2018). Assessment of the SMAP-Derived Soil Water Deficit Index (SWDI-SMAP) as an agricultural drought index in China. *Remote Sens.*10:1302. doi: 10.3390/rs10081302

Bai, X., Shen, W., Wu, X., and Wang, P. (2020). Applicability of long-term satellite-based precipitation products for drought indices considering global warming. *J. Environ. Manage.* 255:109846. doi: 10.1016/j.jenvman.2019.109846

Baik, J., Zohaib, M., Kim, U., Aadil, M., and Choi, M. (2019). Agricultural drought assessment based on multiple soil moisture products. *J. Arid Environ.* 167, 43–55. doi: 10.1016/j.jaridenv.2019.04.007

Bezdan, J., Bezdan, A., Blagojević, B., Mesaroš, M., Pejić, B., Vranešević, M., et al. (2019). SPEI-based approach to agricultural drought monitoring in vojvodina region. *Water* 11:1481. doi: 10.3390/w11071481

Chen, B., Li, H., Cao, X., Shen, W., and Jin, X. (2015). Vegetation pattern and spatial distribution of NDVI in the yarlung zangbo river basin of China. *J. Desert Res.* 35, 120–128. doi: 10.7522/j.issn.1000-694X

Chen, H., and Sun, J. (2018). Projected changes in climate extremes in China in a 1.5°C warmer world. *Int. J. Climatol.* 38, 3607–3617. doi: 10.1002/joc.5521

Chen, S., Gan, T., Tan, X., Shao, D., and Zhu, J. (2019). Assessment of CFSR, ERA-Interim, JRA-55, MERRA-2, NCEP-2 reanalysis data for drought analysis over China. *Clim. Dyn.* 53, 737–757. doi: 10.1007/s00382-018-04611-1

Chen, X., Mei, M., Ding, Y., Chao, Q., Song, Y., Wu, Q., et al. (2015). The impacts of climate change on several major projects in China. *Progr Inquisit Mutat Climat.* 11, 337–342. doi: 10.3969/j.issn.1673-1719.2015.05.007

Dai, A. (2011). Drought under global warming: a review. *Wiley Interdiscip. Rev. Clim. Chang.* 2, 45–65. doi: 10.1002/wcc.81

Ding, J., Yang, T., Zhao, Y., Liu, D., Wang, X., Yao, Y., et al. (2018). Increasingly important role of atmospheric aridity on tibetan alpine grasslands. *Geophys. Res. Lett.* 45, 2852–2859. doi: 10.1002/2017GL076803

Dong, Y., Chen, H., Yu, D., and Li, C. (2012). "Satellite observations on agricultural adaptation to drought in southwestern China," in *2012 First International Conference on Agro-Geoinformatics* (Shanghai: IEEE), 1–4. doi: 10.1109/Agro-Geoinformatics.2012.6311704

Feng, S., and Fu, Q. (2013). Expansion of global drylands under a warming climate. *Atmos. Chem. Phys.* 13, 10081–10094. doi: 10.5194/acp-13-10081-2013

Fu, C., and Wang, Q. (1992). The definition and detection of the abrupt climatic change. *Sci. Atmos. Sin.* 16, 482–493.

Greve, P., Orlowsky, B., Mueller, B., Sheffield, J., Reichstein, M., and Seneviratne, S. I. (2014). Global assessment of trends in wetting and drying over land. *Nat. Geosci.* 7, 716–721. doi: 10.1038/ngeo2247

Han, X., Zuo, D., Xu, Z., Cai, S., and Gao, X. (2018). Analysis of vegetation condition and its relationship with meteorological variables in the yarlung zangbo river basin of China. *Proc. Int Assoc. Hydrol. Sci.* 379, 105–112. doi: 10.5194/piahs-379-105-2018

Hao, Z., Hao, F., and Singh, V. P. (2016). A general framework for multivariate multi-index drought prediction based on Multivariate Ensemble Streamflow Prediction (MESP). *J. Hydrol.* 539, 1–10. doi: 10.1016/j.jhydrol.2016.04.074

Herrera, D., and Ault, T. (2017). Insights from a new high-resolution drought atlas for the Caribbean spanning 1950 to 2016. *J. Clim.* 30, 7801–7825. doi: 10.1175/JCLI-D-16-0838.1

Huang, S., Leng, G., Huang, Q., Xie, Y., Liu, S., Meng, E., et al. (2017). The asymmetric impact of global warming on US drought types and distributions in a large ensemble of 97 hydro-climatic simulations. *Sci. Rep.* 7:5891. doi: 10.1038/s41598-017-06302-z

Huang, S., Wang, L., Wang, H., Huang, Q., Leng, G., Fang, W., et al. (2019). Spatio-temporal characteristics of drought structure across China using an integrated drought index. *Agric. Water Manage.* 218, 182–192. doi: 10.1016/j.agwat.2019.03.053

Ji, L., and Peters, A. J. (2003). Assessing vegetation response to drought in the northern Great Plains using vegetation and drought indices. *Remote Sens. Environ.* 87, 85–98. doi: 10.1016/S0034-4257(03)00174-3

Jiang, L., Jiapaer, G., Bao, A., Kurban, A., Guo, H., Zheng, G., et al. (2019). Monitoring the long-term desertification process and assessing the relative roles of its drivers in Central Asia. *Ecol. Indic.* 104, 195–208. doi: 10.1016/j.ecolind.2019.04.067

Kelly, C., Ferrara, A., Wilson, G. A., Ripullone, F., Nolè, A., Harmer, N., et al. (2015). Community resilience and land degradation in forest and shrubland socio-ecological systems: evidence from Gorgoglione, Basilicata, Italy. *Land Use Pol.* 46, 11–20. doi: 10.1016/j.landusepol.2015.01.026

Kendall, M. G. (1975). *Rank Correlation Methods*. London: Charles Griffin.

Konings, A. G., Williams, A. P., and Gentine, P. (2017). Sensitivity of grassland productivity to aridity controlled by stomatal and xylem regulation. *Nat. Geosci.* 10, 284–288. doi: 10.1038/ngeo2903

Lesk, C., Rowhani, P., and Ramankutty, N. (2016). Influence of extreme weather disasters on global crop production. *Nature* 529, 84–87. doi: 10.1038/nature16467

Lewinska, K., Ivits, E., Schardt, M., and Zebisch, M. (2016). Alpine forest drought monitoring in South Tyrol: PCA based synergy between scPDSI data and MODIS derived NDVI and NDII7 time series. *Remote Sens.* 8:639. doi: 10.3390/rs8080639

Li, B., Yu, Z., Liang, Z., and Acharya, K. (2014). Hydrologic response of a high altitude glacierized basin in the central tibetan plateau. *Glob. Planet. Change* 118, 69–84. doi: 10.1016/j.gloplacha.2014.04.006

Li, B., Zhou, W., Zhao, Y., Ju, Q., Yu, Z., Liang, Z., et al. (2015). Using the SPEI to assess recent climate change in the yarlung zangbo river basin, South Tibet. *Water* 7, 5474–5486. doi: 10.3390/w7105474

Li, H., Liu, L., Shan, B., Xu, Z., Niu, Q., Cheng, L., et al. (2019a). Spatiotemporal variation of drought and associated multi-scale response to climate change over the Yarlung Zangbo River Basin of Qinghai-Tibet Plateau, China. *Remote Sens.* 11:1596. doi: 10.3390/rs11131596

Li, X., He, B., Quan, X., Liao, Z., and Bai, X. (2015). Use of the Standardized Precipitation Evapotranspiration Index (SPEI) to characterize the drying trend in southwest China from 1982–2012. *Remote Sens.* 7, 10917–10937. doi: 10.3390/rs70810917

Li, X., Liu, L., Li, H., Wang, S., and Heng, J. (2019b). Spatiotemporal soil moisture variations associated with hydro-meteorological factors over the yarlung zangbo river basin in Southeast Tibetan Plateau. *Int. J. Climatol.* 40, 188–206. doi: 10.1002/joc.6202

Li, X., You, Q., Ren, G., Wang, S., Zhang, Y., Yang, J., et al. (2019c). Concurrent droughts and hot extremes in northwest China from 1961 to 2017. *Int. J. Climatol.* 39, 2186–2196. doi: 10.1002/joc.5944

Liu, J., Xu, Z., Zhao, H., Peng, D., and Zhang, R. (2018a). Spatiotemporal variation of extreme precipitation events in the yarlung zangbo river basin from 1973 to 2016, China. *Mountain Res.* 36, 750—764. doi: 10.7522/j.issn.10000240.2018.0070

Liu, J., Yao, Z., and Chen, C. (2007). Evolution trend and causation analysis of the runoff evolution in the yarlung zangbo river basin. *J. Nat. Res.* 122, 471–477. doi: 10.11849/zrzyxb.2007.03.017

Liu, J., Zhang, W., Deng, C., and Nie, N. (2018b). Spatiotemporal variations of snow cover over yarlung zangbo river basin in tibet from 2000 to 2014 and its response to key climate factors. *J. Glaciol. Geocryol.* 40, 643–654. doi: 10.7522/j.issn.1000-0240.2018.0070

Liu, L., Niu, Q., Heng, J., Li, H., and Xu, Z. (2019). Transition characteristics of the dry-wet regime and vegetation dynamic responses over the yarlung zangbo river basin, southeast qinghai-tibet plateau. *Remote Sens.* 11:1254. doi: 10.3390/rs11101254

Liu, L., Xu, Z., and Huang, J. (2012). Spatio-temporal variation and abrupt changes for major climate variables in the Taihu Basin, China. *Stoch. Environ. Res. Risk Assess.* 26, 777–791. doi: 10.1007/s00477-011-0547-8

Liu, M., Xu, X., Xu, C., Sun, A. Y., Wang, K., Scanlon, B. R., et al. (2017). A new drought index that considers the joint effects of climate and land surface change. *Water Resour. Res.* 53, 3262–3278. doi: 10.1002/2016WR020178

Liu, T., Zhang, X., Xiong, S., Qin, X., and Yang, X. (2002). Glacial environments on the tibetan plateau andglobal cooling. *Quat. Int.* 97, 133–139. doi: 10.1016/S1040-6182(02)00058-7

Liu, X. (2015). *Analysis of the Meteorological and Hydrological Charateristics in the Yarlung Zangbo River Basins*. Beijing: Tsinghua University.

Liu, X., Ren, L., Yuan, F., Xu, J., and Liu, W. (2012). Assessing vegetation response to drought in the Laohahe catchment, North China. *Hydrol. Res.* 43, 91–101. doi: 10.2166/nh.2011.134

Liu, X., Zhu, X., Pan, Y., Li, S., Liu, Y., and Ma, Y. (2016). Agricultural drought monitoring: progress, challenges, and prospects. *J. Geogr. Sci.* 26, 750–767. doi: 10.1007/s11442-016-1297-9

Liu, Z., Yao, Z., Huang, H., Wu, S., and Liu, G. (2014). Land use and climate changes and their impacts on runoff in the yarlung zangbo river basin, China. *Land Degrad. Dev.* 25, 203–215. doi: 10.1002/ldr.1159

Luo, C., Bao, X., Wang, S., Zhu, X., Cui, S., Zhang, Z., et al. (2015). Impacts of seasonal grazing on net ecosystem carbon exchange in alpine meadow on the tibetan plateau. *Plant Soil* 396, 381–395. doi: 10.1007/s11104-015-2602-6

Lv, L., Liu, X., Zhou, H., and Wu, L. (2013). Analysis on the change trend of the annual runoff in the middle-lower yarlung zangbo river. *Yellow River* 35, 27–29. doi: 10.3969/j.issn.1000-1379.2013.05.009

Mann, H. B. (1945). Non-parametric tests against trend. *Econometrica* 13, 245–259. doi: 10.2307/1907187

Martínez-Fernández, J., González-Zamora, A., Sánchez, N., and Gumuzzio, A. (2015). A soil water based index as a suitable agricultural drought indicator. *J. Hydrol.* 522, 265–273. doi: 10.1016/j.jhydrol.2014.12.051

Martínez-Fernández, J., González-Zamora, A., Sánchez, N., Gumuzzio, A., and Herrero-Jiménez, C. M. (2016). Satellite soil moisture for agricultural drought monitoring: assessment of the SMOS derived soil water deficit index. *Remote Sens. Environ.* 177, 277–286. doi: 10.1016/j.rse.2016.02.064

Massmann, A., Gentine, P., and Lin, C. (2019). When does vapor pressure deficit drive or reduce evapotranspiration? *J. Adv. Model. Earth Syst.* 11, 3305–3320. doi: 10.1029/2019MS001790

McKee, T. B., Doesken, N. J., and Kleist, J. (1993). "The relationship of drought frequency and duration to time scales," in *Eighth Conference on Applied Climatology* (Anaheim, CA: American Meteorological Society).

Mishra, A. K., and Singh, V. P. (2010). A review of drought concepts. *J. Hydrol.* 391, 202–216. doi: 10.1016/j.jhydrol.2010.07.012

Mishra, A. K., and Singh, V. P. (2011). Drought modeling-A review. *J. Hydrol.* 403, 157–175. doi: 10.1016/j.jhydrol.2011.03.049

Monteith, L. J. I. (1965). Evaporation and environment. *Symp. Soc. Exp. Biol.* 19, 205–234.

Novick, K. A., Ficklin, D. L., Stoy, P. C., Williams, A. C., Bohrer, G., Oishi, A. C., et al. (2016). The increasing importance of atmospheric demand for ecosystem water and carbon fluxes. *Nat. Clim. Chang.* 6:1023. doi: 10.1038/nclimate3114

Palmer, W. C. (1965). *Meteorological Drought*. Washington, DC:US Department of Commerce Weather Bureau.

Penman, H. L. (1948). Natural evaporation from open water, bare soil and grass. *Proc. R. Soc. London Ser. A Math. Phys. Eng. Sci.* 193, 120–145. doi: 10.1098/rspa.1948.0037

Rawson, H. M., Begg, J. E., and Woodward, R. G. (1977). The effect of atmospheric humidity on photosynthesis, transpiration and water use efficiency of leaves of several plant species. *Planta* 134, 5–10. doi: 10.1007/BF00390086

Schoppach, R., and Sadok, W. (2012). Differential sensitivities of transpiration to evaporative demand and soil water deficit among wheat elite cultivars indicate different strategies for drought tolerance. *Environ. Exp. Bot.* 84, 1–10. doi: 10.1016/j.envexpbot.2012.04.016

Schwalm, C. R., Anderegg, W. R. L., Michalak, A. M., Fisher, J. B., Biondi, F., and Koch, G., et al. (2017). Global patterns of drought recovery. *Nature* 548, 202–205. doi: 10.1038/nature23021

Shao, D., Chen, S., Tan, X., and Gu, W. (2018). Drought characteristics over China during 1980-2015. *Int. J. Climatol.* 38, 3532–3545. doi: 10.1002/joc.5515

Sheffield, J., Wood, E. F., and Roderick, M. L. (2012). Little change in global drought over the past 60 *years*. *Nature* 491, 435–438. doi: 10.1038/nature11575

Shen, M., Piao, S., Cong, N., Zhang, G., and Jassens, I. A. (2015). Precipitation impacts on vegetation spring phenology on the tibetan plateau. *Glob. Change Biol.* 21, 3647–3656. doi: 10.1111/gcb.12961

Shiru, M. S., Shahid, S., Chung, E., and Alias, N. (2019). Changing characteristics of meteorological droughts in Nigeria during 1901–2010. *Atmos. Res.* 223, 60–73. doi: 10.1016/j.atmosres.2019.03.010

Spinoni, J., Vogt, J. V., Naumann, G., Barbosa, P., and Dosio, A. (2018). Will drought events become more frequent and severe in Europe? *Int. J. Climatol.* 38, 1718–1736. doi: 10.1002/joc.5291

Teweldebirhan Tsige, D., Uddameri, V., Forghanparast, F., Hernandez, E. A., and Ekwaro-Osire, S. (2019). Comparison of meteorological- and agriculture-related drought indicators across Ethiopia. *Water* 11:2218. doi: 10.3390/w11112218

Tong, S., Lai, Q., Zhang, J., Bao, Y., and Zhang, F. (2017). Spatiotemporal drought variability on the Mongolian Plateau from 1980–2014 based on the SPEI-PM, intensity analysis and Hurst exponent. *Sci. Total Environ.* 15, 1557–1565. doi: 10.1016/j.scitotenv.2017.09.121

Van der Schrier, G., Barichivich, J., Briffa, K. R., and Jones, P. D. (2013). A scPDSI-based global data set of dry and wet spells for 1901-2009. *J. Geophys. Res. Atmos.* 118, 4025–4048. doi: 10.1002/jgrd.50355

Vicente-Serrano, S. M., Beguería, S., and López-Moreno, J. (2010). A multiscalar drought index sensitive to global warming: the standardized precipitation evapotranspiration index. *J. Clim.* 23, 1696–1718. doi: 10.1175/2009JCLI2909.1

Vicente-Serrano, S. M., Van der Schrier, G., Beguería, S., Azorin-Molina, C., and Lopez-Moreno, J. (2015). Contribution of precipitation and reference evapotranspiration to drought indices under different climates. *J. Hydrol.* 526, 42–54. doi: 10.1016/j.jhydrol.2014.11.025

Wagner, W., Hahn, S., Kidd, R., Melzer, T., Bartalis, Z., and Hasenauer, S., et al. (2013). The ASCAT soil moisture product: a review of its specifications, validation results, and emerging applications. *Meteorol. Z* 22, 5–33. doi: 10.1127/0941-2948/2013/0399

Wang, H., Vicente-serrano, S. M., Tao, F., Zhang, X., Wang, P., and Zhang, C., et al. (2016). Monitoring winter wheat drought threat in Northern China using multiple climate-based drought indices and soil moisture during 2000–2013. *Agric. For. Meteorol.* 228–229, 1–12. doi: 10.1016/j.agrformet.2016.06.004

Wang, L. (2016). *Study on Hydrochemical Characteristics and Its Influencing Factors in YarlungTsangpo River Basin*. Beijing: Institute of Geographic Sciences and Natural Resources Research, CAS.

Wells, N., Goddard, S., and Hayes, M. J. (2004). A self-calibrating Palmer Drought Severity Index. *J. Clim.* 17, 2335–2351. doi: 10.1175/1520-0442(2004)017<2335:ASPDSI>2.0.CO;2

White, D. H., and Walcott, J. J. (2009). The role of seasonal indices in monitoring and assessing agricultural and other droughts: a review. *Crop Pasture Sci.* 60:599. doi: 10.1071/CP08378

Yamamoto, R., Iwashima, T., Kazadi, S., and Hoshiai, M. (1985). Climatic jump: a hypothesis in climate diagnosis. *J. Meteorol. Soc. Jpn.* 63, 1157–1160. doi: 10.2151/jmsj1965.63.6_1157

Yang, M., Mou, Y., Meng, Y., Liu, S., Peng, C., and Zhou, X. (2020). Modeling the effects of precipitation and temperature patterns on agricultural drought in China from 1949 to 2015. *Sci. Total Environ.* 711:135139. doi: 10.1016/j.scitotenv.2019.135139

Yang, Q., Mingxing, L. I., Zheng, Z. Y., and Zhuguo, M. A. (2017). Regional applicability of seven meteorological drought indices in China. *Sci. China Earth Sci.* 147–162. doi: 10.1007/s11430-016-5133-5

You, Q., Kang, S., Wu, Y., Xu, Y., Zhang, Y., and Huang, J. (2007). Climate change over the yarlung zangbo river basin during 1961-2005. *J. Geogr. Sci.* 17, 409–420. doi: 10.1007/s11442-007-0409-y

Yu, M., Li, Q., Hayes, M. J., Svoboda, M. D., and Heim, R. R. (2014). Are droughts becoming more frequent or severe in china based on the standardized precipitation evapotranspiration index: 1951–2010? *Int. J. Climatol.* 34, 545–558. doi: 10.1002/joc.3701

Yuan, W., and Zhou, G. (2004). Theoratical study and research prospect on drought indices. *Adv. Earth Sci.* 19, 982–991. doi: 10.3321/j.issn:1001-8166.2004.06.016

Zambrano Mera, Y. E., Rivadeneira Vera, J. F., and Pérez-Martín, M. Á. (2018). Linking El niño southern oscillation for early drought detection in tropical climates: the ecuadorian coast. *Sci. Total Environ.* 643, 193–207. doi: 10.1016/j.scitotenv.2018.06.160

Zargar, A., Sadiq, R., Naser, B., and Khan, F. I. (2011). A review of drought indices. *Environ. Rev.* 19, 333–349. doi: 10.1139/a11-013

Zeng, Q. (1974). *The Principle of Atmospheric Infrared Remote Sensing*. Beijing:Science Press.

Zeng, Z., Wu, W., Zhou, Y., Li, Z., Hou, M., and Huang, H. (2019). Changes in reference evapotranspiration over Southwest China during 1960–2018: attributions and implications for *drought*. *Atmosphere* 10:705. doi: 10.3390/atmos10110705

Zhai, J., Su, B., Krysanova, V., Vetter, T., Gao, C., and Jiang, T. (2010). Spatial variation and trends in PDSI and SPI indices and their relation to streamflow in 10 large regions of China. *J. Clim.* 23, 649–663. doi: 10.1175/2009JCLI2968.1

Zhai, P., Zhou, B., and Chen, Y. (2018). A review of climate change attribution studies. *J. Meteorol. Res.* 32, 671–692. doi: 10.1007/s13351-018-8041-6

Zhang, B., AghaKouchak, A., Yang, Y., Wei, J., and Wang, G. (2019a). A water-energy balance approach for multi-category drought assessment across globally diverse hydrological basins. *Agric. For. Meteorol.* 264, 247–265. doi: 10.1016/j.agrformet.2018.10.010

Zhang, D., Zhang, L., Yang, J., and Feng, G. (2010). The impact of temperature and precipitation variation on drought in China in last 50 years. *Acta Phys. Sin.* 59, 655–663. doi: 10.7498/aps.59.655

Zhang, Q., Fan, K., Sing, V. P., Song, C., Xue, C., and Sun, P. (2019b). Is Himalayan-Tibetan Plateau "drying"? *Historical estimations and future trends of surface soil moisture. Sci. Total Environ.* 658, 374–384. doi: 10.1016/j.scitotenv.2018.12.209

Zhang, Q., Kong, D., Singh, V. P., and Shi, P. (2017). Response of vegetation to different time-scales drought across China: spatiotemporal patterns, causes and implications. *Glob. Planet. Change* 152, 1–11. doi: 10.1016/j.gloplacha.2017.02.008

Zhang, Q., Yu, H. Q., Sun, P., Singh, V. P., and Shi, P. (2019c). Multisource data based agricultural drought monitoring and agricultural loss in China. *Glob. Planetary Change* 172, 298–306. doi: 10.1016/j.gloplacha.2018.10.017

Zhao, F. F., Xu, Z. X., Huang, J. X., and Li, J. Y. (2008). Monotonic trend and abrupt changes for major climate variables in the headwater catchment of the yellow river basin. *Hydrol. Process.* 22, 4587–4599. doi: 10.1002/hyp.7063

Zhou, S., Wang, J., Xu, L., Wang, X., Colgan, P. M., and Mickelson, D. M. (2010). Glacial advances in southeastern tibet during late quaternary and their implications for climatic changes. *Quat. Int.* 218, 58–66. doi: 10.1016/j.quaint.2009.11.026

Zhou, S., Williams, A. P., Berg, A. M., Cook, B. I., Zhang, Y., Hagemann, S., et al. (2019a). Land-atmosphere feedbacks exacerbate concurrent soil drought and atmospheric aridity. *Proc. Natl. Acad. Sci. U.S.A.* 116, 18848–18853. doi: 10.1073/pnas.1904955116

Zhou, S., Zhang, Y., Park, W. A., and Gentine, P. (2019b). Projected increases in intensity, frequency, and terrestrial carbon costs of compound drought and aridity events. *Sci. Adv.* 5:u5740. doi: 10.1126/sciadv.aau5740

Zhu, Q., Luo, Y., Xu, Y., Tian, Y., and Yang, T. (2019). Satellite soil moisture for agricultural drought monitoring: assessment of SMAP-derived soil water deficit index in xiang river basin, China. *Remote Sens.* 11:362. doi: 10.3390/rs11030362

Zhu, Y., Liu, Y., Ma, X., Ren, L., and Singh, V. (2018). Drought analysis in the yellow river basin based on a short-scalar palmer drought severity index. *Water* 10:1526. doi: 10.3390/w10111526

Conflict of Interest: The authors declare that the research was conducted in the absence of any commercial or financial relationships that could be construed as a potential conflict of interest.

frontiers in Earth Science

BRIEF RESEARCH REPORT
published: 17 July 2020
doi: 10.3389/feart.2020.00225

Modeling Downward Groundwater Leakage Rate to Evaluate the Relative Probability of Sinkhole Development at an Under-Construction Expressway and Its Vicinity

*Han Xiao and Haiming Li**

Department of Environmental Sciences, College of Marine and Environmental Sciences, Tianjin University of Science and Technology, Tianjin, China

Sinkhole development has been recognized as a major geohazard, as sinkholes pose great threats to infrastructure, such as buildings, roads, bridges, and pipelines, resulting in huge financial losses to society. Previous studies indicated that the spatial density of sinkholes increases linearly with the downward groundwater leakage rate (DGLR) (inter-aquifer flow rate from an unconfined to a confined aquifer through the aquitard between them) and that the spatial variation of annual-average DGLR is a useful indicator of the relative probability of sinkhole development. In this study, a groundwater flow model using the MODFLOW computer code was developed and calibrated to simulate the spatial variation of annual-average DGLR to evaluate the relative probability of sinkhole development at an under-construction expressway and its vicinity. The results indicated that the expressway construction site has a relatively high probability of sinkhole development in the designed range of the pavement structures, and it is concluded that engineering action should be taken in advance to minimize potential sinkhole hazards.

Keywords: groundwater modeling, MODFLOW, leakage rate, relative probability, sinkhole development

OPEN ACCESS

Edited by:
Xingcai Liu,
Chinese Academy of Sciences, China

Reviewed by:
Lizhi Zheng,
Tianjin Normal University, China
Derek Wu,
Memorial University of Newfoundland, Canada

****Correspondence:***
Haiming Li
Lhm@tust.edu.cn

Specialty section:
This article was submitted to Hydrosphere, a section of the journal Frontiers in Earth Science

Received: *08 March 2020*
Accepted: *27 May 2020*
Published: *17 July 2020*

Citation:
Xiao H and Li H (2020) Modeling Downward Groundwater Leakage Rate to Evaluate the Relative Probability of Sinkhole Development at an Under-Construction Expressway and Its Vicinity. Front. Earth Sci. 8:225. doi: 10.3389/feart.2020.00225

INTRODUCTION

The major landforms known as cover-collapse and cover-suffosion sinkholes (abbreviated as "sinkholes" in the following text) have been identified as the primary geohazards in central Florida (United States) since the 1950s and have resulted in large financial losses to society, especially in populated cities, due to the catastrophic damage they cause to buildings, roads, bridges, and pipelines (Maroney et al., 2005; Lindsey et al., 2010; Brinkmann, 2013; Kuniansky et al., 2015). Sinkholes were identified statewide by field surveys and geomorphological mapping from 1950 to 2014 and are recorded in a downloadable subsidence incident report database created by the Florida Geological Survey (one of the divisions of Florida Department of Environmental Protection). In spite of drawbacks such as under-reporting of sinkholes in rural areas, the subsidence incident report database has been validated to be the most complete, accurate, and representative sinkhole inventory statewide (Brinkmann et al., 2008; Fleury et al., 2008), and previous studies regarding sinkhole research in Florida have been developed through the use of these data.

In central Florida mantled (buried) karst terrains, the reported sinkholes are not evenly distributed: some areas have many, while others have none (Gray, 2014). The underlying cause of sinkhole formation is limestone dissolution/removal by infiltrated weakly acidic rainwater (dissolution/removal rate extremely slow; as little as millimeters per thousand years), and the major triggering factors include heavy rainfall, rapid decline of potentiometric level due to groundwater over-exploitation, and high rate of downward groundwater leakage (Beck, 1986; Ford and Williams, 2007; Brinkmann and Parise, 2009; Gutiérrez et al., 2014). Here, downward groundwater leakage rate (DGLR) refers to inter-aquifer flow rate from an overlying unconfined aquifer to an underlying confined aquifer through an aquitard (see the black arrow in **Figure 1**). Jammal (1982) found that the sinkholes reported in Winter Park in central Florida are more likely to form at the beginning of the wet season when DGLR rises to its annual highs. Wilson and Beck (1992) pointed out that the reported uneven distribution of sinkholes in the greater Orlando area in central Florida might be attributed to spatial variation in annual-average DGLR. Xiao et al. (2016, 2018) conducted statistical analyses of the relationships between the spatial distribution of reported sinkholes and the spatial variation of annual-average DGLR in central Florida and found that sinkholes are likely to occur in those areas that have higher DGLR since sinkhole spatial density increases linearly with DGLR. Based on these findings, spatial variation of annual-average DGLR has been recognized as a useful indicator of the relative probability of sinkhole development in central Florida. The main limitation to quantifying it analytically in the central Florida sinkhole-prone areas is a lack of observed data, since local-scale groundwater observation systems have not been installed ubiquitously, and monitoring work has not been conducted routinely. Due to the recent rapid development of high-speed computers and simulation codes (Zhou and Li, 2011; Anderson et al., 2015), however, groundwater models have been successfully applied in many case studies worldwide for quantifying DGLR numerically (Sanford, 2002; Scanlon et al., 2002; Chitsazan and Movahedian, 2015; Mali and Singh, 2016; Sahoo and Jha, 2017), and these can be adopted to evaluate the relative probability of sinkhole development in central Florida.

The objective of this study is to evaluate the relative probability of sinkhole development at an under-construction expressway and its vicinity in northern Orlando, central Florida (United States), based on spatial variation of annual-average DGLR quantified by developing a groundwater model using the MODFLOW computer code, aiming at (1) providing a good reference for determination of whether the expressway construction site and its vicinity are at risk for sinkhole development, (2) providing a warning that immediate action (from engineering perspectives) should be taken in advance to minimize the hazards of sinkhole development at the designed range of the pavement structures, and (3) providing knowledge and understanding of sinkhole development in central Florida mantled karst terrains for engineers/technicians working in the field of sinkhole hazards, as well as for residents dwelling in sinkhole-prone areas.

OVERVIEW OF THE STUDY AREA

The study area, shown in **Figure 1**, is an under-construction expressway (see the solid white line) that connects two important state roads (SR46 and SR 429) (see the black dot-dash line) and its vicinity in northern Orlando (see the red star), central Florida (United States). The boundaries of the area are either parallel or perpendicular to the water table contours generated by the output from the north-central Florida groundwater flow model (St. Johns River Water Management District), and regional groundwater flow directions are from southwest to northeast and southeast (see the light green arrows). The land surface elevations vary from 5 to 30 m [NAVD88], with a regional average of approximately 16-17 m [NAVD88]. The study area has a subtropical and humid climate with humid/hot summers (mean maximum temperatures exceeding 30°C) and dry/mild winters (mean minimum temperatures dropping below 10°C) with mean annual rainfall varying from 1200 to 1300 mm (wet season from June to October and dry season from November to May) (Tibbals, 1990). The hydrostratigraphic units shown in **Figure 1** consist of (from top to bottom) the (unconfined) surficial aquifer, the upper confining unit (aquitard), the (confined) Floridan aquifer, and the lower confining unit (aquiclude); detailed descriptions of their characteristics can be found in Miller (1986) and Williams and Kuniansky (2016). The surficial aquifer (thickness varying from 5 to 15 m) is primarily composed of medium to medium dense sand with moderate transmissivity. The Floridan aquifer (thickness varying from 600 to 650 m) is primarily composed of limestone/dolomite with high transmissivity (varying from 500 to 100,000 m^2/day) since it is highly karstified, with sinkholes, sinking streams, and springs present over most of its extent. The upper confining unit (thickness varying from 20 to 25 m) is primarily composed of clay, silty clay, and sandy clay with relatively low permeability, which limits inter-aquifer flow from/to the overlying surficial aquifer to/from the underlying Floridan aquifer.

NUMERICAL MODELING

A groundwater model was developed to quantify spatial variation in annual-average DGLR to evaluate the relative probability of sinkhole development at the under-construction expressway and its vicinity, and the groundwater model developed was calibrated using the trial-and-error method by adjusting the values of horizontal/vertical hydraulic conductivities until the simulated groundwater levels and spring discharges matched the field-measurements to a satisfactory degree. Note that groundwater flow within the study area was assumed to be matrix flow, and local-scale conduit flow conditions were not considered, since the locations/dimensions of the subsurface cavities/voids,

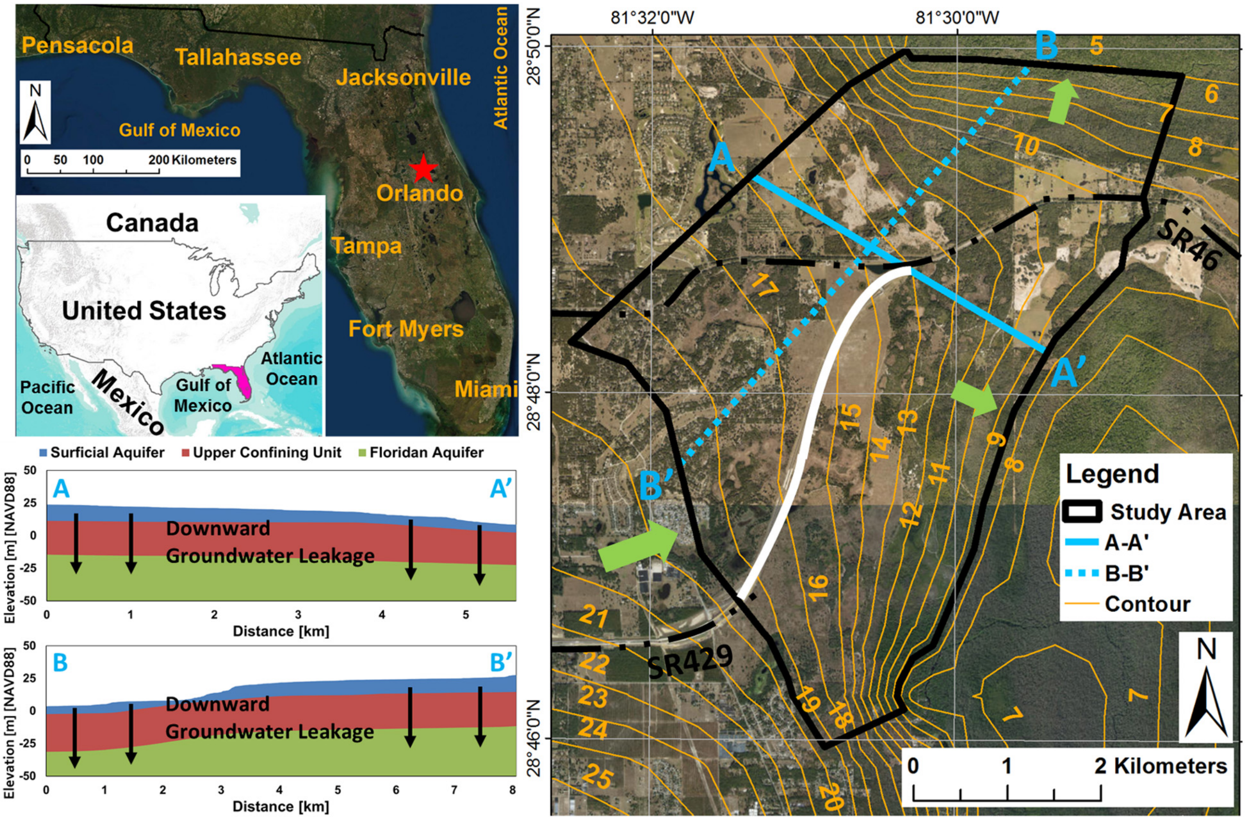

FIGURE 1 | Location of the study area and cross-sections A–A' and B–B' showing the hydrostratigraphic units (the bottom of the Floridan aquifer is much deeper than −50 m).

sinking streams, and springs were unknown due to lack of geophysical surveys.

Simulation Code

The MODFLOW computer code developed and released by the US Geological Survey was selected to develop the groundwater model in this study. MODFLOW was developed based on the concept of mass balance and Darcy's Law and is primarily utilized to simulate 3D constant-density groundwater flow through porous media (Harbaugh and McDonald, 1996). The governing equation is described in partial differential form:

$$\frac{\partial}{\partial x}\left(K_{xx}\frac{\partial h}{\partial x}\right)+\frac{\partial}{\partial y}\left(K_{yy}\frac{\partial h}{\partial y}\right)+\frac{\partial}{\partial z}\left(K_{zz}\frac{\partial h}{\partial z}\right)+W=S_s\frac{\partial h}{\partial t}$$

where, K_{xx}, K_{yy}, and K_{zz} are values of hydraulic conductivity along the x, y, and z axes (L/T), h is the potentiometric head (L), W is a volumetric flux per unit volume representing sources and/or sinks of water (T^{-1}), S_s is the specific storage of the porous material (L^{-1}), and t is time (T).

Spatial and Temporal Discretization

Spatially, the model domain was horizontally discretized into 248 rows and 218 columns with a uniform grid spacing of 30 m in both the x and y directions and was vertically divided into three layers, with Layer 1 representing the surficial aquifer, Layer 2 representing the upper confining unit, and Layer 3 representing the Floridan aquifer. The top elevations of Layers 1, 2, and 3 are shown in **Figures 2A–C**, and the bottom elevations of Layer 3 are shown in **Figure 2D**.

Temporally, the model was steady-state under long-term annually averaged hydrologic and hydrogeologic conditions.

Parameters

For Layer 1, values of 30 m/day, 3 m/day, and 0.2 were assigned to horizontal hydraulic conductivity, vertical hydraulic conductivity, and porosity, respectively. For Layer 2, values of 0.01 m/day, 0.01 m/day, and 0.3 were assigned to horizontal hydraulic conductivity, vertical hydraulic conductivity, and porosity, respectively. For Layer 3, values of 600 m/day, 60 m/day, and 0.4 were assigned to horizontal hydraulic conductivity, vertical hydraulic conductivity, and porosity, respectively (Motz et al., 1995). Note that these values representing the characteristics of each layer were adjusted during the model calibration process.

Boundary Conditions

For Layer 1, general-head, no-flow, recharge, and evapotranspiration boundaries were assigned (**Figure 2E**). The

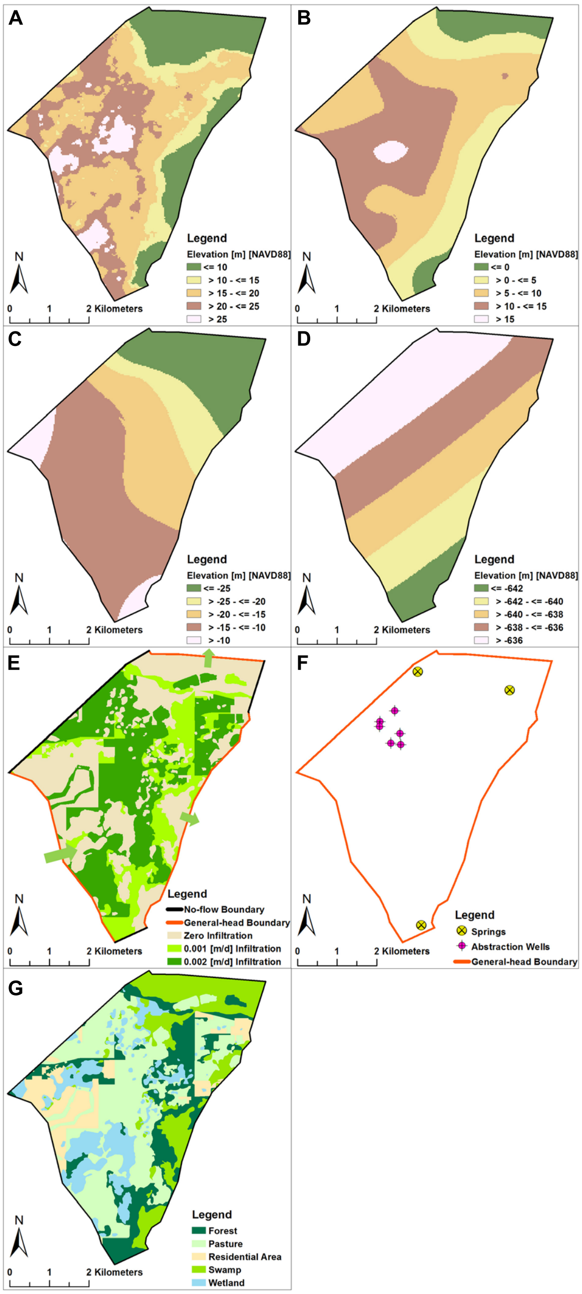

FIGURE 2 | (A) Top elevations of Layer 1 (modified after US Geological Survey National Elevation Dataset); **(B)** top elevations of Layer 2 (modified after Williams and Kuniansky, 2016); **(C)** top elevations of Layer 3 (modified after Williams and Kuniansky, 2016); **(D)** bottom elevations of Layer 3 (modified after Williams and Kuniansky, 2016); **(E)** boundary conditions assigned to Layer 1; **(F)** boundary conditions assigned to Layer 3; **(G)** map of land use and land cover (modified from the GIS database maintained by St. Johns River Water Management District).

lateral boundaries that are parallel to the water table contours where groundwater flows into or out of the model domain were designated general-head boundaries. The lateral boundaries that are perpendicular to the water table contours where groundwater flux is zero were designated no-flow boundaries. The top of Layer 1 for representing infiltrated rainwater and groundwater evapotranspiration were designated recharge and evapotranspiration boundaries, respectively. Infiltrated rainwater was calculated by rainfall and infiltration/rainfall ratio (dependent on land use and land cover, which are shown in **Figure 2G**), and evapotranspiration rate was calculated by potential evapotranspiration rate.

Layer 2 was assigned a no-flow boundary.

For Layer 3, general-head, no-flow, well, and drain boundaries were assigned (**Figure 2F**). The criteria for designating a boundary as general-head or no-flow were exactly the same as above and are not repeated here. A well boundary was assigned at abstraction wells, and a drain boundary was assigned at springs.

Initial Conditions

Initial heads were estimated based on the water table contours shown in **Figure 1**.

RESULTS AND INTERPRETATION

Calibration

As mentioned above, the model was calibrated using the trial-and-error method by adjusting the values of the horizontal/vertical hydraulic conductivities within a reasonable range until the simulated groundwater levels and spring discharges matched the field measurements to a satisfactory degree (**Figure 3A**). The field-measurements included: (1) the observation well (L-1020) that monitors potentiometric levels; (2) the observation station that monitors Mt. Plymouth Lake stages; (3) the observation stations that monitor the Droty Spring, Snail Spring, and Sulphur Spring discharges. Note that the time range of the observed groundwater levels and spring discharges is from 2010 to 2016, and the annual-average values are computed to serve as calibration targets since the temporal discretization of the groundwater flow model is steady-state.

DGLR and Relative Probability of Sinkhole Development

Based on the output from the calibrated model, the spatial variations of annual-average water tables, potentiometric levels, and DGLR are shown in **Figures 3B–D**, respectively. It can be observed that: (1) water tables are higher in the southwest and central portion and lower in the northeast and east portion (partly consistent with the topographic changes shown in **Figure 2A**); (2) potentiometric levels are higher in the southwest portion and lower in the northeast portion; (3) DGLR values are higher in the southwest and central portion and lower in the north, northeast, and east portion. Based on the simulated annual-average DGLR, the relative probabilities of sinkhole development were identified as low (DGLR $\leq$ 50 mm/year), intermediate low (DGLR $>$ 50 mm/year but $\leq$ 100 mm/year), intermediate-high (DGLR $>$ 100 mm/year but $\leq$ 150 mm/year), and high (DGLR $>$ 150 mm/year), and spatial variation of relative probability of sinkhole development is shown in **Figure 4A**. Note

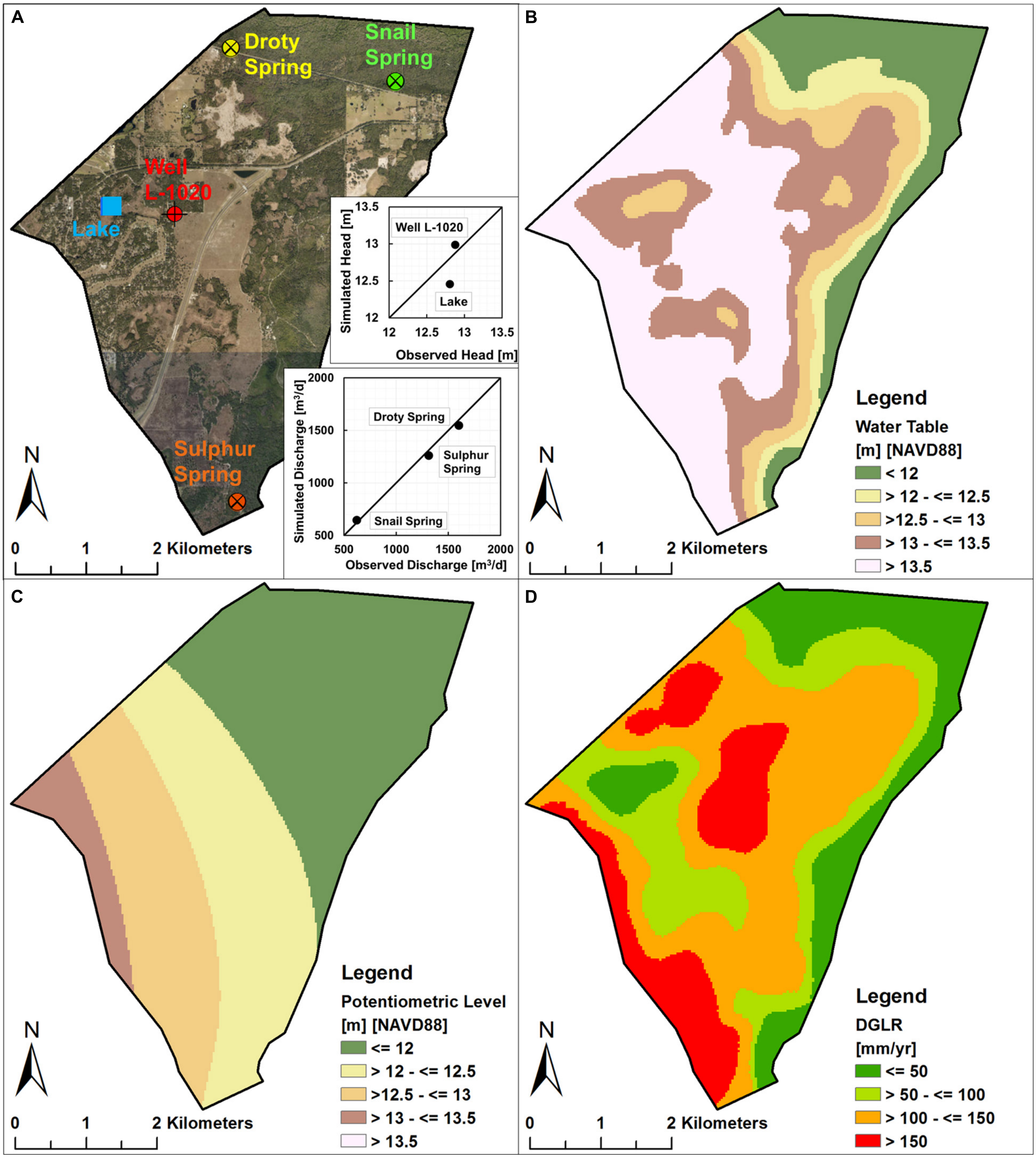

FIGURE 3 | (A) Locations of field-measurements (modified from the GIS database maintained by St. Johns River Water Management District) and scatter diagram showing the goodness of fit between the observed and simulated heads and spring discharges; **(B)** spatial variation of simulated water tables; **(C)** spatial variation of simulated potentiometric levels; **(D)** spatial variation of simulated DGLR.

that the locations of reported sinkholes (recorded by subsidence incident reports provided by the Florida Geological Survey) within the study area are also shown on **Figure 4A** (black dots). It can be observed that most of the reported sinkholes are located within areas where relative probability was classified as "high," and the remaining ones are located within areas where relative probability was classified as "intermediate high," indicating that the approach of using annual-average DGLR to identify the relative probability of sinkhole development in the study area is valid.

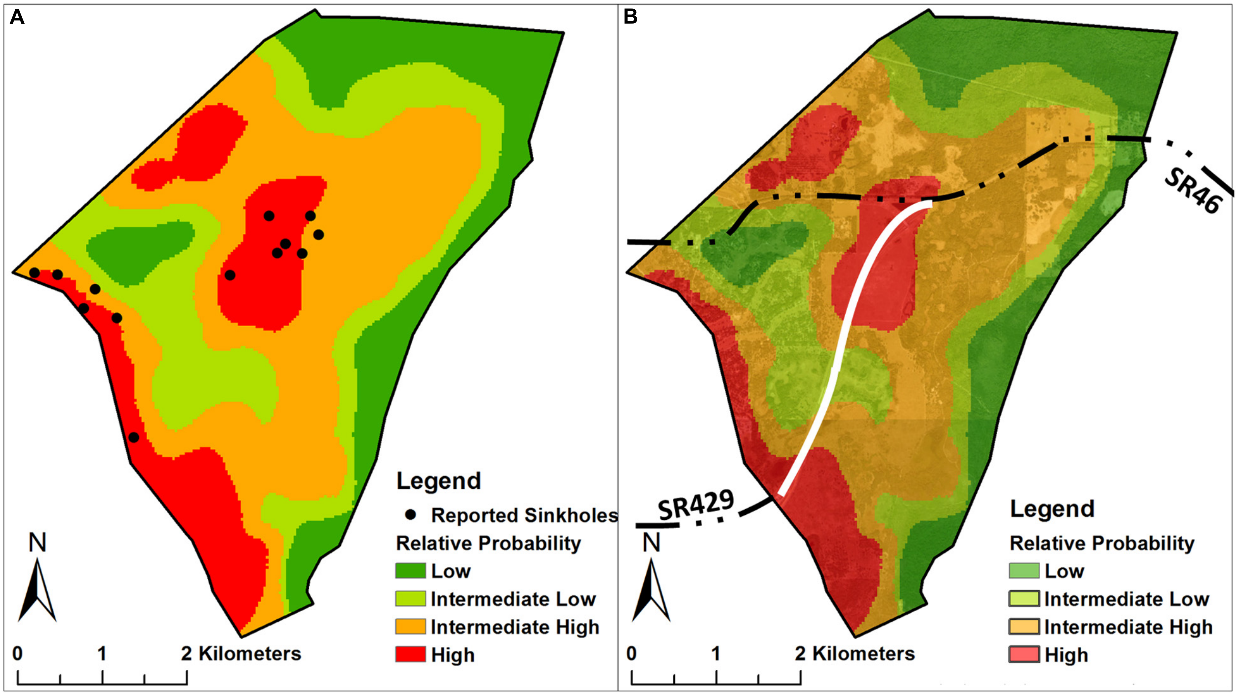

FIGURE 4 | (A) Spatial variation of the relative probability of sinkhole development and locations of reported sinkholes; **(B)** relative probability of sinkhole development at the under-construction expressway (see the solid white line) and its vicinity.

The relative probabilities of sinkhole development at the under-construction expressway and its vicinity are shown in **Figure 4B**. It can be observed that more than half of the under-construction expressway (see the solid white line) is located within areas where the relative probability of sinkhole development was classified as "high" or "intermediate high," indicating that engineering action (e.g., bridging over the "dangerous" areas) should be taken in advance to minimize the potential hazards of sinkhole development within the designed range of the pavement structures.

DISCUSSION

The simulated DGLR output from the developed/calibrated groundwater model can be used to generate a sinkhole susceptibility zonation map of the study area, and **Figure 4B** is a good example of such, serving as a useful indicator of the relative probability of sinkhole development. The development of regional- and local-scale groundwater models can contribute to the implementation of sinkhole warning systems to (1) help engineers and technicians to minimize the ground stability problems caused by sinkholes, (2) provide an information source for insurance companies and the public, and (3) implement a broad research platform for researchers.

There are some limitations to this study, along with a certain degree of uncertainty associated with simulation results. Firstly, this study ignored heterogeneity of the aquifer systems, which simplifies model implementation but sacrifices local-scale simulation accuracy. The spatial variations in hydrogeologic parameters are unknown due to lack of borehole data and pumping test data, and the aquifer systems are considered to be homogenous, with uniform values initially assigned to all model grid cells expected to be adjusted during calibration. Secondly, this study ignored local-scale conduit flow within the aquifer systems. The locations and dimensions of subsurface voids/conduits are unknown due to lack of geophysical surveys, and the real local-scale groundwater flow rate and directions may deviate from the simulated results. Thirdly, the spatial discretization is relatively "coarse" (30 m × 30 m). Finer spatial discretization would indeed improve computing accuracy and make model results more reliable and precise, especially as regards the hydraulic gradient at those areas where topographic change are huge and groundwater pumping rates are high. However, numerical instability is one of the problems that numerical simulations generally encounter. In order to lower the risk of numerical instability and maintain a reasonable computation runtime, one has to sacrifice computing accuracy to some extent. Fourthly, local-scale simulation results have uncertain range, since there is insufficient monitoring data on groundwater levels.

Note that evaluation of the relative probability of sinkhole development in this study is based on the finding that sinkholes are likely to occur in those areas that have higher DGLR. This finding has been demonstrated to be true in central Florida karst terrains in that it is developed based on local karst conditions, but it has not yet been verified in other places. In fact, the processes of sinkhole development are complicated and can be affected by multiple hydrological, geological, and geochemical factors such as heavy rainfall, rapid decline of groundwater level, thickness and composition of overburden sediments, surface loading, and subsurface transport of dissolved carbon dioxide. It is hard to tell whether DGLR would be the dominant factor affecting sinkhole development in other karst areas. To eliminate the geographical bias of this approach, future work would be extended to involve more impact factors to implement complex sinkhole development warning systems that can be applied for other vulnerable karst areas in west-central and north-central Florida.

SUMMARY

In this study, a groundwater model using the MODFLOW computer code was developed and calibrated against field-measured groundwater levels and spring discharges to quantify annual-average DGLR for the purpose of evaluating the relative probability of sinkhole development at an under-construction expressway (built to connect two important state roads, SR46 and SR 429) and its vicinity in the central Florida sinkhole-prone area. It was indicated that most of the expressway construction site has a relatively high probability of sinkhole development and that engineering action (e.g., bridging over the "dangerous" areas) should be taken in advance to minimize potential sinkhole hazards.

DATA AVAILABILITY STATEMENT

The datasets generated for this study are available on request to the corresponding author.

AUTHOR CONTRIBUTIONS

Both authors listed have made a substantial, direct and intellectual contribution to the work, and approved it for publication.

FUNDING

This research was partly supported by the Youth Program of the Natural Science Foundation of Tianjin (19JCQNJC08400), the Start-up Grant from Tianjin University of Science & Technology, and the Young Talent Fund of College of Marine and Environmental Sciences of TUST.

ACKNOWLEDGMENTS

We thank Dr. Boo Hyun Nam and Dr. Dingbao Wang from the University of Central Florida (United States) for sharing their experiences and advice. We also thank the US Geological Survey, Florida Geological Survey, and St. Johns River Water Management District for providing data. The opinions, findings, and conclusions expressed in this manuscript were those of the authors and are not necessarily those of these agencies.

REFERENCES

Anderson, M. P., Woessner, W. W., and Hunt, R. J. (2015). *Applied Groundwater Modeling: Simulation of Flow and Advective Transport*, 2nd Edn. Amsterdam: Elsevier.

Beck, B. F. (1986). A generalized genetic framework for the development of sinkholes and Karst in Florida. USA. *Environ. Geol. Water Sci.* 8, 5–18. doi: 10.1007/bf02525554

Brinkmann, R. (2013). *Florida Sinkholes: Science and Policy*. Gainesville, FL: University Press of Florida.

Brinkmann, R., and Parise, M. (2009). The timing of sinkhole formation in Tampa and Orlando. Florida. *Florida Geographer.* 41, 22–38.

Brinkmann, R., Parise, M., and Dye, D. (2008). Sinkhole distribution in a rapidly developing urban environment: hillsborough county, Tampa Bay area, Florida. *Eng. Geol.* 99, 169–184. doi: 10.1016/j.enggeo.2007.11.020

Chitsazan, M., and Movahedian, A. (2015). Evaluation of artificial recharge on groundwater using MODFLOW model (case study: Gotvand Plain-Iran). *J. Geosci. Environ. Prot.* 3, 122–132. doi: 10.4236/gep.2015.35014

Fleury, E. S., Carson, S., and Brinkmann, R. (2008). Testing reporting bias in the Florida Sinkhole Database: an analysis of sinkhole occurrences in the Tampa metropolitan statistical area. *Southeast. Geogr.* 48, 38–52. doi: 10.1353/sgo.0.0012

Ford, D. C., and Williams, P. (2007). *Karst Hydrogeology and Geomorphology*. Chichester: Wiley.

Gray, K. M. (2014). *Central Florida sinkhole evaluation. Technical Publication, Florida Department of Transportation*. District 5 Materials & Research.

Gutiérrez, F., Parise, M., De Waele, J., and Jourde, H. (2014). A review on natural and human-induced geohazards and impacts in karst. *Ear. Sci. Review* 138, 61–88. doi: 10.1016/j.earscirev.2014.08.002

Harbaugh, A. W., and McDonald, M. G. (1996). *User's Documentation for MODFLOW-96 – An Update to the U.S. Geological Survey Modular Finite-Difference Groundwater Flow Model*, Open-File Report 96-485 (Reston, VA: USGS).

Jammal, S. E. (1982). *The Winter Park Sinkhole and Central Florida Sinkhole Type Subsidence*. Winter Park, FL: Jammal and Associates, Inc.

Kuniansky, E. L., Weary, D. J., and Kaufmann, J. E. (2015). The current status of mapping karst areas and availability of public sinkhole-risk resources in karst terrains of the United States. *Hydrogeol. J.* 24, 613–624. doi: 10.1007/s10040-015-1333-3

Lindsey, B. D., Katz, B. G., Berndt, M. P., Ardis, A. F., and Skach, K. A. (2010). Relations between sinkhole density and anthropogenic contaminants in selected carbonate aquifers in the eastern Unites States. *Environ. Earth Sci.* 60, 1073–1090. doi: 10.1007/s12665-009-0252-9

Mali, S. S., and Singh, D. K. (2016). Groundwater modeling for assessing the recharge potential and water tablebehaviour under varying levels of pumping and recharge. *Indian J. Soil Conserv.* 44, 93–102.

Maroney, P. F., Cole, C. R., Corbett, R. B., Dumm, R. E., Eastman, K. L., Gatzlaff, K. M., et al. (2005). *Final Report: Insurance Study of Sinkholes*, Florida: Florida State Univ.

Miller, J. A. (1986). "Hydrogeologic framework of the Floridan aquifer system in Florida and in parts of Georgia, Alabama, and South Carolina," *Paper Presented U.S. Geological Survey Professional Paper 1403-B*. (Reston, VA: USGS).

Motz, L. H., Beddow, I. I. W. D., Caprara, M. R., Gay, J. D., and Sheaffer, S. M. (1995). *North-Central Florida Regional Ground-Water Investigation and Flow Model (Final Report)*, (Gainesville, FL: University of Florida).

Sahoo, S., and Jha, M. K. (2017). Numerical groundwater-flow modeling to evaluate potential effects of pumping and recharge: implications for sustainable groundwater management in the Mahanadi delta region. India. *Hydrogeol. J.* 25, 2489–2511. doi: 10.1007/s10040-017-1610-4

Sanford, W. (2002). Recharge and groundwater models: an overview. *Hydrogeol. J.* 10, 110–120. doi: 10.1007/s10040-001-0173-5

Scanlon, B. R., Healy, R. W., and Cook, P. G. (2002). Choosing appropirate techniques for quanfitying groundwater recharge. *Hydrogeol. J.* 10, 18–39. doi: 10.1007/s10040-001-0176-2

Tibbals, C. H. (1990). "Hydrology of the Floridan aquifer system in east-central Florida – regional aquifer system analysis – Floridan aquifer system," *Paper Presented U.S Geological Survey Professional Paper 1403-E*. (Gainesville, FL: University of Florida)

Williams, L. J., and Kuniansky, E. L. (2016). "Revised hydrogeologic framework of the Floridan aquifer system in Florida and parts of Georgia, Alabama, and South Carolina" *Paper Presented U.S. Geological Survey Professional Paper 1807*. (Gainesville, FL: University of Florida).

Wilson, W. L., and Beck, B. F. (1992). Hydrogeologic factors affecting new sinkhole development in the Orlando area. Florida. *Groundwater* 30, 918–930. doi: 10.1111/j.1745-6584.1992.tb01575.x

Xiao, H., Kim, Y. J., Nam, B. H., and Wang, D. (2016). Investigation of the impacts of local-scale hydrogeologic conditions on sinkhole occurrence in East-Central Florida, USA. *Environ. Earth Sci.* 75, 1274–1289.

Xiao, H., Li, H., and Tang, Y. (2018). Assessing the effects of rainfall, groundwater downward leakage, and groundwater head differences on the development of cover-collapse and cover-suffosion sinkholes in central Florida (USA). *Sci. Total. Environ.* 644, 274–286. doi: 10.1016/j.scitotenv.2018.06.273

Zhou, Y., and Li, W. (2011). A review of regional groundwater flow modeling. *Geosci. Front.* 2, 205–214. doi: 10.1016/j.gsf.2011.03.003

Conflict of Interest: The authors declare that the research was conducted in the absence of any commercial or financial relationships that could be construed as a potential conflict of interest.

frontiers
in Earth Science

ORIGINAL RESEARCH
published: 06 October 2020
doi: 10.3389/feart.2020.541664

Modeling Water Allocation under Extreme Drought of South-to-North Water Diversion Project in Jiangsu Province, Eastern China

Chunfen Zeng[1]*, Jingsong Ma[2], Minglin Cao[2], Chen Xu[3], Wanyu Qi[1] and Lachun Wang[2]*

[1] Key Laboratory of Surface Processes and Environment Remote Sensing in the Three Gorges Reservoir Area, School of Geography and Tourism, Chongqing Normal University, Chongqing, China, [2] School of Geographic and Oceanographic Sciences, Nanjing University, Nanjing, China, [3] Multi-scale Land Surface Hydrology Laboratory, Department of Civil and Environmental Engineering, Voiland College of Engineering and Architecture, Washington State University, Pullman, WA, United States

OPEN ACCESS

Edited by:
Xingcai Liu,
Chinese Academy of Sciences, China

Reviewed by:
Danlu Guo,
The University of Melbourne, Australia
Xiaofan Zeng,
Huazhong University of Science and Technology, China

***Correspondence:**
Lachun Wang
wang6312@263.net.cn
Chunfen Zeng
cfzeng18@163.com

Specialty section:
This article was submitted to Hydrosphere, a section of the journal Frontiers in Earth Science

Received: *10 March 2020*
Accepted: *01 September 2020*
Published: *06 October 2020*

Citation:
Zeng C, Ma J, Cao M, Xu C, Qi W and Wang L (2020) Modeling Water Allocation under Extreme Drought of South-to-North Water Diversion Project in Jiangsu Province, Eastern China. Front. Earth Sci. 8:541664. doi: 10.3389/feart.2020.541664

Along with China's economic development and social progress, water scarcity has become increasingly challenging. Optimized allocation of water resources, especially through water transfer project, is one of the important approaches to mitigate water shortages. In this study, authors built a model of water resources allocation simulation and the microcosmic configuration based on a complex water network in the east route of the South-to-North Water Transfer Project in Jiangsu Province, east China. Selecting data from the typical years with assurance rates of P = 95%, 75%, and 50%, the simulation of supply and demand of water resources under the present situation and the tapping scenario of planning project was carried out. The results showed that water supply capacity increased while water deficits decreased remarkably for the diversion projects. Under the assurance rates of P = 95%, 75%, and 50%, the rate of water shortage decreased by 10.3%, 8.0%, and 5.2%, respectively. Under the planning work situation, the amount of water increased by 2,800 million m^3 even during the period of extreme drought. Based on the results, it also provided an effective plan for the hydraulic engineering to optimize the allocation and management of water resources. It is helpful for policy makers to mitigate water shortage in Jiangsu Province and other areas with water transfer projects in China and other countries.

Keywords: water transfer system simulation, water resources allocation modeling, water supply and demand, South-to-North Water Transfer Project, extreme drought

INTRODUCTION

Water is one of the most important resources for human survival and development. As the second largest economic body with dramatically increasing water demand, China has been suffering water scarcity, uneven spatiotemporal distribution, and low utilization. Water allocation has great significance on easing the contradiction between the supply and demand of water resources and promoting regional socioeconomic development (Wada, et al., 2014; Nazemi and Wheater, 2015). Water resources allocation involves several aspects such as engineering, finance, technology, and management (Xu, et al., 2013; Li M, et al., 2015; Zhong et al., 2015). In this modeling, through engineering and nonengineering measures, advices are given for allocation of the limited water resources of different forms in a certain area to meet the water demand of various levels, objectives, and water use.

Studies on optimized allocation of water resources started in the early 1960s. A large number of studies on the theory and application of water resources emerged with mathematics (Li M, et al., 2015), computer technology (Xu et al., 2001; Yao et al., 2018), large-scale reservoirs (Li C, et al., 2015), multiobjective optimization (Li et al., 2017), and the increasing prominent contradiction of supply and demand for water (Wang, 2006; Abed Elmdoust and Kerachian.2013).Among them, many scholars actively studied optimized allocation of water resources with the South-to-North Water Transfer Project (Yang et al., 2007; Sang et al., 2018; Liu et al., 2020). The South-to-North Water Diversion Project is a major strategic project to alleviate the serious shortage of water resources in North China. It is divided into three lines: east, central, and west. Among them, the eastern route of the South-to-North Water Diversion Project is a state-level transprovincial regional project that transports water from Jiangdu Water Conservancy Project in Yangzhou, Jiangsu, through Jiangsu, Shandong, and Hebei provinces to North China. Of the related study, self-optimization simulation model technical program is widely used in the water transfer project under a macroscopic scale because of its succinct and compact hierarchical structure, fast convergence rate, and so on. Wang et al. (2001) set up the three-level hierarchical model. The principle and methods of hierarchical analysis for this large-scale system are applied to solve the problems of optional water operation for the middle route of the South-to-North Water Diversion Project. On the fulfillment of the total system water supply objects, the optimal regulation diagram of the reservoir is determined via simulation technique combined with the optimization methods. In addition, considering the problems that occurred in the process of large-scale water transfer, some scholars constructed the South-to-North Water Transfer Project water allocation simulation system and water-scheduling model with modern computer simulation technology (Zhao et al., 2002; Liu et al., 2003; Zeng et al., 2018).Previous studies on the South-North Water Transfer Project water allocation model focused more on macro-scale water allocation (Wang et al., 2001; Sang et al., 2018). There was a certain disconnection between water users' actual microscopic demand and its universality; the practicality and operability were weak. At the same time, the study area has a complicated river system and dense river networks (Xu et al., 2020).

As a very important section of the east route of the South-to-North Water Diversion Project, water allocation in Jiangsu Province is vital for the water transfer to North China, but water allocation in Jiangsu Province lacks operational basis with scientific simulation background. As the construction and operation of the east route of the South-to-North Water Diversion Project, it is very urgent to study water allocation (Zhao et al., 2012). The purpose of this study was to improve the allocation and utilization efficiency of water resources based on the micro-level simulation of water supply and demand. Taking the South-to-North Water Transfer Project intake in Jiangsu Province as the research area, researchers estimated water supply and demand in the intake district and proposed two water allocation schemes under different engineering conditions (benchmark and planning) that were compared accordingly. In the simulation calculation of water resource supply and demand, the data used are accurate to the water intake lock of the water use. Therefore, the model can simulate and output the multi-scale calculation results of different administrative units, such as villages, counties, and cities, as well as segments, trunk lines, and water resources zoning. It is helpful to solve the disconnection between simulation calculation and water resource management. Based on the results, it also provided an effective plan for the hydraulic engineering sector to optimize the allocation and management of water resources. The study is helpful for policy makers to mitigate the water shortage in Jiangsu Province and other areas with water transfer projects in China and other countries.

METHODOLOGY

Study Area

The study area is between 32°27′N–34°50′N latitude and 117°57′E–119°34′E longitude covering all of Huaian, Suqian, Xuzhou, and Lianyungang in Jiangsu Province and Jiangdu, Gaoyou, and Baoying in Yangzhou as well as Funing in Yancheng. It covers 43143.7 km^2, and the total population is about 24 million. It is a subtropical and warm temperate transition zone with an annual average temperature of 14–17°C, annual average rainfall of 700–1,300 mm, and evaporation of 900–1,100 mm. There is flat open terrain, many lakes, and a densely covered drainage network. From south to north, the main five storage lakes are Gaoyou Lake, Baima Lake, Hongze Lake, Luoma Lake, and Nansi Lake. The main river channels include Liyun River, the main irrigation artery in north Jiangsu as well as Zhongyun River, Xuhong River, Hanzhuang River, and Bulao River. The scope of the study area is shown in **Figure 1**.

Water Allocation Model

The water resource allocation model constructed by the research team mainly includes submodules such as confluence, water resource supply and demand, and water engineering scheduling. The main steps include river network generalization, data collection, water resource demand calculation, water supply priority determination, water resources scheduling, water resources allocation scheme, and so on.

Model Building

Framework

The framework is shown in **Figure 2**. The steps of model are as follows:

1) Survey and basin information collection such as rainfall, evaporation, land use and land cover, drainage features,

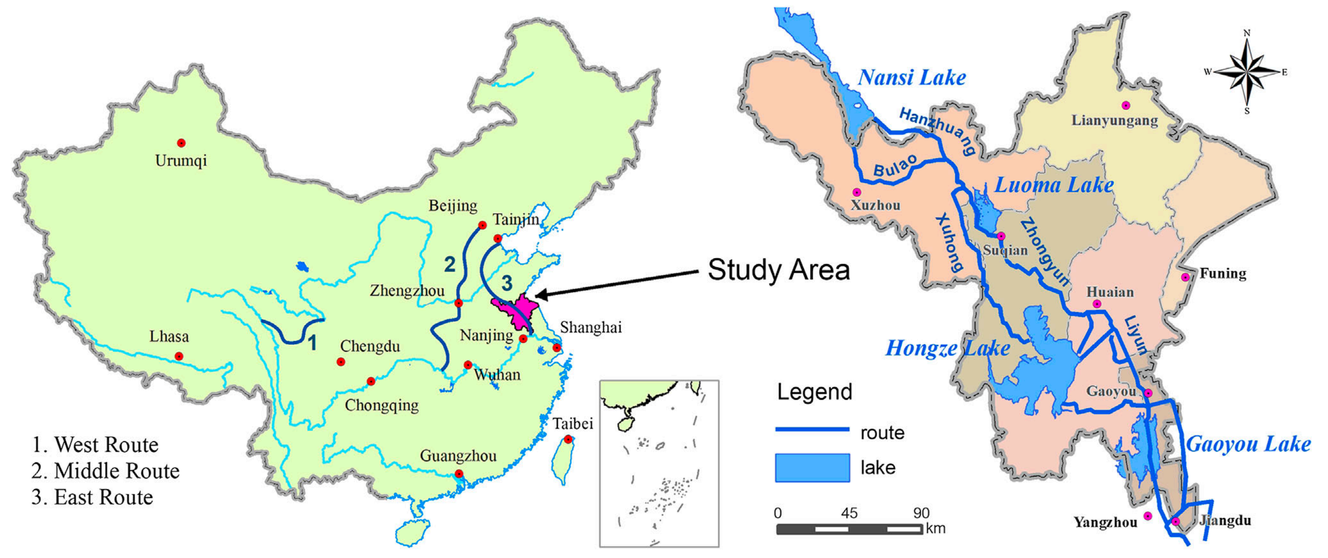

FIGURE 1 | Jiangsu intake district of the South-to-North Water Diversion Project.

lock station properties, lock scheduling, and categories and distribution of different types of water use.

2) Water supply network generalization including water channel, nodes, and lakes. Of these, the water channel is divided into main waterline, branch waterline, and other watercourse; nodes are generalized into pump and lock station, water use, management, boundary, ordinary water channel, and so on. The result is shown in **Table 1** and **Figure 3**.
3) Runoff and confluence modeling, water supply and demand calculation, water allocation, and other submodels. The calculation of runoff is divided into four types with different LUCC such as water, paddy field, dry land, and town. The confluence calculation is classified into plain area, hilly, and lakes water confluence. The curve confluence method was used for plain area confluence (Zeng et al., 2014). The unit confluence method was used for the hilly area (Zeng et al., 2014) and direct confluence for lakes. The calculation formula of runoff is as follows, and the parameter meanings are shown in **Table 2**.

Water Runoff: The runoff of water is formed by the difference between the rainfall and evaporation, and if precipitation is less than evaporation, the value of surface runoff generation is negative. The calculation formula is as follows:

$$R_1 = P - \beta E$$

Paddy Field Runoff: The formula for calculating the runoff in paddy field is as follows:

$$H_2 = H_1 + P - \alpha \cdot \beta \cdot E - f$$

$$\text{If } H_2 \geq H_p,\ R_2 = H_2 - H_p,$$
$$\text{if } H_u < H_2 \leq H_p,\ R_2 = 0,$$
$$\text{if } H_d < H_2 \leq H_u,\ R_2 = 0,$$
$$\text{if } H_2 \leq H_d,\ R_2 = H_2 - H_u$$

Dry Land Runoff: The formulas for calculating the runoff in dry land are as follows:

$$W_b = W_m{}^{*}1.2$$
$$W_{MM} = W_M{}^{*}(1+B)$$
$$W_{bM} = W_b{}^{*}(1+B)$$
$$W_{mM} = W_m{}^{*}(1+B)$$
$$A = W_{MM}{}^{*}\left[1-\left(1-\frac{W}{W_M}\right)^{\frac{1}{1+B}}\right]$$
$$\text{If } W > W_M$$

$$EE = K^{*}\mathrm{E}$$

$$\text{If } W \leq W_M \ \ EE = K^{*}\mathrm{E}^{*}\frac{\mathrm{W}}{\mathrm{W_M}}$$
$$\text{If } P - EE \leq 0 \ \ R_s = 0,\ \ R_u = 0$$
$$\text{If } P + W > W_{bM}$$
$$R_s = P - EE - (W_b - W),\ \ R_u = W_b - W_m$$
$$\text{If } W_{mM} < P + W \leq W_{bM}$$
$$R_s = P - EE - (W_b - W) + W_m{}^{*}\left(1-\frac{P-EE+A}{W_{MM}}\right)^{(1+B)},$$
$$R_u = P - EE - R_s$$
$$\text{If } P + W \leq W_{mM}$$
$$R_s = 0,$$

$$R_u = P - EE - (W_m - W) + W_m{}^{*}\left(1-\frac{P-EE-R_s+A}{W_{MM}}\right)^{(1+B)}$$
$$R_3 = R_s + R_u$$

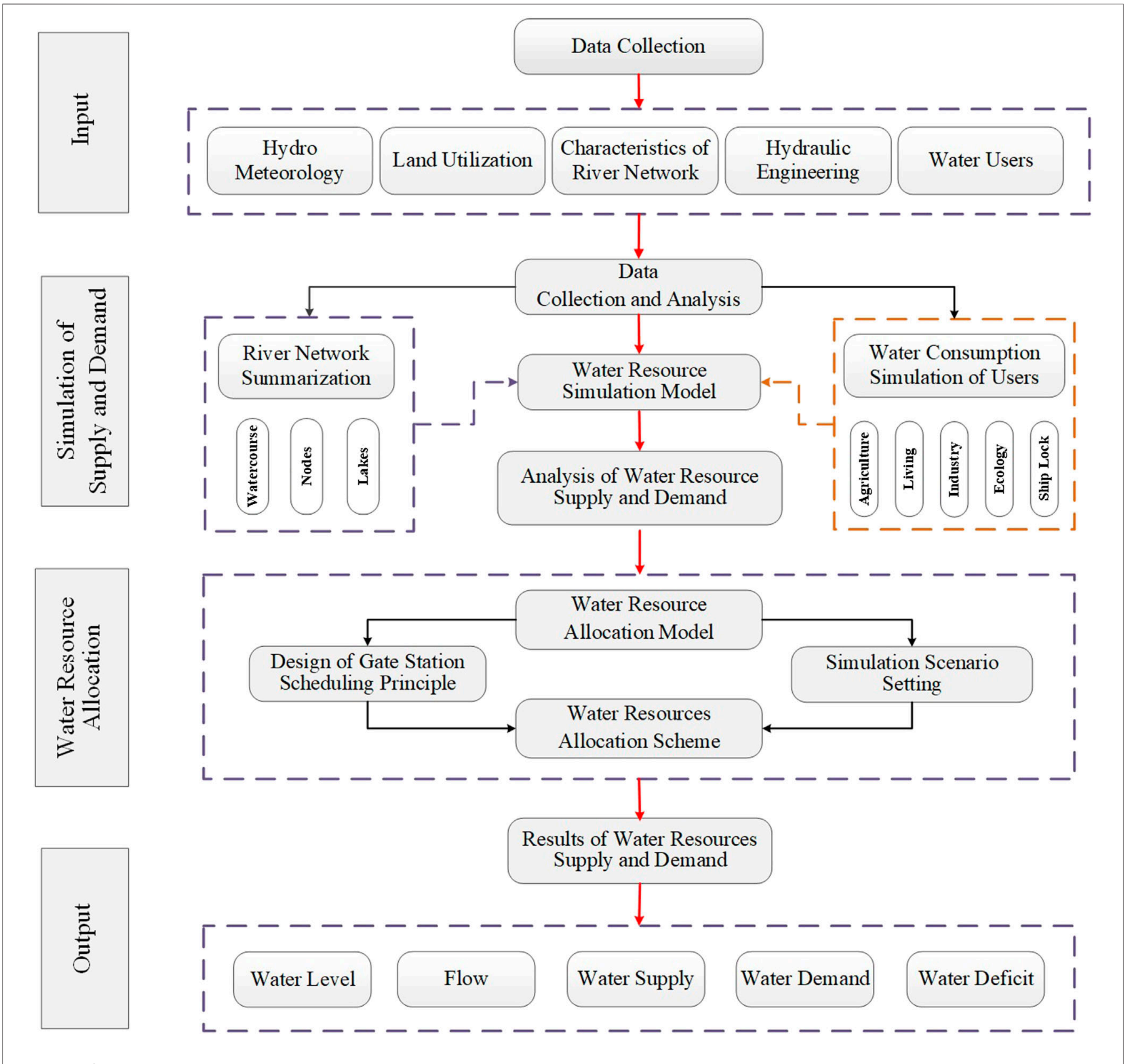

FIGURE 2 | Framework of water allocation.

Town Runoff: On comprehensive consideration of the urban road runoff coefficient, the model can be simply expressed as:

$$R_4 = \varphi P$$

Data

The data and the main parameters that the model required are listed as follows (Zeng et al., 2018). IData: Based on annual precipitation data from 1956 to 2000, typical years are selected according to row frequency—Pearson three curve. Three typical years are 50% assurance representative year (normal flow year), 75% assurance typical years (general drought years), and 95% assurance representative years (special drought years). The benchmark and planning year are selected for the simulation and calculation of the model, which are determined according to the matching of the new construction of the South-to-North Water Diversion Project, so that the model can provide the optimal water resource allocation scheme under different water conservancy project operation and management. Moreover, for the benchmark year and the typical representative years, hydrology, meteorology, surface covering, five categories of water users, river characteristics, brake properties and scheduling, policies in the utilization of water resources, and other related data were collected and calculated, which were provided by the Jiangsu Provincial Water Resources Department. Hydrology, meteorology, land use (**Figure 3**), water conservancy, river

Table 1 | Generalization of water supply network nodes.

Project generalization		Generalized result	
Water channel generalization	The number of water channel		171
Node generalization	Lock node	Pumps lock	177
		Ship lock	77
	Ordinary water channel node	Ordinary water channel node	264
	Control and management node	County-level administrative node	66
		Water management node	12
		Hydrological monitoring points	34
		Administrative section	63
		Water partition	10
	Boundary node	Boundary node	31
	Water user node	Water use	173
		Water intake entrance	213
Lakes generalization	Storage node		4

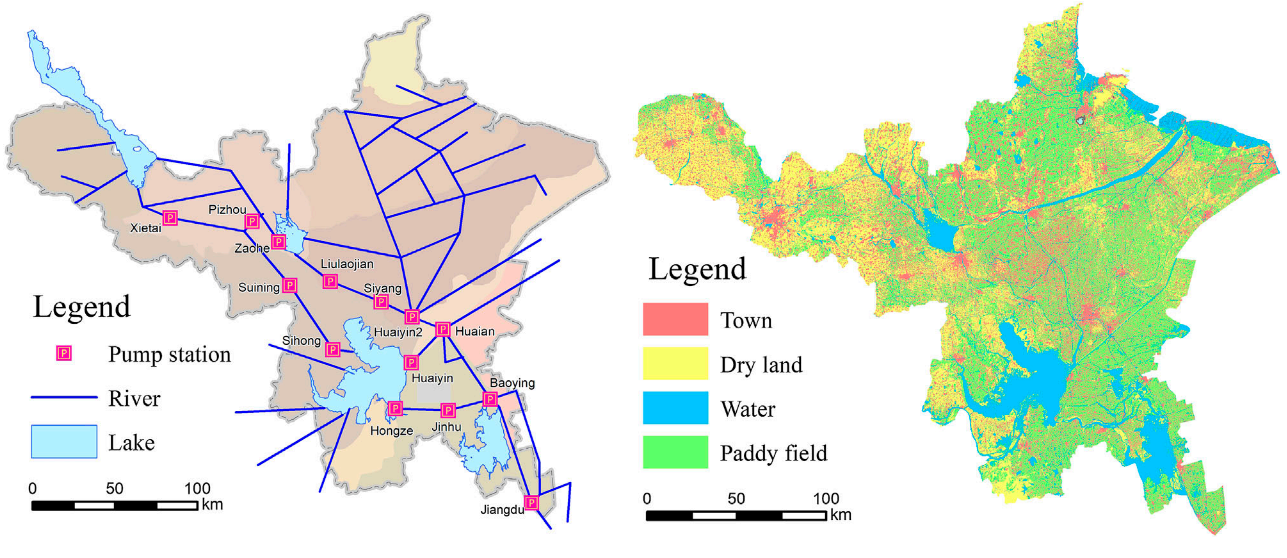

FIGURE 3 | (A) River channel generalization and **(B)** LUCC.

network, water users, and other data are monitored and predicted by water conservancy departments. Among them, the calculation description of the five water users is shown in the part 2.2.2.

Water Demand and Supply Calculation

(1) Water Demand Calculation: Water use in the study area is mainly classified into river channel water use and surface water use. The river channel water use means to take water from the trunk channel. The surface use means the water is used before drain into rivers. The river channel water use include agriculture, industry, domestic, ecology, and ship lock use, which need to take water from the generalized water channel. The agricultural water use demand is calculated by the irrigation system. The other four classes of nonagricultural use and surface water users' demand are calculated by the quota method.

I. Agricultural water user (irrigation and water area) demand scale is calculated according to the system of irrigation and irrigation area. The irrigation water use coefficient of field is between 0.91 and 0.94, and the irrigation water use coefficient of the river channel is between 0.609 and 0.738 (Xiong et al., 2008; Peng and Ai, 2012). The calculation formula is given as follows:

$$W_a = A_a{}^{*}K_a/J_f/J_c$$

where W_d (m^3) is the agricultural water use, A_a (m^2) is the area of farmland, K_u (m^3/m^2) is the water consumption per square meter of farmland, J_f is the field use coefficient of irrigation water, and J_c is the water consumption per rural resident.

II. Domestic water use demand scale intake from the river channel (urban and rural water use). The calculation formula is as follows:

$$W_d = N_u{}^{*}K_u + N_r{}^{*}K_r$$

where W_d (m^3) denotes domestic water use, N_u (person) the urban population, K_u (m^3/person) water consumption per urban resident, N_r (person) the rural population, person, and K_r (m^3/person) water consumption per rural resident.

Table 2 | Parameters of runoff module.

Runoff submodules	Parameters	Meaning of the parameters
Water	P (mm)	Daily average rainfall
	E (mm)	Daily evaporation (E601 evaporating dish)
	B	Evaporation reduction coefficient
	R_1 (mm)	Daily runoff depth of water
Paddy field	A	Water requirement coefficient during rice growing stages
	H_1 (mm)	Water depth at early stage of paddy field
	H_2 (mm)	Water depth at later stage of paddy field
	H_p (mm)	Rice submergence tolerance water depth during growth stages
	H_u (mm)	Rice suitable water depth during growth stages
	H_d (mm)	Rice suitable water depth lower limit during growth stages
	f (mm)	Daily permeate (leakage) quantity of paddy field
	R_2 (mm)	Daily runoff depth of paddy field
Dry land	B	Evaporation reduction coefficient of dry land
	E (mm)	Water storage capacity curve index
	EE (mm)	Evaporation of rainfall period
	A (mm)	Evaporation of dry land
	W (mm)	Soil water content at early stage
	W_{MM} (mm)	Soil moisture content at the initial moment
	W_M (mm)	Maximum value of water storage capacity curve
	W_b (mm)	Basin average water storage capacity
	W_m (mm)	Saturated water content
	W_{bM} (mm)	Maximum saturated water content
	R_3 (mm)	Runoff depth of dry land
	R_s (mm)	Surface runoff depth of dry land
	R_u (mm)	Underground runoff depth of dry land
Town	R_4 (mm)	Runoff depth of town
	Φ	Runoff coefficient of urban road

IVModel parameters calibration and model validation based on the current confluence, water use, water deficit, water level, and the main process for station over the water.

III. Industrial water use: Its demand-scale use (self-built water engineering, specializing in industrial plant) is determined according to the design of the survey data. The calculation formula is as follows:

$$\mathrm{W_i = N_i{*}K_i}$$

where $\mathrm{W_i}$ ($\mathrm{m^3}$) denotes the industrial water use, $\mathrm{N_i}$ (million RMB) industrial production, and $\mathrm{K_i}$ ($\mathrm{m^3}$/million RMB) water consumption per million RMB industrial product.

IV. Ecological water use (river ecological water users who take water from the main rivers): the minimum value of the demand scale is determined according to the lowest navigable water level of lock design and the lowest water level of water inlet design in the water plant as well as the results of integrated water resources planning research project of ecological water demand in Jiangsu Province. The ecological water requirement out of the river channel without intake from the main rivers as surface water demand is figured out by survey and calculation. The calculation formula is as follows:

$$\mathrm{W_e = A_e{*}K_e}$$

where $\mathrm{W_e}$ ($\mathrm{m^3}$) denotes ecological water use, $\mathrm{A_e}$ ($\mathrm{m^2}$) the area of green plants, and $\mathrm{K_e}$ ($\mathrm{m^3/m^2}$) water consumption per square meter of green plants.

V. Ship lock use is determined according to water consumption every time the lock is opened and the times of daily use of the lock. The calculation formula is as follows:

$$\mathrm{W_{sl} = N_{sl}{*}K_{sl}}$$

where $\mathrm{W_{sl}}$ ($\mathrm{m^3}$) denotes ship locks water use, $\mathrm{N_{sl}}$ (time) the times of daily use of the lock, and $\mathrm{K_{sl}}$ ($\mathrm{m^3}$/time) water consumption per use of the lock.

(2) Water Supply: Water supply is determined by considering the minimum value of the three, such as water use demand, water channel supply, and supply ability of water intake locks. According to the actual needs of the development of national economy, agricultural, industrial, domestic, ecological, and ship lock water have different reliabilities. Thus, water use order is given according to the priority of water use, which is originally proposed by the research team. And it is applied to this study for the first time. Domestic water demand takes first priority. Industrial demand is in second place followed by ship lock water, ecological water, and agricultural water. Specific priorities are listed as follows:

I. Domestic water use and industrial water users should keep the river flowing normally and healthy ecology when water is retrieved from the water channel.

II. Agriculture, ship locks, and green plant ecological water use should keep the water channel level higher than the ecological water level when water is drained for use from the water channel. Defining the priority of water supply can prevent the water channel from drying up to meet the water use demand, especially when water use demand is particularly large.

III. The ecological water level is set in the model, which is the bottom line that the river can provide agricultural water, ship locks water, and ecological water demand. It is designed to avoid excessive intake of water from the river channel, which would affect the ecological health of the river channel and lead to drying. The determination of the ecological water level has not yet set a clear standard. In this research, mainly the Beijing-Hangzhou Canal canalized water level from the first phase of the Eastern Route Project feasibility study report (I), river ecological water table in Jiangsu Province, and the lowest navigable water level of the lock are used to estimate the ecological water level of the generalized rivers in the South-to-North Water Diversion Project.

IV. If at least one of the above three levels is in the same water channel or node location, then it adopts the lowest water level. If not, then formulate via interpolation methods.

(3) Supply and Demand Balance: Different statistical calibration methods were used as the calculating unit. These include the prefectural-level administrative region, water resource division, trunk channel, and others. Researchers balanced the supply and demand of the water source, entrance, and water channel according to the supply ability of the water resources, water conservancy project, and water demand in the study area. If the locks supply size is smaller than the water demand scale, then the insufficient part is the lack of water locks supply ability. Otherwise, it does not result in water shortage. Thus, the water supply is the minimum value of water demand at the water locks and resource. If water supply is less than the water demand, then record the accumulated water shortage. This is supplied through the optimized water allocation in the South-to-North Water Transfer Project. Researchers also analyze the balance of different calibers and formulate an optimized water allocation scheme for the demand, supply, and shortage of entire study area and mains. The main means of the optimization method, on the one hand, adopt the dual objective constraint of minimum water shortage and minimum water diversion of the Yangtze River. On the other hand, the regional lake regulation and storage capacity can be used to balance the abundance and depletion, via storing water in advance to reduce the water shortage caused by the limitation of water supply capacity.

(4) 4 Water Resource Dispatch: The scheduling scheme was developed for the operation of the North-to-South Water Transfer Project in Jiangsu Province based on different time periods, control nodes, and water resources conditions. Time periods include flood period, nonflood period, drainage period, nondrainage period, and irrigation period. Control nodes include ship locks nodes and lake nodes. Water resources conditions mainly include water, flow, and rain.

RESULTS

Simulation Results and Analysis

The research is based on the status and planning of two different processes of engineering and water resource allocation simulation. The process of benchmark engineering is based on the projects which are used to divert water from the Yangtze River to the north of Jiangsu Province. The process of planning engineering, based on the benchmark engineering, adds new construction engineering of the South-to-North Water Transfer Project, which expands the pumping capacity of the river to 500 m^3/s. There is 8,900 million m^3 of pumped river water and 1,900 million m^3 supply in Jiangsu Province. According to actual irrigation assurance rate level in Jiangsu, water demand and water deficit under water frequency are 95%, P = 75%, and P = 50%.

Results of Water Resources Supply and Demand

As shown in **Table 3**, according to the simulation results, contrast variation of water demand for the planning year and benchmark year, the water demand of P = 95, 75, and 50% increases by 0.8, 4.5, and 5%. It is concluded that when the assurance rate of water demand becomes low, the amount of water demand change increases. In the drought situation, the ship locks, industrial, domestic, and ecological water demand remain constant, but agricultural water demand increases. Agriculture water demand increases by 3 million m^3 in the special drought year vs. average year. Under the same assurance rate, but a different pumped ability of the engineering, the transport remains constant and agriculture and ecological water demand change slightly; industry and living water demand change markedly (41% and 65%, respectively, vs. benchmark). For planning vs. benchmark

TABLE 3 | Water demand based on different pump engineering situation (unit: 100 million m^3).

Water use	P = 95%		P = 75%		P = 50%	
	Benchmark	Planning	Benchmark	Planning	Benchmark	Planning
Ship locks	7.9	7.9	7.9	7.9	7.9	7.9
Industry	23.5	33.2	23.6	33.3	23.5	33.2
Agriculture	138.1	121.4	107.4	95.7	102.6	91.5
Domestic	11.3	18.7	11.3	18.7	11.3	18.7
Ecology	5.1	6.2	5.2	6.6	5.1	6.6
Total	185.9	187.3	155.2	162.2	150.3	157.8

TABLE 4 | Water supply based on different engineering progresses (unit: 100 million m³).

User name	P = 95%		P = 75%		P = 50%	
	Benchmark	Planning	Benchmark	Planning	Benchmark	Planning
Ship locks	7.8	7.8	7.9	7.8	7.8	7.8
Industry	22.7	33.0	22.7	33.0	23.3	33.0
Agriculture	113.7	113.6	93.7	92.7	93.2	89.0
Domestic	10.7	18.4	10.8	18.6	11.1	18.6
Ecology	3.4	6.1	4.0	6.2	4.1	6.2
Total	158.3	178.8	139.1	158.3	139.5	154.6

years, the water demand when P = 95% increases by 13.0%. When water demand is P = 75%, it increases by 13.8%, and at P = 50%, it increases by 10.8%. It is concluded that the water supply increases. Based on analysis, under different processes of engineering or under the assurance rate, water supply and demand trends are held consistent (**Table 4**).

Table 5 shows that under the same pump engineering situation, the amount of the water deficit increases when the assurance rate becomes higher, especially the amount of the water deficit is 276 million m^3 under the typically drought and benchmark engineering situations. The water deficit of agriculture use is rather prominent, which receives 88.4% of the water deficit. In contrast to the same assurance rate but planning pump engineering situation, it is easy to recognize that water deficit greatly reduces for planning pump's operation. The water deficit decreases to 69.2% at P = 95%, decreases to 75.8% at P = 75%, and decreases to 70.4% at P = 50%. Of these, water deficit for ship locks remains, water deficit for industry remains unchanged, but it decreases to 75% in the special drought year and general drought year. Under the three typical years, the agriculture water deficit was between 26.6 and 78%, and the domestic water deficit was between 50 and 80%. The most apparent is the ecological water deficit, which is decrease by 94% in a special drought year.

Temporal Variations

The month was chosen as the unit of time to analyze the distribution characteristics of water demand, water supply, and water deficit. The water demand, supply, and deficit results of planning engineering contrasted with the benchmark engineering situation under different assurance rates (**Figure 4**). The values in **Figure 4** are the result of the planning situation minus the benchmark situation. According to the results, water supply all increased under planning engineering vs. benchmark engineering. Water demand reduced in June to August, while it increased in the other months. The variations of water demand, water supply, and water deficit seem alike in January to May, while in June to December, changes are obvious. Changes are greatest during the rainy season. Under assurance rate P = 95%, water demand increases the most in December. The maximum change amount is 400 million m^3; water supply changes a large amount in December and August. In the other months, the water supply is between 80 and 200 million m^3. The water deficit decreases the most during June to September in the amount of 1,450 million m^3, which is 75% of the rest of the year.

At an assurance rate of P = 75%, in contrast to the benchmark engineering situation, the water demand decreased in June to August in planning situation. Most of the decrease was in June. The maximum change value is 260 million m^3. The added value of water demand in drought typical year is stable and is between 110 and 14,000 million m^3. The added value of water supply in each month changes is about 150 million m^3. The water deficit decreases every month. The water deficit decreases most during June to September with an amount of 1,020 million m^3 and 83% of the total deficit amount of the whole year. Under an assurance rate P = 50%, the change in water demand is the same for every month similar to a general drought year. In June, water demand decreases the most at a maximum value of 210 million m^3. The water supply increases the least of a minimum value of 30 million m^3. Water deficit decreases every month, but it is not clear in drought season. In June to September, it decreases the most for a total of 690 million m^3 or 91% of the year.

TABLE 5 | Water deficit based on different engineering progresses (unit: 100 million m³).

User name	P = 95%		P = 75%		P = 50%	
	Benchmark	Planning	Benchmark	Planning	Benchmark	Planning
Ship locks	0.1	0.1	0.1	0.1	0.1	0.1
Industry	0.8	0.2	0.9	0.3	0.2	0.2
Agriculture	24.4	7.8	13.7	3	9.4	2.5
Domestic	0.6	0.3	0.5	0.1	0.2	0.1
Ecology	1.7	0.1	1.2	0.4	1.0	0.4
Total	27.6	8.5	16.4	3.9	10.7	3.3

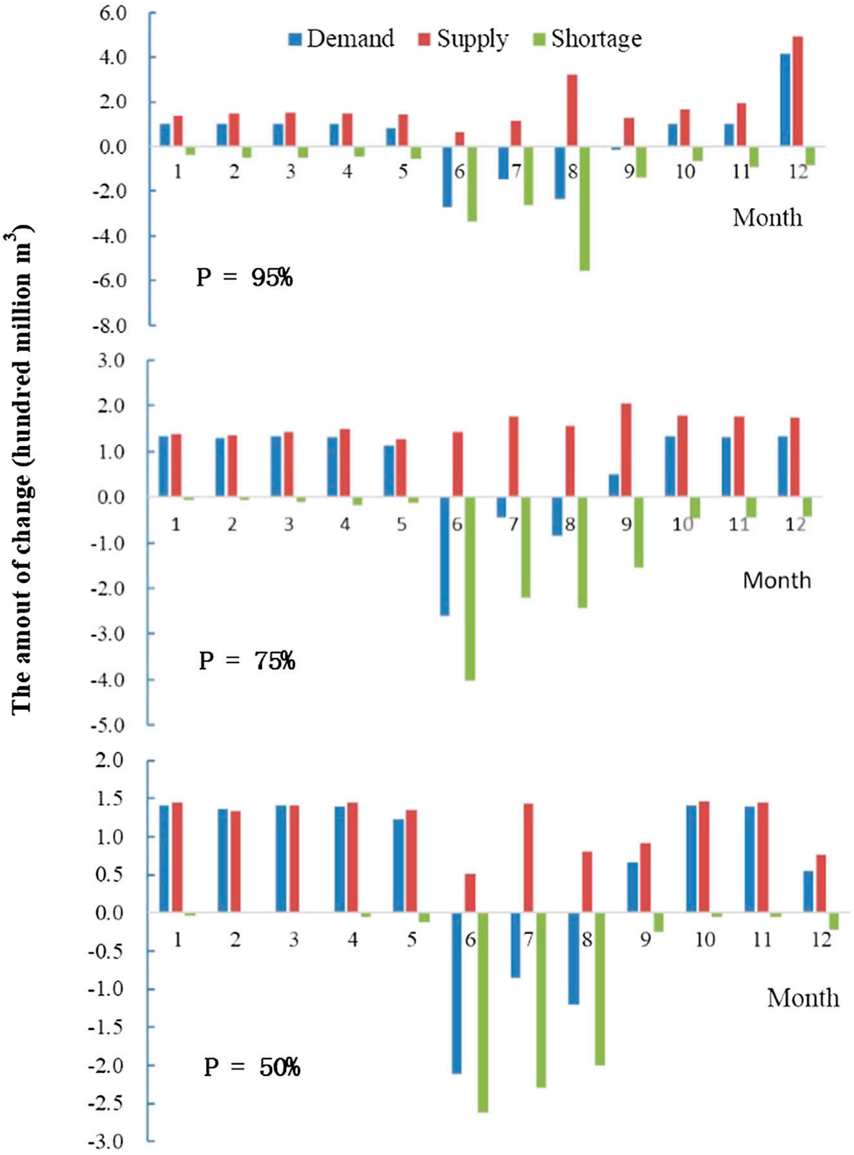

FIGURE 4 | Contrast variation of water supply, water demand, and water deficit for planning and benchmark engineering situation under the 95%, 75%, and 50% assurance.

According to model simulation results, the water supply would definitely improve by 2020 and the total water deficit will decrease by a large margin in Jiangsu Province. In the years when P = 95%, the water deficit value is 850 million m^3, and the water deficit rate is 4.5% which is decrease 10.3%. When P = 75%, the water deficit value is 390 million m^3, and the water deficit rate is 2.4% which is decrease 8.0%. When P = 50%, the water deficit value is 330 million m^3, and the water deficit rate is 2.0% which is decrease 5.2%. The water security of the region is obviously improved via the South-to-North Water Diversion Project.

DISCUSSION AND CONCLUSIONS

Researchers studied the intake area of the South-to-North Water Transfer in Jiangsu Province and realized a combination of macro-allocation of water resources and microdemand of water use. The water resource allocation model of this study is built based on agricultural irrigation water demand and optimal water resource allocation, so the proposed water resource allocation scheme is conducive to efficient utilization and protection of water resources. It is used to describe the water security both local and overall including temporal components and overall demand for water resources. Researchers also used benchmark and planning engineering situation to analyze and compare water supply, water demand, and water shortages under different conditions. The planning pump engineering is effective. And the results provide a scientific basis to water resources allocation in the eastern route of the South-to-North Water Transfer Project.

On the basis of water resources quantity estimation, water supply and demand forecast, and analysis and the research of water resource regulation, a reasonable allocation of water resources had been studied. Furthermore, water resources allocation schemes of benchmark and planning engineering situation were put forward. The model can provide different configurations of water supply based on benchmark and planning pump engineering under a different assurance rate of P = 50%, 75%, and 95%. Results showed that the water demand of planning engineering situation increased slightly compared with that in benchmark, and water supply increased obviously. Water deficit is greatly reduced, especially in the common drought typical situation; water deficit of planning engineering situation decreased 76.1% compared with that of benchmark. According to the simulated results of water pumped ability in different typical years based on the benchmark and planning engineering, it was proved that water pumped ability significantly increased in the planning engineering situation, which helps to improve regional water shortage.

It is concluded that when the assurance rate of water demand becomes low, the amount of water demand change will increase. During drought event, the ship locks, industrial, domestic, and ecological water demand remain constant, but agriculture water demand increases. The water deficit of agriculture use is rather prominent, and it is the main part of water shortage. Under the three typical precipitation situation, the agriculture water deficit was between 26.6 and 78%. According to model simulation results, the water supply will definitely improve by 2020 and the total water deficit will decrease by a large margin in Jiangsu Province. Water supply in each period all increased with planning approach *vs.* benchmark engineering. Water deficit is significantly reduced in June to August, which is helpful to solve the agricultural water shortage.

DATA AVAILABILITY STATEMENT

All datasets generated for this study are included in the manuscript/supplementary material.

AUTHOR CONTRIBUTIONS

CZ is the first author and led this research as well as the preparation of the manuscript. Corresponding author is Professor LW offered technical guidance. The second author is Professor JM, and he is the main programmer of the model used in this article. MC helped with hydrological data processing and also evaluated the results. WQ is responsible for preparing figures and CX has assisted with revising the English manuscript.

FUNDING

This study has been financially supported by National Natural Science Funds of China (Grant numbers 41401021), Chongqing natural science foundation project (cstc2019jcyj-msxmX0227), Chongqing Normal University Fund Project (No. 19XL13 011), the china scholarship council (No. 201606195014) and Science and Technology Project of Jiangsu Provincial Water Resources Bureau (Grant No. 2014016).

ACKNOWLEDGMENTS

We thank LetPub (www.letpub.com) for its linguistic assistance during the preparation of this manuscript.

REFERENCES

Abed-Elmdoust, A., and Kerachian, R. (2013). Incorporating economic and political considerations in inter-basin water allocations: a case study. *Water Resour. Manag.* 27, 859–870. doi:10.1007/s11269-012-0219-6

Li, C., Zhou, J., Ouyang, S., Wang, C., and Liu, Y. (2015). Water resources optimal allocation based on large-scale reservoirs in the upper reaches of Yangtze River. *Water Resour. Manag.* 29, 2171–2187. doi:10.1007/s11269-015-0934-x

Li, M., Guo, P., and Ren, C. F. (2015). Water resources management models based on two-level linear fractional programming method under uncertainty. *J. Water Resour. Plann. Manag.* 141, 05015001. doi:10.1061/(asce)wr.1943-5452.0000518

Li, Y., Cui, Q., Li, C., Wang, X., Cai, Y., Cui, G., et al. (2017). An improved multi-objective optimization model for supporting reservoir operation of China's South-to-North water diversion project. *Sci. Total Environ.* 575, 970–981. doi:10.1016/j.scitotenv.2016.09.165

Liu, J., Li, M., Wu, M., Luan, X., Wang, W., and Yu, Z. (2020). Influences of the south-to-north water diversion project and virtual water flows on regional water resources considering both water quantity and quality. *J. Clean. Prod.* 244, 118920. doi:10.1016/j.jclepro.2019.118920

Liu, J. L., Ma, B., Xie, J. C., and Zhao, Y. (2003). Simulation model of multi-reservoir and multi-consumer and multi-work for water unite regulation of cross-drainage basin for example of the East-route of South-to-North water transfer project. *J. Soil Water Conserv.* 17, 75–79.

Nazemi, A., and Wheater, H. S. (2015). On inclusion of water resource management in Earth system models–Part 2: representation of water supply and allocation and opportunities for improved modeling. *Hydrol. Earth Syst. Sci.* 19, 63–90. doi:10.5194/hess-19-63-2015

Peng, S. Z., and Ai, L. K. (2012). Improving irrigation water use coefficient and ensuring national food and water safety. *Water Resour. Prot.* 28, 79–82.

Sang, X., Wang, H., Wang, J., Zhao, Y., and Zhou, Z. (2018). Water resources comprehensive allocation and simulation model (WAS), part Ⅰ. theory and development. *Shuili Xuebao.* 49, 1451–1459.

Wada, Y., Wisser, D., and Bierkens, M. F. P. (2014). Global modeling of withdrawal, allocation and consumptive use of surface water and groundwater resources. *Earth Syst. Dynam.* 5, 15–40. doi:10.5194/esd-5-15-2014

Wang, H. (2006). The present and future of water resources allocation. *Water Resour. Hydropower Eng.* 37, 7–14.

Wang, Y. T., Hu, S. Y., Zhou, Q. L., Wen, D., Wang, F. Q., and Wu, Z. Y. (2001). Optimal water operation for the water transfer project from south to north (middle route). *Adv. Water Sci.* 12, 72–80.

Xiong, J., Cui, Y. L., and Xie, X. H. (2008). Spatial distribution of irrigation water use efficiency and its isogram. *J. Irrig. Drain.* 27, 1–5.

Xu, J., Tu, Y., and Zeng, Z. B. (2013). Bilevel optimization of regional water resources allocation problem under fuzzy random environment. *J. Water Resour. Plann. Manag.* 139, 246–264. doi:10.1061/(asce)wr.1943-5452.0000248

Xu, Y., Liu, X., and Xu, L. (2020). A dynamic expert contribution-based consensus model for hesitant fuzzy group decision making with an application to water resources allocation selection. *Soft Comput.* 24, 4693–4708. doi:10.1007/s00500-019-04229-3

Xu, Z. X., Ito, K., Schultz, G. A., and Li, J. Y. (2001). Integrated hydrologic modeling and GIS in water resources management. *J. Comput. Civ. Eng.* 15, 217–223. doi:10.1061/(asce)0887-3801(2001)15:3(217)

Yang, S. T., Jiang, Y., and Hua, P. (2007). Result analysis of water resources allocation in Jiangsu Province. *China Water Resour.* 5, 22–25.

Yang, Y., Yin, L., and Zhang, Q. (2015). Quantity versus quality in China's South-to-North water diversion project: a system dynamics analysis. *Water* 7, 2142–2160. doi:10.3390/w7052142

Yao, Z., Zeng, C., Li, Y., Cao, M., Ma, J., and Wang, L. (2018). Development and application of complex water resources joint dispatching system based on information technology. Taking the Jiangsu section of the East route of South-to-North water diversion project as an example. *Water Resour. Hydropower Eng.* 49. 30–37.

Zeng, C., Ma, J., Cao, M., Yang, S., Geng, J., and Wang, L. (2018). The key technology of water resources utilization assessment research based on the strictest water resources management system taking the Jiangsu section of the east route of South-to-North water diversion project as an example. *Water Resour. Hydropower Eng.* 49, 22–29.

Zeng, C. F., Yang, S. T., Wang, L. C., and Song, D. D. (2014). "Research on water resources allocation of the East route of the South-to-North water diversion project in Jiangsu province. Water science and disaster prevention and mitigation under changing environment," in Proceedings of the 12th China water forum, Beijing, China (China Water Resources and Hydropower Press), 182–189.

Zhao, H. Q., Chang, B. C., Yang, S. T., and Wang, L. C. (2012). A preliminary discussion on water shortage in water-receiving areas in Jiangsu Province in South-to-North water diversion project area based on water allocation model. *Water Resour. Prot.* 28, 24–28.

Zhao, Y., Xie, J. C., and Ma, B. (2002). Water dispatch of east-route of South-to-North Water transfer project based on system simulation method. *J. Hydraul. Eng.* 11, 38–43.

Zhao, Z.-Y., Zuo, J., and Zillante, G. (2017). Transformation of water resource management: a case study of the South-to-North water diversion project. *J. Clean. Prod.* 163, 136–145. doi:10.1016/j.jclepro.2015.08.066

Zhong, S., Shen, L., Sha, J., Okiyama, M., Tokunaga, S., Liu, L., et al. (2015). Assessing the water parallel pricing system against drought in China: a study based on a CGE model with multi-provincial irrigation water. *Water* 7, 3431–3465. doi:10.3390/w7073431

Zhuan, X., Zhang, L., Li, W., and Yang, F. (2018). Efficient operation of the fourth Huaian pumping station in East route of South-to-North water diversion project. *Int. J. Electr. Power Energy Syst.* 98, 399–408. doi:10.1016/j.ijepes.2017.10.041

Conflict of Interest: The authors declare that the research was conducted in the absence of any commercial or financial relationships that could be construed as a potential conflict of interest.

frontiers
in Earth Science

ORIGINAL RESEARCH
published: 11 December 2020
doi: 10.3389/feart.2020.542686

Prediction of Sediment Yield in the Middle Reaches of the Yellow River Basin Under Extreme Precipitation

Suzhen Dang[1,2], Xiaoyan Liu[3], Huijuan Yin[1,2] and Xinwei Guo[1,2]*

[1]Yellow River Institute of Hydraulic Research, Yellow River Conservancy Commission, Zhengzhou, China, [2]Key Laboratory of Soil and Water Loss Process and Control in the Loess Plateau, MWR, Yellow River Institute of Hydraulic Research, Zhengzhou, China, [3]Yellow River Conservancy Commission, Zhengzhou, China

The Yellow River is one of the rivers with the largest amount of sediment in the world. The amount of incoming sediment has an important impact on water resources management, sediment regulation schemes, and the construction of water conservancy projects. The Loess Plateau is the main source of sediment in the Yellow River Basin. Floods caused by extreme precipitation are the primary driving forces of soil erosion in the Loess Plateau. In this study, we constructed the extreme precipitation scenarios based on historical extreme precipitation records in the main sediment-yielding area in the middle reaches of the Yellow River. The amount of sediment yield under current land surface conditions was estimated according to the relationship between extreme precipitation and sediment yield observations in the historical period. The results showed that the extreme rainfall scenario of the study area reaches to 159.9 mm, corresponding to a recurrence period of 460 years. The corresponding annual sediment yield under the current land surface condition was range from 0.821 billion tons to 1.899 billion tons, and the median annual sediment yield is 1.355 billion tons, of which more than 91.9% of sediment yields come from the Hekouzhen to Longmen sectionand the Jinghe River basin. Therefore, even though the vegetation of the Loess Plateau has been greatly improved, and a large number of terraces and check dams have been built, the flood control and key project operation of the Yellow River still need to be prepared to deal with the large amount of sediment transport.

Keywords: extreme precipitation, sediment yield, Yellow River basin, frequency distribution, sediment yield index

Edited by:
Xingcai Liu,
Chinese Academy of Sciences, China

Reviewed by:
Guangju Zhao,
Chinese Academy of Sciences, China
Dunxian She,
Wuhan University, China

Correspondence:
Suzhen Dang
dangsz_hky@163.com

Specialty section:
This article was submitted to Hydrosphere, a section of the journal Frontiers in Earth Science

Received: *13 March 2020*
Accepted: *26 October 2020*
Published: *11 December 2020*

Citation:
Dang S, Liu X, Yin H and Guo X (2020) Prediction of Sediment Yield in the Middle Reaches of the Yellow River Basin Under Extreme Precipitation. Front. Earth Sci. 8:542686. doi: 10.3389/feart.2020.542686

INTRODUCTION

Global warming increases the water holding capacity of the atmosphere, which is expected to increase the probability of extreme precipitation at the regional scale (Meehl et al., 2000; IPCC, 2012). Extreme climate events have received increasingly attentions in hydro-meteorological research since they are the driving forces behind many natural disasters, such as floods and landslides (Alexander et al., 2006; Du et al., 2013). Extreme precipitation also plays a key role in soil erosion processes (Frich et al., 2002; Trenberth, 2011; Fischer et al., 2012). The amount of soil erosion caused by a rainstorm can account for 60% or even more than 90% of the total annual erosion (Wang et al., 2016; Comino et al., 2017).

Many studies have investigated the effects of extreme precipitation on sediment yields worldwide. Buendia et al. (2015) found that when extreme rainfall changed in the Mediterranean region, river sediment discharge significantly decreased or increased. Zhong et al. (2017) found that there was a significant correlation between the river sediment discharge and extreme precipitation indicators in the Songhua River basin, China. Keo et al. (2018) analyzed the change in rainfall erosivity over the past 50 years in the Loess Plateau and found that extreme rainfall was the main factor affecting soil erosion. By combining climate models with hydrological models, Garbrecht et al. (2014) indicated that the amount of sediment discharge in different basins in the United States would increase by 127–157% compared with the period of 1970–1999 due to the increase in extreme precipitation events. Kao and Milliman (2008) found that the sediment discharge during the transit of Typhoon Dandelion was twice the average annual sediment discharge. Moreover, many studies have found that even if the total precipitation is constant, the increase in rainfall intensity will cause an increase in soil erosion (Nearing et al., 2005; Garbrecht et al., 2014).

The Yellow River is one of the rivers with the highest sediment content in the world. About 90% of the sediment comes from the Loess Plateau in the middle reaches of the YRB (Wang et al., 2007). The average annual sediment discharge at the Shanxian section of the YRB was 1.6 billion tons during the period 1919–1959, and the maximum sediment discharge was 3.91 billion tons in 1933. However, the sediment discharge of the YRB has gradually decreased since 1980. The average annual sediment discharge from 2000 to 2018 was only 250 million tons, of which the maximum was 620 million tons in 2003. The prediction of the sediment discharge is essential in the YRB, which directly affects the water resources management and planning, the allocation of sediment resources, and the application of water conservancy projects. Therefore, the causes of the changes in sediment yields have been the focus of previous studies on the YRB since the 1990s (Liu et al., 2014a; Shi and Wang, 2015; Xin et al., 2015; Dang et al., 2018; Zhao et al., 2018). Many studies have been carried out on the causes of sediment reduction, changes in precipitation and their effects on sediment discharge, and changes in extreme precipitation in the YRB (Miao et al., 2011; Wang et al., 2016; Gao et al., 2017; Gao and Wang, 2017; Zhang et al., 2018; Dang et al., 2019).

In terms of the impact of extreme precipitation on the sediment discharge of the YRB, some scholars have carried out comparative analyses of some small watersheds in the middle reaches of the YRB. Ran et al. (2015) analyzed the effects of soil and water conservation measures on the sediment discharge of the Jialu River Basin during an extraordinary rainstorm in 2012. Cheng et al. (2016) revealed the impact of changes in precipitation of different intensities on sediment discharge in the Yanhe River Basin and found that with the increase in precipitation intensity, the impact of precipitation on sediment discharge gradually increased. Jiao et al. (2017) analyzed the effects of vegetation changes on sediment yield during heavy rainstorms in the Yanhe River Basin in 2013. Chen et al. (2018) performed a comparative analysis of the changes in sediment discharge and the causes of two heavy rainstorms in the Yanhe River Basin in 1977 and 2013. These studies have analyzed the impact of heavy rainfall on the sediment discharge in a typical year in a tributary in the middle reaches of the YRB, and there are still few studies on the prediction of the possible sediment yield of the YRB under large-scale extreme precipitation in the Loess Plateau. However, the average annual sediment yield and the maximum sediment yield in the case of extreme rainstorms are both important basic data influencing the decisions about major issues in the management of the YRB, among which the maximum sediment yield is more important for the arrangement and application of major water conservancy projects.

In the context of substantial vegetation improvement and large-scale construction of soil and water conservation projects in the Loess Plateau (Liu et al., 2014a; Fu et al., 2017), the maximum sediment yield of the YRB in the event of extreme rainfall in the future has received increasing concerns. Floods caused by extreme precipitation is the key driving force for soil erosion and sediment yield. In this study, the main sediment-yielding area in the middle reaches of the YRB was taken as the study area, and extreme precipitation scenarios were constructed based on the analysis of historical extreme precipitation. According to recent sediment yield indicators and the relationship between precipitation and sediment yield, the corresponding sediment yield under the current surface conditions in the study area was analyzed.

MATERIAL AND METHODS

Study Area

The sediment in the YRB mainly comes from the Loess Plateau in the middle reaches. Considering that the sediment from the Fenhe River Basin has been stable at extremely low levels in the past 40 years, it is not included in the study area. Therefore, the study area in this article includes four subregions, namely, the HLR, the area above Liujiahe in the Beiluo River Basin (BLR), the area above Jingcun in the Jinghe River Basin (JHR), and the area above Tuoshi in the Weihe River Basin (WHR), also known as the main sediment yield region of the YRB (**Figure 1**).

The upper reaches of the Wuding River Basin and the upper reaches of the Tuwei River Basin in the HLR are mostly covered by sand, and the erosion modulus in most areas is relatively small. Moreover, 55% of the medium and large reservoirs and 1/3 of the small reservoirs in the HLR are concentrated, and there is very little sediment moving downstream, therefore, it is not included in the study area of this paper. The study area is 163,500 km^2, mainly in the loess hilly and gully area of the Loess Plateau, with some feldspathic sandstone area. According to the measured data from 1934–1959, the average annual sediment discharge in the study area is 1.495 billion tons, accounting for 86.9% of the total sediment discharge in the region above Tongguan station in the YRB.

Data

Precipitation Data

The precipitation data from the 436 precipitation stations from 1966 to 2018 were from the hydrological yearbook and Hydrological Bureau of Yellow River Conservancy Commission (**Figure 1**). The annual precipitation with daily

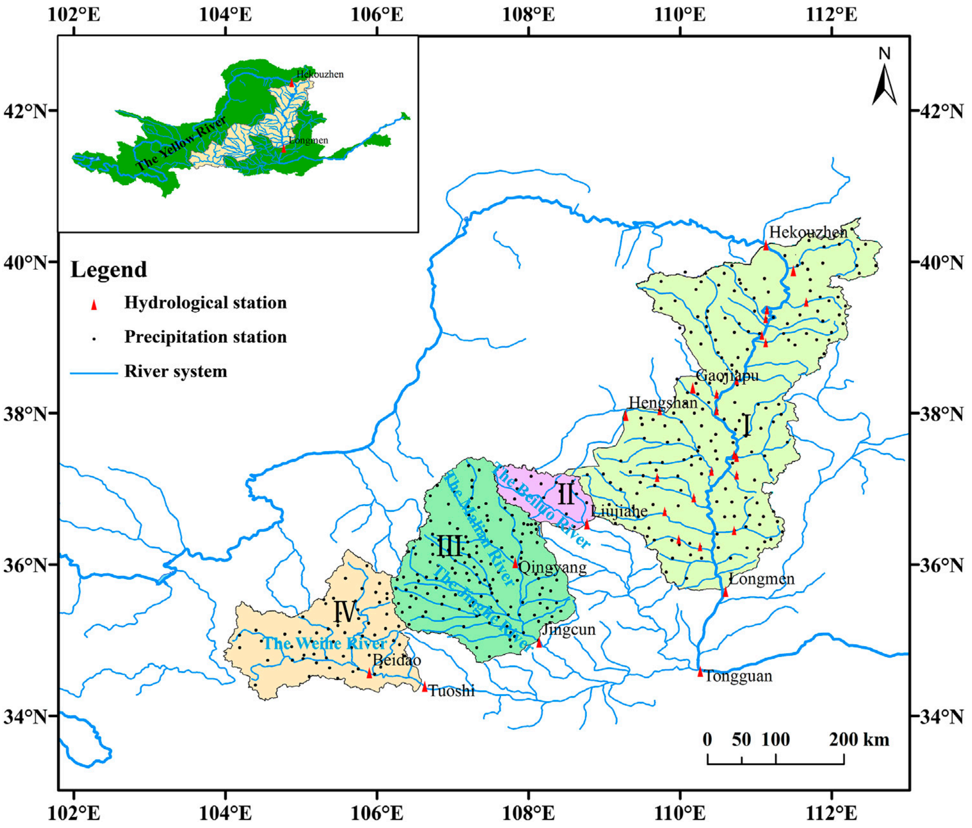

FIGURE 1 | Sketch map of the study area: I. HLR (excluding the sandy area in the upper reaches of the Wuding River Basin and Tuwei River Basin); II. BLR; III. JHR; and IV. WHR.

rainfall greater than 10, 25, 50, and 100 mm for each station was calculated, represented by P_{10}, P_{25}, P_{50} and P_{100}, respectively, and in units of mm. The surface average precipitation of each watershed or subregion was interpolated by the Thiessen polygon method.

Based on historical extreme precipitation records in the main sediment-yielding area in the middle reaches of the Yellow River, three extreme precipitation scenarios were constructed in this study.

Scenario A

Most of the rainfall in the Loess Plateau does not produce runoff and sediment (Tang, 2004; Wang et al., 2019), and the measured data show that the main factor that determines the annual sediment load of the YRB is several heavy storms or extraordinarily heavy storms, most of which have rainfall of more than 50 mm (Wang et al., 2019). According to the statistics of annual P_{50} and the corresponding sediment yield of typical tributaries in the middle reaches of the YRB, although the proportion of P_{50} in annual rainfall is only 2.3–7.8%, the corresponding sediment yield accounts for 44% of the annual sediment yield, of which the proportion of the HLR reached 50.5% (Liu et al., 2016).

The analysis of the changes in P_{50} and P_{100} in the study area from 1966 to 2018 showed that except in 2011 and 2015, the heavy rainfall in the other seven years since 2010 was significantly higher and was the most abundant period since 1966, as shown in **Figure 2**. During this period, P_{50} was 43.5% more than its multiyear average value, and P_{100} was 93.7% higher. It is assumed that the years with the heaviest rainstorms in each tributary since 2010 are all relocated to one year, indicating that all tributaries have experienced the heaviest rainstorm measured from 2010 to 2018 in the same year, but not simultaneously. This extreme precipitation scenario is called scenario A.

For scenario A, the covered areas of maximum daily rainfall ≥50 mm and maximum daily rainfall ≥100 mm are 153,900 and 45,500 km^2, respectively (**Figure 3A**), and the regional average rainfall of P_{50} and P_{100} is 142.3 and 39.1 mm, respectively. As shown in **Figure 3**, this value is much larger than that of any other year from 1966 to 2018. The area with P_{50} reaching three times of the average annual P_{50} from 1966 to 2018 accounts for approximately 70% of the study area.

Scenario B

The rainstorm in August 1933 was the most famous rainstorm in the Loess Plateau. The measured sediment discharge at Shanxian station in that year was 3.91 billion tons, which was the largest since 1919. The rainstorm formed the largest flood peak (22,000 m^3/s) at Shanxian station in the main stream of the Yellow River since 1919, the second largest flood peak at

Zhangjiashan station in the Jinghe River, Longmen station in the Yellow River and Xianyang station in the Weihe River since 1919. The maximum 12 days flood volume at the Shaanxi section was 9.07 billion m^3, which was ranked as the largest flood in the YRB since 1919 (Yellow River Conservancy Commission, 2008). Therefore, the flood in 1933 was recognized as a rare hydrological event in the YRB (Liu, 2016), and the flood control department of the Yellow River Conservancy Commission always took it as a key flood prevention object (Yellow River Conservancy Commission, 2008).

Based on the rainstorm analysis results in 1933 (Zheng, 1981; Shi and Yi, 1984), the P_{50} and P_{100} in 1933 in the study area were calculated by using the relationship between rainfall and sediment discharge in 1956–1975, known as scenario B. The results showed that the regional average rainfall of P_{50} and P_{100} in the study area in 1933 was 122.2 and 76.4 mm, respectively. Among them, the P_{50} of the HLR, WHR, JHR and BLR in 1933 were 90.8, 111.3, 188.8, and 180.4 mm, respectively. **Figure 5** shows the estimated ranges of P_{50} and P_{100} during the entire flood season of 1933, with a total rainfall of 23.88 billion m^3. The coverage area of maximum daily rainfall ≥50 mm is 122,000 km^2 (**Figure 3B**), which is less than that of scenario A. However, the range of maximum daily rainfall ≥100 mm is 69,500 km^2, which is 1.5 times that of scenario A.

Scenario C

It can be seen from **Figure 3A** and **Figure 3B** that the rainstorm center of scenario A is mainly located in the HLR, and P_{50} and P_{100} are larger than that of scenario B (**Table 2**). The rainstorm center of scenario B is mainly located in the BLR, JHR and WHR, and the P_{50} and P_{100} in these three regions are larger than those of scenario A (**Table 1**). Therefore, when designing the extreme precipitation scenario, both the rainstorm amount and the distribution of the storm center were considered, and scenarios A and B were combined. That is, the rainfall data of scenario A were used in the HLR, while the rainfall data of scenario B were used in other areas to construct a new extreme rainfall scenario, scenario C. The proportion of rainfall coverage area of the maximum daily rainfall ≥50 mm and maximum daily rainfall ≥100 mm for scenario C in the study area was 92.7 and 56.2%, respectively (**Figure 3C**). **Table 2** shows that the regional average rainfall of P_{50} and P_{100} in the study area is 159.9 and 83.7 mm, respectively, and both P_{50} and P_{100} in the study area and each subregion were the largest in scenario C.

Sediment Data

The sediment discharge data from 1966 to 2018 were from the hydrological yearbook and Hydrological Bureau of Yellow River Conservancy Commission. The locations of the hydrological stations are shown in **Figure 1**. The sediment yield capacity of the basin is expressed by the sediment yield index (S_i), which refers to the sediment yield per unit area per unit of rainfall in the erosion-prone area of the basin, in units of t/(km^2 mm). The rainfall index $P_{25,}$ which is more sensitive to the sediment yield in the basin, was used to calculate S_i.

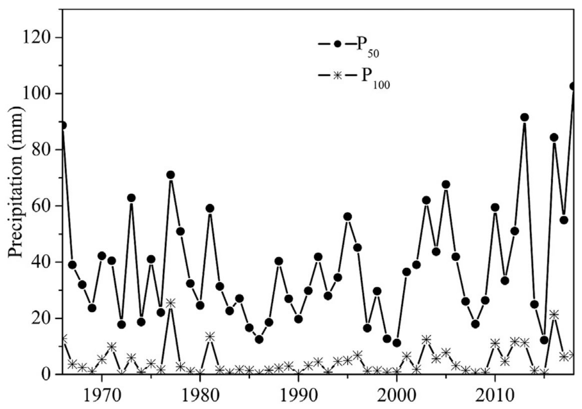

FIGURE 2 | Changes in P_{50} and P_{100} in the study area from 1966 to 2018.

$$S_i = \frac{W_s}{A_e} \times \frac{1}{P_{25}} \tag{1}$$

where S_i is the sediment yield index, t/(km^2 mm); W_s is the annual sediment yield of the basin, 10^4 t; A_e is the area of erosion-prone area of the basin, km^2; and P_{25} is the rainfall index, mm.

Vegetation Data

Vegetation coverage of forest and grassland (referred to as forest and grassland coverage) refers to the proportion of the projected area of leaves and stems of forest and grassland (A_{ls}) to the area of forest and grassland in erosion-prone areas (A_v), represented by V_c (%), and can be calculated as follows.

$$V_C = A_{ls} / A_v \tag{2}$$

On a large spatial scale, the normalized difference vegetation index (NDVI) extracted from remote sensing images can be used to calculate V_c (Carlson and Ripley, 1997) as follows:

$$\begin{aligned} V_C &= (NDVI - NDVI_{soil}) / \left(NDVI_{veg} - NDVI_{soil}\right) \\ NDVI &= (NIR - R) / (NIR + R) \end{aligned} \tag{3}$$

where $NDVI_{soil}$ is the $NDVI$ value of the bare soil or no vegetation coverage area; $NDVI_{veg}$ is the $NDVI$ value of the fully vegetated areas; NIR is the near infrared band; and R is the red light band. The $NDVI$ values used in each year are the maximum for that year. The NDVI data of the HLR from 2000 to 2018 were obtained from MODIS satellite remote sensing images with a spatial resolution of 250 m.

V_c can reflect the vegetation coverage in forest and grassland itself but cannot reflect the projected degree of vegetation to the erosion-prone area of the whole basin. Therefore, the concept of forest and grassland vegetation coverage in the erosion-prone area is introduced, and it refers to the proportion of A_{ls} in the erosion-prone area of the basin (A_e), which is expressed as V_e (%) and referred to as the effective forest and grassland coverage. The calculation formula is as follows:

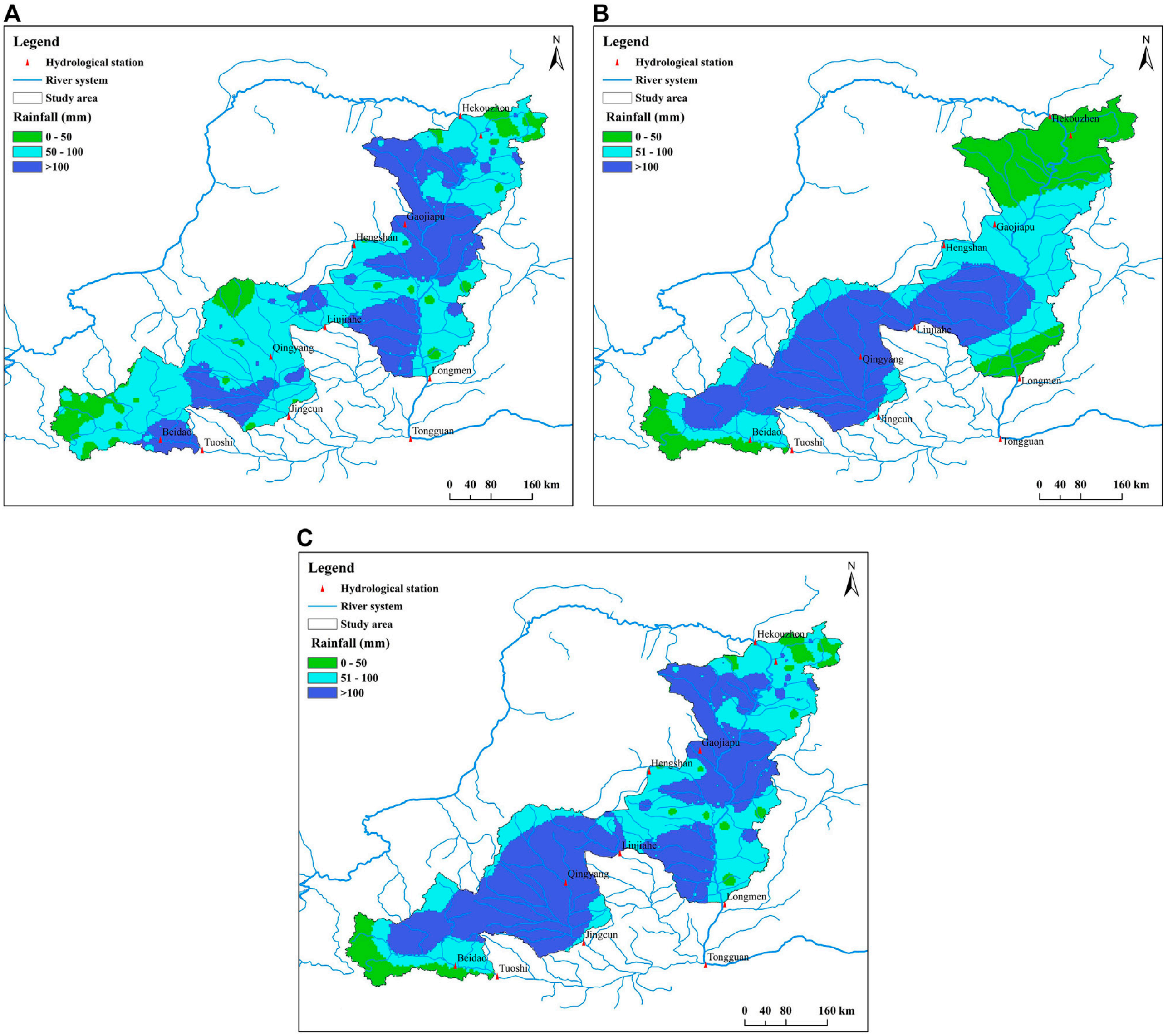

FIGURE 3 | The covered area of rainstorms for **(A)** scenario A, **(B)** scenario B and **(C)** scenario C in the study area.

$$V_e = \frac{A_{ls}}{A_e} = \frac{A_{ls}}{A_v} \times \frac{A_v}{A_e} = V_c \times \frac{A_v}{A_e} \tag{4}$$

The erosion-prone areas and the forest and grassland areas in the study area in 2010 were obtained based on the satellite remote sensing images of HJ CCD with a spatial resolution of 30m (Liu et al., 2014a; Liu et al., 2018).

Terraces Data

The construction of terraces is also an important human activity that affects sediment yield. The terrace area in the study area in 2012 and 2017 was obtained from China Resources No. 3 satellite remote sensing data with a spatial resolution of 2.1 m. The images are mainly from January to May and partly from October to December to minimize the impact of dense vegetation on the identification of terraces. The terrace area of each tributary before 2012 was obtained from the statistics of counties. To scientifically describe the scale of terraces in different regions, the concept of effective terrace coverage (T_e) is introduced, and it refers to the proportion of terrace area to the erosion-prone area in the basin, in units of %. Then, the effective coverage of forest, grassland and terraces (V_{et}, %) is the sum of V_e and T_c.

Methods

Precipitation Frequency Distributions

To describe the characteristics of the precipitation series and the probability of extreme precipitation, it is necessary to identify the optimal fitting statistical models. Three commonly used statistical models, i.e., generalized extreme value distribution, generalized Pareto distribution (GP) and Pearson type III distribution (PE3),

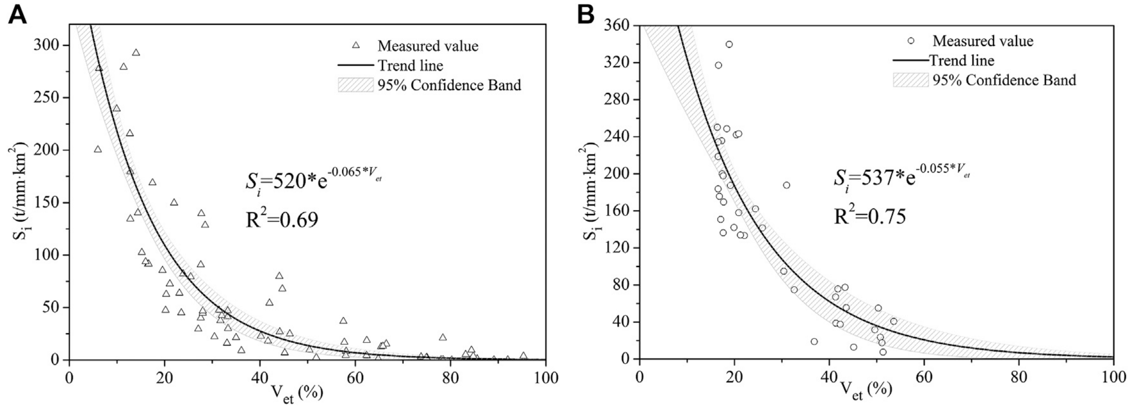

FIGURE 4 | The relationships between S_i and V_{et} in the loess hilly area **(A)** and feldspathic sandstone area **(B)**.

TABLE 1 | Precipitation in different scenarios in the study area.

Scenarios	Precipitation index	Precipitation (mm)				
		HLR	BLR	JHR	WHR	Study area
Scenario A	P_{50}	158.6	121.7	158.6	86.9	142.3
	P_{100}	60.4	27.1	28.2	14.0	39.1
Scenario B	P_{50}	90.8	180.4	188.8	111.3	122.2
	P_{100}	47.6	121.4	145.0	58.7	76.4
Scenario C	P_{50}	158.6	180.4	188.8	111.3	159.9
	P_{100}	60.4	121.4	145.0	58.7	83.7

were used in this study to fit the precipitation series. The cumulative distribution functions of the selected models are shown in **Table 2**.

The L-moments method proposed by Hosking is a convenient and robust method for parameter estimation (Hosking, 1990; Hosking, 1997; Hosking and Wallis, 1997; She et al., 2013; Chen et al., 2014), and it was used to estimate the parameters of the three selected models in this study. The optimal distribution was selected by three goodness-of-fit methods: the Kolmogorov-Smirnov (K-S) test method, Akaike Information Criterion (AIC) and OLS (Akaike, 1974).

The test statistic of the K-S method can be calculated as

$$D_n = \max_{1 \le i \le n} \left[\frac{i}{n} - F_0\left(x_{(i)}\right), F_0\left(x_{(i)}\right) - \frac{i-1}{n} \right] \tag{5}$$

where $x_{(i)}$ is the empirical frequency, $F_0\left(x_{(i)}\right)$ is the function of the cumulative distribution, and n is the sample size. If D_n is smaller than the critical value $D_\alpha(n)$ at the significance level α, a particular distribution is considered a significantly fit model to the precipitation data. The probability distribution that corresponds to the minimum value of D_n represents the optimal distribution in presenting the distribution of precipitation series.

The *OLS* and *AIC* can be calculated as follows:

$$OLS = \sqrt{\frac{1}{n} \sum_{i=1}^{n} \left(p_{ei} - p_i\right)^2} \tag{6}$$

TABLE 2 | The cumulative distribution functions (CDF) and precipitation amount under the return period of T years of GEV, GP and PE3 distributions.

Distribution	CDF	Precipitation amount under the return period of T years
GEV	$F(x) = \exp\{-[1-(k(x-\xi))/\alpha]^{1/k}\}$	$X_T = \widehat{\xi} + \frac{\widehat{\alpha}}{\widehat{k}}\left(1-(-\ln(1-1/T))^{\widehat{k}}\right)$
	$F(x) = 1 - e^{-y}\ k \neq 0$	
	$y = -\ln[1-k(x-\xi)/\alpha]/k, k \neq 0$	$X_T = \widehat{\xi} + \frac{\widehat{\alpha}}{\widehat{k}}\left(1-(1/T)^{\widehat{k}}\right)$
GP	$y = (x-\xi)/\alpha, k = 0$	
PE3	$F(x) = \frac{\alpha^k}{\Gamma(k)} \int_x^\infty (x-\xi)^{k-1} e^{-(x-\xi)\alpha} dx$	$X_T = F^{-1}(F(X_T))$

α, ξ and k are the scale, location and shape parameters, respectively.

$$AIC = n \log(RSS/n) + 2m \tag{7}$$

where P_{ei} is the empirical frequency, P_i is the theoretical frequency, *RSS* is the residual sum of squares, and *m* is the number of parameters. The distribution with the minimum values of *OLS* or *AIC* was selected. If the results given by these three goodness-of-fit methods were different, the best-fit model was selected by the result of the K-S test.

The return period values can be obtained from the best-fitted distribution.

Prediction of Sediment Yield

Rainfall and land surface conditions are the key factors influencing sediment yield, among which vegetation, soil and terrain are the main land surface factors. The terrain and soil are relatively stable for a region, but the vegetation in the study area has changed significantly in recent years (Feng et al., 2016). To analyze the relationship between vegetation change and sediment yield in the study area, and ensure that the sediment yield change is only the result of vegetation change, the selected sample watershed should have few terraced fields, preferably have no check dams or reservoirs, or alternatively, the sediment volume of check dams and

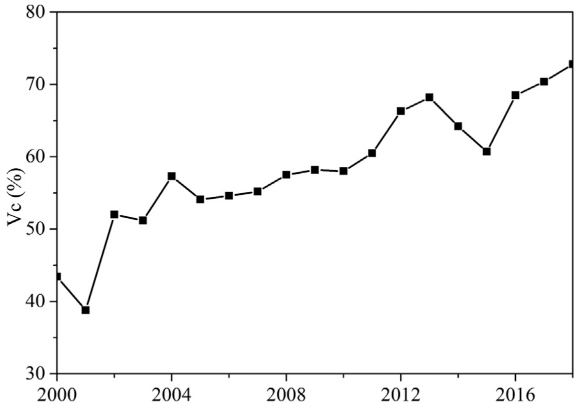

FIGURE 5 | Changes in vegetation coverage in the HLR from 2000 to 2018.

reservoirs can be accurately obtained, and there are no alluvial channels in the sample watershed. Based on these principles, 77 and 40 pairs of data were selected in the loess hilly area and feldspathic sandstone area to analyze the relationships between S_i and V_e. By calculating S_i and V_e in different sample watersheds with **Eqs 1**, **4**, respectively, the relationship between S_i and V_e was established on the watershed scale. When calculating the sediment yield in a basin by using the sediment yield index, the effective coverage of terraces (T_e) was equally included in V_e (Liu et al., 2014b; Liu et al., 2014c), and V_e was changed to V_{et}. The exponential relationships between S_i and V_{et} in the loess hilly area and feldspathic sandstone area are shown in **Figure 4**, which can be expressed by **Eqs 8**, **9**, respectively, and the correlation coefficients were 0.69 and 0.75, respectively.

$$S_i = 520 \times e^{-0.065 \times V_{et}} \tag{8}$$

$$S_i = 537 \times e^{-0.055 \times V_{et}} \tag{9}$$

According to **Figure 6**, it can be seen that the sediment yield index S_i decreases with the increase of the effective forest and grass coverage rate V_{et}, and the two are exponentially related. In the range of $V_{et} \leq 40$–45%, S_i decreases rapidly with the increase of V_{et}. However, when V_{et} is greater than 40–45%, S_i decreases slowly with the improvement of vegetation. Especially when V_{et} is greater than 60%, the S_i value of 75% of the sample points is less than 7 t/(km^2 a).

Based on the relationship between S_i and V_{et} , the following steps can be used to predict the sediment yield of the basin under different underlying surface and precipitation scenarios. First, vegetation and terrace data were obtained by satellite remote sensing images to calculate V_{et}. Second, S_i was calculated according to the relationship of S_i and V_{et} as expressed in **Eqs 8–9**. Finally, according to the definition of the sediment yield index, the sediment yield of the basin can be calculated as follows.

$$W_s = S_i \times A_e \times P_{25} \tag{10}$$

RESULTS

Frequency Analysis of Extreme Precipitation

Three distribution functions, generalized extreme value, GPD and PE3, were used to fit the P_{50} and P_{100} series in the study area, and the results are shown in **Table 3**. The optimal distribution function of the P_{50} series is PE3, and the optimal distribution function of the P_{50} series is generalized Pareto. The sample size of the P_{50} and P_{100} series is 53, and the critical value of the K-S test is 0.1868 at the significance level of 0.05. According to the K-S test results in **Table 3**, both of the optimal distribution functions of the P_{50} and P_{100} series passed the significance test.

The probability distribution function corresponding to the bolded values is the distribution function most suitable for the P_{50} or P_{100} series. The smaller the goodness-of-fit test value is, the better the probability distribution function.

According to the optimal probability distribution function of the P_{50} series, the recurrence periods of P_{50} under extreme precipitation scenarios A, B and C are 250, 116, and 460 years, respectively, and scenario C has the largest recurrence period. Therefore, scenario C was used in this paper as an extreme precipitation scenario to calculate the potential sediment yield in the study area in the future.

Calculation of the Sediment Yield Under Extreme Precipitation

The sediment yield under current land surface conditions in the study area was composed of two parts, that is, the sediment yield in the HLR was calculated using the sediment yield index, and the sediment yield in the other regions was calculated according to the relationships between rainfall and sediment yield from 2010 to 2018.

Sediment Yield in the HLR

According to the change in vegetation coverage in the HLR from 2000 to 2018 (**Figure 5**), the vegetation coverage in the HLR has been improved continually since 2000. After 2012, the vegetation coverage significantly improved compared with that in 2000–2011 and tended to be stable. Moreover, the terrace area and the quantity of check dams and reservoirs in the HLR have been basically stable since 2012, so the land surface for 2012–2018 was set as the current land surface.

Based on the remote sensing data of vegetation, terraces, and dam field, V_{et} in different tributaries was calculated first, and then S_i under the current underlying surface of each tributary in the HLR was calculated using formulas **8**, **9**. At the 95% confidence level, the S_i for each tributary was shown in Table 4. According to the calculation result of S_i , the areas with higher sediment yield capacity are mainly distributed in the northwest region of the HLR. By using A_e , P_{25} of the extreme precipitation scenario C and the calculated S_i of each tributary, the sediment yield in the case of large-scale extreme rainfall in the HLR can be calculated by formula **Eq. 10**, which is range from 496.4 million tons to

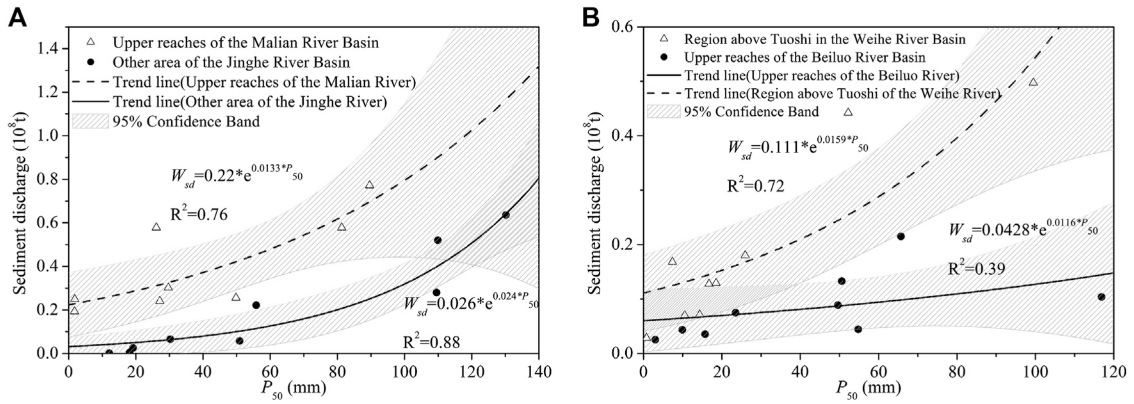

FIGURE 6 | The observed rainfall and annual sediment discharge of **(A)** the JHR and **(B)** the WHR and BLR from 2010 to 2018.

TABLE 3 | Goodness-of-fit test results of the P_{50} and P_{100} series in the study area

Series	Test	Distributions		
		GEV	GPD	PE3
P_{50}	K-S	0.0439	0.0703	**0.0405**
	AIC	−199.5	−186.2	**−208.9**
	OLS	0.0207	0.0266	**0.0173**
P_{100}	K-S	0.1079	**0.07**	0.9815
	AIC	−157.3	**−182.7**	−23.4
	OLS	0.0459	**0.0284**	0.5741

TABLE 4 | Sediment yield index of the main tributaries in the HLR under current underlying surface conditions [t/(km^2 mm)].

Tributary	Si	Tributary	Si
Huangfuchuan river basin	51.7–75.1	Pianguan river basin	6.4–11.6
Gushanchuan river basin	10.1–6.8	Xianchuan river basin	5.8–10.7
Kuye river basin	5.8–10.7	Zhujiachuan river basin	7.1–12.9
Jialu river basin	18.2–29.7	Lanyi river basin	8.2–14.6
Wuding river basin	24.4–38.5	Qingliangsigou watershed	3.4–6.7
Qingjian river basin	5.7–10.6	Qiushui river basin	6.7–12.2
Yanhe river basin	3.9–7.4	Sanchuan river basin	6.7–12.1
Yunyan river basin	1.1–2.4	Quchuan river basin	11.1–19.1
Shiwangchuan river basin	0.7–1.6	Xinshui river basin	6.1–11.2

TABLE 5 | Relationships between W_{sd} and P_{50} of the JHR, WHR and BLR.

Regions		Relationship between W_{sd} and P_{50}	R^2
JHR	Upper reaches of the Malian river basin	$W_{sd} = 0.22 \times e^{(0.0133 \times P_{50})}$	0.76^a
	Other area	$W_{sd} = 0.026 \times e^{(0.024 \times P_{50})}$	0.88^a
WHR		$W_{sd} = 0.111 \times e^{(0.0159 \times P_{50})}$	0.72^a
BLR		$W_{sd} = 0.0428 \times e^{(0.0116 \times P_{50})}$	0.39^a

W_{sd} is the annual sediment discharge, 10^8 t; P_{50} *is the precipitation index, mm.*
^{a}Represents the regression equation is significant at the 95% confidence level.

758.2 million tons. The tributaries with large sediment yields include the Wuding River Basin, the Huangfuchuan River Basin and the Kuye River Basin. It is worth noting that the sediment yield of the Kuye River Basin is larger, but the sediment yield index is smaller. The sediment yield index of the Jialu River Basin is relatively large, and it still has high sediment yield capacity.

Sediment Yield in the Other Areas

The annual sediment yield in the other regions of the study area was calculated according to the relationships between rainfall and annual sediment yield from 2010 to 2018.

Based on the measured rainfall and annual sediment discharge data from 2010 to 2018, the relationships between rainfall (P_{50}) and annual sediment discharge (W_{sd}) in the upper reaches of the Malian River Basin, the other regions of the Jinghe River Basin, BLR and WHR were established under the current land surface conditions (**Figure 6** and **Table 5**). Then, using the P_{50} of extreme rainfall scenario C in each region, the W_{sd} in the upper reaches of the Malian River Basin and other areas of the Jinghe River Basin were from 89.6 million tons to 468.3 million tons and from 139.8 million tons to 457.5 million tons at the 95% confidence level, respectively, and the W_{sd} in the BLR and WHR were from 7.8 million tons to 59.6 million tons and from 36.1 million tons to 94.4 million tons at the 95% confidence level, respectively. If the sediment deposited in the check dams and reservoirs was added, the maximum annual sediment yield of the JHR would reach 967.4 million tons, while those of the BLR and WHR would be 61.2 million tons and 102.7 million tons, respectively. And the minimum annual sediment yield of the JHR would be 271.0 million tons, while those of the BLR and WHR would be 9.4 million tons and 44.4 million tons, respectively.

In summary, under the current underlying surface conditions, the annual sediment yield in the study area is range from 0.821 billion tons to 1.889 billion tons under extreme precipitation, and the median annual sediment yield is 1.355 billion tons. The median annual sediment yield of the HLR, JHR, WHR and BLR was 627.3 million tons, 619.2 million tons, 73.5 million tons, and 35.3 million

TABLE 6 | Annual sediment discharge and sediment yield in the HLR under extreme rainfall.

Regions	Year	W_{sd} (10^8 t)	W_{sc} (10^8 t)	W_{sr} (10^8 t)	W_r (10^8 t)
Huangfuchuan RB, Qingshuichuan RB, Gushanchuan RB, region above Xinmiao in the Kuye RB, Jialu RB, Pianguan RB, Xianchuan RB, Zhujiachuan RB, uncontrolled area between Hekouzhen and Fugu section	2012	0.569	0.767	0.260	6.614
Kuye RB (except the area above Xinmiao), Tuwei RB, Qiushui RB, Qingliangsigou RB, uncontrolled area between Fugu and wubu section	2016	1.126	0.835		
Wuding RB, Sanchuan RB	2017	0.911	0.497		
Area between wubu and longmen section, Hunhe RB	2013	1.046	0.603		
Total	—	3.652	2.702	0.260	6.614

RB is short for river basin, W_{sc} represents the sediment deposited in the check dams, and W_{sr} represents the sediment deposited in the reservoirs. The year at the head of the second list indicates the year with the largest sediment discharge. Data source: Liu et al., 2019.

tons, respectively. The annual sediment yield of HLR and JHR accounted for 91.9% of the total sediment yield in the study area. The areas with high sediment yield capacity are the Wuding River Basin, Huangfuchuan River Basin and Jialu River Basin in the HLR and the area above Qingyang in the Jinghe River Basin.

DISCUSSION

Rationality Analysis of the Calculated Sediment Yield

The calculated sediment yield in the HLR was verified by the restored sediment yield, which is the sum of measured sediment discharge and the sediment deposited in the check dams and reservoirs. In scenario C, the measured sediment discharge of each tributary in the year with the maximum rainstorm during 2010–2018 in the HLR was added up, and the result was the measured sediment discharge under the current land surface conditions and this extreme precipitation scenario. Then, the sediment yield under the current land surface conditions and this extreme precipitation scenario can be obtained by adding the sediment deposited in the check dams and reservoirs in the corresponding year of each tributary.

For tributaries controlled by hydrological stations (hereinafter referred to as controlled tributaries), the maximum annual sediment discharge from 2010 to 2018 can be directly obtained from measured data. For the area of 25,500 km^2 not controlled by hydrological stations in the HLR (hereinafter referred to as uncontrolled area), the maximum annual sediment discharge from 2010 to 2018 was calculated, according to the area ratio based on the assumption that the sediment discharge per unit area of controlled tributaries is the same as that of the uncontrolled area. Based on the measured data from 2010 to 2018, the annual sediment discharge and sediment yield (W_r) in the HLR under extreme precipitation were calculated to be 365.2 million tons and 661.4 million tons (**Table 6**), respectively.

According to the sediment yield index method, the annual sediment yield in the HLR is range from 496.4 million tons to 758.2 million tons, and the median calculated annual sediment yield is 627.3 million tons, which is 5.2% smaller than the W_r. The results of annual sediment yield calculated by the two methods are similar, indicating that the annual sediment yield based on the sediment yield index is reliable and can be used to predict annual sediment yield in the HLR under different rainfall scenarios in the future.

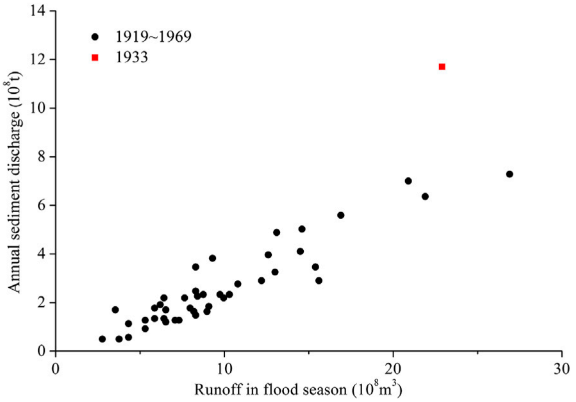

FIGURE 7 | Comparison of runoff in the flood season and annual sediment discharge relationships at the Zhangjiashan station in the Jinghe River Basin in 1933 and other years.

The Effect of Gravity Erosion on Sediment Yield

Gravity erosion refers to the process of deformation, destruction, movement and accumulation of rock and soil on the slope under the action of gravity, including collapse, landslide, mud flow and so on. Gravity erosion is an important component of soil erosion (Neill and Mollard, 1982; Wetzel, 1994). Due to the large porosity, vertical joints and fragility of the loess (Derbyshire, 2001), collapse and landslide events are common in the Loess Plateau (Zhang et al., 2009; Zhang and Liu, 2010). Due to the fragile natural environment and intensified human activities, gravity erosion in the Loess Plateau is particularly serious, and its occurrence and development have an important impact on erosion and sediment yield in the basins (Cai, 1997; Han et al., 2011; Yang et al., 2013). Gravity erosion not only affects the total amount of soil erosion but also increases the sediment concentration of water flow to 1,000 kg/m^3 (Li et al., 2009).

In 1933, the sediment discharge at the Zhangjiashan station in the Jinghe River Basin was 1.17 billion tons. The relationship between the annual sediment discharge and runoff during the flood season (**Figure 7**) shows that the sediment discharge of the Jinghe River Basin was unusually high in 1933. This outcome is related not only to the large-scale and high-intensity rainstorms in the basin but also to gravity erosion during the continuous 11 years dry period from 1922 to 1932. The Jinghe River Basin has a special landform, most of which belongs to the loess tableland area, and gravity erosion accounts for a high proportion of sediment yield in the basin. The measured data of the small Nanxiaohegou watershed in the basin from 1955 to 1974 showed that the sediment yield from gravity erosion accounts for 57.4% of the annual sediment yield (Tian et al., 2008), while the proportion of sediment yield by gravity erosion in the loess hilly area generally accounts for no more than 25%.

Gravity erosion occurs all year round in the Loess Plateau, and the erosion products accumulate at the foot of gullies and slopes and are carried out of the gullies when heavy rains and floods occur (Tian et al., 2008). During the 11 years continuous drought in 1922–1932, gravity erosion still occurred, which increased the sediment supply sources during the heavy rainfall flood in 1933. Therefore, the sediment yield in the study area affected by gravity erosion should be greater than the current calculated value, when extreme rainfall occurs after continuous drought.

The randomicity of gravity erosion is large, so it is difficult to perform effective continuous observations at fixed points in the field. Field investigation is an important method for the study of gravity erosion in typical areas and has been widely used (Shakoor and Smithmyer, 2005; Wang et al., 2016). The rare Earth tracer method (Shi et al., 2012; Heimsath, 2014), remote sensing technology and other new methods and technologies have been applied to the monitoring of gravity erosion (Velicogna and Wahr, 2006; Roering et al., 2009; Zhao et al., 2012; Fuller et al., 2016), but gravity erosion and hydraulic erosion still cannot be distinguished. It is easier to measure large-scale landslides with remote sensing technology, but it is more difficult to monitor gravity erosion with small volumes. Therefore, the establishment of a new method for the quantitative observation of gravity erosion and the quantitative analysis of sediment yield by gravity erosion would be a focus and challenge for future research.

Impact of Check Dam on Sediment Discharge

The survey shows that there are 55,124 check dams in the Loess Plateau above Tongguan station, including 5,546 main check dams, 8,596 medium-sized dams, and 40,982 small dams, about 88% of which are located in the HLR and BLR. The designed sediment retention life of main check dams, medium-sized dams and small-sized dams is 15–30 years, 5–10 years, and 3–5 years, respectively. 33% of main dams, 57% of medium-sized dams and 85% of small-sized dams were built before 1979 and distributed in the HLR and BLR. After decades of sand interception, about 46% of large and medium-sized dams and 95% of small dams have lost their sand control capacity. Moreover, many check dams are aging and out of repair, making them at great risk of water damage. In the future, once it encounters a large-scale extreme rainstorm, it is very likely to appear the phenomenon of mass water destruction, increasing sediment discharge.

Effects of Reverse Vegetation Development Risk on Sediment Yield

The significant improvement of forest and grass vegetation in the Loess Plateau occurred mainly after 1998, especially from 2006 to 2008 (Liu et al., 2016; Jia et al., 2019). People and sheep leaving the land is the main social reason, followed by planting trees and grass, suitable rainfall and temperature conditions, which are the main driving force of natural vegetation restoration in recent years (Liu et al., 2016). The contribution of vegetation improvement to sediment reduction accounts for about 50% (Liu et al., 2016; Gao et al., 2019). If the Loess Plateau can continue to implement the policies of returning farmland to forest and grassland, forbidding grazing and natural restoration, and the social and economic environment can remain stable, the future vegetation status in the study area will be mainly determined by the objective laws of local vegetation succession. However, the ecological environment in the main sediment-yielding area of the Yellow River basin is very fragile. The fluctuation of climatic conditions and human production activities will significantly affect the forest and grass vegetation conditions.

Uncertainties

The maximum sediment yield scenario projected in this paper is based on the current underlying surface conditions and the constructed extreme rainfall scenario in the study area. The uncertainty of the calculation results mainly comes from three aspects. Firstly, uncertainties associated with the input data may still exist, even though the data used in this study has undergone rigorous quality control. Rainfall is a key driving force for regional erosion and sediment yield. The uncertainty of extreme rainfall prediction and the influence of rainfall spatial distribution will increase the uncertainty of sediment yield forecast. Both the extreme rainfall scenarios constructed in this study and the prediction results of the Global Climate Model are subject to certain uncertainties. The simulation results of hydrological models show that the rainfall intensity and spatial distribution of rainstorm have significant influence on the simulation of runoff and sediment yield, and the uncertainty of simulated sediment yield is greater than that of rainfall (Chaubey et al., 1999; Hao et al., 2003; Inamdar and Naumov, 2006). Secondly, the model adopted is a statistical model, which lacks mechanism analysis of the influence of different factors on sediment yield. In particular, the calculations of the JHR, WHR and BLR only use the measured data in recent years to establish the relationship between rainfall and sediment yield, and the data series are relatively short. Thirdly, the interference of human activities may cause statistical models to be inapplicable in the future. It is necessary to further determine the definable observables of human activities, as well as the specific functions or regression equations between it and other natural elements and the sediment yield of the watershed. This will be the focus and challenge for future research.

CONCLUSION

In this study, the extreme precipitation scenario of the main sediment-yielding areas in the middle reaches of the YRB was constructed, and the corresponding sediment yield under the current underlying surface conditions was calculated. The results showed that the areal rainfall of rainstorms in the constructed extreme rainfall scenario was 159.9 mm, and the recurrence period was 460 years. The corresponding annual sediment yield of the study area was range from 0.821 billion tons to 1.899 billion tons, and the median value is 1.355 billion tons. The median annual sediment yield of the HLR, JHR, WHR and BLR was 627.3, 619.2, 73.5, and 35.3 million tons, respectively. The annual sediment yield of HLR and JHR accounted for 91.9% of the total sediment yield in the study area. The areas with high sediment yield capacity are the Wuding River Basin, Huangfuchuan River Basin and Jialu River Basin in the HLR and the area above Qingyang in the Jinghe River Basin. If extreme rainfall occurs after a continuous drought period, the sediment yield in the study area would be greater.

Although the vegetation in the Loess Plateau has been greatly improved in recent years and large-scale terraces and check dams have been built, the sediment yield of the YRB will still be large if extreme rainfall occurs. The water and sediment regulation projects and flood control projects in the YRB must always be prepared for major floods and large sediment discharge. The main factors of erosion and sediment yield were changed by vegetation improvement in the Loess Plateau, this study only discusses the regional sediment yield of extreme rainfall under the current land surface conditions, and the change of regional sediment yield should be studied in the future by combining vegetation change and other factors.

DATA AVAILABILITY STATEMENT

The datasets generated for this study will not be made publicly available as they are licensed by the Hydrological Bureau of Yellow River Conservancy Commission. Requests for the original datasets can be directed to the Hydrological Bureau of Yellow River Conservancy Commission, Email: swjyrcc@sohu.com.

AUTHOR CONTRIBUTIONS

All authors contributed to this study. SD analyzed the data; XL provided important advice on the results of this study; HY and XG contributed to data collection and processing. SD wrote the main manuscript, and all authors reviewed the manuscript and contributed to editing it.

FUNDING

This research was supported by the National Key R&D Program of China (2017YFC0403604, 2016YFC0402403) and the National Natural Science Foundation of China (51779099, 51809104, and 51909099).

REFERENCES

Akaike, H. (1974). A new look at the statistical model identification. *IEEE Trans. Automat. Contr.* 19, 716–723. doi:10.1007/978-1-4612-1694-0_16

Alexander, L. V., Zhang, X. B., Peterson, T. C., Caesar, J., and Vazquez-Aguirre, J. L. (2006). Global observed changes in daily climate extremes of temperature and precipitation. *J. Geophys. Res. Atmos*. 111, D05109. doi:10.1029/2005JD006290

Buendia, C., Bussi, G., Tuset, J., Vericat, D., Sabater, S., Palau, A., et al. (2015). Effects of afforestation on runoff and sediment load in an upland Mediterranean catchment. *Sci. Total Environ.* 540, 144–157. doi:10.1016/j.scitotenv.2015.07.005

Cai, Q. G. (1997). Relationship of sediment production between hillslope and gully slope in a small basin in the hilly loess region, North China. *Int. J. Sediment Res.* 12 (3), 353–359. doi:10.13031/2013.18122

Carlson, T., and Ripley, D. A. (1997). On the relation between NDVI, fractional vegetation cover, and leaf area index. *Remote Sens. Environ*. 62 (3), 241–252. doi:10.1016/S0034-4257(97)00104-1

Chaubey, I., Haan, C. T., Salibury, J. M., and Grunwald, S. (1999). Quantifying model output uncertainty due to spatial variability of rainfall. *J. Am. Water Resour. Assoc.* 35 (5), 1113–1123. doi:10.1111/j.1752-1688.1999.tb04198.x

Chen, R. D., Wen, Y. F., Gao, P., Mu, X. M., Zhao, G. J., and Sun, W. Y. (2018). Comparative analysis of flow and sediment characteristics of the Yanhe River under extreme rainfall conditions and research on influence factors. *Acta Ecol. Sin.* 38 (6), 1920–1929 [in Chinese, with English summary].

Chen, Y., Zhang, Q., Xiao, M. Z., Singh, V. P., Leung, Y., and Jiang, L. G. (2014). Precipitation extremes in the Yangtze River Basin, China: regional frequency and spatial-temporal patterns. *Theor. Appl. Climatol.* 116 (3–4), 447–461. doi:10.1007/s00704-013-0964-3

Cheng, Y., He, H. M., Cheng, N. N., and He, W. M. (2016). The effects of climate and anthropogenic activity on hydrologic features in Yanhe River. *Adv. Meteorol.* 9, 1–11. 10.1155/2016/5297158

Comino, J. R., Senciales, J. M., Ramos, M. C., Ramos, M. C., Casasnovas, J. A. M., Lasanta, T., et al. (2017). Understanding soil erosion processes in Mediterranean sloping vineyards (Montes de Málaga, Spain), *Geoderma* 296, 47–59. doi:10.1016/j.geoderma.2017.02.021

Dang, S. Z., Liu, X. Y., Li, X. Y., Yao, M. F., and Zhang, D. (2018). Changes in different classes of precipitation and the impacts on sediment yield in the Hekouzhen-Longmen region of the Yellow River basin, China. *Adv. Meteorol.* 1–15. doi:10.1155/2018/3537512

Dang, S. Z., Yao, M. F., Liu, X. Y., and Dong, G. T. (2019). Variations and statistical probability characteristic analysis of extreme precipitation in the Hekouzhen-Longmen region of the Yellow River, China. *Asia-Pacific J. Atmos. Sci.* doi:10.1007/s13143-019-00117-w

Derbyshire, E. (2001). Geological hazards in loess terrain, with particular reference to the loess regions of China. *Earth Sci. Rev.* 54 (1–3SI), 231–260. doi:10.1016/S0012-8252(01)00050-2

Du, H. B., Wu, Z. F., Zong, S. W., Meng, X. J., and Wang, L. (2013). Assessing the characteristics of extreme precipitation over northeast China using the multifractal detrended fluctuation analysis. *J. Geophys. Res. Atmos.* 118, 6165–6174. doi:10.1002/jgrd.50487

Feng, X., Fu, B., Piao, S., Wang, S., Ciais, P., Zeng, Z. Z., et al. (2016). Revegetation in China's Loess Plateau is approaching sustainable water resource limits. *Nat. Clim. Change* 6, 1019–1022. doi:10.1038/nclimate3092

Fischer, T., Gemmer, M., Liu, L. L., and Su, B. D. (2012). Change-points in climate extremes in the Zhujiang river basin, south China, 1961-2007. *Clim. Change* 110, 783–799. doi:10.1007/s10584-011-0123-8

Frich, P. L., Alexander, L., Della-Marta, P. M., Gleason, B., Haylock, M., Klein, T. A., et al. (2002). Observed coherent changes in climatic extremes during the second half of the twentieth century. *Clim. Res.* 19, 193–212. doi:10.3354/cr019193

Fu, B. J., Wang, S., Liu, Y., Liu, J. B., Liang, W., and Miao, C. Y. (2017). Hydrogeomorphic ecosystem responses to natural and anthropogenic changes in the Loess Plateau of China. *Annu. Rev. Earth Planet Sci.* 45, 223–243. doi:10.1146/annurev-earth-063016-020552

Fuller, I. C., Riedler, R. A., Bell, R., Marden, M., and Glade, T. (2016). Landslide-driven erosion and slope-channel coupling in steep, forested terrain, Ruahine Ranges, New Zealand, 1946-2011. *Catena* 142, 252–268. doi:10.1016/j.catena.2016.03. 019

Gao, G. Y., Zhang, J. J., Liu, Y., Ning, Z., Fu, B. J., and Sivapalan, M. (2017). Spatio-temporal patterns of the effects of precipitation variability and land use/cover changes on long-term changes in sediment yield in the Loess Plateau, China. *Hydrol. Earth Syst. Sci.* 21, 4363–4378. doi:10.5194/hess-21-4363-2017

Gao, H. D., Liu, H., Jia, L. L., Pang, G. W., and Wang, J. (2019). Attribution analysis of precipitous decrease of sediment loads in the Hekou-Longmen section of Yellow River since 2000. *Acta Geograph. Sin.* 74 (09), 1745–1757 [in Chinese, with English summary]. doi:10.11821/dlxb201909004

Gao, T., and Wang, H. L. (2017). Trends in precipitation extremes over the Yellow River basin in North China: changing properties and causes. *Hydrol. Process.* 31, 2412–2428. doi:10.1002/hyp.11192

Garbrecht, J. D., Nearing, M. A., Shields, F. D., Tomer, M. D., Sadler, E. J., Bonta, V., et al. (2014). Impact of weather and climate scenarios on conservation assessment outcomes. *J. Soil Water Conserv.* 69, 374–392. doi:10.2489/jswc.69.5.374

Han, P., Ni, J. R., Hou, K. B., Miao, C. Y., and Li, T. H. (2011). Numerical modeling of gravitational erosion in rill systems. *Int. J. Sediment Res.* 26 (4), 403–415. doi:10.1016/S1001-6279(12)60001-8

Hao, F. H., Chen, L. Q., Liu, C. M., and Zhang, X. S. (2003). Model output uncertainty due to spatial variability of rainfall. *Prog. Geogr.* 22 (5), 446–453 [in Chinese, with English summary].

Heimsath, A. M. (2014). Limits of soil production? *Science* 343 (6171), 617–618. doi:10.1126/science.1250173

Hosking, J. R. M. (1990). L-moments analysis and estimation of distributions using linear combination of order statistics. *J. Roy. Stat. Soc.* 52 (1), 105–124. doi:10.2307/2345653

Hosking, J. R. M., and Wallis, J. R. (1997). *Regional frequency analysis*. Cambridge, England: Cambridge University Press.

Inamdar, S., and Naumov, A. (2006). Assessment of sediment yields for a mixed-landuse Great Lakes Watershed: lessons from field measurements and modeling [J]. *J. Great Lake. Res.* 32 (3), 471–488. doi:10.3394/0380-1330(2006)32 [471: AOSYFA]2.0.CO;2

IPCC (2012). Managing the risks of extreme events and disasters to advance climate change adaptation. A special report of Working Groups I and II of the Intergovernmental Panel on Climate Change. Cambridge, UK: Cambridge University Press. . Available at: https://www.ipcc.ch/site/assets/uploads/2018/03/SREX_Full_Report-1.pdf (Accessed October 14, 2012).

Jia, P. P., Xue, H. Z., Dong, G. T., Zhou, J. L., Yin, H. J., and Dang, S. Z. (2019). Variations of NDVI and its response to climate in Hekouzhen-Tongguan reach of the Yellow River. *Yellow River* 41 (4), 31–41 [in Chinese, with English summary].

Jiao, J. Y., Wang, Z. J., Wei, Y. H., Su, Y., Cao, B., and Li, Y. (2017). Characteristics of erosion sediment yield with extreme rainstorms in Yanhe watershed based on field measurement. *Trans. Chin. Soc. Agric. Eng.* 33 (13), 159–167. [in Chinese, with English summary]. doi:10.11975/j.issn.1002-6819.2017.13.021

Kao, S. J., and Milliman, J. (2008). Water and sediment discharge from small mountainous rivers, Taiwan: the roles of lithology, episodic events, and human activities. *J. Geol.* 116, 431–448. doi:10.1086/590921

Keo, S., He, H. Y., and Zhao, H. F. (2018). Analysis of rainfall erosivity change and its impacts on soil erosion on the Loess Plateau over more than 50 years. *Res. Soil Water Conserv.* 25 (2), 1–7. [in Chinese, with English summary].

Li, T. J., Wang, G. Q., Xue, H., and Wang, K. (2009). Soil erosion and sediment transport in the gullied Loess Plateau: scale effects and their mechanisms. *Sci. China Technol. Sci.* 52 (5), 1283–1292. doi:10.1007/s11431-009-0076-6

Liu, X. Y. (2016). *Causes of sharp decrease in water and sediment in recent years in the Yellow River*. Beijing, China: Science Press.

Liu, X. Y., Dang, S. Z., and Gao, Y. F. (2019). Sediment yield of current underlying surface under simulated extreme rainstorm in middle reaches of Yellow River Basin. *Trans. Chin. Soc. Agric. Eng.* 35 (11), 131–138 [in Chinese, with English summary].

Liu, X. Y., Dong, G. T., Gao, Y. F., Xia, R. L., Sun, Y., and Dang, S. Z. (2018). The sediment producing mechanism of the No. 5 sub-region of the loess hilly region in the Loess Plateau. *J. Hydraul. Eng.* 49 (3), 282–290 [in Chinese, with English summary]. doi:10.13243/j.cnki.slxb.20171082

Liu, X. Y., Li, X. Y., and Dang, S. Z. (2016). Spatial pattern of precipitation change in the main sediment-yielding area of the Yellow River basin in recent years. *J. Hydraul. Eng.* 47 (4), 463–472 [in Chinese, with English summary]. doi:10.13243/j.cnki.slxb.20150875

Liu, X. Y., Wang, F. G., Yang, S. T., Li, X. Y., Ma, H. B., and He, X. Z. (2014c). Sediment reduction effect of level terrace in the hilly-gully region in the Loess Plateau. *J. Hydraul. Eng.* 45 (7), 793–800 [in Chinese, with English summary]. doi:10.13243/j.cnki.slxb.2014.07.005

Liu, X. Y., Yang, S. T., Dang, S. Z., Luo, Y., Li, X. Y., and Zhou, X. (2014a). Response of sediment yield to vegetation restoration at a large spatial scale in the Loess Plateau. *Sci. China Technol. Sci.* 57 (8), 1482–1489. doi:10.1007/s11431-014-5605-2

Liu, X. Y., Yang, S. T., Wang, F. G., He, X. Z., Ma, H. B., and Luo, Y. (2014b). Analysis on sediment yield reduced by current terrace and shrubs-herbs-arbor vegetation in the Loess Plateau. *J. Hydraul. Eng.* 45 (11), 1293–1300 [in Chinese, with English summary]. doi:10.13243/j.cnki.slxb.2014.11.004

Meehl, G. A., Karl, T., Easterling, D., Changnon, S., Pielke, R., Changnon, D., et al. (2000). An Introduction to trends in extreme weather and climate events: observations, socioeconomic impacts, terrestrial ecological impacts, and model projections. *Bull. Am. Meteorol. Soc.* 81, 413–416. doi:10.1175/1520-0477(2000)081<0413: AITTIE>2.3.CO;2

Miao, C. Y., Ni, J. R., Borthwick, A. G. L., and Yang, L. (2011). A preliminary estimate of human and natural contributions to the changes in water discharge and sediment load in the Yellow River. *Global Planet. Change* 76, 196–205. doi:10.1016/j.gloplacha.2011.01.008

Nearing, M. A., Jetten, V. G., Baffaut, C., Cerdan, O., Couturier, A., Hernandez, M., et al. (2005). Modeling response of soil erosion and runoff to changes in precipitation and cover. *Catena* 61 (2–3), 131–154. doi:10.1016/j.catena.2005.03.007

Neill, C. R., and Mollard, J. D. (1982). Erosional processes and sediment yield in the upper oldman river basin, Alberta, Canada. *Hydrol. Sci. J.* 27 (2), 239.

Ran, D. C., Qi, B., and Xiao, P. Q. (2015). Response of extraordinary rainstorm and flood to the harnessing for underlying surface in Jialu River Basin. *Res. Soil Water Conserv.* 22 (6), 7–13 [in Chinese, with English summary].

Roering, J. J., Stimely, L. L., Mackey, B. H., and Schmidt, D. A. (2009). Using DInSAR, airborne LiDAR, and archival air photos to quantify landsliding and sediment transport. *Geophys. Res. Lett.* 36, L19402. doi:10.1029/2009GL040374

Shakoor, A., and Smithmyer, A. J. (2005). An analysis of storm-induced landslides in colluvial soils overlying mudrock sequences, southeastern Ohio, USA. *Eng. Geol.* 78 (3–4), 257–274. doi:10.1016/j.enggeo.2005.01.001

She, D. X., Xia, J., Song, J. Y., Du, H., Chen, J. X., and Wan, L. (2013). Spatio-temporal variation and statistical characteristic of extreme dry spell in Yellow River Basin, China. *Theor. Appl. Climatol.* 112 (1–2), 201–213. doi:10.1007/s00704-012-0731-x

Shi, F. C., Yi, Y. J., and Gao, Z. D. (1984). Flood in the middle reaches of the Yellow River in August 1933. *J. China Hydrol.* 4 (6), 55–58. [in Chinese with English abstract]

Shi, H. Y., and Wang, G. Q. (2015). Impacts of climate change and hydraulic structures on runoff and sediment discharge in the middle Yellow River. *Hydrol. Process.* 29, 3236–3246. doi:10.1002/hyp.10439

Shi, Z., Wen, A., Zhang, X., He, X., Li, H., and Yan, D. (2012). Cs-137 and Pb-210(ex) as soil erosion tracers in the hilly Sichuan Basin and the three Gorges area of China. *J. Mt. Sci.* 9 (1), 27–33. doi:10.1007/s11629-012-2200-5

Tang, K. L. (2004). *Soil and water conservation in China*. Beijing, China: Science Press. [in Chinese, with English summary].

Tian, X. F., Jia, Z. X., and Liu, B. (2008). *Analysis and study on the law of soil and water loss and benefits of soil and water conservation in typical small watersheds in the loess gully region*. Zhengzhou: Yellow River Conservancy Press [in Chinese, with English summary].

Trenberth, K. E. (2011). Changes in precipitation with climate change. *Clim. Res.* 47, 123–138. doi:10.3354/cr00953

Velicogna, I., and Wahr, J. (2006). Measurements of time-variable gravity show mass loss in Antarctica. *Science* 311 (5768), 1754–1756. doi:10.1126/science.1123785

Wang, H. J., Yang, Z. S., Saito, Y., Liu, J. P., Sun, X. X., and Wang, Y. (2007). Stepwise decreases of the Huanghe (Yellow River) sediment load (1950–2005): impacts of climate change and human activities. *Global Planet. Change* 57 (3–4), 331–354. doi:10.1016/j.gloplacha.2007.01.003

Wang, S., Fu, B. J., Piao, S. L., Lu, Y. H., Ciais, P., Feng, X. M., et al. (2016). Reduced sediment transport in the Yellow River due to anthropogenic changes. *Nat. Geosci.* 9 (1), 38–41. doi:10.1038/ngeo2602

Wang, W. Z., Jiao, J. Y., and Wei, Y. H. (2019). Relationship between sediment and rainfall and sediment variation in the main sediment yield area of the Yellow River. *J. Sediment. Res.* 44 (2), 41–47 [in Chinese, with English summary].

Wei, Y. H., Jiao, J. Y., Zhao, G. J., Zhao, H. K., He, Z., and Mu, X. M. (2016). Spatial–temporal variation and periodic change in streamflow and suspended sediment discharge along the mainstream of the Yellow River during 1950–2013. *Catena* 140, 105–115. doi:10.1016/j.catena.2016.01.016

Wetzel, K. (1994). “The significance of fluvial erosion, channel storage and gravitational processes in sediment production in a small mountainous catchment area,” in *Dynamics and geomorphology of mountain rivers*. Editors P. Ergenzinger and K. H. Schmidt (New York: Springer Berlin Heidelberg), 141–160.

Xin, Z. B., Yu, B. F., and Han, Y. G. (2015). Spatiotemporal variations in annual sediment yield from the middle Yellow River, China, 1950–2010. *J. Hydrol. Eng.* 20. doi:10.1061/(ASCE)HE.1943-5584.0001113

Yang, J., Yao, W., and Wang, L. (2013). Study on the mechanism and process of gravity erosion on the gully slope of Qiaogou Watershed. Proceedings of the 35th IAHR World Congress, Chengdu, China, September 8–13, 2013, VOLS I AND II, 4083–4091.

Yellow River Conservancy Commission (2008). *Flood control planning for the Yellow River basin*. Zhengzhou, China: Yellow River Conservancy Press [in Chinese, with English summary].

Zhang, D. X., Wang, G. H., Luo, C. Y., Chen, J., and Zhou, Y. X. (2009). A rapid loess flowslide triggered by irrigation in China. *Landslides* 6 (1), 55–60. doi:10.1007/s10346-008-0135-2

Zhang, M. S., and Liu, J. (2010). Controlling factors of loess landslides in western China. *Environ. Earth Sci.* 59 (8), 1671–1680. doi:10.1007/s12665-009-0149-7

Zhang, Y., Xia, J., and She, D. X. (2018). Spatiotemporal variation and statistical characteristic of extreme precipitation in the middle reaches of the Yellow River Basin during 1960–2013. *Theor. Appl. Climatol.* 135 (15), 1–18. doi:10.1007/s00704-018-2371-2

Zhao, C. Y., Lu, Z., Zhang, Q., and Fuente, J. D. L. (2012). Large-area landslide detection and monitoring with ALOS/PALSAR imagery data over Northern California and Southern Oregon, USA. *Rem. Sens. Environ.* 124, 348–359. doi:10.1016/j.rse.2012.05.025

Zhao, G. J., Mu, X. M., Jiao, J. Y., Peng, G., Sun, W. Y., Li, E. H., et al. (2018). Assessing response of sediment load variation to climate change and human activities with six different approaches. *Sci. Total Environ.* 639, 773–784. doi:10.1016/j.scitotenv.2018.05.154

Zheng, S. P. (1981). Contour map of heavy rainfall in August 1933 in the middle reaches of the Yellow River. *Yellow River, 1981*, 3 (5), 28–32. (in Chinese with English abstract)

Zhong, K. Y., Zheng, F. L., Wu, H. Y., and Qin, C. (2017). Effects of precipitation extremes change on sediment load in Songhua River basin, China. *Trans. Chin. Soc. Agric. Mach.* 48 (8), 245–253 [in Chinese, with English summary]. doi:10.6041/j.issn.1000-1298.2017.08.028

Conflict of Interest: The authors declare that the research was conducted in the absence of any commercial or financial relationships that could be construed as a potential conflict of interest.

Advantages of publishing in Frontiers

OPEN ACCESS
Articles are free to read
for greatest visibility
and readership

FAST PUBLICATION
Around 90 days
from submission
to decision

HIGH QUALITY PEER-REVIEW
Rigorous, collaborative,
and constructive
peer-review

TRANSPARENT PEER-REVIEW
Editors and reviewers
acknowledged by name
on published articles

Frontiers
Avenue du Tribunal-Fédéral 34
1005 Lausanne | Switzerland

Visit us: www.frontiersin.org
Contact us: frontiersin.org/about/contact

REPRODUCIBILITY OF RESEARCH
Support open data
and methods to enhance
research reproducibility

DIGITAL PUBLISHING
Articles designed
for optimal readership
across devices

FOLLOW US
@frontiersin

IMPACT METRICS
Advanced article metrics
track visibility across
digital media

EXTENSIVE PROMOTION
Marketing
and promotion
of impactful research

LOOP RESEARCH NETWORK
Our network
increases your
article's readership